Biomimetic vascular self-healing systems for cementitious materials

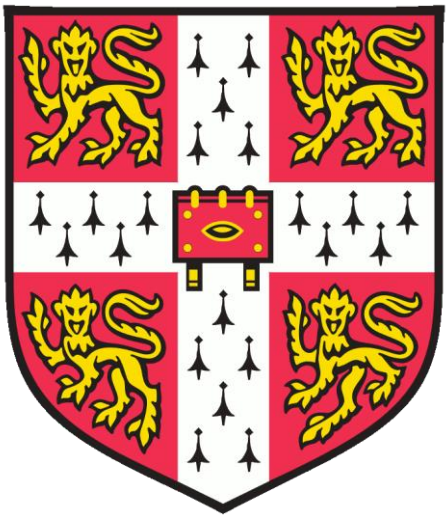

Zijing Li

Department of Engineering

University of Cambridge

This dissertation is submitted for the degree of

Doctor of Philosophy

Girton College

November 2020

Dedicated to my loving parents…

Declaration

I hereby declare that this dissertation is the result of my own work and includes nothing, which is the outcome of work done in collaboration except where specifically indicated in the text. The contents of this dissertation are original and have not been previously submitted, or, are being concurrently submitted, in part or whole, for consideration for a degree or diploma or other qualification at the University of Cambridge or any other University or similar institution except as declared in the Preface and specified in the text. In accordance with the Department of Engineering guidelines, this thesis does not exceed 65,000 words, inclusive of appendices, footnotes, tables and equations and it does not contain more than 150 figures.

Signed: _____

Date: _____

Zijing Li

Cambridge, November 2020

Abstract

Infrastructure, such as roads and skyscrapers are used by everyone in the city. They enable trade, power businesses, and protect cities from an increasingly unpredictable natural environment. Most of infrastructure is made out of cementitious materials. But the fact is, they all crack, no matter how carefully they are stored or reinforced. Most of the damaged cementitious structures will end up being replaced and reconstructed.

To address this national critical challenge, nature has always been a source of inspiration in engineering applications and vascular networks, as in human skin and in a tree leaf, are one attribute that has received attention in the design of resilient structures. A vascular system houses healing agent within its interconnected networks which are incorporated within a cement matrix. It is perhaps the only self-healing approach that has the capability to address different scales of damage in cementitious materials.

The main aim of the work is to develop novel vascular networks inspired by nature for self-healing in cementitious systems. Thus, the objective of this research is to explore the self-healing plastic-based networks/connected channels and healing mechanisms for both physically and chemically triggered self-healing in cementitious materials.

To achieve this, biomimetic three-dimensional (3D) vascular networks were designed and generated circulatory fluid volume transfer. The designed structures were constructed through 3D printing and assessed in a cement-based matrix. Mechanical testing assessed the compatibility of the system with the surrounding matrix as well as the functionality of the network in delivering and releasing the healing agent at the location of the damage. This initial proof of concept work confirmed the ability of the vascular systems to deliver the healing agent via physical and chemical triggers and demonstrated a significantly enhanced healing performance.

Acknowledgement

I must first begin by expressing my sincere gratitude to my supervisor, Professor Abir Al-Tabbaa, for the opportunity she provided in conducting this research, and her immeasurable support and invaluable inspiration over the past three years. Secondly, a huge thank to my advisor Dr. Athina E. Markaki for her kind advice on my papers and warm support on my first year and second year review meeting.

I would like to acknowledge the support from EPSRC for the Materials for Life project (EP/K06631/1), Ford of Britain fund and Pillman fund which allow me to pursue my PhD at Cambridge.

To my colleagues and friends in the lab: thank you all for your kind support and company during my research. In particular, I would like to thank Chris Knight, who has been always the core technical support in the lab, helping me go through the days when the 3D printers went crazy; Also I would like to thank David, Lorna, Phil, Martin, Anthony, Ket and Simon for assisting with my experiments in Structure Lab, Zoology Biotomography Centre, and Materials Science Department. My gratitude also goes to Dr. Lívia Ribeiro de Souza, Dr. Chrysoula Litina, Dr. Fei Jin, Dr. Amir Zomorodian, Dr Regeane Bagonyi, and Dr Rami Alghamri who has been mentors and esteemed friends, to Benyi, Ioanna, Yunhui, Wenting, Jingtao, Heba, Zixuan, Zijun, Qiaofeng, Regana, Xueying, Tianzheng, Jiang for their much valued friendship and support in my life at Cambridge. I would further like to thank the amazing partner and friends: Joshua, Maryam, Xiangyi and Consuelo who made Cambridge a home to me.

Finally, I would like to give my special my gratefulness to my parents for their affection and support providing the most patient backing to my research. Without your love, I would never go this far【感谢父母对我无条件的支持，是你们的爱让我走的更远】

“此去经年，不忘初心”

List of publications

The author is named as the first author and co-author on the following journal papers:

Li, Z., Souza, L.R., Litina, C., Markaki, A.E., Al-Tabbaa, A. 2019. Feasibility of Using 3D Printed Polyvinyl Alcohol (PVA) for Creating Self-Healing Vascular Tunnels in Cement System. Materials 2019, 12, 3872.

Li, Z., Souza, L. R., Litina, C., Markaki, A. E., Al-Tabbaa, A. 2020. A novel biomimetic design of a 3D vascular structure for self-healing in cementitious materials using Murray's law. Materials & Design, 190, 108572.

Litina C., Cao B., Chen J., **Li Z.**, Papanikolaou I., Al-Tabbaa A. (2019) 'First UK commercial deployment of microcapsule-based self-healing reinforced concrete', Journal of Materials in Civil Engineering – Accepted

Li, Z., Souza, L.R., Litina, C., Markaki, A.E., Al-Tabbaa, A. Self-healing mechanisms of a biomimetic vascular mortar system under varying healing agent circulation conditions, under review.

The author is named as the first author and co-author on the following conference papers and proceedings:

Li, Z., Souza, L.R., Litina, C., Al-Tabbaa, A. 2019. Biomimetic vascular network for self-healing cementitious materials. In ICSHM 2015: The 7th International Conference on Self-Healing Materials. Yokohama, Japan.

Li, Z., Al-Tabbaa, A. 2019. A biomimetic design of vascular network in self-healing cementitious materials. In the 1st SARCOS PhD Conference Self-healing Concrete Structures, Novi Sad, Serbia.

Li, Z., Al-Tabbaa, A. 2020. Healing performance of 1D/2D/3D vascular networks in cementitious materials. In the 2nd PhD Students and ECI meeting - Durability challenges in concrete with self-healing/repair technology, Guimarães, Portugal.

Li, Z., Al-Tabbaa, A. 2020. Behaviour of a porous vascular network in self-healing cementitious materials. In proceedings of the RM4L2020 International Conference, Cambridge, United Kingdom.

Litina C., Cao B., Chen J., **Li Z.,** Papanikolaou I., Al-Tabbaa A., Microcapsule-based self-healing concrete: From development to commercial deployment in 7th International Conference on Self-Healing Materials (ICSHM 2019), Yokohama, Japan, 2019.

List of contents

Chapter 4 3D self-healing vascular model design & performance in cementitious materials

Chapter 5 Feasibility of creating PVA (Poly-vinyl alcohol) channels

List of Figures

List of Tables

Symbol & Abbreviations

M_w	Water uptake quantity uptake per unit area of inflow surface
R_K	Stiffness recovery
σ_f	Stress in the surface midpoint
τ_0	Yield stress
γ	Shear rate
Δm	Mass changes
ρ	Water density
τ	Shear stress
ΔP	Pressure drop
1D/2D/3D	1/2/3 dimentional
A	Inflow area
ABS	Acrylonitrile butadiene styrene
Ag-Alg	Silver alginate
BS	British standards
CA	Crystalline additive/ cyanoacrylate
CEMI	Ordinary cement
Cl	Chloride
CO_2	Carbon dioxide
CS	Colloidal silica
CSA	Calcium sulfoaluminate cement
C-S-H	Calcium silicate hydrates
CT	Computational tomography
DCPD	Dicyclopentadiene
DIW	Direct ink writing
DTA	Differential thermal analysis
DTG	Differential thermogravimetry
EDX	Energy dispersive x-ray analysis
FDM	Fused deposition modelling
FTIR	Fourrier Transform Infrared Spectroscopy
HGFS	Hollow glass fibres
ILs	Ionic liquids

IPC	Inorganic phosphate cement
K	Bending stiffness/ consistency coefficient
L	Support span
LMA	Lauryl methacrylate
LWA	Lightweight aggregate
MF	Melamine formaldehyde
MgO	Magnesium oxide
MMP	Methyl methacrylate
MVN	Mini-vascular networks
Na_2SiO_3	Sodium silicate
Na-Alg	Sodium alginate
P	Load
PE	Polyethylene
PET	Polyethylene terephthalate
PET	Polyethylene terephthalate
pH	Negative logarithm of hydrogen ion concentration
PLA	Poly(lactic acid)
PMMA	Poly-methyl methacrylate
PP	Polypropylene
PS	Polystyrene
PSD	Particle size distribution
PVA	Polyvinyl alcohol
PVC	Polyvinyl chloride
PVDF	Polyvinylidene fluoride
Q	Volumetric flow rate
R	Hydraulic resistance
RCPT	Rapid Chloride Penetration test
s	Sorptivity coefficient
SAP	Super absorbent polymers
SC	Steel cords
SEM	Scanning electron microscopy
Si	Silica
SiO_2	Silica oxide (S)
SLA	Stereolithography
SMP	Shape memory polymers
SS	Sodium silicate
TEOS	Tetraethyl orthosilicate
TGA	Thermogravimetric Analysis
UF	Urea formaldehyde
UPF	Poly urea–formaldehyde
UV	Ultraviolet
w	Deflection
WoS	Web of Science
XRD	X-ray diffraction

Chapter 1
Introduction

The term “biomimetics” is derived from the Greek word “biomimesis”, “bios” (life) and “mimesis” (to imitate). It involves the interpretation of biological principles and design of commercial engineered products.

1.1 Motivation and rationale

Biomimicry is the transferal of biological principles to technology, applying concepts that will help us to go beyond conventional approaches in engineering. Examples of biomimetic studies include shape of bullet train copied from kingfisher (Hwang et al., 2015), boat paint inspired by the scales on sharks (Oeffner and Lauder, 2012), bubble shaped Chinese national aquatic centre developed from watercube in foam (Rao, 2014).

These inventions inspire us to facilitate the idea of self-healing into infrastructure, since we are facing critical national challenges in the construction field. Cement based infrastructure deteriorates over time under aggressive conditions (Sangadji, 2017). In the EU, 20% of all concrete repair works fail in the first 5 years, 55% within the first 10 years and all within 25 years. This leads to significant maintenance and repairing costs. Maintenance costs of existing cement-based structures accounts for approximately 45% of the total expenditure of construction industry, at around 40 billion pounds per year, in the U.K. (Tilly and Jacobs, 2007). In addition, some environments are inaccessible and do not lend themselves easily to inspection and repair. The repair methods and techniques, which have been applied to date, such as resin or grout injection into macro-cracks, bolting or gluing fibre reinforced strips to the tension face, ‘remove and replace’ techniques for parts of members, or in the most severe cases, replacement of structural

members in their entirety (Joseph, 2008). Traditional repairing works mostly requires the workforce to reach the damaged area, which makes it almost impossible to frequently send labour force to access infrastructure such as radioactive disposal containers, underground space and tunnels.

Self-healing systems from plants or animals has been mimicked to propose a delivery system to address damage events and enable multiple healing cycles. Recent advances in smart materials have led to the emergence of the field of self-healing materials and biomimetic structures in general. In particular, significant advances have been made on the development of self-healing cementitious systems using a number of different self-healing techniques generally over the last 20 years.

The healing process in cementitious material is divided into two categories: autogenous healing, which related with intrinsic properties of cementitious materials; and autonomic healing, which is associated with embedding of healing agents in the matrix (De Rooij et al. 2013). However, autogenous healing and some methods (e.g. microcapsules) in autonomic healing are limited by crack width – the crack needs to be roughly below 1 mm (Wang et al., 2014).

To pursue a long term and continuous healing process, the vascular network self-healing system was seen to be one of the most competitive methods, which could address larger damage and repeated damage. Dry (1992) was the first to demonstrate a vascular self-healing system in 1992, which was for repairing cracks in concrete and restoring its mechanical properties. This invention has been adapted into polymeric materials, such as fibre-reinforced composites (Bleay et al., 2001), carbon nanotubes (Sinha-Ray et al., 2012) and PVDF (polyvinylidene fluoride) nanofibres (Kolbasov et al., 2016).

The majority of work to date has focused on developing individual hollow tubes or gridded two dimensional (2D) networks for self-healing cementitious material and there has been little focused investigation on the three-dimensional (3D) networks or biomimetic structures in the cement-based specimens. Manufacture of complex vasculature has been restricted by small vessel diameters, large network coverage, high vessel strength and high network interconnectivity (Wang et al., 2015), thereby limiting fabrication process. Compared with 1D or 2D vascular structures, 3D or biomimetic networks have higher tunnel flexibility and more interaction with the cement-based matrix, so that they are more likely to have higher crack closure rate and better healing

efficiency. Besides, three dimensional (3D) networks are more complicated and consist of interconnected structures, which are capable of transporting healing agent to the damaged areas across the specimen's volume.

One worry is that the use of non-cementitious complex 3D vascular structures filled with healing agents would weaken the mechanical properties of cementitious materials. If a reduction in mechanical properties is observed, this must be outweighed by the increase in performance arising following a healing event. This part will be investigated in my PhD research as different dimensions of the structures, selected materials and pumping/non-pumping mode, will also be included as significant factors.

In general, in my PhD research, different vascular systems were developed for treating damages in terms of cracks triggering types (physical triggering and chemical triggering). For the physical-triggered approach, plastic based vascular structures were applied in treating large damage. Their healing performances were then evaluated by specimens' strength recovery, crack closure rate, bending stiffness and other factors. In addition, channel creation in the cement matrix using fugitive materials was explored to avoid tube monitoring. Tests were conducted to investigate the feasibility of applying this technology. When it comes to chemical triggering use cases, an alginate based ion sensitive material was synthesised to adapt on vascular systems, with the aim of controlling healing agent release over time.

1.2 Aims and objectives

The aim of this research project is to develop novel vascular networks for self-healing in cementitious systems. The system will address large damage (crack size >500 μm) and will be able to react with chemical attack and will hence be applicable to relevant scenarios. Development of vascular self-healing systems in cementitious materials will be the main focus of my PhD study, which follows a investigating process: (i) designing and manufacturing vascular networks in terms of different use cases; (ii) investigating the properties of fabricated structures; (iii) investigating vascular structure integration behaviours; (iv) characterising specimens mechanical and chemical properties; (v) validating damage and evaluating healing performance.

This research project focuses on investigating the use of vascular system in cementitious materials in terms of different use cases. For the first scenario, PLA (Polylactic acid) was selected to build up vascular systems due to its brittleness and workability, in reacting to physical triggered damage in the structures. Considering extra maintenance of the plastic based vascular after being embedded, creating hollow channels within cementitious mix directly could be a more ideal choose. PVA (Polyvinyl alcohol) was then chosen to act as a sacrificial material to create interconnected 3D channels in cement, since PVA is water soluble and able to be printed by 3D printers. The overall healing performance of cementitious materials was a main focus, and the feasibility of using PVA and chemical triggering vascular system were interests in this study. The objectives are therefore to:

1. Internal PLA vascular networks in cementitious materials for physical triggering

- Design internal 3D PLA printed vascular systems for cementitious materials.
- Characterise 3D printed vascular networks in cementitious materials thereby verifying their suitability for use in self-healing applications.
- Investigate the self-healing performance of cementitious materials incorporating vascular systems and healing agents using a series of testing procedures and microstructural analysis techniques.

2. Feasibility of creating PVA vascular tunnels

- Investigate feasibility of applying PVA as a sacrificial material.
- Evaluate PVA model survival capability in cementitious material.
- Fabricate and characterise hollow channels in the cementitious materials.

3. Chemical triggering vascular system

- Synthesise and investigate the behaviour of chemical triggering materials used in vascular systems.
- Evaluate the effects and sensitivity of using chemical triggering materials during chemical attack events.
- Design and evaluate suitable vascular models for chemical sensitive materials.

1.3 Structure of the report

This report has been divided into seven chapters. Chapter 1 provides an introduction to the main motivations for choosing this topic, and the aims and objectives of this work. In Chapter 2, a critical literature review is presented, addressing main technologies and applications for both autogenous healing and autonomic healing processes. This chapter further discusses detailed classification of circular systems in terms of their dimensions and various approaches. In particular, biomimetic approaches in fabricating circular systems are being explained in relevance with their biological background. Chapter 3 describes the materials, experimental and characteristic methods used in producing vascular structures and analysing healing performance. Chapter 4 presents findings relating to the design of a biomimetic vasculature and their self-healing performances in cement and mortar specimens; Chapter 5 presents findings relating to the feasibility of creating hollow connective tunnels in cement via a water soluble PVA material, while the results of the coating materials and chemical triggering viability between coating materials and chloride solution are presented in Chapter 6. Then, conclusions are made in Chapter 7 throughout this work, which follows up with the final recommendations for future research within this area.

Chapter 2
Literature Review

This chapter critically reviews the various literature sources relevant to the topic of vascular-based self-healing. It starts with a brief overview of the sustainability and durability concerns, challenges outlining the global problems associated with the cement and concrete industries, and the proposed solutions to tackle these challenges. In reacting with the challenges of cost-effective, durability and sustainability encountered in the construction industry, a review of different categories of the advanced materials and structures is also presented with a particular focus on the engineered self-healing materials. Before diving further to the details, a data-driven literature analysis on self-healing research development is presented in understating the research development trend in self-healing. Then, self-healing in the cement-based materials is reviewed thoroughly. The latter includes both autogenous and autonomous self-healing concepts, processes and techniques. Thereafter, the performance of each technique including encapsulation, vascular system and chemical triggered system was explained and reviewed in detail. Finally, the chapter concludes the research gaps and rationale behind the research work.

2.1 Global infrastructure challenges and demand

> *"We shape our buildings and, afterwards, our buildings shape us."*
>
> *— Winston Churchill, 1944*

Infrastructure is the backbone of modern society. They enable trade, power businesses, connect workers to their jobs, create opportunities for struggling communities and protect cities from an increasingly unpredictable natural environment. As an industry, demand

in global infrastructure is increasing over time. The construction sector accounts for 6% of global GDP (Gross Domestic Product), with total annual revenues of almost $10 trillion and added value of $3.6 trillion (World Bank, 2014). More specifically, it accounts for roughly 5% of total GDP in developed countries. While in developing countries, it tends to account for more than 8% of GDP. The industry is expected to grow greatly in the coming years, to estimated revenues of $15-20 trillion by 2030 (World Economic Forum, 2016).

The construction industry is greatly affected by megatrends in four domains: 'markets & customers', 'sustainability & resilience', 'society & workforce', and 'politics & regulation' (Flyvbjerg et al., 2003). Investment gap, climate change, complex projects and ageing for infrastructure from 'sustainability & resilience' and 'market & customers' metrics have been presented with both high impact and significance in the global construction industry (Figure 2.1).

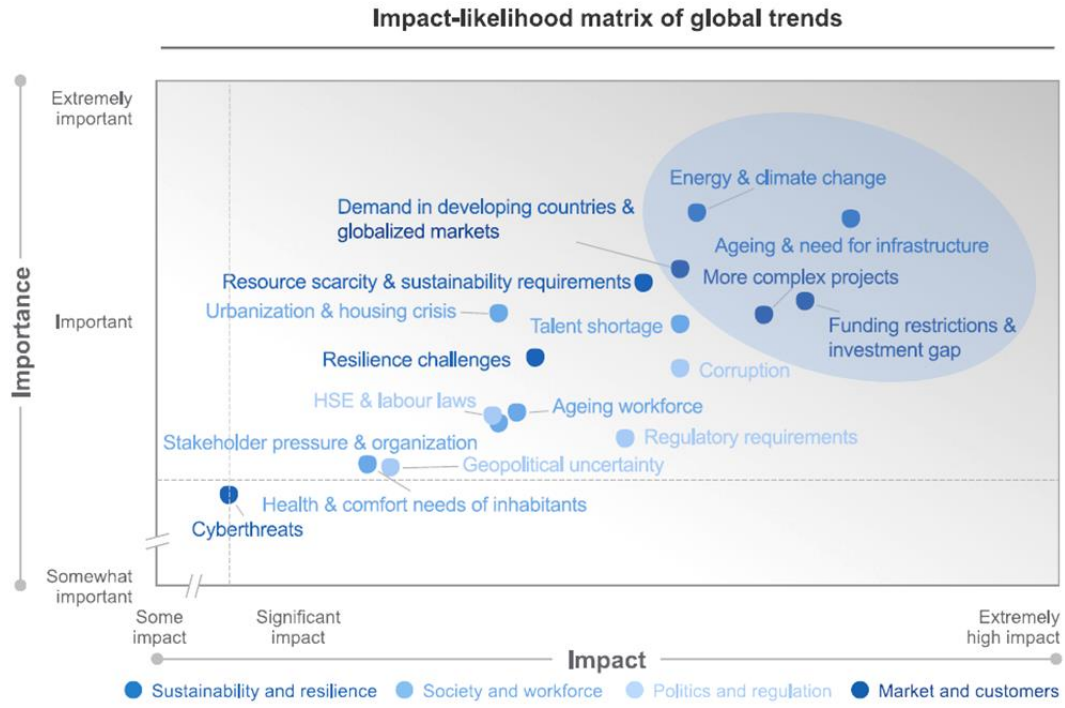

Figure 2.1 Global Trends – Their Importance for and Impact on the E&C Industry (diagram adopted from Future of Construction Survey (World Economic Forum, 2015)), the blue shaded area highlighted the top 4 driven forces in megatrend.

All four megatrend driven forces are linked with each other: A comprehensive investment gap of around US$ 1 trillion has been built up each year since the global demand reached a value of about US$ 3.7 trillion, with only about US$ 2.7 trillion being physically invested in development each year (BCG, 2014). This financial gap in the

construction industry could be narrowed by (i) reducing demand in new infrastructure via optimising the maintenance of existing buildings, therefore the age of establishments were extended; on the other hand, carbon emissions from rebuilding could be therefore mitigated; (ii) creating new establishments with durability performance and extended lifespans to reduce maintenance costs, and these new durable engineered structures made it possible to complete sophisticated projects.

In this case, the value, therefore, lies in improving the quality of construction and the quality of materials used, in contributing to a more durable infrastructure, increasing its sustainability and reducing its cost (BCG, 2015). Any endeavour towards this goal will generate welcome benefits.

2.1.1 Challenges in existing infrastructure

Developed countries have been typically facing the problem of dealing with ageing infrastructure that were established mostly in the second half of the last century (Polder et al., 2012) while expanding the current infrastructure constitutes a minor portion in these nations' construction activity (Figure 2.2).

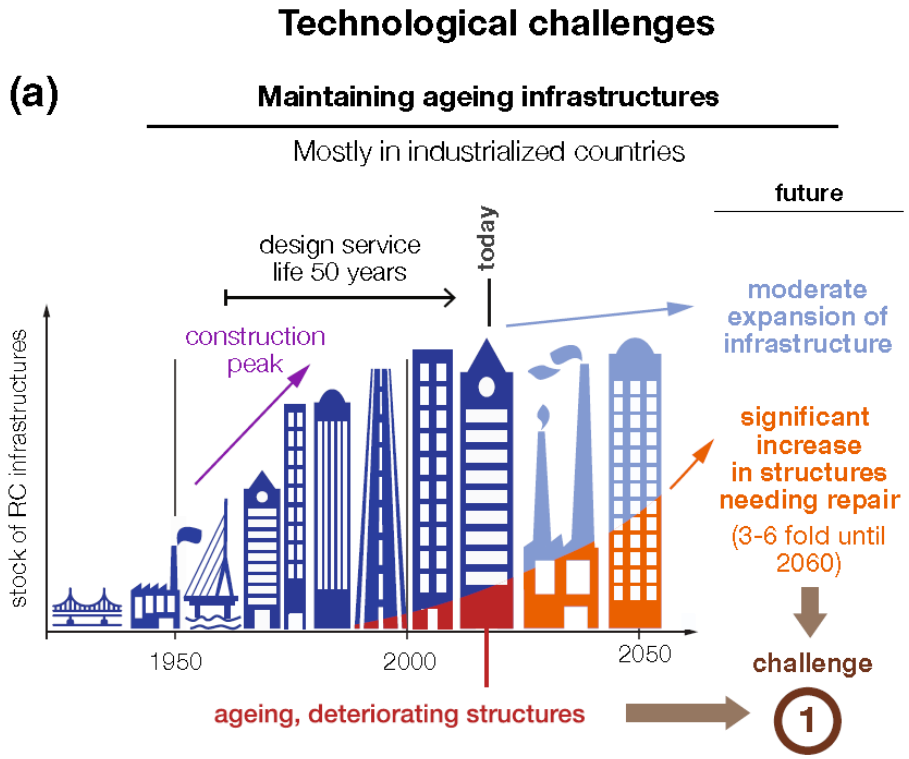

Figure 2.2 Technological challenges in industrialised countries are mainly challenged to maintain their stock of existing infrastructure (Adopted from Angst, 2018)

Cracking is the dominant source of damage to existing concrete structures with roughly 90% of all respondents voted in the survey, water ingress and impact damage are also highly influenced with around 85% respondents voted, (Figure 2.3, Gardener et al., 2018). Although single crack opening may not hamper the overall safety of structures, the reason of this initial brittleness is related with steel reinforcement corrosion, early age shrinkage, brittleness of concrete and loading damage (Safiuddin et al., 2018). Additionally, cracks also threaten general retaining of infrastructure. For instance, cracks may provide undesirable paths for fluid ingress (Bentz, 2008), such as water, petroleum, toxic materials and radioactive leaching to unexpected areas, causing health, economic and ecological issues. For instance, Daiichi Nuclear power plant in Fukushima was reported leaking a few million tons of highly radioactive water into the sea via cracks in the reactor pit after seismic damage (Morita et al., 2020), consequently polluting fishery products and inducing health concerns.

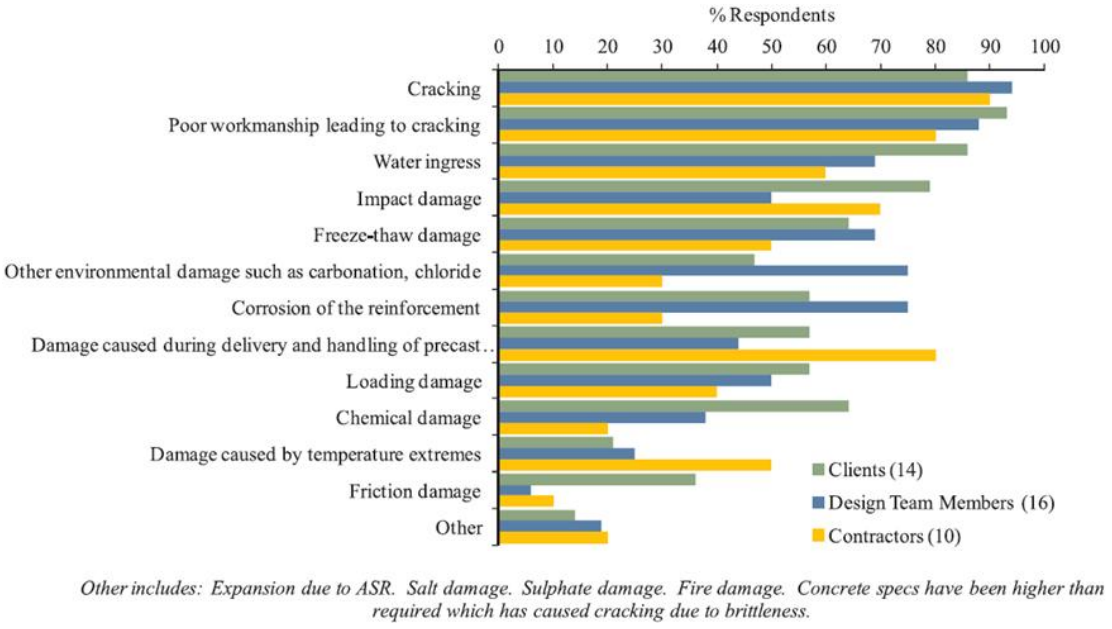

Other includes: Expansion due to ASR. Salt damage. Sulphate damage. Fire damage. Concrete specs have been higher than required which has caused cracking due to brittleness.

Figure 2.3 The main causes of damage in concrete structures (Gardner et al., 2018)

By 2021, the UK committed to an investment of £100 billion in infrastructure (UK Treasury, 2016). Its maintenance costs in existing cement-based structures account for approximately 45% of the total expenditure of the construction industry, at around 40 billion pounds per year (DTI, 2006). In Europe, similarly, approximately 50% of the European annual national budget was spent on the repair and maintenance of existing structures (Sangadji and Schlangen, 2012). Among the many elements of this complex

system, road infrastructure (including bridges) is especially important and the most vulnerable due to aggressive environments (Gardener et al., 2018) such as increasing traffic volumes and heavier truckloads, (Asakura et al., 1991) which degrade the long-term performance of road infrastructure at an alarming rate (Frangopol and Liu, 2007). Figure 2.4 reveals the annual repair and maintenance cost of road infrastructure in 10 leading countries (data collected from OECD (Organisation for Economic Cooperation and Development) in 2020). Infrastructure maintenance data covers spending on the preservation of the existing transport network only via public administrations. As shown in the figure, developed countries such as the US, Japan, Italy, Canada and the UK invested more in annual road infrastructure repair and maintenance than others mainly due to several major road renovation works undertaken in last two decades (Burchell et al., 2010; Akai, 2016; European Commission, 2019).

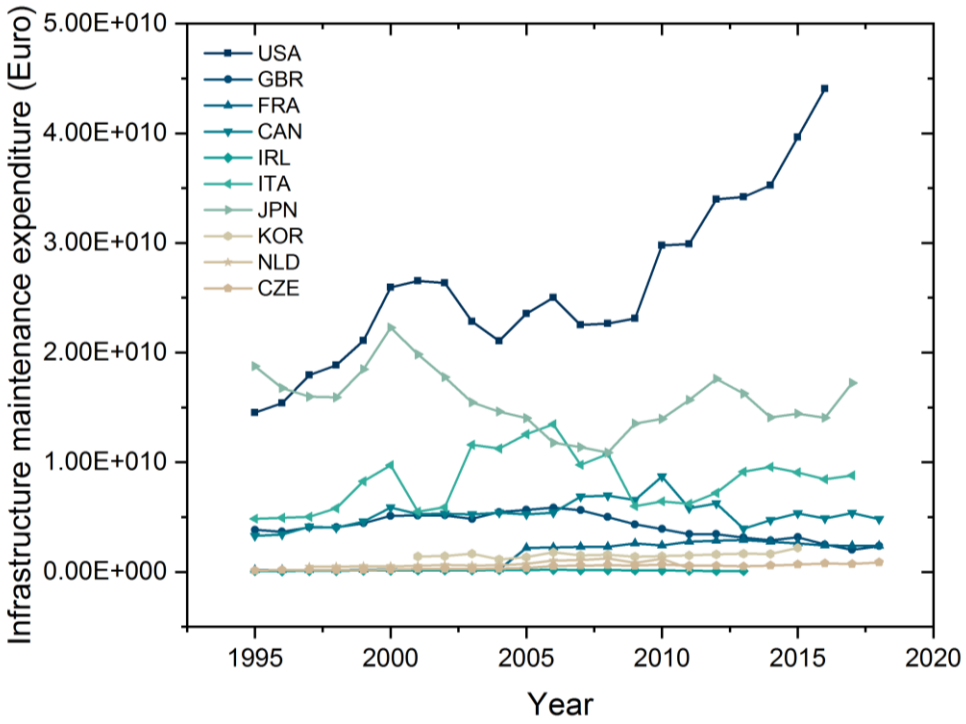

Figure 2.4 Road infrastructure annual repair and maintenance cost of 10 highlighted countries (data collected from OECD (Organisation for Economic Cooperation and Development)/ITF, (2020)).

However, it is also widely acknowledged that repair works of infrastructure are generally not very effective (Al-Tabbaa et al., 2018). In the EU, 20% of all concrete repair works fail in the first 5 years, 55% within the first 10 years and all within 25 years (Tilly and Jacobs, 2007).

Most of the damaged cementitious structures will end up with being replaced and reconstructed, which runs counter to maintaining sustainability. Considering the expected increase in needed repair works over the coming decades (Polder et al., 2012), there is certainly an urgent need in requesting innovative and cost-effective technologies.

2.1.2 Challenges in sustainable new infrastructure

In emerging countries, on the other hand, there is still a large need in expanding their infrastructure (Schwab, 2017) in line with the economic growth and urbanisation, and thus their main challenge lies in the design of durable new structures (Figure 2.5).

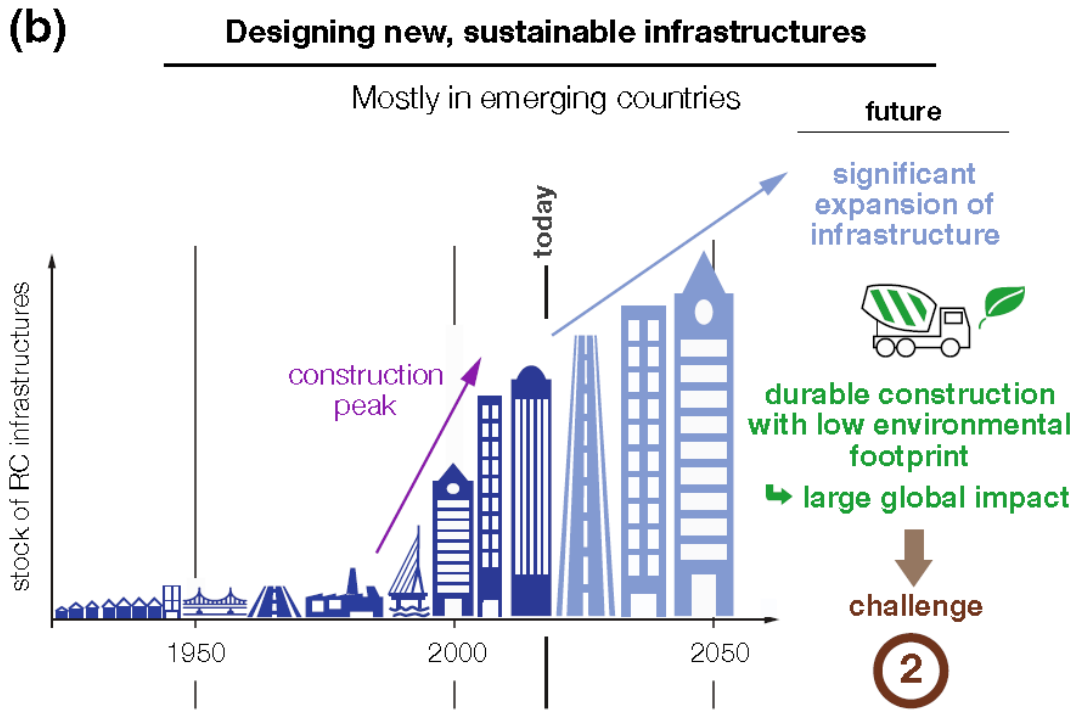

Figure 2.5 Technological challenges in developing countries are mainly challenged to design sustainable and durable new structures in expanding their infrastructure, where the everincreasing diversity in construction materials and processes does not anymore permit relying on empirical long-term experience (Adopted from Angst, 2018)

Urban population in developing regions such as China, India, South-Eastern Asia and Sub-Saharan Africa have grown rapidly since the 1990s (Figure 2.6). Demand for new infrastructure is also growing. Specifically in China, the number of highway bridges increased from 658,100 in 2016 to 878,300 in 2019 (Statista, 2019). According to the forecast from Statista, China was predicted to need over US$ 23.6 trillion, of which 63% for new infrastructure between 2017 and 2035.

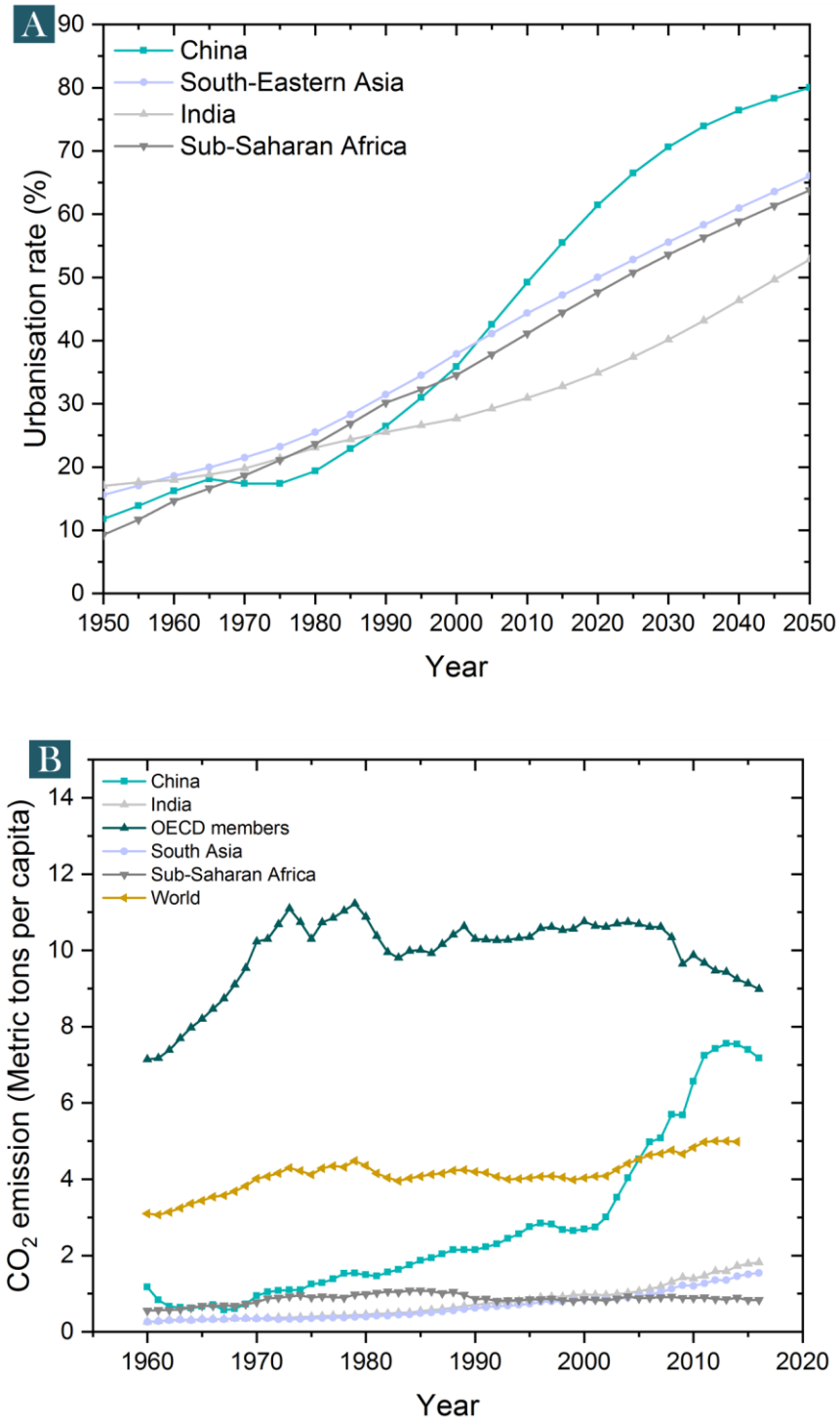

Figure 2.6 Urbanisation rate in developing countries and regions (A, data collected from UN, World Urbanisation Prospects division) and CO_2 emission (B, data collected from World Bank)

Emerging countries like China have a massive demand for new infrastructure to fulfil their need for economic growth and urbanisation. However, construction of new infrastructure will increase carbon emissions, as most of the infrastructure is made from cement-based materials (Damtoft et al., 2008). Concrete, as the major infrastructure

material, embodies anthropogenic carbon emission of about 0.35 kg C/kg (Sangadji, 2017). The production of cement alone, for instance, generates between 5-8% of global anthropogenic CO_2 emissions (IPCC, 2004, 2018). The high CO_2 emission from concrete can be partitioned into three primary categories: (i) 55 % to 60 % to the thermal decomposition of limestone (i.e., to produce lime, the base reagent needed for production), (ii) 30 % to 35 % to energy needs of the process, and (iii) 10 % to transportation (Ke et al., 2013).

Besides, operating and constructing related activities account for 36% of global final energy use and 39% of energy-related CO_2 emissions according to a recent IPCC (2018) special report. In this context, IPCC also states that "1.5 °C-consistent pathways require building emissions to be reduced by 80–90% by 2050, new construction to be fossil-free and near-zero energy by 2020". To achieve this goal, a number of countries, mostly in developed countries, such as the UK, Ireland, Japan etc., have already implemented CO_2 taxes that range from $2 (USD) to $168 per equivalent short ton (tCO_2e) of CO_2 produced (World Bank, 2014) to motivate construction companies in managing CO_2 emissions.

In order to mitigate the CO_2 emission, renewable energy sources could be applied to minimise CO_2 burden produced in the transportation process. However, managing the CO_2 release associated with limestone decomposition is an unresolved challenge. This might point that cement production will be forced to change due to environmental factors (Schneider et al.,2011; Biernacki et al., 2017)

Thus, in emerging regions, a huge positive sustainability impact can potentially be made if proper construction materials are used, i.e., by combining low environmental footprint of the material with long service lives.

2.2 Biomimicry in smart infrastructure

2.2.1 Biomimitic cementitious materials

In reacting to the challenges of cost-effectiveness, durability and sustainability encountered in the construction industry, Flatt et al. (2012) proposed six solutions for upgrading tomorrow's materials for the future cementitious-based infrastructure:

i. Partial cement replacement by supplementary cementitious materials;

ii. Development of alternative binders;

iii. Broader use of concrete mix designs that limit cement content;

iv. Recycling of demolished concrete in new concretes;

v. Enhancement of durability (designing new infrastructure for longer service life)

vi. Rehabilitation of existing infrastructure (extending the service life of existing infrastructure)

Considering the technological challenges in maintaining existing establishments and building 'greener' new infrastructure, a quest for the design of resilient infrastructure responding to both mechanical and environmental needs, has led to the development of biomimetic materials. A few researchers realised that the security and reliability of structures could be significantly improved if construction materials have the biomimetic capacities, such as self-sensing, self-adjusting and self-healing, to monitor the potential defects, and thereby reducing substantial maintenance and enable further sustainability (Wang et al., 2016).

Materials with the function of sensing & responding to the variation of environment, with self-sensing, self-healing and self-shaping were defined as intelligent materials (Spillman et al., 1996). Since then, extensive research on composition, proceeding, property and mechanism, measurement and application of various intelligent construction materials has been conducted via experimental study, theoretical analysis and numerical simulation (Han et al., 2015). Thirteen self-x concrete types were summarised in Figure 2.7, intelligent concrete with performances of self-compacting, self-expanding, self-curing, self-sensing, self-healing, self-adjusting, self-damping, self-heating, self-sacrificing, self-cleaning, self-shaping, self-draining and self-luminous (Wang et al., 2016).

For instance, self-shaping concrete (3D printing technology) is a new manufacturing paradigm for the 21st century, which removes many design tethers, reduces material consumption and the associated labour force (Biernacki et al., 2017). Moreover, it could get stronger under pressure, inspired specifically by arthropods, whose shells become stronger when pressure applied (Gu et al., 2016). Self-shaping concrete is already being demonstrated at moderately large scales in the US, China and Europe in recent years (Charron, 2015).

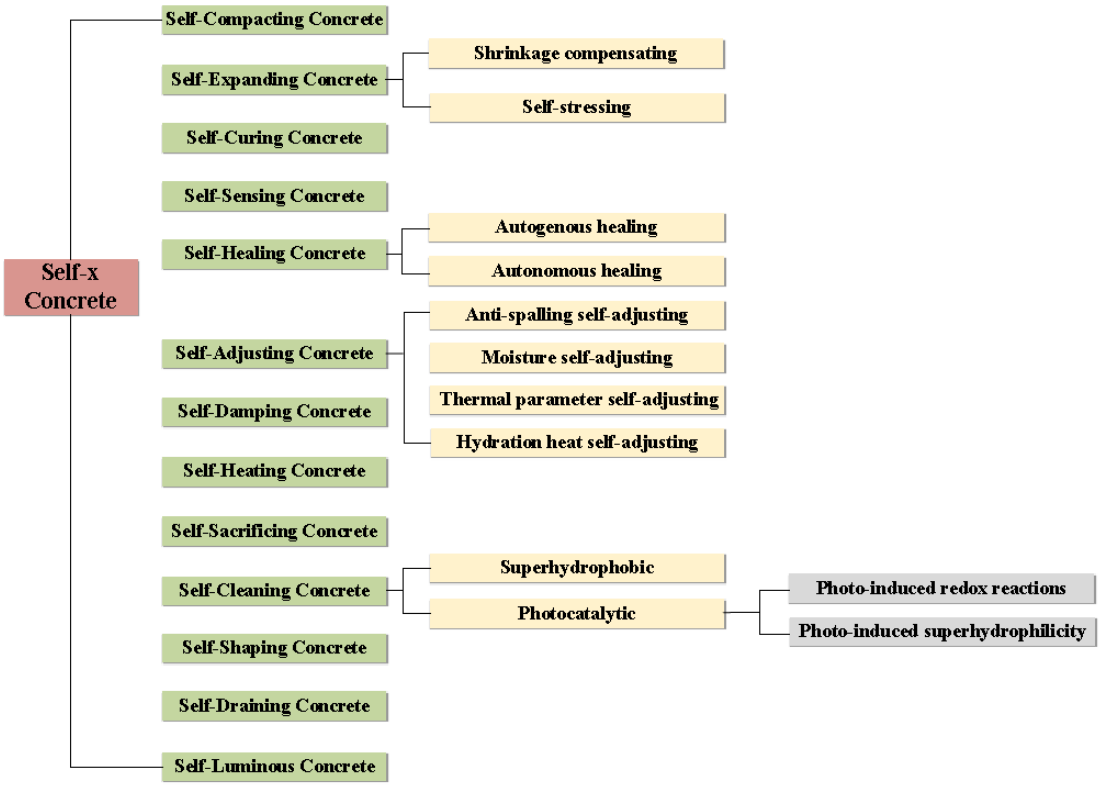

Figure 2.7 Categories of self-x concrete (Wang et al., 2016)

Self-cleaning concrete is another novel biomimetic invention inspired by the Lotus Effect (Koch et al., 2008), as the leaves of the lotus plant remain clean and free of dirt from muddy habitats. The durability of self-cleaning concrete can be optimised by the characteristic of superhydrophobicity to decrease water absorption (Ganesh et al., 2011), which makes concrete valuable in the long run of construction for reducing the restore costs (Wang et al., 2016).

Possibly the most significant and transformative technology to emerge is self-healing. Inspired by the nature of blood clotting or remoulding of fractured bones in living things, the same concept is incorporated into the engineering materials by scientists, making them possess the ability to repair or heal damage by themselves (Dry, 1994). Applying the concepts of self-healing in cementitious material could increase infrastructure sustainability and boost biosphere stability, which perfectly fit the requirements of future cementitious materials. Two full-scale self-healing projects have been trialled successfully in the UK firstly, a demonstration project on the Welsh Government A465 Heads of the Valleys Upgrade project (Teall et al., 2016), and secondly, a commercial application on the new James Dyson Building extension to the Department of Engineering at the University of Cambridge – both conducted by the M4L project team in 2015 (Al-Tabbaa

et al., 2018). Thus, the self-healing technique in cementitious materials showed great potential benefits and provided confidence that can be expected in the near future.

2.3 Self-healing in cementitious materials

2.3.1 Definition of self-healing

Self-healing is a natural process that automatically initiates repair of damage for living organisms. Inspired by nature, researchers are trying to adopt this special ability into artificial materials to extend their longevity (Diesendruck et al, 2015). The idea of self-healing was first introduced in polymeric materials in 1969 (Malinskii et al., 1969). In 1994, Dry was the first one who introduced the self-healing concept into concrete and then researchers started to work on this field (Dry, 1994; Dry, 1996).

2.3.2 A scientometric analysis of self-healing development trend

In the past few decades, a large number of papers and scholars have emerged in the self-healing field, which is developing vigorously. This may make it tough to grasp the research focus and status quo from hundreds of papers. So, before diving further into the details, a data-driven literature analysis on self-healing research development is presented in this section with the aim of exhibiting a more intuitive research and development process with a visualisation tool.

In this section, the focus was on revealing the changes and information dynamics in the self-healing cementitious field over the time cycle and the literature data were from WoS (Web of Science). A Java-based visualisation tool CiteSpace 5.7.R1.2020(Chaomei Chen, Drexel University, Philadelphia, USA) was employed and could generate literature keyword networks, citation burst, and so on to determine the internal structure of the field, knowledgebase, research hotspots, and research frontiers in different time periods (Chen, 2006).

As the literature related to self-healing concrete included in the WoS started in 1995, the search time of this article was set from 1995 to 2020. It was shown that there were 1085 documents in the WoS core database (data collected in August 2020).

The size of the circle corresponding to the keywords in Figure 2.8 A is proportional to the co-occurrence frequency of the keywords, and the lines between the circles represent

the mutual relationship between the keywords (Chen, 2017). On the basis of this network, summarised keywords shown could provide the research frontier that is constantly developing in the field.

Aside from self-healing (which is the main research question), the most mentioned category of keywords, such as “cracking”, “crack sealing”, “crack width”, are related to the cracking issues in cementitious materials (Figure 2.8 C). These terms are in line with the research priorities in the cracking challenge encountered in construction industry discussed in section 2.1.

The second category of keywords in Figure 2.8 B, such as “protection”, “immobilisation”, “durability” are related to the behaviours before and after the healing process. The reason is that the healing performance affects the general strategy in extending the lifespan of structures for further sustainability; it runs through the entire testing and trial process and is an important part of the research.

The third category of keywords, such as “microcapsules”, “microencapsulation”, “encapsulation” are related to capsule based self-healing in concrete. This is a widely used self-healing technique that is able to deal with cracks generated in cementitious material (Souza, 2017). Co-occurrence frequency of capsule-based technique implying it has been a research hotspot in self-healing field, and this technique will be further discussed in the following sections.

The fourth category of keywords, such as “bioconcrete”, “bacillus pasteurii”, “bacterial biomineralsation”, “bacillus sphaericus” are related to bio-based self-healing concrete. Jonkers and coworkers applied bacterial spores and nutrients into the fresh concrete mix, and then the bacteria initiate the production of $CaCO_3$ crystals which deposit at the crack faces (Jonkers, 2007). This category shows bioconcrete have been through detailed studies and could be a competitive candidate in building up sustainable infrastructure.

Other keywords did not form a systematic category of keywords in scientometric analysis, which indicated that they were either with relatively lower impact than the ones discussed above or haven’t transformed into research hotspots yet.

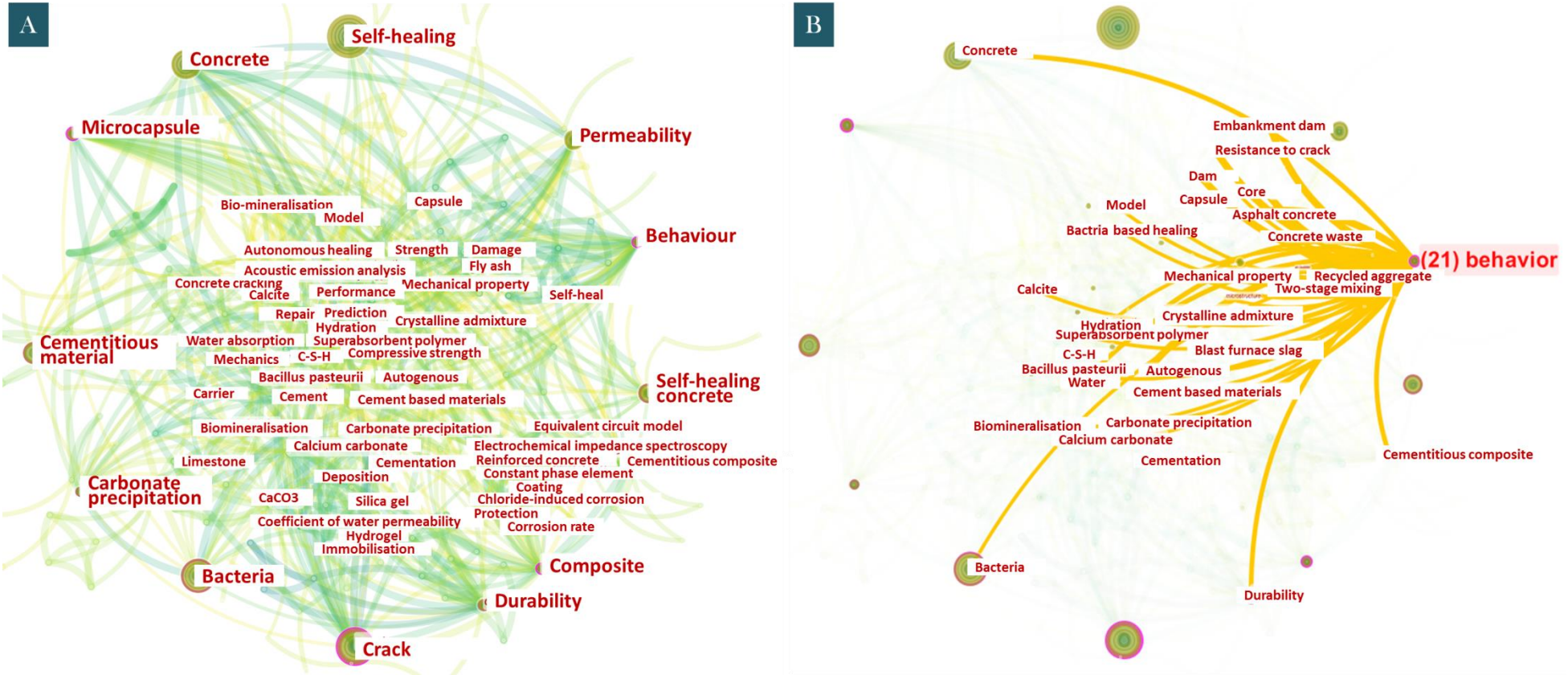
A
Self-healing
Concrete
Microcapsule
Permeability
Behaviour
Cementitious material
Self-healing concrete
Carbonate precipitation
Bacteria
Composite
Durability
Crack
Bio-mineralisation
Capsule
Model
Autonomous healing
Strength
Damage
Acoustic emission analysis
Fly ash
Concrete cracking
Calcite
Performance
Mechanical property
Self-heal
Repair
Prediction
Crystalline admixture
Hydration
Water absorption
Superabsorbent polymer
Mechanics
C-S-H
Compressive strength
Bacillus pasteurii
Autogenous
Carrier
Cement
Cement based materials
Biomineralisation
Carbonate precipitation
Equivalent circuit model
Calcium carbonate
Electrochemical impedance spectroscopy
Limestone
Cementation
Reinforced concrete
Cementitious composite
Deposition
Constant phase element
CaCO3
Silica gel
Coating
Chloride-induced corrosion
Protection
Coefficient of water permeability
Corrosion rate
Hydrogel
Immobilisation
B
Concrete
Embankment dam
Resistance to crack
Dam
Core
Capsule
Model
Asphalt concrete
Bactria based healing
Concrete waste
(21) behavior
Mechanical property
Recycled aggregate
Two-stage mixing
Calcite
Crystalline admixture
Hydration
Superabsorbent polymer
Blast furnace slag
C-S-H
Bacillus pasteurii
Autogenous
Water
Cement based materials
Biomineralisation
Carbonate precipitation
Calcium carbonate
Cementitious composite
Cementation
Bacteria
Durability

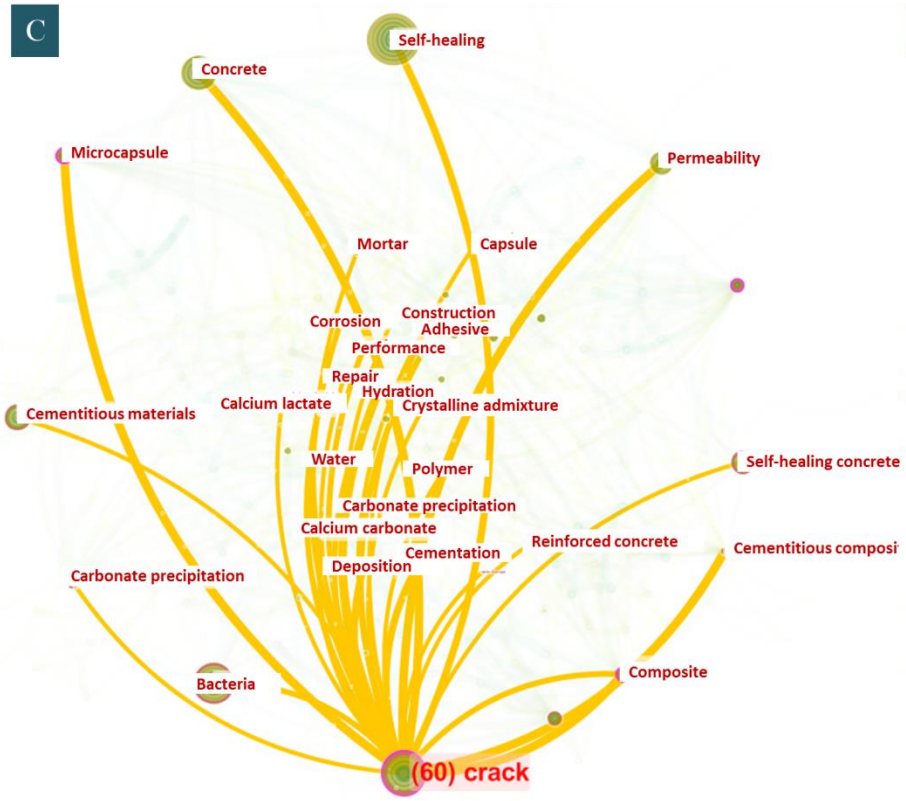
C
Self-healing
Concrete
Microcapsule
Permeability
Mortar
Capsule
Corrosion
Construction
Adhesive
Performance
Repair
Hydration
Calcium lactate
Crystalline admixture
Cementitious materials
Water
Polymer
Self-healing concrete
Carbonate precipitation
Calcium carbonate
Cementation
Reinforced concrete
Cementitious composi
Deposition
Carbonate precipitation
Bacteria
Composite
(60) crack

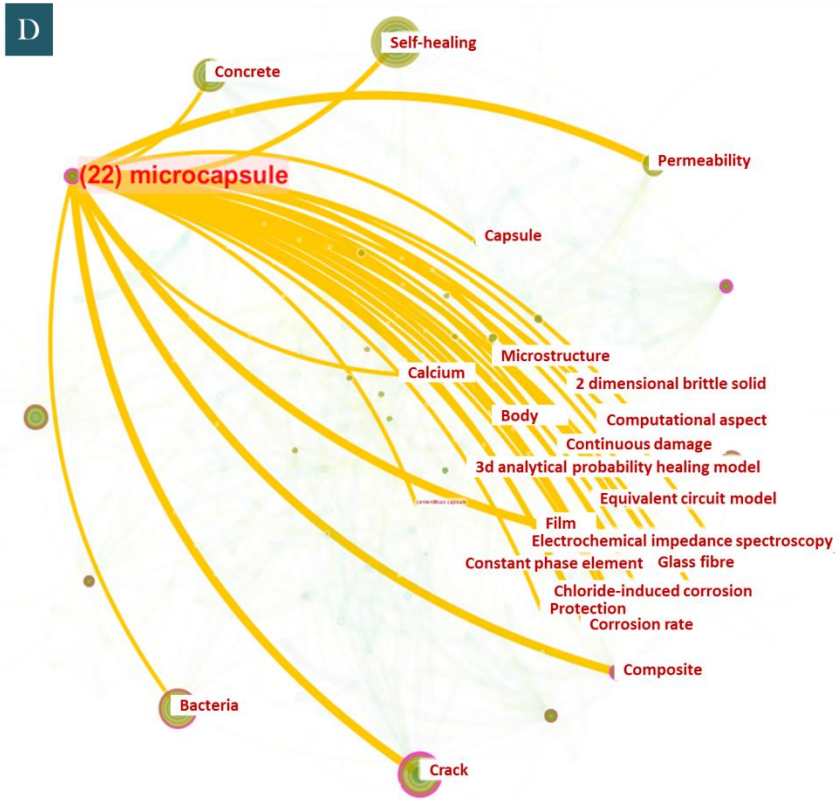
D
Self-healing
Concrete
Permeability
(22) microcapsule
Capsule
Microstructure
Calcium
2 dimensional brittle solid
Body
Computational aspect
Continuous damage
3d analytical probability healing model
Equivalent circuit model
Film
Electrochemical impedance spectroscopy
Constant phase element
Glass fibre
Chloride-induced corrosion
Protection
Corrosion rate
Composite
Bacteria
Crack

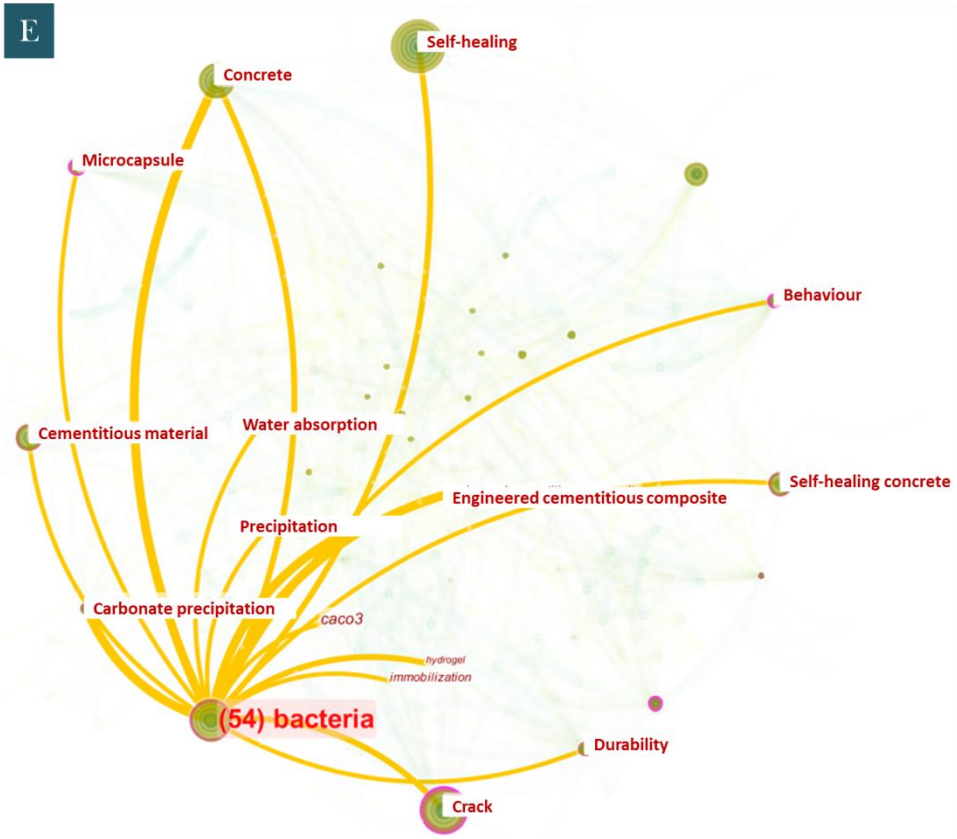

Figure 2.8 Keyword co-occurrence diagram of self-healing (A, blue to yellow representing the year of publication, blue representing earlier publications since 1995, yellow representing new publications till 2020), connection of keyword 'behaviour' (B), connection of keyword 'crack' (C), connection of keyword 'microcapsule' (D), connection of keyword 'bacteria' (E)

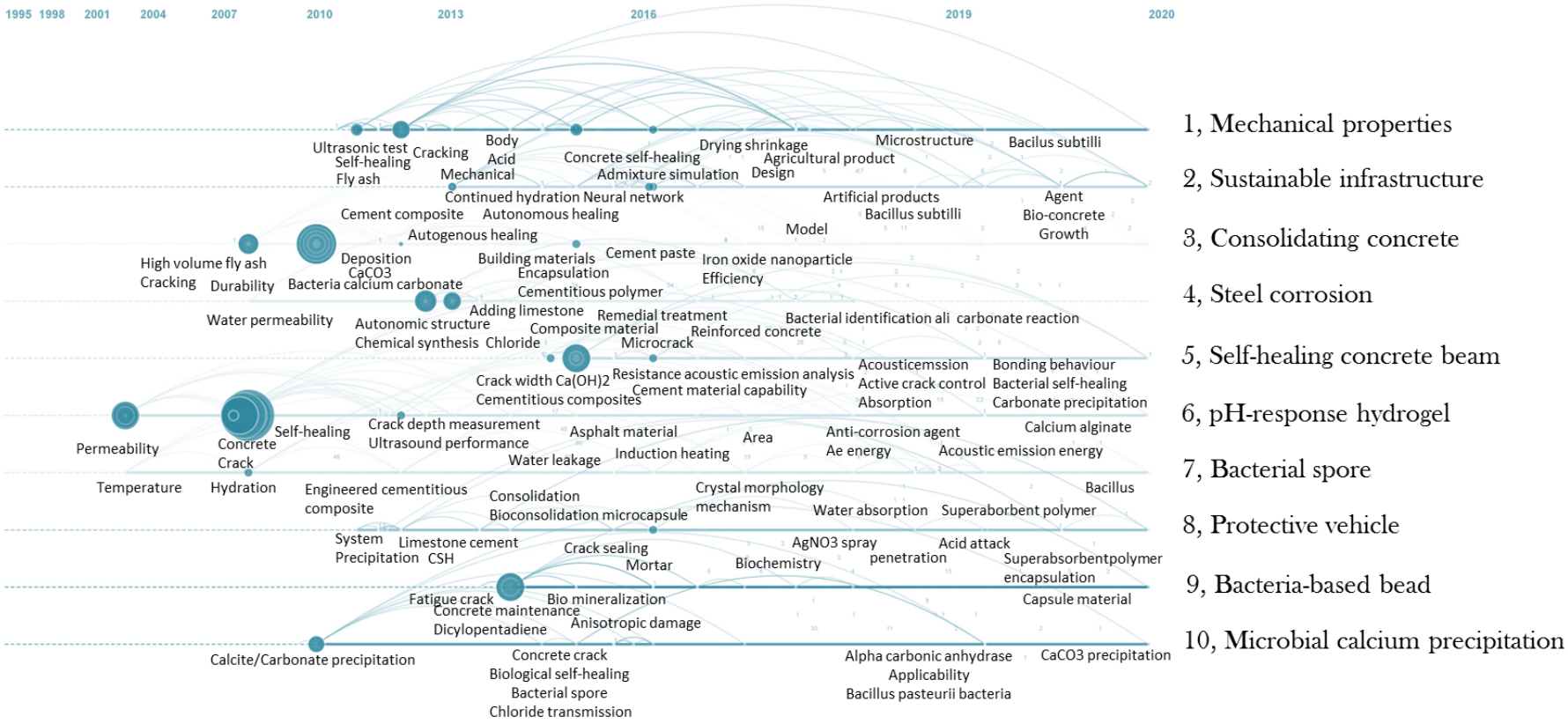

Figure 2.9 Visualisation of keywords by time series with top 10 highly mentioned clusters (Note the bubble size was the sub-keywords frequency mentioned in literatures in each cluster)

The co-occurrence network diagram only shows the frequency and their connections, while cannot be efficiently combined with the time relationship. To discover the research trend in cementitious self-healing, a timeline diagram was used (Figure 2.9) for delineating the relationship between clusters and the historical span of a certain cluster keyword. The historical axis represents time, and the vertical axis on the right represents the name of each cluster. Top 10 clusters were selected by Citespace corresponding to 10 timelines.

High-frequency keywords appeared mostly before 2016. The clusters in which they appear are as follows: "3 consolidating concrete", "4 steel corrosion", and "5 self-healing concrete beam", "6 pH-response gel" and "9 bacteria-based beads". Concerns of cracking, concrete permeability and steel corrosion triggered damages among researchers were emerged firstly in around 2000, thus pH-response gel and consolidating concrete gained research popularity between 2000 and 2010. Then, following studies paid more attention to evaluating concrete behaviours after new engineered materials added. Keywords such as "$Ca(OH)_2$", "crack width", "ultrasonic test" became the new hotspots after 2010. While few keywords hotspots were seen from the timeline diagram in all clusters after 2016. It is unlikely that the popularity of self-healing in concrete was declined since the publications in this field have been rising over the past few years, with roughly 180 publications in 2019 and 140 publications in the first half of 2020 according to WoS data. On the other hand, a more reasonable explanation is that self-healing in concrete has become a highly differentiated and connected field over the last three decades, multiple solutions, such as autogenous self-healing, capsule self-healing, bio-based self-healing, were available in dealing national construction challenge, and still need further research and development.

Combing both keywords co-occurrence development and publication/citation from WoS, the entire field of self-healing in concrete could be divided into mainly three stages:

Emerging stage (1994-2006): At this stage, there were only 27 papers published regarding to self-healing technique in concrete. Autogenous healing and its water permeability was mostly studied before the year of 2006, specifically, Edvardsen (1999) and Reinhardt and Jooss (2003) were the most influential publications with 416 and 267 citations, respectively. The overall development at this stage was still in its infancy.

Rapid development stage (2007-2015): self-healing in cementitious material developed rapidly at this stage, with 307 papers published by 2015. Evaluation of concrete

performance after healing process was intensively studied combining both laboratorial and numerical investigations. Technological reviews in self-healing materials such as Hager et al. (2010) and bio-based self-healing review such as de Muynck et al. (2010) were the most cited articles, with 604 and 462 citations, respectively. Microcapsule (37 articles) and bio-based (27 articles) self-healing were the research hotspots and had been developed rapidly during this time.

Post-development stage (2016-present): Publication numbers at this stage have been experiencing continuous growth. 751 papers were published by August 2020 from 2016, according to the WoS database. The research at this stage, compared with the previous stage, the overall research direction in self-healing has been further specific, with the emergence of fast-emerging and highly differentiate research areas, such as vascular based self-healing (Li et al., 2020), ECC self-healing (Zhang et al., 2019), field trial studies (Al-Tabbaa et al., 2019) in recent years.

2.3.3 Self-healing approaches

After understanding the overall trend of self-healing development, a deep-dived review on detailed approaches is followed to parsing down their current challenges and achievements, thereby revealing the niche for further studies.

For cementitious materials, the mechanisms for achieving self-healing can be classified broadly into two main categories: Autogenous healing and Autonomic healing, according to the International Union of Laboratories and Experts in Construction Materials (RILEM). The first takes advantage of the natural autogenous self-healing properties of the cementitious matrix, as described in De Rooij et al. (2013) 'The self-healing process is autogenic when the recovery process uses materials components that would otherwise also be present when not specifically designed for self-healing (own generic materials'. However, the second relies on the use of engineered added in cementitious materials, as 'The self-healing is autonomic when the recovery process uses materials components that would otherwise not be found in the materials (engineered additions).' (De Rooij et al., 2013)

Autogenous healing

Cementitious materials have autogenic abilities to heal their cracks. These can be broadly classified into three causes, Physical, Chemical and Mechanical Causes, as shown in the figure below (Figure 2.10).

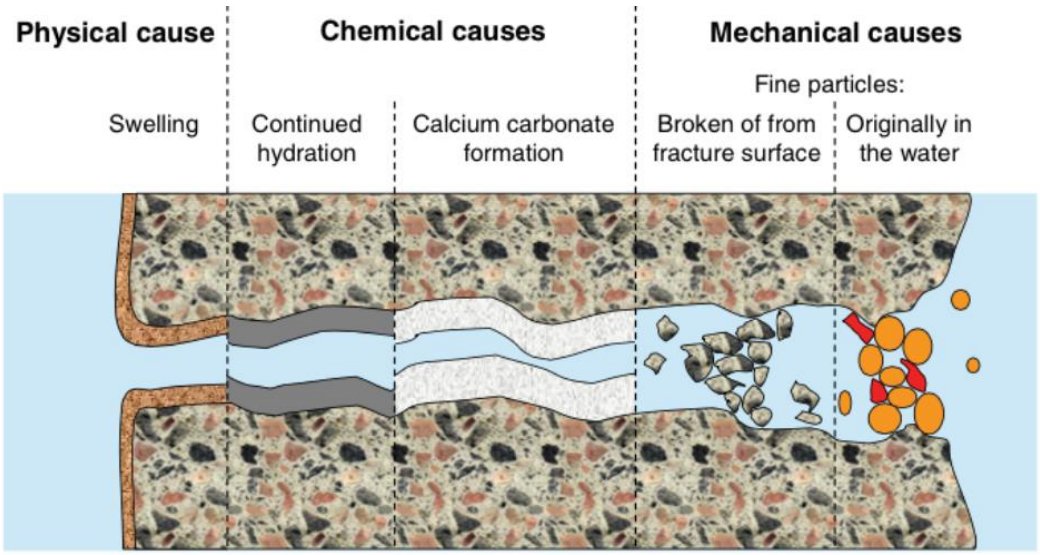

Figure 2.10 Mechanisms of autogenous healing in cement (de Rooij et al. 2013)

Autogenous healing is mainly attributed to two chemical-based mechanisms (Van Tittelboom and De Belie, 2013): (i) hydration of the unhydrated cementitious materials; (ii) dissolution and secondary carbonation, such as calcium carbonate or calcium hydroxide (Edvardsen, 1999).

As for carbonation process, the reactions take place when calcium oxide leached out from concrete; the released calcium ions then react with the dissolved CO_2 thereby generating secondary minerals to fill the cracks (Edvardsen, 1999):

$$H_2O + CO_2 \rightleftharpoons H_2CO_3 \rightleftharpoons H^+ + HCO_3^- \rightleftharpoons 2H^+ + CO_3^{2-} \quad (2.2)$$

$$Ca^{2+} + CO_3^{2-} \rightleftharpoons CaCO_3 \ (pH_{water} > 8) \quad (2.3)$$

$$Ca^{2+} + HCO_3^- \rightleftharpoons CaCO_3 + H^+ \ (7.5 < pH_{water} < 8) \quad (2.4)$$

Other mechanisms such as swelling and fine particles blocking could also result in the autogenic process. Besides, Van Tittelboom and De Belie (2013) pointed out that the autogenous healing efficiency depends on the age of cementitious materials when

cracking appears. Hydration precipitation dominates the reactions in young concrete because it has a high proportion of unhydrated cement particles. While, the calcium carbonate precipitation caused autogenic process, will be the main reason at the later age (Neville, 2012).

However, utilizing autogenous healing in cementitious materials is mostly restricted by crack widths. Edvardsen (1999) and Aldea et al. (2000) observed sealed cracks of around 100 μm. Hence, the autogenic self-healing is effective within the crack width up to 50–150 μm (Li and Yang, 2007). Additionally, water supply and recrystallisation within cracks are the other two main limitations that determine whether cracks could be healed successfully or not (Figure 2.11). This is because continuing water supply to unreacted cement particles during the hydration process would boost the autogenous healing of young concrete. As for recrystallisation, dissolved calcium ions could react with carbonate ions and form carbonate, which will then precipitate in the cracks, therefore improving concrete healing capacity.

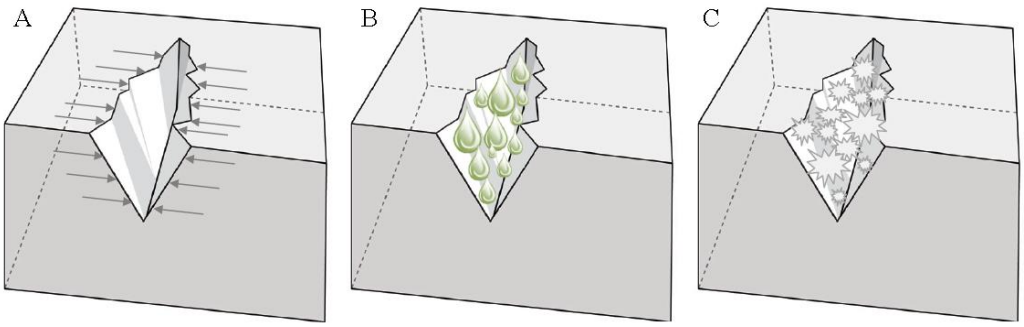

Figure 2.11 Summary of autogenous healing restriction factors: (A) cracks widths; (B) water supply; (C) improved hydration and crystallisation (Van Tittelboom and De Belie, 2013)

Autonomic healing

Without further modification or improvement, the efficiency of autogenous healing activities is relatively low. Therefore, autonomic self-healing strategy has been developed in recent years to improve healing performance. To endow cementitious systems with an enhanced ability to self-healing larger and more complex damage, that is more representative of realistic scenarios, functional engineered additions can be developed and embedded in the cementitious matrix.

Autonomic healing process uses engineered addition of materials or components for filling gaps that cannot be found in cementitious materials, and this type of healing is widely divided into intrinsic healing, capsule-based healing and vascular-based healing (Souza, 2017; Figure 2.12).

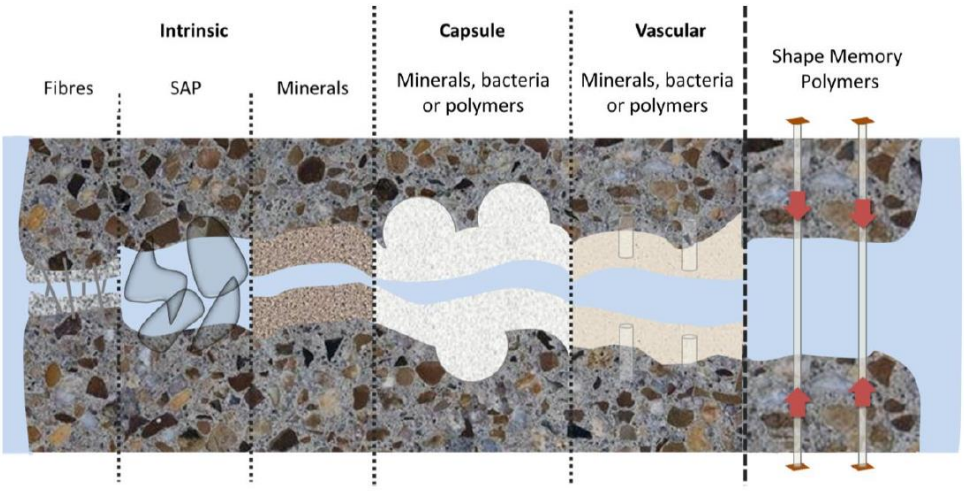

Figure 2.12 A schematic representation of the mechanisms of autonomic self-healing (Souza, 2017)

Intrinsic Healing

Intrinsic healing is a physical triggered healing process, and it commonly applies fibres, polymers and minerals into cementitious materials to improve the autogenous healing process and alleviate the three limitations (width of the crack, water supply and recrystallisation) listed in the previous autogenous section.

Applying steel cords (SC), polyethylene (PE) fibres, poly vinyl alcohol (PVA) fibres and polypropylene (PP) fibres (Nishiwaki et al., 2014) directly into cementitious materials would be the most direct way to restrict and control cracks width. PVA was examined by Nishiwaki et al. (2014) to have the highest healing efficiency as the hydroxyl groups on PVA fibres could improve the deposition of certain minerals by attracting cations (especially for Ca^{2+}). However, SC fibres showed that the steel began to corrode within the cracks, thereby having the lowest healing efficiency amongst the above (Homma et al., 2009). Jefferson et al. (2010) and Issacs et al. (2013) in Cardiff University developed a shape memory polymers (SMP) system for healing cracks in cementitious materials, which are shrinkable polyethylene terephthalate (PET) tendons with superelastic behaviour. Crack closure can then be achieved by thermally activating the shrinkage

mechanism of the restrained tendons after the cement-based material has undergone initial curing, therefore enhancing the autogenous self-healing process in concrete.

Other researchers such as Snoeck et al. (2012, 2016) introduced additional water suppliers to promote autogenic healing, called super absorbent polymers (SAPs). SAPs are cross-linked polymers that have the capability to absorb and retain the amount of water up to 500 times their weight (Jensen and Hansen, 2001; 2002). When cracks appear, water will travel into the cracks; and surrounding SAPs will absorb ingressing water and swell, thereby blocking the cracks from further ingress and stimulating autogenous healing by later release of retained water (Snoeck et al., 2012; Mignon et al., 2017). The main concern raised by Lopez-tendero et al. (2011) and Mignon et al. (2017) of using SAPs is that the swelling of SAPs may generate unexpected pores and reduce the strength of the concrete matrix.

Promoting deposition of crystals within cracks is another approach of stimulating autogenous healing method. Pozzolanic materials such as Fly ash (Şahmaran et al., 2014), blast furnace slag (Liu and Zuo, 2011) are being added into cement to promote the healing process. Ahn and Kishi (2010) proposed an optimum mixing ratio for healing is to replace 10% of cement with expansive agents or geo-based materials. Qureshi and Al-Tabbaa (2016) added MgO, which promoted the autogenous drying shrinkage crack self-healing capacity of cement. Similar agents were investigated by Jiang et al. (2015) and Ahn et al. (2016) when water travelled into cracks, those agents expand, swell or causes crystals precipitation, thereby improving the healing process.

2.4 Capsule based self-healing system

Capsule based self-healing systems have become increasingly popular over the past decade and originated from the research conducted in polymer composite by White et al. in 2001. It is a successful healing case based on healing agents being released from discrete microcapsules (White et al., 2001; Brown et al., 2004). Regarding feasibility, capsule-based self-healing allows the easy addition during the mixing of concrete, followed by controlled release of the healing agent upon damage (Souza, 2017). Compared with autogenous healing, the capsule-based system mainly targets cracks that are larger than 200 μm; while autogenic healing only focuses on healing cracks with a width within 150 μm (Van Tittelboom et al., 2013).

2.4.1 Healing mechanism of capsule based system

Mechanisms of capsule-based self-healing are various, and the healing agents released and (i) react with air or being activated by heat (Van Tittelboom and De Belie, 2010; Sun et al., 2011; Dry, 2000). Dry (1994) developed cylindrical PP capsules filled with methyl methacrylate (MMA) and coated with wax, which was able to release the agent when the wax coating was heated. Another study from Dry's group switched healing agents into cyanoacrylate (CA), which cured upon contact with air when being triggered by physical cracks (Dry, 1999). Instead of using CA, Pang et al. (2009) selected a less reactive one-part epoxy to mitigate hardening inside the capsules occurred in CA cases before crack appearance. (ii) Agent release is achieved via interacting with cementitious materials and form stable products to heal the cracks according to Huang and Ye (2011) and Pelletier et al. (2011). In their studies, sodium silicate (SS) was encapsulated into capsules, which is then reacted with $Ca(OH)_2$ from concrete, forming a calcium silicate hydrate (CSH) product with good compatibility in a cementitious matrix. Kanellopoulos et al. (2015) in Cambridge assessed the efficacy of four mineral healing agents (colloidal silica (CS), sodium silicate (SS), tetraethyl orthosilicate (TEOS) and magnesium oxide (MgO)) encapsulated in cylindrical glass capsules. The increased performance was observed in all mineral agents, specifically, in the samples with SS and CS. Both flexural strength recovery and sorptivity presented a significant positive performance in crack healing compared with controlled samples, making them ideal candidates in mineral-based healing. (iii) Healing agents are released and able to react with additional materials and capsules (different types with the released agents, could be additional catalysts) in the matrix (Mihashi et al., 2000; Wang et al.,2012b; Van Tittelboom et al., 2011a; Van Tittelboom et al., 2011b). For instance, two-part epoxy was encapsulated separately and mixed in the cementitious mixture, where healing could be achieved when cracks initialled both types of capsules (Feng et al.). However, researchers raise concerns on difficulties for the two-component epoxy to harden due to insufficient mixing of both components in the crack, which is still an unsolved problem (Van Tittelboom et al., 2013).

All different types of mechanism in encapsulation systems equipped with common functions in protecting the healing agent from the external cementitious environment, and allowing healing agent escape only when damage occurs to trigger self-healing. This requires capsules should be rupture as soon as cracks appear, and release healing agents immediately and sufficiently for target cracks (Van Tittelboom and de Belie, 2013).

Therefore, high brittleness and geometry parameters are necessary for qualified capsules (Xue et al., 2016).

2.4.2 Transitional cylindrical capsules -- from capsule to vascular

Spherical capsules (Sisomphon et al. 2011; Alghamri and Al-Tabbaa 2016; Souza, 2017, also see Table 2.1) have been widely used and investigated because they (i) can provide a controlled and (ii) enhanced release of the healing agent; (iii) and could also reduce the stress concentrations from empty capsules (Schlangen and Joseph, 2009).

In terms of healing efficiency, crack healing is largely related with and time available for the healing process and the amount of cargo capsules provided. Mookhoek et al. (2009) investigated and revealed that the amount of healing agents spherical capsules deliver scales linearly with their diameter, dosage as well as healing efficiency. Fang et al. (2018) applied capsules with 300-400 μm in diameter containing calcium sulfoaluminate cement (CSA), and observed the initial volume of cracks and pores is around 1.63%. After 21, 42, 63, 84 and 105 days of healing, the total volume fraction drops to 1.11%, 0.78%, 0.48%, 0.29% and 0.28%, respectively (Figure 2.13). Longer healing period significantly reduced the volume fraction, from 1.63% to 0.28% after 105 days of healing. However, discrete distribution of capsules and limited amount of healing agent carried restrict the crack healing, leaving discrete crack sections in the matrix (Figure 2.13).

Intending to overcome the limits above, tubular/cylindrical capsules/fibres shape (Thao, 2011, Van Tittelboom et al. 2016; Hilloulin et al. 2015; Formia et al. 2015. see Figure 2.14) caught more attention recently since (i) they have a relatively larger internal area of influence for the same volume of healing agent compared with spherical capsules, (ii) the advantage of being able to store a larger amount of repairing agent, and (iii) have a stronger bond between capsules and cement matrix in ensuring that cracks are able to propagate through the capsules (Maes et al., 2014), therefore potentially achieve multiple healings (de Belie et al., 2018), together to prevent adhesive degradation over time. As with spherical capsules, healing agents in tubular/cylindrical capsules were activated and released due to the shell breaking with crack formation.

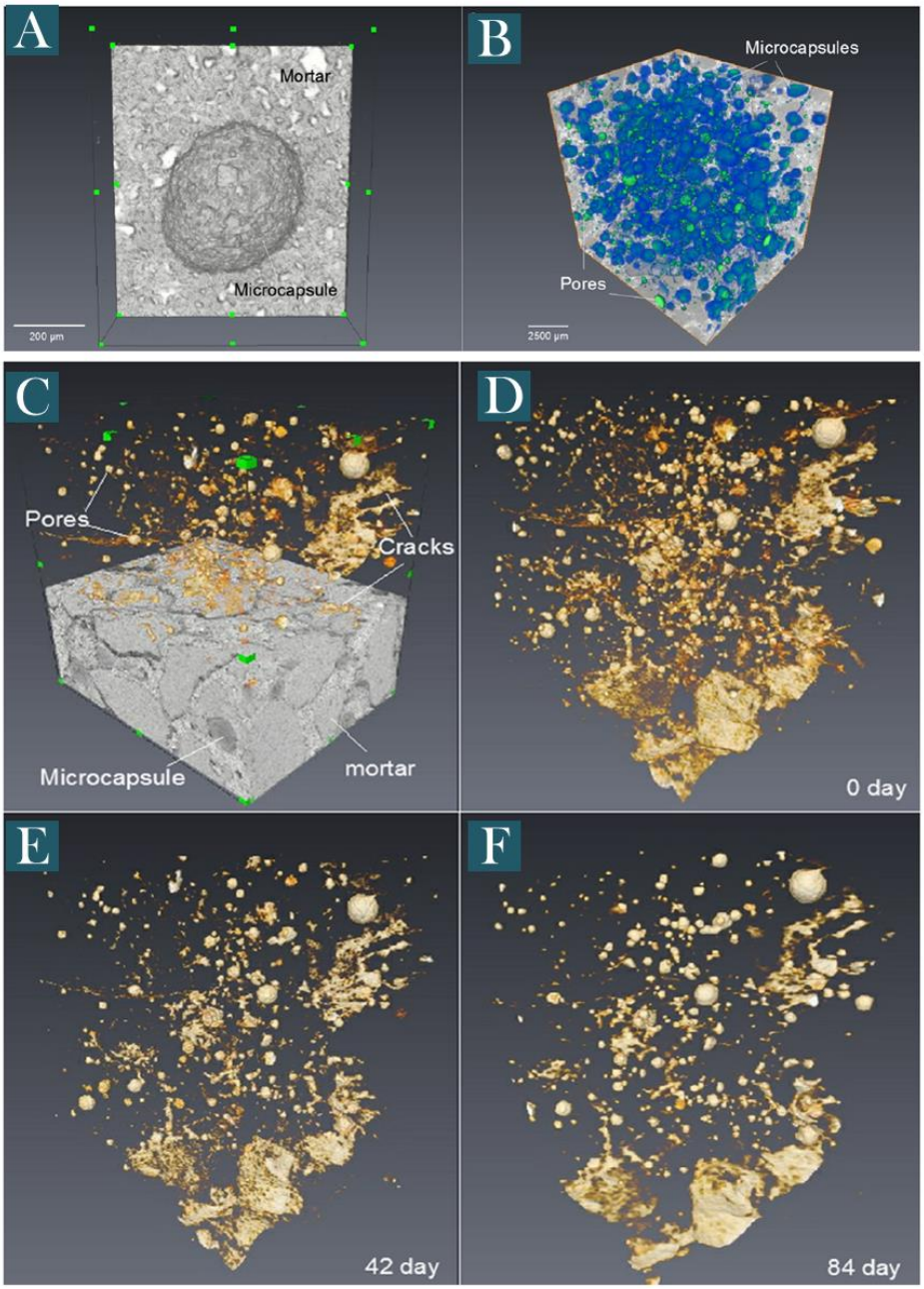

Figure 2.13 Computed tomography reconstructed image of mortar with spherical capsules embedded (A, B); general information of the specimen, yellow parts representing pores and cracks (C); cracks and pores distribution, 0 day after cracking (D), 42 days after cracking (E) and 84 days after cracking (F) (Fang et al., 2018).

Classification of the early individual hollow glass fibres (HGFs) approaches is not yet in agreement, due to their shapes. Giannaros (2017) included early works, such as Dry (1994), Bleay et al. (2001) and Thao (2011), into elongated capsule class. While Wang et al. (2015), Blaiszik et al. (2010), Patrick et al. (2017) and Van Tittelboom et al. (2013) considered their works into one-dimensional (1D) vascular networks. Here we define HGFs as still in the class of cylindrical capsules since no external linked tubes, pumps

and healing agent reservoirs were adopted in these structures. Individual channels with external tubing systems will be considered as the 1D vascular system, which will be discussed in the following section.

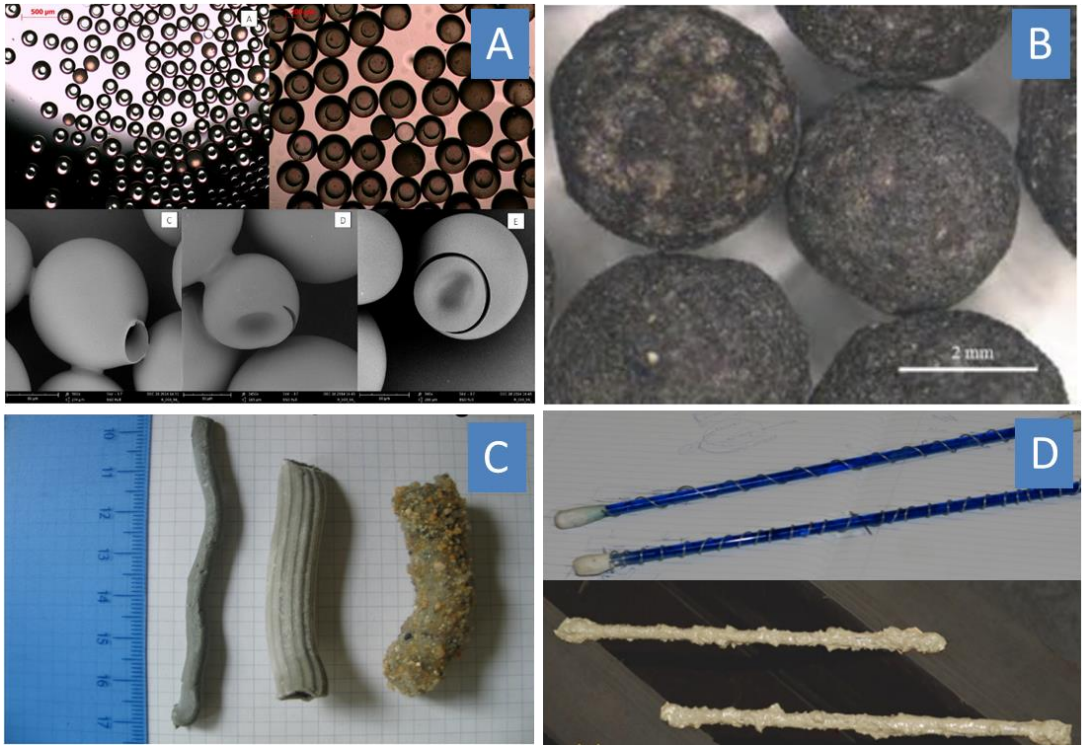

Figure 2.14 Different shapes of microcapsules, (A) spherical capsules containing sodium silicate as core (Souza, 2017); (B) impregnated LWAs coated with PC (Sisomphon et al., 2011); (C) hollow pasta like tubes made with cement paste and acrylic resin with 5mm diameter; 10mm diameter; and 10mm diameter coated with sand on the surface (Formia et al., 2015); (D) glass capsules with protective spiral wire coated with 3.5 mm-thick mortar layer (Thao, 2011).

Glass cylindrical capsules have been predominately applied in the cementitious matrix due to their brittleness in reacting to cracks and flexibility in shapes. According to Table 2.1, glass cylindrical capsules normally have inner diameters of 0.8 mm to 6.15 mm, and with the length between 50 and 250 mm. Li et al. (1998) used hollow glass capsules (fibres), with 0.8 mm inner diameter and 100 mm in length, that were filled with ethyl cyanoacrylate, which showed an improved recovery of stiffness capacity after repairing. Aside from polymer-based agents, multiple expansive minerals were also enveloped in glass cylindrical capsules in Qureshi's studies (Qureshi et al., 2015). Results showed a significant sealing efficiency improved up to 95%, and with 25% of strength recovery after 28 days. Among all the developed encapsulating materials, glass-based capsules have gained the highest preference in laboratory-scale tests (Xue et al., 2018). However, glass capsules are usually not able to survive the aggressive mixing and compaction process in

producing concrete, thus the glass capsules were normally pre-embedded into the cementitious matrix or are protected using an extra protective coating.

To protect glass capsules in the cementitious matrix, Thao (2011) applied protective mesh and spiral wires upon cylindrical capsules (Figure 2.14 D) and found the combination of both mesh and spiral wires received the best performance to avoid early breakage. Besides, another concern in using glass capsules is the potential onset of undesired alkali-silica reactions in the cementitious environment (de Belie et al., 2018). To avoid this drawback, cementitious and ceramic capsules were investigated. Formia et al. (2015) produced 'pasta' shaped cementitious hollow capsules different internal diameters (2 and 7.5 mm) and a length of 40-50 mm (Figure 2.14 C) consisting of acrylic resin as core material coated with wax before adopting to cement paste, presented increasing survivability with the thickness increases.

Table 2.1 Summary of spherical and cylindrical capsules reported in the literature.

Spherical Capsules				
Shell material	**Cargo material**	**Mixing rate**	**Diameter(mm)**	**Reference**
PC	LMA (SMF)	1.086% (Cement weight)	$D_0 \leqslant 4.000$	Sisomphon et al., 2011
	PC/Pozzolans	7.8-12.5% (Sand weight)	/	Hung and Kishi, 2013
PVA	MgO	10% (LWA Replacement)	$1.000 \leqslant D_0 \leqslant 2.000$	Alghamri and Al-Tabbaa, 2016
	LWA	100% (LWA Replacement)	$4.000 \leqslant D_0 \leqslant 8.000$	Alghamri et al., 2016
PU	MMA	5%(Cement weight)	0.300×10^{-3}	Litina et al., 2014
	Water	2%(water volume)	$0.040 \leqslant D_0 \leqslant 0.800$	Pelletier et al., 2011
	CS	1%, 5% (Cement weight)	$0.030 \leqslant D_0 \leqslant 0.060$	
Silica	MMA	5%(Cement weight)	0.035 (Average)	Litina et al., 2014
	Epoxy	5%(Cement weight)	0.07 (Average)	Perez and Erkizia et al., 2015
	Epoxy	10%(Cement weight)	$0.005 \leqslant D_0 \leqslant 0.180$	Perez and Erkizia et al., 2015
UF	Epoxy	3%, 6%, 9% (Cement weight)	0.166	Wang et al., 2013
		2%, 4%, 6%, 8% (Cement weight)	$0.100 \leqslant D_0 \leqslant 0.250$	Dong et al., 2018
		3%, 6%, 9% (Cement weight)	0.122	Wang et al., 2017
		2%, 4%, 6%, 8% (Cement weight)	$0.132 \leqslant D_0 \leqslant 0.180$	Dong et al., 2018
		3%, 6%, 9% (Cement weight)	0.122	Wang et al., 2017
	SS	0.5%, 1%, 2.5%, 5% (Cement weight)	$0.081 \leqslant D_0 \leqslant 0.701$	Gilford et al., 2014
	DCPD	0.25% (Cement weight)	$0.289 \leqslant D_0 \leqslant 0.987$	Gilford et al., 2014
	Calcium nitrate	0.25%, 0.5%, 1%, 2% (Cement weight)	$D_0 \leqslant 0.100$	Hassan et al., 2016
	Calcium nitrate	0.5%, 0.75%, 1%, 1.25% (Cement weight)	0.070	Al-Ansari et al., 2017
PUF	Epoxy	1%, 2%, 4% (Cement weight)	0.100	Li et al., 2017
PUrea	SS	0.8% (Cement weight)	0.130	Giannaros et al., 2016
MF	Epoxy	1%, 2%, 4% (Cement weight)	$0.010 \leqslant D_0 \leqslant 1.000$	Li et al., 2016

Cylindrical Capsules (transitional vascular)				
Wall material	**Cargo material**	**Length (mm)**	**Inner Diameter (mm)**	**Reference**
Glass	SS	50	6.15	Qureshi et al., 2016
	CS			
	TEOS			
	MgO			
	Epoxy	250 20≤L≤80	3.00 2.00≤D_0≤3.00	Thao et al., 2009 Van Tittelboom et al., 2011
	PU	50	3	Maes et al., 2014
		50	3.35	Van Tittelboom et al., 2016
	CA	100	0.80	Li et al., 1998
		200	3.20	Sun et al., 2011
		20-80	2.00≤D_0≤3.00	Van Tittelboom et al., 2011
	PA	20-80	2.00≤D_0≤3.00	
	Bacteria	20-80	2.00≤D_0≤3.00	Wang et al., 2012
	TEOS	50	6.15	Kanellopoulos et al., 2015
	SS	50	6.15	
	CS	50	6.15	
	MgO	50	6.15	
	MgO/water	50	11.40/6.15	Qureshi et al., 2016
	PC/water	50	11.40/6.15	
	Bentonite/water	50	11.40/6.15	
	CaO/water	50	11.40/6.15	
	MgO, CaO, bentonite/water	50	11.40/6.15	
	PC, MgO, CaO, Bentonite/water	50	11.40/6.15	
PLA/PMMA/PS	PU	50	1.10≤D_0≤3.20	Hilloulin et al., 2015
Cement	Na/ K silicate	50≤L≤60	2.00≤D_0≤7.50	Formia et al., 2015, 2016
	acrylic resin	50≤L≤60	2.00≤D_0≤7.50	Formia et al., 2015
Ceramics	PU	15≤L≤50	2.50≤D_0≤3.50	Van Tittelboom et al., 2011

LMA: Lauryl methacrylate; LWA: Lightweight aggregate; SS: sodium silicate ($NaSiO_3$); CS: colloidal silica; UF: urea formaldehyde; PUF: poly urea–formaldehyde; PUrea: polyurea; CSA: calcium sulfoaluminate; DCPD: dicyclopentadiene; MF: melamine formaldehyde; PS: polystyrene; PU: polyurethane; PMMA: Poly-methyl methacrylate; TEOS: Tetraethyl orthosilicate; PLA: Poly(lactic acid); CA: Cyanoacrylate

Mineral-based core materials, such as sodium silicate and potassium silicate were also examined in shaped cementitious hollow capsules, and received load recovery indices up to around 70% and stiffness recovery of 50% in healing large cracks (> 1mm) (Formia et al., 2016).

Alternatively, brittle thermoplastics with a relatively low glass transition temperature, such as PLA (poly lactic acid), PMMA (poly methyl methacrylate) and PS (polystyrene) were applied to develop cylindrical capsules in the research from Hilloulin et al. (2015). These capsules were able to survive 1 minute of the concrete mixing process. However, a major drawback of using discrete plastic-based capsules is that the capsules tended to float and present a less uniformed distribution in the concrete beam compared with glass capsules (Araújo et al., 2018).

To date, capsule-based system is a promising method that could deal with larger cracks and maintain the strength of cementitious materials. In the case of cylindrical capsules, the main advantage in using them is that they have a relatively larger internal area of influence for the same volume of healing agent and being able to store a larger amount of repairing agent compared with spherical capsules (de Belie et al., 2018). However, this increased area of influence is hindered by the inferior release, particularly in the occurrence of multiple cracks around one capsule (Joseph, 2008). To improve agent release, cylindrical capsules should be designed to have diameters ranging from 0.8 to 5 mm, which are wider than crack width of the matrix. This will enable that both the capillary attractive force of the crack and the gravitational force on the fluid mass is sufficient to overcome the capillary resistive force of the cylindrical capsules and the negative pressure forces caused by the sealed ends (Li et al., 1998, Hilloulin et al., 2015, Joseph, 2008).

The key points for the success of capsule-based system are; (i) capsules should be adequately mixed with cementitious material, (ii) must carry sufficient cargo to heal cracks when they are triggered (Van Tittelboom and De Belie, 2013), (iii) be able to overcome both negative pressure and capillary force to achieve agent release (Li et al., 1998, Hilloulin et al., 2015, Joseph, 2008). However, neither spherical capsules nor cylindrical-shaped capsules can provide unlimited healing agents for long term repairing damage in the cementitious matrix. Damage scenarios require larger volumes of healing agents and the capability of dealing with repeated damage, therefore larger reservoirs are needed.

2.5 Vascular based self-healing system

Vasculature from plants or animals has been mimicked to propose a delivery system to address damage events and enable multiple healing cycles. Recently, self-healing via vascular networks is becoming an active topic (Williams et al., 2007) and is the only type of self-healing methods that has the capability to address all sorts of cracks in cementitious materials (Table 2.2; Gardner et al., 2018). Similarly, vascular systems house the healing agents in hollow channels that allows a healing agent to be distributed from a reservoir throughout a structure so that damage can be completely infiltrated with the healing agent was identified as an advance for liquid-based healing approaches (Trask et al. 2007a, Williams et al., 2008)

The major advantage in using vascular based system compared with the encapsulation approach is that the healing agent can be continually supplied. Moreover, different healing agents can also be switched anytime during the healing process to treat various types of damages in concrete, since the healing agent reservoirs were designed externally. With a circulation system, healing agents could be recycled and refined, which provide a continuous healing agent delivery process (Blaiszik et al., 2010), theoretically, no limit to the volume of damaged material is repaired.

Furthermore, a vascular based self-healing system is able to overcome difficulties in insufficient agent release from the capsule-based system resulted by negative pressure and capillary force. The healing agent instead can be supplied under pressure to ensure that it reaches the required damage zones (Davis et al., 2015).

Table 2.2 Summary of self-healing technologies (Adopted from Gradner et al., 2018)

Technology	Crack Scale	Form of Technology	Healing action	Construction requirements
Microcapsules	Nano/Micro	Microcapsules randomly distributed throughout cementitious matrix	Microcapsule is ruptured via propagation of a crack. Release of healing agent into crack plane	Inclusion of microcapsules as a standard component of the concrete matrix
Bacteria	Micro/Meso	Bacterial spores and nutrient sources randomly distributed throughout cementitious matrix	Exposure of spores to water and nutrient source in favourable conditions. Bacteria deposit calcium carbonate on crack surface	Inclusion of bacterial spores and nutrients as a standard component of the concrete matrix
Flow networks	**All**	Small diameter hollow network formed in cementitious matrix. Tubes filled with healing agent. Potential for pressurisation of system	Cracks in concrete will rupture the flow network allowing the release of healing agent into crack plane. Network allows for repeated damage/healing events.	Placement of network in concrete prior to casting
Shape memory polymers	Meso/Marco	Standard of PET (polyethylene terephthalate) in tendon format anchored in the matrix. Similar in nature to post-tensioning strands. Heat activation via an electric current. PET shrinkage cause post tensioning effect	Cracks are closed to a level in which either natural autogenic healing can occur, or one of the other healing technologies directed at nano/micro scale healing	Placement in concrete moulds similar to a post-tensioning system

2.5.1 Vascular self-healing in polymer composite

Dry (1992) was the first one who demonstrated a vascular self-healing system in 1992, which was for repairing cracks in concrete and restoring its mechanical properties. This invention has been adopted into polymeric materials, such as fibre-reinforced composites (Bleay et al., 2001), carbon nanotubes (Sinha-Ray et al., 2012) and PVDF (polyvinylidene fluoride) nanofibres (Kolbasov et al., 2016).

Early pilot studies were mainly one-dimensional vessels embedded in the composites directly. Bleay et al. (2001) proposed a method of filling micro-diameter hollow fibres (external diameter 15 μm; internal diameter 5 μm) with healing agent to come up with a self-healing fibre laminate composite. Surprisingly, compressive strength of the damaged specimen after healing was 10% higher than that of the controlled specimen (without treatment). Pang & Bond (2005) fabricated 60 -μm -diameter vessels for more effective fluid filling and incorporated into a hybrid laminate and tested a two-part epoxy resin system.

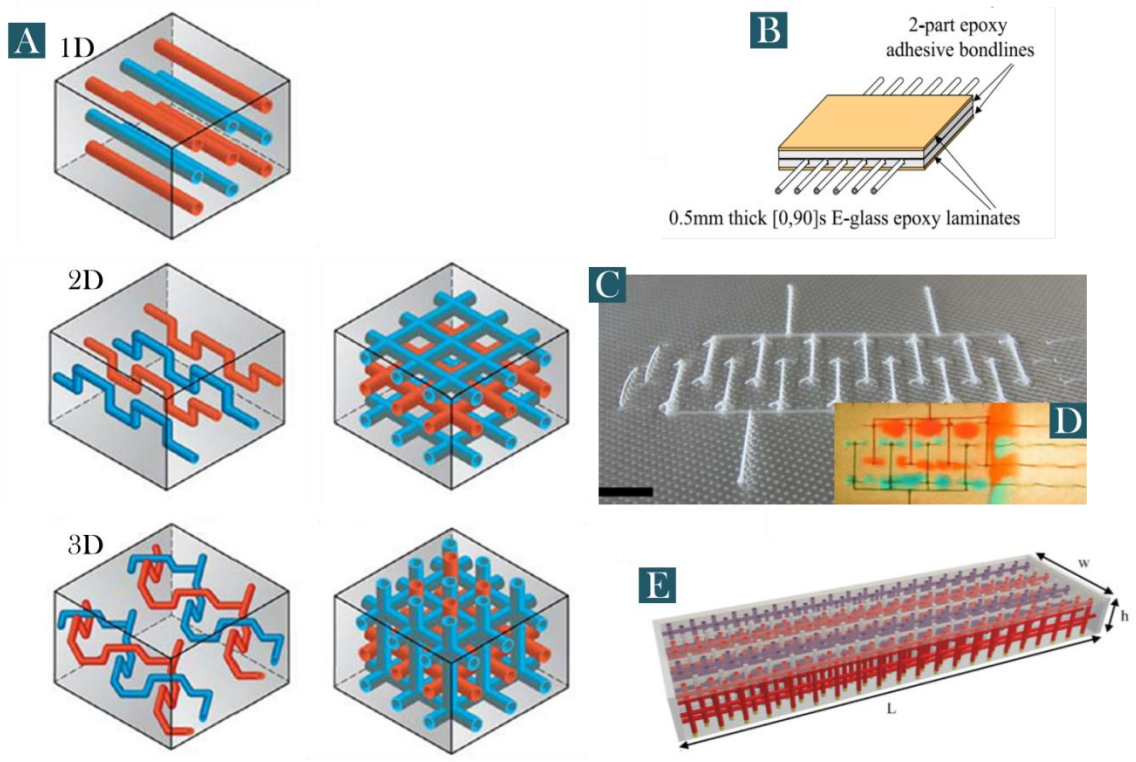

Figure 2.15 (A) Schematic view of vascular hierarchy (One-dimensional (1D) straight channels; Two-dimensional (2D) segregated channels, 2D coplanar interconnected networks; Three-dimensional (3D) interpenetrating channels and 3D spatial interconnected networks) (Patrick et al., 2017); (B) vascular sandwich panels (Williams et al., 2007b); (C) Hierarchical 2D woven (E-

glass) reinforcement with stitched (through-thickness) sacrificial PLA fibers that are solvent-welded to planar branched network templates (Patrick et al., 2017); (D) Delivery via branched (redundant) networks circumvents damage and provides fluid access to the entire fracture plane (scale bars = 10 mm); (Patrick et al., 2017); (E) Network for the delivery of a two-part healing agent, with different parts marked as red and blue tubes (Toohey et al., 2009).

Then, Bond and co-workers further improved this structure and created millimetre-scale vascular networks as sandwich structures (Figure 2.15 B) for self-healing composites by placing parallel polyvinyl chloride vessels along the central plane of the core and drilling vertical risers through the thickness of the material followed by the application of the surface skins. Samples achieved good resin/hardener mixing and showed full recovery of compression strength after impact (Williams et al., 2007, 2008b). Although self-healing networks made from these individual vessels enjoy several advantages in terms of practicality, they are restricted to 1D connectivity.

Discrete 1D structures are limited by the difficulty in replacing fluid to depleted channels. The need for each channel to fill specific damage volumes for complete healing process places constraints on how sparsely the channels can be distributed, which affects the healing efficiency. Creating interconnected networks reduces that constraint while opening up alternative applications for the network that takes advantage of fluid flow. Later studies followed up and developed two-dimensional (2D) and three-dimensional (3D) structures, since those interconnected networks may act as useful intermediates between discrete channels and increased degree of interconnectivity (Blaiszik et al., 2010). A 2D woven, glass-fibre composite preform (Patrick et al., 2017) was developed by hand stitching melt-spun and drawn sacrificial PLA fibres (300 lm) in a parallel undulating configuration. Sacrificial PLA was then removed after a post-cure treatment at 200℃, forming a 2D interconnected microvascular network within the composite laminate (Figure 2.15 C). Dyed liquids were used in demonstrating redundant flow capabilities (Figure 2.15 D), and showed that delivery limits fluid access to only four vascular openings at the crack (delamination) front, indicating efficient self-healing requires a more interconnected structure and the access to the external intervention (liquid pumping or mechanical cycling).

Then three-dimensional gridded vasculatures were developed by Illinois group since 2007 (Toohey et al., 2007) to enhance healing efficiency and enable cyclic healing. 3D Network in Toohey and his co-workers (Toohey et al., 2007, 2009) was formed of two

circuits via direct ink printing technique, with a two-part healing agent that hardened on contact with each other (Figure 3.15, D).

This system achieved an astonishing healing performance over 16 damage cycles under two parts healing agent system, and 7 damage cycles under one-part, with a strength recovery 100% (Toohey et al., 2009). In Hamilton's work, this system achieved 13 cracking cycles and the researchers discovered that the tubes pinned and hence halted the advancement of the cracks, allowing the cracks to be filled with the healing agent (Hamilton et al., 2010). And in Hansen et al. (2009), they achieved greater control over network architecture through the use of a dual ink writing method to make complex, isolated interpenetrating networks in order to optimise stoichiometry and to improve mixing for a two-part epoxy healing system and have achieved more than 30 repeated healing cycles.

The results of these studies on the recovery of self-healing composites after mechanical damage are summarised in Table 2.3. Over the last 20 years, different types of self-healing composites based on vascular systems with 1D, 2D and 3D structures. In most of these studies, two-part epoxies were used as the healing agent, and most of them were confirmed successful healing and impressive healing efficiency over a few cycles.

Table 2.3 Vascular self-healing polymer composites with 1D/2D/3D structures

Dimension	Vascular type	Healing agent types	Performance	Ref
1D	hollow glass vessels	Two-part epoxy	compressive strength 10% higher than controlled samples	Bleay et al., 2001
	60-μm-diameter vessels	Two-part epoxy	regain of 10% in frexural strength than controlled groups, 97% in healing efficiency	Pang and Bond, 2005a
	hollow glass vessels	Two-part epoxy	achieve 93% of healing efficiency	Pang and Bond, 2005b
	hollow glass vessels	Two-part epoxy	achieve ~85% of healing efficiency	Trask and Bond, 2006
	hollow glass vessels	Two-part epoxy	achieve 87% of healing efficiency	Trask and Bond, 2007
	sandwich structure, PVC vessels	Two-part epoxy	full recovery of compression strength	Williams et al., 2007
	hollow glass vessels	Two-part epoxy	achieve 87% of healing efficiency	Zainuddin et al., 2014
	hollow glass vessels	Two-part epoxy	achieve 178% of healing efficiency	Kling and Czigany, 2014
	Co-electrospinning fibres	PDMS(polydimethylsiloxane)	regain 125-140% of healing efficiency	Lee et al., 2015a
	Co-electrospinning fibres	PDMS(polydimethylsiloxane)	achieve 110% of healing efficiency	Lee et al., 2015b
2D	woven glass-fiber composite (PLA removed)	\(dyed liquids)	flow capabilities, delivery limits fluid access to only four vascular openings at the crack (delamination) front	Patrick et al., 2017

	projection-based 3D printing (UV), hydrogel poly(ethylene glycol)diacrylate (PEGDA)	\(dyed liquids)	/(successfully developed for tissue engineering)	Xue et al., 2018
3D	3D grid network of micro-channels (~200 μm),coating with Grubbs' catalyst	DCPD (dicyclopentadiene) monomer healing agent	achieve 33-70% of healing efficiency in 7 cycles	Toohey et al., 2007
	direct write assembly gridded microvascular	Two-part epoxy	achieve 89% of healing efficiency in 23 cycles	Toohey et al., 2009
	direct write assembly gridded microvascular	Two-part epoxy	achieve ~50% of healing efficiency in 30 cycles	Hanson et al., 2009
	direct write assembly gridded microvascular	Two-part epoxy	achieve 30-86% of healing efficiency in 13 cycles	Hamilton et al., 2010
	microvascular networks within poly(methyl methacrylate) and poly(lactic acid) blocks	\	degree of branching and the number and location of entry and exit points can be loosely controlled	Huang et al., 2009
	Sacrificial wire removed channels	Two-part epoxy	achieve 99% of healing efficiency	Norris et al., 2011a
	Sacrificial wire removed channels	Two-part epoxy	achieve 100% of healing efficiency	Norris et al., 2011b
	Sacrificial wire removed channels	Two-part epoxy	achieve 260% of healing efficiency	Norris et al., 2011c
	direct write 3D Microfluidic Networks	\	distribution of carbon nano tubes	Dermanaki-Farahani et al., 2014

2.5.2 Vascular self-healing in cementitious materials

Various forms of vascular networks have been recently applied in concrete and gained increasing popularity in the last 2 years. Physical cracking of cementitious matrix causes the brittle vascular branches to rupture, and then the healing agent is released into crack faces for repairing under the action of capillary force, gravity, surface tension and negative pressure force (Joseph et al., 2010; Gardener et al., 2014).

Similar to the vascular system in a polymer composite, types of vascular structures can also be widely classified into three categories in terms of their dimensions (Table 2.4).

The simplest vasculature comprises a 1D individual channel, of which both ends can be either accessed from the concrete surface or encapsulated within the cementitious materials (Dry, 2001; Joseph et al., 2010; Selvarajoo et al., 2020a). 1D vascular (hollow porous polypropylene tubes coated in wax embedded into concrete beams) was initially used in cementitious materials (Dry 1994), with successful agent release when triggered by heat. The disadvantage of this release mechanism was that it is not autonomous and required external human intervention.

More recently, further research and simple designs for self-healing in cementitious systems continued to consider the use of individual long hollow tubes of different materials (Joseph et al., 2010; Selvarajoo et al., 2020a, 2020b). Joseph et al (2010) used extended hollow glass tubes to create a passive healing mechanism using air-curing cyanoacrylate (CA) aided by negative pressure force (Fig 4C). Results from this study indicated that the test beams peak load was 20% greater than the controls and implied initial cracks were healed under multiple reloading tests. While a drawback of using glass tubes is that they are vulnerable during the casting process. In Selvarajoo et al. (2020)'s study, instead of glass tubes, 4 mm diameter flexible polyurethane terephthalate (PET) tubes were applied to improve its survivability during casting. Moreover, an external tubing system was introduced in providing healing agents when needed. This system achieved significant healing index up to 108% in cracks with 0.2 mm in width, and 100% in all the cracks with 0.15 mm in width, with a healing process in 3 mins.

More complex 2D networks, such as parallel tubes (Heywood, 2016; Minnebo et al., 2017) and gridded networks in square slabs (600 mm by 600 mm, Davis et al., 2015) and real-size concrete slab (4.0 m x 1.0 m x 0.20 m, Tsangouri et al., 2019), have been created in concrete to provide multiple and alternative paths for healing agents to be delivered to

damaged zones. 2D structures have advantages in terms of geometry than 1D vessels in avoiding blockage, as they provided extensive redundancy of flow paths to maintain supply to the critical region (Williams et al., 2008). Glass was barely used in 2D systems due to networks comprise brittle individual glass capillary tubes, which tend to break during mixing and casting (Davis et al., 2015). In this case, glass was gradually replaced by plastics, such as acrylonitrile butadiene styrene (ABS) and polylactic acid (PLA), which are light weighted and less fragile.

Besides, the use of plastics made it possible to fabricate complicated 2D networks using a 3D printing technique. Heywood (2014) developed 3D printed 2D networks (Fig 4E), which were manufactured from PLA using colloidal silica as healing agents. A maximum load recovery of 31% and stiffness recovery of 47% was achieved after 28 days healing. The Davies et al (2015) had a 2D network design of orthogonal tubes of 4mm diameter made from polyurethane with bespoke PLA connections (Fig 4F). This pressurising 2D network enhances the flow of healing agents, which almost permeated a 0.2mm crack in a 3-point bending test. Their study revealed that pressurising the healing agent fluid led to the improved filling of the crack and this type of network can be used with different healing agents and is re-usable, enhancing the ability to promote multi-scale healing. Minnebo's work added 3D printed ABS distribution element for the individual inorganic phosphate cement (IPC) tubes (Fig 4D), providing the tubes with the outside connection. The study showed a recovery in mechanical properties was observed, and multiple healing cycles were achieved. However, the presence of the 3D printed distribution parts had a negative impact on the mechanical behaviour of the samples in both the pre-peak and post-peak loading regime.

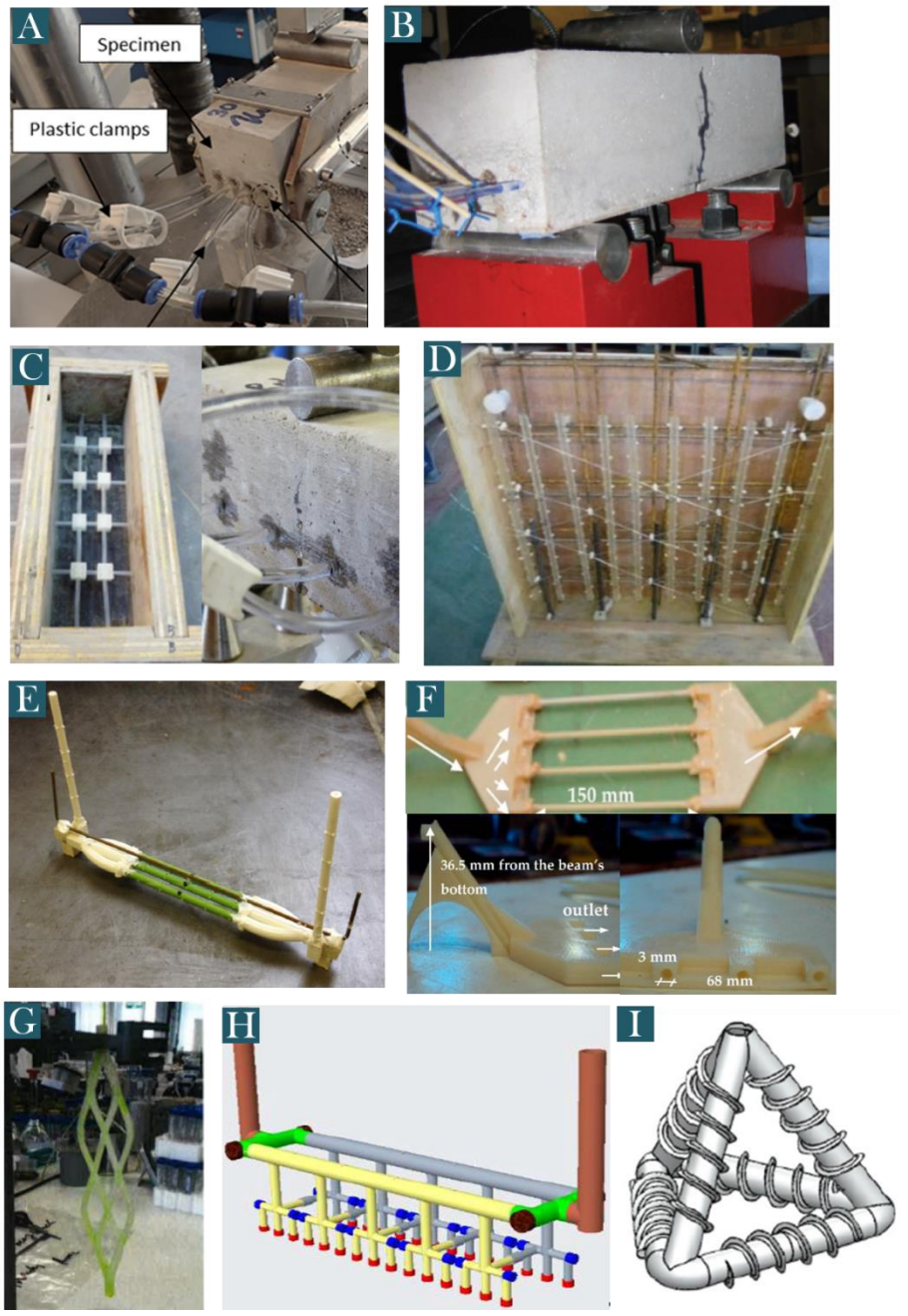

Figure 2.16 Examples of 1D (A-B), 2D (C-F) and 3D (G-I) cementitious vascular systems investigated (A) specimens with individual tubes connected to the external environment (Selvarajoo et al., 2020a) and (B) (Joseph et al., 2010), (C) 2D gridded polyurethane network with PLA connections in specimens and (D) in trials (Davis et al., 2015); (E) layout of a 2D network printed by PLA and ABS (Heywood, 2015); (F) 3D printed ABS distribution with individual inorganic phosphate cement (IPC) tubes (Minnebo et al., 2017); (G) Individual 3D network fabricated by PLA (Kimber, 2014) ; (H) 3D hierarchical structure (Harrop, 2018); (I) 3D TET unit for encapsulated vascular self-healing (de Nardi et al., 2020)

Networks with 2D structures act as intermediates between individual channels and three dimensional interconnected networks. Specifically, 2D structures have limitations in increasing vessel density, making them insufficient for addressing the failure to bleed. For

instance, Tsangouri et al. (2019) stated that its 2D vascular slab repair was limited for larger cracks with widths over 0.5 mm, and only limited sealing and almost no mechanical restoration are measured. Therefore, the vascular network should be tuned to a more interconnected, sensitive, and able to provide sufficient over time.

A 3D interconnected network is a more ideal choice in dealing with both blockage and failure to bleed, as it is consisting of alternative routes for healing agent flow, and is able to ensure rupturing with vessels covered in a three dimensional way. Compared with 1D and 2D vascular structures, 3D or biomimetic networks have higher tunnel flexibility and allow for greater interaction with the cement-based matrix, so that they are more likely to exhibit better healing performance. However, there has been little focused investigation on 3D networks or biomimetic structures in cement-based systems. Studies on self-healing composites (Bejan et al. 2006; Wang et al. 2006; Toohey et al. 2007) applied 3D gridded channels which provide alternative flow paths and high vessel coverage, whereas joint turbulence and blockage become the main concerns in rectangular bend tunnels. To minimise turbulent flow at junctions while also maximizing the volume, researchers such as Justin et al. (2016) investigated a biomimetic vessel structure in cellularised hydrogels following Murray's Law. This provides inspirations for designing interconnected networks in self-healing cementitious materials. Kimber (2014) investigated a biomimetic 3D vascular network in cement pastes. The progression of the network design is shown in Figure 2.16 G. Strength recovery was found to be 72% after a curing time of 48 hours using cyanoacrylate-based adhesives. Harrop (2008) developed hieratical structures via 3D printing technique, which achieved up to 100% crack width closure, 48% and 34.5% more healing compared with controlled groups. On the other hand, de Nardi et al. (2020) created mini-vascular networks (MVNs) that were 3D printed tetrahedral units of interconnected hollow ligaments that have a characteristic dimension. These MVNs were placed in the centre of specimens where prepared for three-point bending tests. Positive healing results were confirmed in that encapsulated mini connective vasculars were able to heal multiple occurrences of damage with strength and stiffness healing recoveries of 11% and 40% respectively for the second loading cycles. However, for this approach, the functionality of MVNs was more close to capsule based self-healing since the healing agents were sealed in a limited tetrahedral unit, and its healing performance was largely influenced by the number of MVNs placed, which is

similar with the capsule system. To be specific, this approach would be more suitable as an interconnected capsule type.

The choice of healing agent to be used in a vascular network is important and was discussed in the past researches (De Rooij et al., 2013, Xue et al., 2018; Gardner et al., 2014; De Nardi et al., 2020). Initially, selection of desirable healing agents need to consider the key requirements in the vascular system: (i) with relatively low viscosity to be transported in vessels and reach the damaged zones; (ii) able to achieve target water/gas permeability and improvement in mechanical performance; (iii) agents are able to be flushed out to enable multiple uses of the system. A summary of current agents used in the vascular system is shown in Table 2.5.

Table 2.4 Vascular networks types and performance in cementitious materials

Dimension	Vascular type	Pumping system	Healing agent types	Performance	Ref
1D	hollow porous polypropylene tubes coated in wax	No	Methylmethacrylate (MMA)	Successfully released	Dry, 2000, 2001
	Individual hollow glass tubes	No	cyanoacrylate (CA)	load was 20% greater than the controls in 2 cycles	Joseph et al., 2010
	4 mm diameter flexible polyurethane terephthalate (PET) tubes	No	cyanoacrylate (CA)	achieve healing index of 30 to 108% (0.2 mm cracks) ; healing index exceeding 100% (0.15 mm cracks)	Selvarajoo et al., 2020a, 2020b
2D	3D printing, PLA, 4 mm internal diameter and 1 mm wall thickness	Yes	colloidal silica (CS)	cracks closure 96% after 10 days; load recovery of 31% and stiffness recovery of 47%	Heywood, 2014
	4mm diameter made from polyurethane with PLA (polylactic acid) connections	Yes	cyanoacrylate (CA)	permeate the majority of a 0.2mm crack	Davis et al., 2015
	4mm diameter made from polyurethane with PLA (polylactic acid) connections	Yes	cyanoacrylate (CA)	Scale up trial (visible healing over a six month period)	Davis et al., 2015
	3D printed ABS distribution element with inorganic phosphate cement (IPC)	No (gravity flow)	polyurethane (PU)	achieve 83% of strength recovery and 101% of stiffness (1st cycle); 46% of strength recovery and 108% of stiffness (2nd cycle)	Minnebo et al., 2017
	hollow tubes with outer diameter of 10.6 mm	Yes	Polyurethane resin (PU)	stiffness recovery receive 53% and 50% at the second and third loading cycle	Tsangouri et al., 2019
3D	3D printed PLA and ABS structure	Yes	cyanoacrylate (CA)	strength recovery regain up to 72%, stiffness recovery up to 70%; 100% crack coverage	Kimber, 2014
	3D printed PLA structure	Yes	sodium silicate (SS)	achieve up to 100% crack width closure, 48% and 34.5% more healing compared with controlled groups	Harrop, 2018
	3D printed PLA tetrahedral units	No(encapsulated)	sodium silicate (SS)	strength and stiffness recoveries of 20%, 80% (1st loading); 11%, 40%(2nd loading); 0%, 5%(3rd loading)	de Nardi et al., 2020

Table 2.5 Summary of healing agents used in vascular systems for self-healing of cementitious matrixes.

Healing agents	Mechanism	Test results	Advantages	Disadvantages	Ref
Sodium silicate (SS)	reacts with the calcium hydroxide in cementitious materials and produces calcium silicate hydrates (C-S-H) gels	desirable strength recovery and stiffness regain	provides long-term compatibility with cementitious matrix; slow reaction rate and stability	not suitable for short term	de Nardi et al., 2020; Harrop, 2018
Colloidal silicate (CS)	reacts with the calcium hydroxide in cementitious materials and produces calcium silicate hydrates (C-S-H) gels	desirable strength recovery and stiffness regain	provides long-term compatibility with cementitious matrix; slow reaction rate and stability	not suitable for short term	Heywood et al., 2014
polyurethane(PU)	accomplishes crack-healing process by foaming and expanding chemical reaction	less strain concentration, desirable strength recovery and stiffness regain	expansion is suitable for larger cracks	remain controversial, variation of the regained mechanical strength	Minnebo et al., 2017; Tsangouri et al., 2019
cyanoacrylate (CA)	one-part healing agents, superglue to seal cracks for cementitious material	desirable strength recovery and stiffness regain	fast reaction	low controllability and can be solidified within the structures	Selvarajoo et al., 2020a, 2020b; Davis et al., 2015
Methylmethacrylate (MMA)	one-part healing agents, seal cracks	Compatible with cement matrix, improvement in the gas permeability	desirable results in the water and gas permeability	low rupture probability	Dry, 2000, 2001

Cyanoacrylates (superglues) are acidic solutions and hence cure rapidly when they come into contact with concrete. It is able to form robust adhesion within one minute at room temperature and especially suitable in structures rapid closure. This type of healing agent was mostly used in the vascular system, especially in 1D systems. This fast curing had advantageous for cyclical loading applications and achieved good strength and stiffness recovery in previous studies (Selvarajoo et al., 2020a, 2020b), and provided ideal healing models in predicting healing behaviour for numerical modelling (Joseph et al., 2010; Freeman and Jefferson, 2020). However, concerns raise in handling the rapid reaction agent since this may set before full crack penetration is achieved (Schlangen and Joseph, 2009).

Similarly, polymer-based healing agents such as polyurethane (PU) and Methylmethacrylate (MMA) were also considered in previous studies. Dry (2000) observed the successful release of MMA from fibres into cement during heating and obtained desirable results in the water permeability test. Minnebo et al., (2017) employed PU as a healing agent in their 2D vascular system, and regained stiffness at 108% and 46% of strength recovery during the second loading cycle. The variation of the regained mechanical strength and regained stiffness among different researches made it a controversial healing agent (Xue et al., 2018).

Mineral compounds such as sodium silicate (SS) and colloidal silicate (CS) were widely used in the vascular system (Heywood, 2014; Davis et al., 2018; Harrop, 2018; De Nardi et al., 2020) as it reacts with the calcium hydroxide present in cementitious materials and produces C-S-H gel. It has nice long-term compatibility with the cementitious matrix due to its ability to react chemically with the products of cement hydration (De Nardi et al., 2020), and could achieve desirable mechanical properties of concrete as it binds together cement particles into a cohesive whole (Heywood, 2014). Most importantly they represent far less of a hazard when pressurised in a vascular network as they are significantly less harmful than both types of glue mentioned above (Ma et al., 2015). Moreover, both SS and CS have relatively slower reaction process than other healing agents introduced. In this case, this slow reaction rate and stability make it a promising healing agent candidate for the pumping and delivering process in vascular channels.

To date, vascular self-healing in cementitious materials was demonstrated mostly in laboratory-scale tests. It was proved an ideal solution to the most difficult challenges of

overcoming water ingress and cracking prevalent in long-term period (De Belie et al., 2018; Gardener et al., 2018). In 2015, M4L project undertook site trials on a live construction project on the A465 Heads of the Valleys (HoV) in South Wales, UK, and firstly applied 2D vascular flow structures in real-sized panels (Davis et al., 2015, 2018). In-situ panels with vascular structures exhibited a reduction in cracks over a 6 six-month period, which successfully demonstrated vascular systems are capable of repeatedly distributing healing agents and repairing damaged zones.

While further follow up large scale trials related to the vascular system haven't been conducted yet. This is because for this system, it recently has been gaining increasing popularity among researchers. More laboratory-scale tests and experimental data were required in investigating repeated healing ability, delivery systems, large scale manufacture, and methods for remotely activating vascular network (De Belie et al., 2018). This highlighted the needs in developing vascular based system designs and manufacturing techniques for commercial trials.

2.5.3 Biomimetic network design for fluid transport

The design of self-healing vasculature plays a significant role in efficiently diagnosing damages in the environment and ensuring the healing agents delivery and reaches the damaged zones. To achieve swift diagnoses in reacting to cracks, vascular channels should reach sufficient coverage in the matrix, while avoiding weakening general structure (Li et al., 2020). Successful delivery can be ensured by avoiding blockage (Williams et al., 2008) and reducing resistance in channels. It is also critical to understand how the flow may change around these branched networks and how the vascular system can be designed to reduce the global resistance to flow, thereby adopting this mechanism into vascular manufacture process (Qamar et al., 2020).

Vascular inspired by nature

Nature has always been a source of inspiration for ideas in addressing engineering materials challenges given that natural materials can be flexible, strong and lightweight and many are able to self-heal. Marrying natural structures with the wide range of synthetic materials could develop and deliver cutting-edge materials, which will extend current applications and break existing limitations in terms of weight, toughness, strength and environmental resistance (Wegst et al., 2014). Wood and bone are prime examples of fibre composites with a hierarchical structure (Figure 2.17). Wood is composed of

cellulose microfibrils, transporting mineral solutions via conduction to store food in the form of carbohydrates (Gibson, 2012). Their exceptional mechanical properties are believed to have high damage tolerance, able to provide paths for transporting fluid and could repeatedly self-heal without external stimuli due to a functional adaptation of the structure at all levels of hierarchy (Fratzl and Weinkamer, 2007; Wegst et al., 2014). Self-healing is a common phenomenon that has evolved naturally in plants and animals (Price et al., 2013; Sanchez et al., 2005). It is the high-efficiency of the 3D hierarchical interconnected network system beneath the skin that promptly delivers blood platelets, or other healing agents, that enable the efficient repair of wounds (Martha et al. 2005). These natural vascular systems have been an inspiration in the development of similar self-healing systems in polymer-based structural composites and more recently cement-based infrastructure and construction material systems.

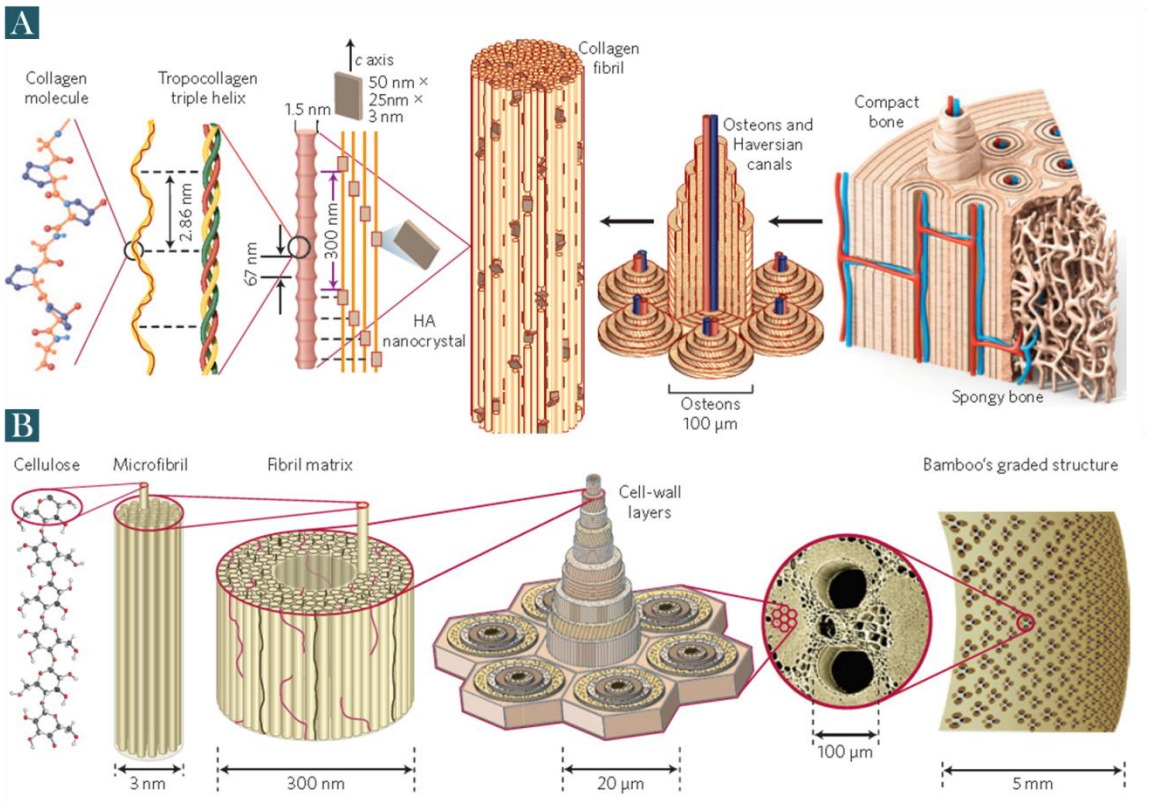

Figure 2.17 Natural hierarchical structures (Wegst et al, 2014) (A) of bone and (B) of bamboo.

In this section, an analysis of biomimetic systems has been undertaken to identify how they are optimised for agent transport and evaluated their potential limitations that may occur when implementing these designs into self-healing systems.

Biomimicy of Bone

Previously, an innovative method developed by Sangadji and Schlangen (2011) for creating an interconnected network within concrete specimens was inspired by the healing process of bones. They created a porous network system in concrete by placing porous concrete cores in a concrete structure. This design mimics the cortical (compact) and trabecular (spongious) constituents of human bone and can transport healing agents through the interconnected pores to damage zones (Figure 2.18). Results of these systems achieved desirable performance and showed it was able to heal both micro and macro cracks.

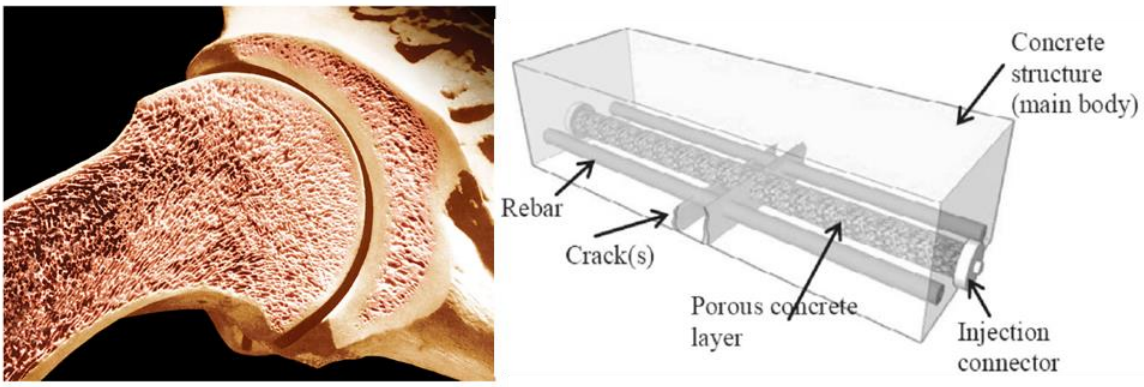

Figure 2.18 Outer compact bone and inner cancellous (spongy) bone (left, Balbas, 2010); Scheme of porous network in concrete (right) (Sangadji and Schlangen, 2011)

Biomimicy of Vascular

Vascular structure in human is one of the most distinctive features for the branching system. For instance, human skin could repetitively repair the same place; also skin has a protective coating, preventing the wound from being infected and settling a set of effective microvascular network, named capillaries. Capillaries link with larger vessels, and then with the main veins and arteries, distributing oxygen, nutrition and blood platelets for healing cracks.

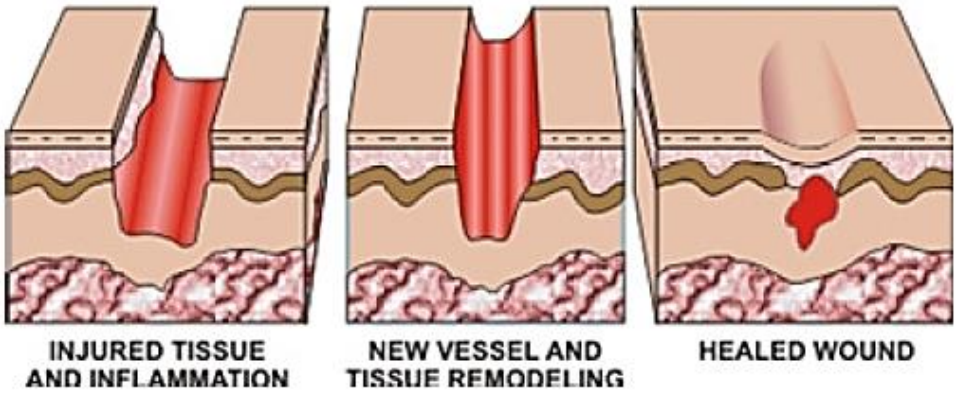

Figure 2.19 Bleeding-based healing mechanisms (Martha et al. 2005)

It is the high-efficiency of the interconnected network system beneath the skin that could deliver blood platelets soon, thereby repairing wounds in a short period (Figure 2.19). Analogous to vessels in the human body, artificial channels are able to transport healing agents into the cementitious materials and specifically to crack locations. To build up a circulatory system for cementitious material, a biomimetic vascular structure is needed to sense cracks and deliver 'blood cells' to the right place.

Murray's law in vascular design

For the vascular networks of blood vessels, Murray (1926a, 1926b) developed the principle of a relationship between the optimum parameters (diameter, length and splitting angle) of daughter branches and parent branches in order to minimise work required for blood transport. He highlighted that the two energy terms contribute to the cost required to maintain blood flow within a vessel: (i) the work required to overcome the viscous drag of the system, and (ii) the cost of metabolically maintaining the blood and the vessel tissue involved. Meanwhile, larger diameter blood vessels require more energy to metabolically maintain the blood as a living fluid (Williams et al., 2008). Thus, greater pumping power is required for smaller blood vessels due to friction losses, whereas larger blood vessels require greater power to maintain the increased volume of blood. Therefore, the optimum radius for subdividing branches resulting in minimum work required for transport can be obtained from Murray's Law. The law states that when a parent blood vessel branches into daughter vessels, the cube of the radius of the parent vessel is equal to the sum of the cubes of the radii of daughter blood vessels (Figure 2.20).

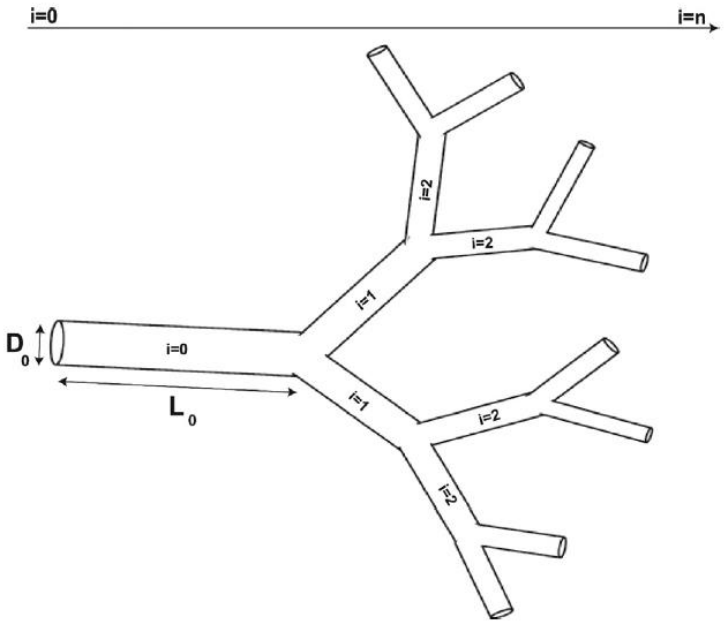

Figure 2.20 Vascular network obeying Murray's law (Miguel, 2016)

Numerical and engineered vascular design

Murray's law has been widely adopted into numerical and engineered designs containing microvascular networks, such as self-healing materials (Bejan, 2000; Wang et al., 2006, 2007), internally cooled materials (Dong et al., 2012; Cetkin et al., 2011) and tissue engineering (Justin et al., 2014).

For instance, Bejan (Wang et al., 2009; Bejan, 2000) applied Murray's law and considered to introduce vasculature into a self-healing composite with a swift diagnose function. Optimised channel sizes following Murray's law is half of the resistance of a corresponding grid with one channel size (Wang et al., 2006), by increasing the number of optimised channel diameters. In their later research, they modelled the crack as a circular defect in a round 2D space and suggested that the network should take the form of a grid, rather than a tree (figure 2.21). Gridded network in this 2D space exhibited better coverage, although tree-based networks provide maximum access from an area to a point. This is because damages are pretty much uncertain in real scenarios, so it is unlikely the crack would trigger targeted areas. The fluid must have the ability to flow into each and every crack, wherever they may form (Wang et al., 2007). However, tree-shaped architectures are more ideal when the locations of the cracks are known in advance.

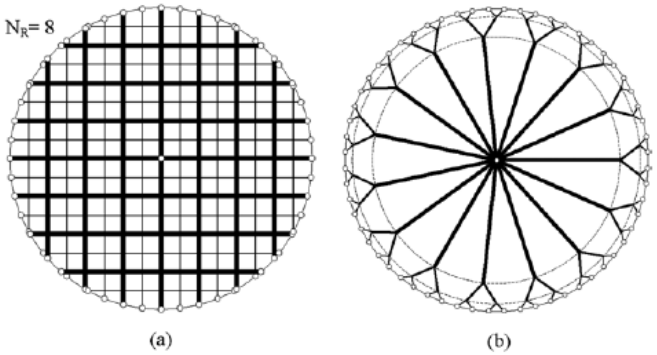

Figure 2.21 Comparison between grids (a) and trees (b) on discs with one sink in the centre (Wang et al., 2007)

Williams et al. (2008) presented an analysis that was particularly useful and could be a key design driver in high-performance applications when combined with interconnections since it encompassed the complete design space between the minimum mass furcating network, the power to manage leakage failures offered by a fully segregated network and negating the effect of blockage using an interconnected grid. The concepts fit within a design triangle as shown in Figure 2.22, which balances reliability against leakage and blockage with the overall driver for minimum system mass.

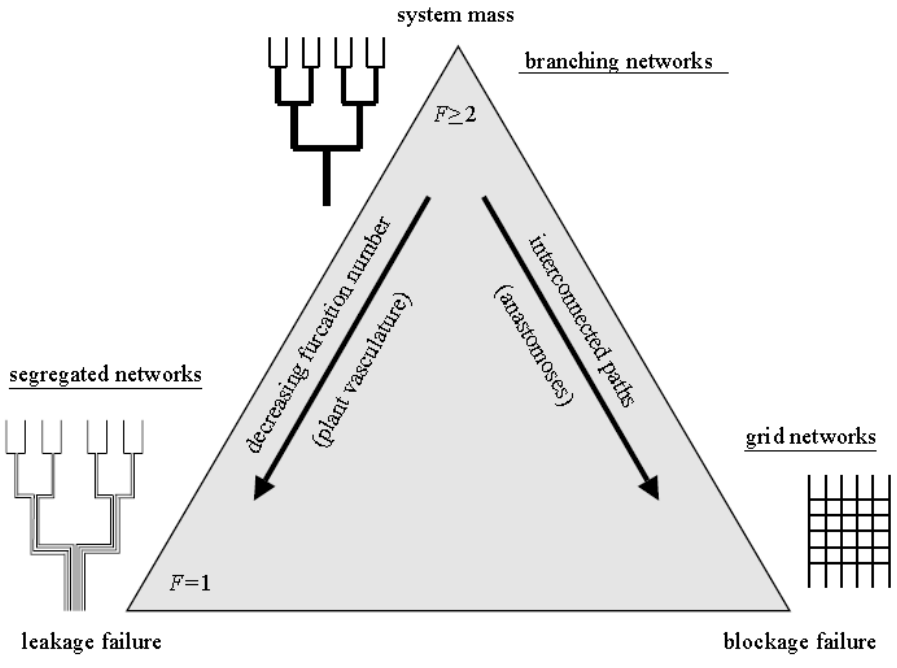

Figure 2.22 Design triangle for reliability driven network configuration (Williams et al., 2008)

They conclude that (i) in an application where leakage is highly improbable, a highly interconnected network with locally redundant paths would be desirable in mitigating

blockage, and in the extreme case, this would favour an interconnected grid arrangement; (ii) while in the application that failure by leakage is highly possible and critical, a highly segregated network would be the most suitable selection.

Besides, Aragon et al. (2008) introduced a scheme for designing 3D networks in terms of channel diameter and channel volume by using NSGA II software. By considering a number of parameters related with functions and constraints (Figure 2.23 A), they investigated the effect of network redundancy, template geometry and diameters of the channels generated by this algorithm and implemented the results within self-healing coating experiments to ensure uniform healing agent distribution with minimum energy cost (Figure 2.23 B).

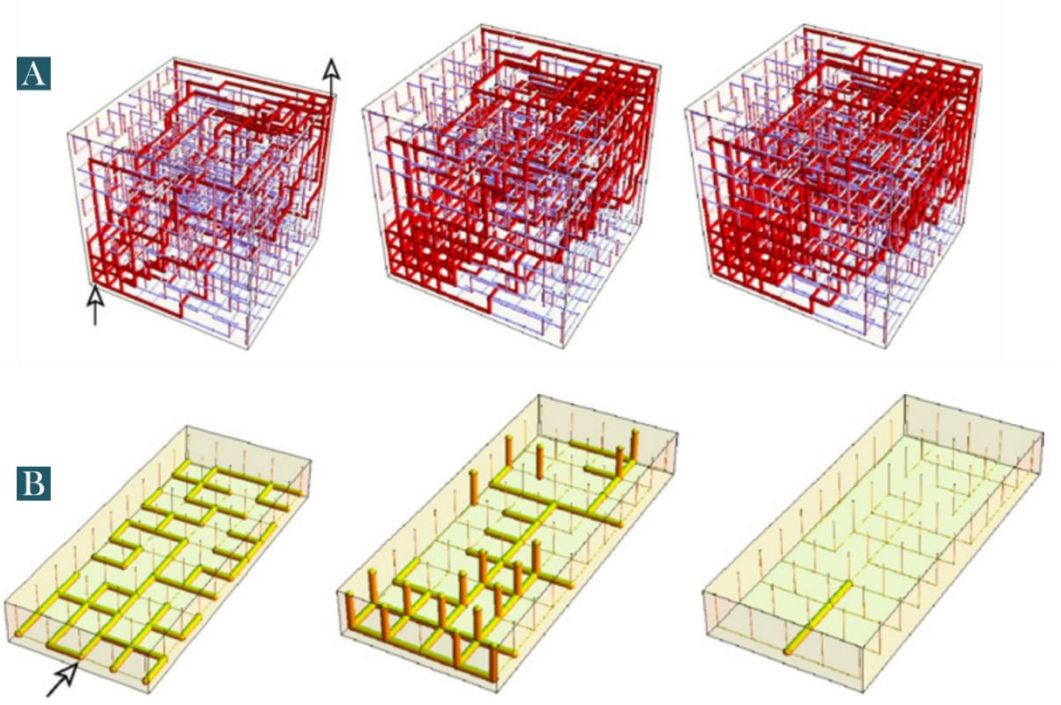

Figure 2.23 NSGA-II results for a 3D optimisation and selected networks through a genetic algorithm for flow efficiency and reduced volume fraction (A); and 3D network optimatisation for self-healing coaitng experiments, based on healing agent distribution to the Pareto-optimal surface for structures. (Aragon et al., 2008)

These studies revealed that optimal solution for microvascular network designs highly depended on parameters, required functions and potential constraints. It is theoretically possible to design a vascular system that could efficiently deliver healing agents to crack zones with low energy cost and minimised impact on structural integrity. However, challenges faced in vascular design were most rooted from practice concerns, ranging from insufficient support from manufacturing technique, the finical cost in prototype

development to the uncertainty of the currently available materials (Qamar et al., 2020). All these challenges could impose critical influence on the design of vascular networks for their intended application.

2.5.4 Methods in fabricating vascular networks

Tube removing and directly apply

There are two main ways of creating simple vascular structures in cementitious materials: (i) by remaining glass/plastic tubes in-situ, so the non-cementitious materials will permanently stay in cementitious bulk; (ii) by removing the none-cementitious tubes after pastes being cured, then the cementitious bulk will have a tube-shaped channel. For the first approach, simple structures such as 1D and some of the 2D tubing networks were directly embedded in a targeted matrix. Tubes were required to be strong enough to withstand mixing and casting but brittle enough to fracture when the concrete cracks (Dry, 2001; Joseph et al., 2010). Early researches such as Dry (1992, 2000) and her co-workers mainly focused on the first approach. Later researchers such as Joseph (2010) further developed one dimensional (1D) glass tubes with outputs opening to the air.

For the second method, instead of heaving tubes inside the matrix, channels can be made by placing solid bars in moulds or shutters prior to casting and then removing them after the concrete has set to leave hollow space within the matrix. This approach avoids long term tube monitoring and enables multi-scale healing over time. Davis et al. (2015) applied shrinkable polyolefin tubes or polyurethane tubes in the mould, and then plastic tubes were removed after casting. A few joints were added in their study, which allowed a crossing matrix of tubes, upon removal of tubes, to leave a 2D interconnected vascular network in a 600 mm square slab. This system is able to allow the healing agent to migrate to all regions of the network via its connected channels. And it provided flexibility in planning and shaping channels together with the reinforcement, which is able to achieve a degree of complexity (limited in 2D) in building up connected hollow networks. Moreover, this removable 2D PU structure provided a way of maintaining multi-use networks that can be re-used over the lifetime of a cementitious structure to enhance and enable multi-scale healing. However, this approach is unlikely to create sophisticated structures in various shapes, leading researchers to pursue more advanced network manufacturing techniques.

On the other hand, three dimensional (3D) networks are more complicated and consist of interconnected structures, which are capable of transporting healing agent to the damaged areas across the specimen's volume. However, it is also hard for 3D vascular structures to monitor glass/plastic tubes after several healing cycles. Removable PU tubes can only be used in simple structures like single channels or 2D grid structures. This is because they cannot be bent to a high curvature to create complex or biomimetic structures. Besides, such complicated structures would make it even harder for pulling PU tubes out after pastes are cured.

Obtaining natural vascular shapes

Directly embedding and tube removal methods could hardly achieve a more complicated network. Fabricating biomimetic shaped vascular networks in 3D seems a mission impossible.

Currently, only a few techniques were feasible for manufacturing networks with natural vascular shapes in polymer composites. These include soft lithography, electrostatic discharge and 3D printing sacrificial materials as fugitive ink. Leaf venation was directly copied and transformed into hydrogel using soft lithography to develop inside vasculature (He et al., 2013, Figure 2.24 C).

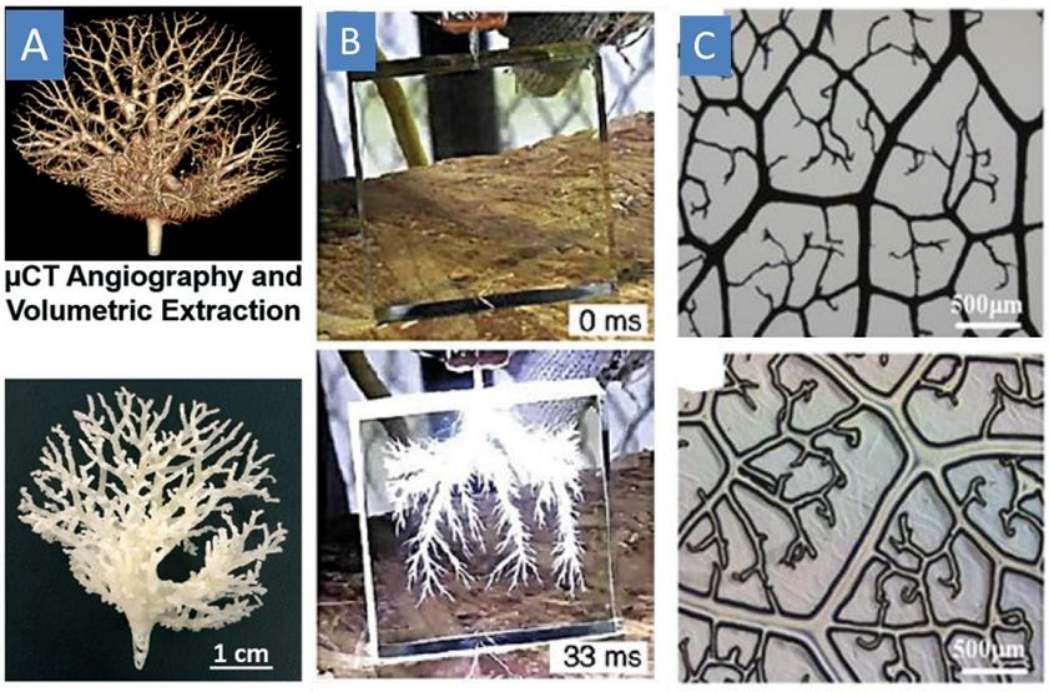

Figure 2.24 Different approaches of vascular structure by (A) printing of scaled-up mouse liver vasculature derived from a μCT angiography scan (Kinstlinger et al., 2016); (B) applying

electrostatic discharge to fabricate vascular patterns (Huang et al., 2009) and (C) using soft lithography for building micro-fluidics devices (He et al., 2013)

Huang et al. (2009) applied electric charges to create a tree-shape branched microvascular network in polymethylmethacrylate (PMMA) block. Fabricating vascular networks directly from nature would inherit biological structures and maximise fluid transferring efficiency. However, the flexibility of soft lithography and electrostatic discharge is limited in terms of coverage area and branching diameters in real applications due to the limited number of real vasculature samples and uncontrollability of electrostatic discharge.

These problems could be solved by using sacrificial materials combing 3D printing technique as coverage area and branching diameters are depending on designing models, which can be fully controlled by developers.

Design + Additive Manufacture

Another way of creating complex vasculature is by understanding abstract laws of nature and then utilizing the laws into vascular designs, then generating workable network models. This is a modified method to create vascular-shape structure with high controllability compared with the methods mentioned above.

In recent years, emerged manufacturing technology and material developments made it possible for them to be adopted in various research fields and industry, with drastic improvement in speed, accuracy and material properties (Guo and Leu, et al., 2014). Interest among scientists has stemmed from the desire to minimise assembly stages, the need to produce more complex parts that incorporate additional functionality, and the ability to create high-end and/or low-volume 'niche' objects (Campbell et al., 2012).

For self-healing networks, accomplishing swift diagnose and efficient delivery of fluid to damaged zones were main design requirements, which can be fulfilled by additive manufacturing due to their abilities in dealing with high degrees of geometrical complexity and enabling a reduction in the total number of manufacturing steps required to produce a self-healing material (Campbell et al., 2012; Conner et al., 2014). Current available additive manufacturing technique for producing complex structures mainly includes: direct ink writing (DIW), material extrusion (FDM 3D printing), and stereolithography (SLA) (Gibson et al., 2015; Wang et al., 2017).

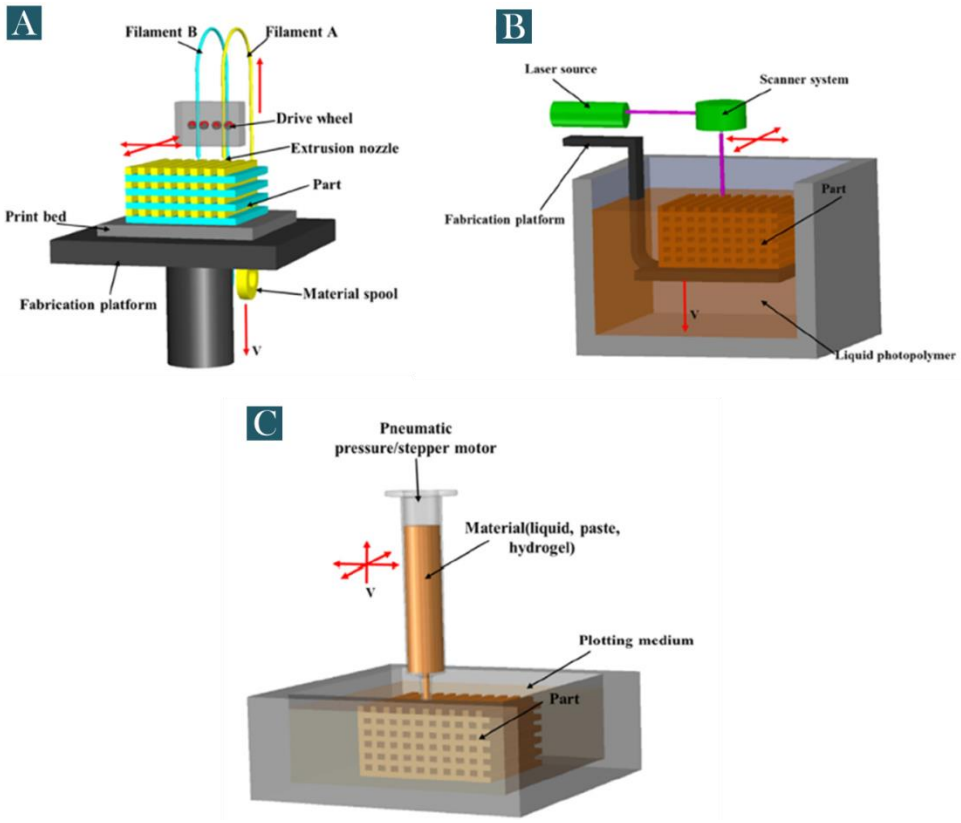

Figure 2.25 Schematic representation of a typical (A) FDM setup; (B) SLA setup; (C) direct ink writing (Wang et al., 2017)

Direct ink writing

DIW has been used to create 3D microvascular networks within epoxy-based materials for the transportation of healing agents to cracks sites. It is based on extruding a viscous material, such as colloid-, nanoparticle-, or organic-based inks, from a pressurised syringe to create the 3D shape of materials, as shown in Figure 2.25 C. Structures are created by depositing inks layer-by-layer, either through a droplet-based or continuous filament-based approach (Wang et al., 2017), then the curing process can be performed under heat or UV light. Normally, temporary, sacrificial materials are needed in supporting the printed structure to avoid the collapse of complex structures. Therriault et al. (2005) used a dispending robot to print paraffin-based fugitive scaffold in epoxy composites. The sacrificial scaffold was then liquefied, leaving hollow 3D complex channels within the composites. Similar sacrificial materials were reported to build up hollow vasculature, such as microcrystalline wax combined with petroleum jelly (Toohey et al., 2007), and

polylactic acid gasified at high temperature (Guo et al., 2013).

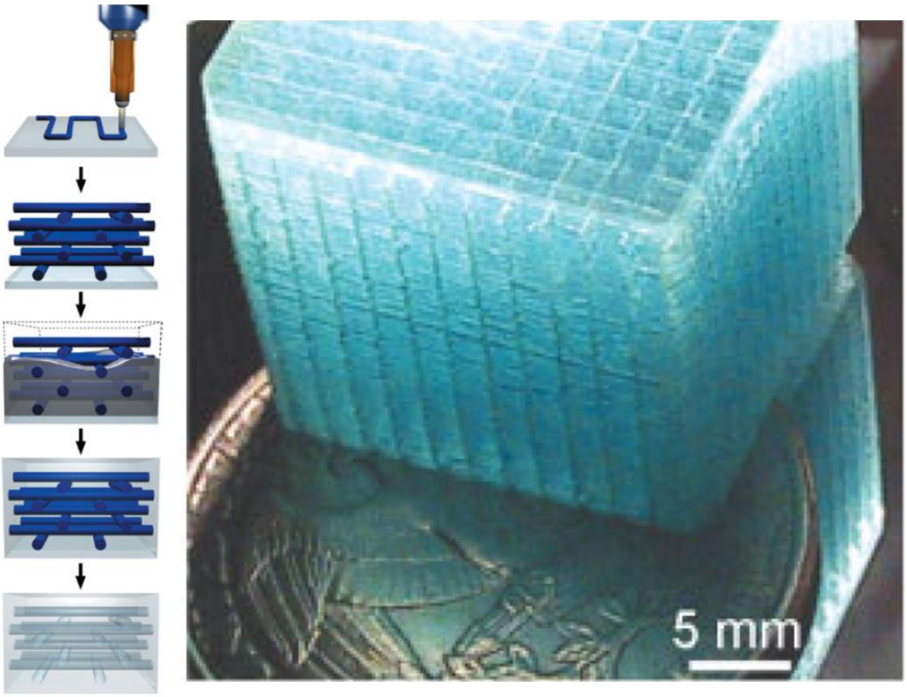

Figure 2.26 Schematic setup of the fabrication procedure for 3D microvascular via DIW (fugitive ink in colour blue, and hollow channels in light blue) with the optical image of a 104-layer microvascular network enclosed in clear epoxy matrix (Therriault et al., 2005)

Stereolithography (SLA)

A UV-laser was used as a 'drawing pen', which controlled in the desired path to shoot in the resin reservoir, and the photocurable resin will polymerise into a 2D patterned layer. After each layer is cured, the platform lowers, and another layer of uncured resin is then ready to be patterned. Typical polymer materials used in SLA are acrylic and epoxy resins, which can be cured by UV laser (Melchels et al., 2010). This method eliminates the problems associated with structural support and nozzle clogging while having the capability to print at high resolution and accuracy. Meyer et al. (2012) fabricated branched vascular networks via stereolithography from photo-cross-linkable biopolymers and achieved structures in the 10–100 μm range (Figure 2.27). However, SLA is mostly limited by the minimum structure size, nozzle size, scattering of the equipment, printing material types.

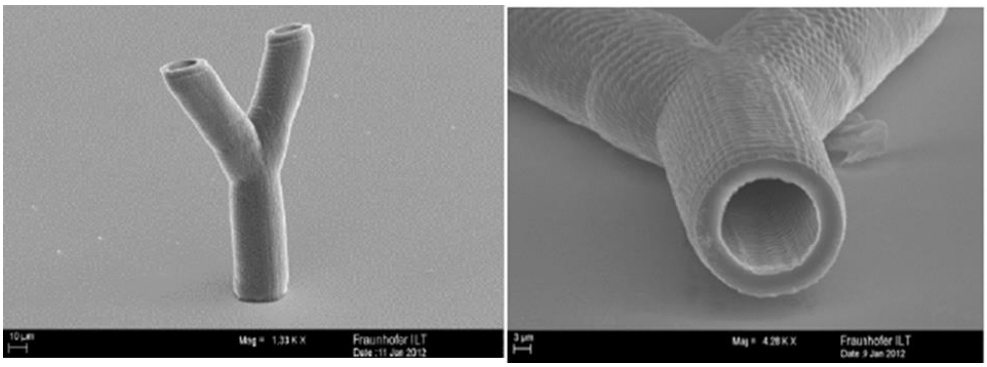

Figure 2.27 SEM images of a branched structure generated via two-photon polymerisation Stereolithography (SLA) (Meyer et al., 2012)

3D Printing (Fused deposition modelling, FDM)

Fused deposition modelling (FDM) 3D printing is the most commonly used in fabricating controlled shaped polymer composites. In FDM printers, thermoplastic filaments, such as PLA, ABS, and slurry polymer gels were heated into a semi-liquid state and extruded from the nozzle and deposited layer by layer onto the build platform where layers are fused and solidified, locking the deposited material in place (Dizon et al., 2018). The quality of prints is controlled by altering parameters in printer-related software, such as layer thickness, printing orientation, raster width, raster angle, supports and air gap (Sood et al., 2010; Wang et al., 2017). Several different components for the vascular network have been prototyped using 3D printing. Recent investigations by De Nardi et al. (2020) developed PLA printed MVNs in self-healing concrete. And Minnebo et al. (2017) explored the use of inorganic phosphate cement together with 3D printed PLA distributive parts in fabricating self-healing vascular systems. The 3D printed distribution piece which allowed one inlet to be connected to several channels embedded in the concrete, which was formerly discussed in the previous section.

Similar to SLA, printing resolution is largely depended on additive manufacturing, which affects and limit the accuracy, layer thickness, and surface smoothness of the printed network, therefore minimum wall thicknesses are currently restricted to the millimetre scale. Common drawbacks of FDM 3D printing are that (i) limitation in size; (ii) usable material is limited to thermoplastic polymers with suitable melt viscosity; (iii) harness in the removal of the support structure used during printing.

However, advantages in using FDM 3D printing are also promising, (i) low cost, (ii) high speed, (iii) simplicity, and enable multiple extrusions (Dizon et al., 2018). Low financial investment and high producing efficiency made the use of FDM 3D printing a high-value candidate in fabricating vascular networks for self-healing materials.

2.5.5 Challenges in manufacturing vascular networks for self-healing

With the aim of elevating self-healing vascular system to be more resilient and intelligent, Qamar et al. (2020) summarised eight grand breakthroughs in fabricating self-healing vascular networks that might fundamentally change the future in three aspects: Vascular design, Additive manufacturing and Healing chemistry, (as illustrated in Figure 2.28).

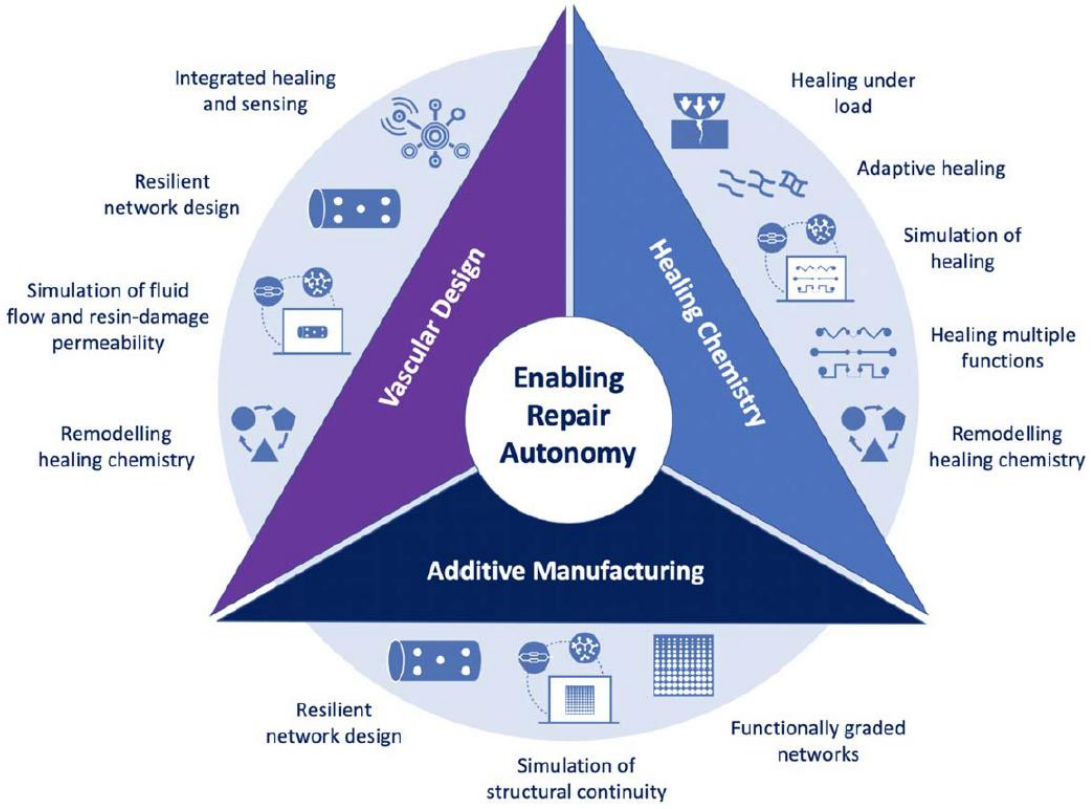

Figure 2.28 Grand breakthroughs in the design and manufacture of self-healing vascular networks in the future (Qamar et al., 2020)

In the vascular design section, four main challenges were identified including integrated healing and sensing, resilient network design, simulation, and remodelling of healing chemistry. More specifically, to promote durability and sensitivity of a vascular system, the design should be able to deliver healing potential without fracturing, or has built-in redundancy, thus maintaining its structural and flow continuity throughout the damage

event-healing cycle. However, in most of the cases (Joseph et al., 2010; Selvarajoo et al., 2020a; Harrop, 2018; De Nardi et al., 2020), healing events were mostly triggered by physical cracks, which would result in variation of the vascular structures. Thus, connectivity and alternatively in designing vascular channels need to be considered to avoid potential blockages and leakages (Williams et al., 2008) in physical triggering systems. Simulations would also be needed to confirm its workability by mimicking flow within the network, flow into the damage, the changing cure kinetics, the change in mechanical performance locally and the restoration of the structural performance when subjected to the matrix. Other approaches also need to be investigated in terms of avoiding monitoring of vascular structures and potentially switching to a non-fracturing triggering system such as chemical triggering (This will be mentioned in the following section). More importantly, the design should ideally provide the designer/operator with direct feedback on the state of the structure's performance before, during and after self-healing. This may require other techniques such as sensing to be able to equip the vascular systems with remote monitoring function.

When it comes to manufacturing, the main challenges are (i) feasibility of achieving desirable vascular designs and (ii) availability of techniques. One of the biggest problems is scaling up since current additive manufacturing devices are limited by its enclosed printing workplace. Harrop (2018) and Li et al. (2020) overcame this by assembled vascular structure segments after being printed separately in FDM 3D printers. In this approach, connective joints required carefully designs to ensure sufficient flow delivery. Alternatively, manufacture outreach is an ideal option for massive production considering the time required for fabrication, and less size restriction in commercial scaled machines.

As for healing chemistry part, healing under load requires the structure to have the ability to heal under a static or cyclic load (which has caused the original fracture/failure) is the ultimate challenge for the self-healing community. Researches such as Joseph et al. (2010), Tsangouri et al. (2019) and De Nardi et al. (2020) examined vascular self-healing systems under cyclic loading and achieved impressive mechanical recovery after a few cycles of loading. Besides, to ensure full functionally of s vascular system, wall materials in vascular structures could autonomously adjust, remodel and monitor the structures to ensure entire structural fracture is avoided, before returning subsequently to full load-carrying capability. This request the next generation of the self-healing vascular system to equip with multiple functions and impart the restoration of both primary and secondary

structural functionality simultaneously, e.g. strength promotion and energy disruption would be for contrition materials; toughness and transparency would be required for glass screens; high conductivity and structural repairs will be needed for self-healing batteries, solar cells, flexible electronics and energy storage devices.

2.6 Chemical triggered self-healing system

The durability of concrete is one of the greatest challenges in the construction industry, and it is largely depending on the exposed environment. Corrosion has been identified as one of the key factors that would determine the durability and integrity of a concrete structure (Hoff, 1991; Taheri et al., 2020). Environments such as oil platforms, underground tunnel structures, marine and hydraulic structures are among the most critical infrastructure assets for modern urban societies and are highly affected by concrete corrosion (Wiener et al., 2005).

Chemical ions attack and acid attack have been the most reasons for inducing corrosion in concrete structures. Saline water or seawater environment tends to increase the risk of corrosion when the structure is exposed to air. The most damaging effect of saline or seawater on concrete structures arises from the attack of chloride since steel bars in reinforcement concrete are prone to corrosion induced by chloride ions (Zeng and Song, 2013). The Cl ions are able to penetrate through massive concrete bulk and reach the steel/concrete interface, therefore inducing corrosion. When the Cl ions concentration exceeds a threshold, the surface protective passive layer of steel could be destroyed and comes vulnerable under the threat of Cl ions. The protection of reinforced concrete will be significant by lowering the Cl concentration, which provides a key design parameter for corrosion reduction (Söylev and Richardson, 2008).

Besides, acid attack, a form of the chemical attack on concrete subjected to low pH environments, causes microstructural changes in concrete due to the dissolution and leaching of acid-susceptible elements from the cement paste (Erbektas et al., 2020; Allahverdi & Škvára, 2000). Acid attack on concrete structures might occur on the surface and inside structures such as slabs, floors and concrete overlays, is mainly exposure to acidic rainwater in that the dissolution of CO_2, SO_2 and NOx in rainwater reduces the pH to 4–5 (Sersale et al., 1998).

Intending to deal with the damage resulted by corrosion, various studies have investigated the use of self-healing materials based on encapsulation technique (Pelletier et al., 2011, Hilloulin et al., 2015), which were mechanically triggered by the cracks when damage appears. The healing agent, such as sodium silicate, is released when the capsule was triggered by physical cracks, and deposits on the metal reinforcement bars, forming a passive film on the surface of the metal to protect it from further corrosion (Pelletier et al., 2011). However, it is unlikely that this mechanical triggered system is able to respond to early corrosion when Cl concentration increases or the pH in the cementitious matrix goes down (Liang et al., 2018). Therefore, an effective encapsulation of repairing materials is required to control the release, enabling early response to potential damage. The common mechanism is that the shell material is triggered by chemical changes in the matrix inducing the disassembly of the shell (De Belie et al., 2018). Thus, the key investigation in a controlled release system focuses on chemical sensitive shell materials.

2.6.1 pH sensitive material for chemical triggering

Recent investigations on the chemical triggering system have been focused on investigating of pH-sensitive shell materials since there is a particular matter of concern for concrete is the decrease of alkalinity caused by the acid attack (Sersale et al., 1998, Erbektas et al., 2020).

Currently, pH-sensitive materials, such as the hydrogel, degrading polymers, were widely investigated in drug delivery systems in reacting to various pH environments in human body (Rizwan et al., 2017). Amongst the pH-responsive materials, hydrogels are the most studied. This is because collapse and swelling are the abrupt changes that occur when pH-sensitive hydrogels are exposed to a certain working pH range, leading to volume phase transition and disassembly (Buenger et al., 2012).

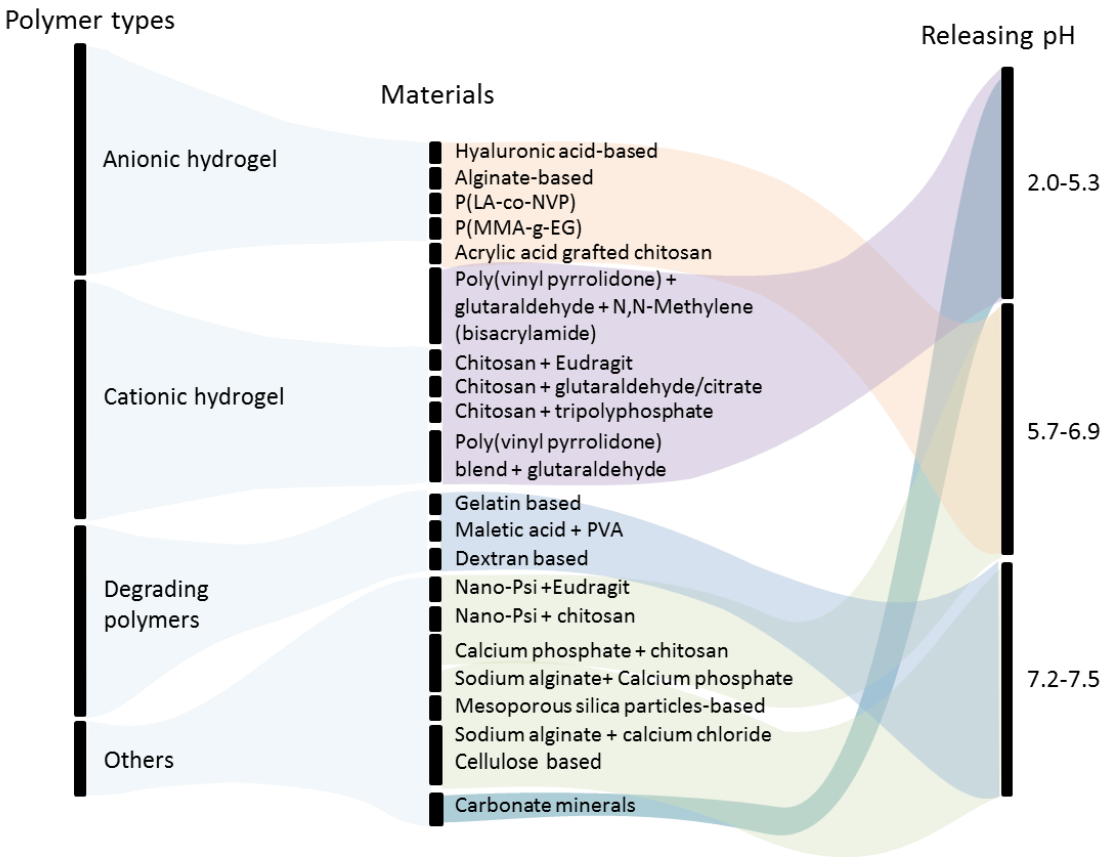

Figure 2.29 pH sensitive polymers and their working pH range (summarised from literatures: Rizwan et al., 2017; Risbud et al., 2000; Vibhooti et al., 2013; Schmaljohann, 2006; Liu et al., 2017)

Most of the cationic hydrogels swell at lower pH (2.0-5.3) due to protonation of amino/imine groups (Figure 2.29). The protonated positively charged moieties on the polymer chains cause repulsion and hence are responsible for swelling (Schmaljohann, 2006), which is normally used in drug (antibiotic) delivery to the stomach. The anionic hydrogel, such as hyaluronic acid, similarly, swells at acid-medium pH (around 5.7-6.9) due to ionisation of the acidic groups (Du et al., 2015). However, for cementitious materials, the low pH trigger threshold made it hard to be adopted in responding to early acid attack.

On the other hand, composite hydrogels with other synthetic materials could achieve successful sensitivity in an alkaline environment, at around and even above pH 7. For instance, Lim et al. (2015) synthesised a cellulose nanocrystals/poly(acrylamide) hydrogel that started swelling at pH 7, and Zhou et al. (2014) created a cellulose-based composite and showed swelling at pH 7.4. In cementitious material, Xing and his co-worker from Shenzhen University (Wang et al. 2016; Hong et al., 2019) fabricated self-immunity ethyl

cellulose (EC) shelled microcapsule which can be triggered at pH 10 by the low concentration of hydroxide in the solution. Higher pH response threshold related to higher sensitivity in responding to the acid attack in an alkaline environment (cementitious materials, pH=13). Their pH-sensitive EC shell successfully designed to achieve and prevent corrosion in concrete reinforcing bars by responding to early pH changes.

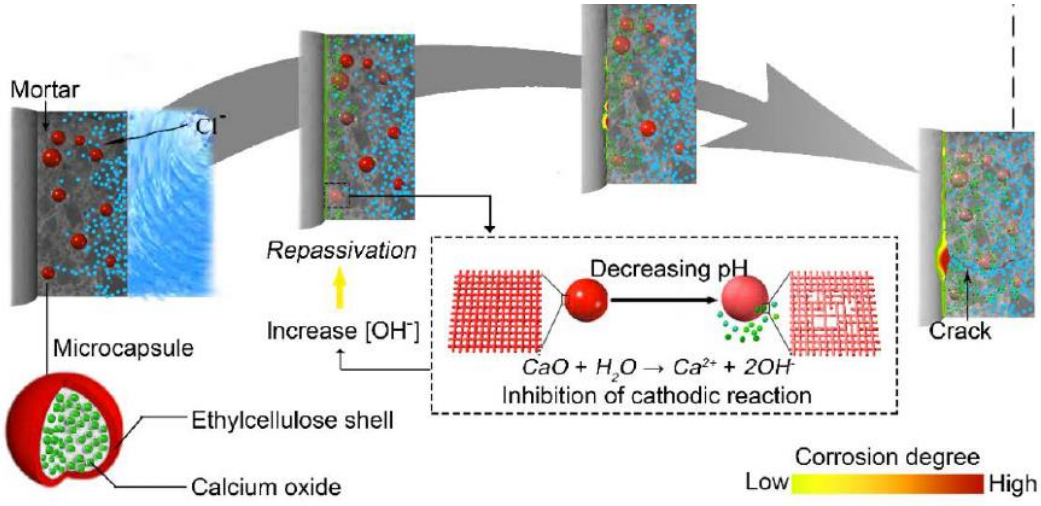

Figure 2.30 OH-regulated intelligent microcapsules for the corrosion protection of the reinforcing bar in reinforced concrete (Hong et al., 2019)

2.6.2 Ion sensitive material for chemical triggering

Another concern for concrete is the damage causing by depassivation of steel reinforcement, which is related to the ingress of ions, specifically chloride. pH-sensitive materials, however, could hardly cover this type of damage. And it is difficult to adjust local pH or initiate cracking under saline and seawater environment. Thus, the release of corrosion healing agents triggered by Cl ions is highly desirable because it is the most abundant anion in the saline water and seawater (Liang et al., 2018).

Polyol coated fibre

Dry and her coworkers invented a world first time-controlled release in responding to chemical ions in 1996 (Dry & Corsaw, 1998; Dry & McMillan, 1996). In their experiments, the time of corrosion onset could be improved by the release of anticorrosion agents from hollow porous polypropylene or fibreglass fibres. These fibres were coated with a polyol, which dissolves in saltwater. The encapsulated chemical is released onto the metal rebar when the saltwater dissolves the coating. The results showed concrete samples containing either no protection or the conventional freely mixed

calcium nitrite, this system of internal release form fibres performed well in a series of tests (Figure 2.31). And more impressively, this delayed the onset of corrosion by at least three weeks, in the laboratory specimens, and reduced the amount of total corrosion by more than half (Dry, 2015). To follow this technique, however, needs further investigation since polyol is a very broad concept, and the reaction mechanism of chemical trigger in Dry's work hadn't been revealed clearly.

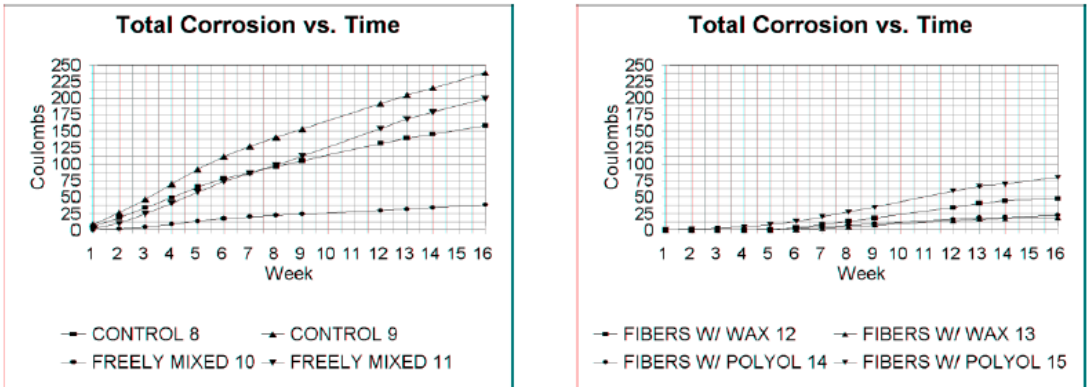

Figure 2.31 Comparison of onset and severity of corrosion, for fibres containing anticorrosion chemical on the right, versus those without, on the left (Dry, 2015)

Ionic liquids (ILs) shell

Recently, the ionic liquids (ILs) have attracted increasing research attention due to their high ionic conductivity, chemical stability and flame resistance capabilities (Lv et al., 2016; Liang et al., 2018).

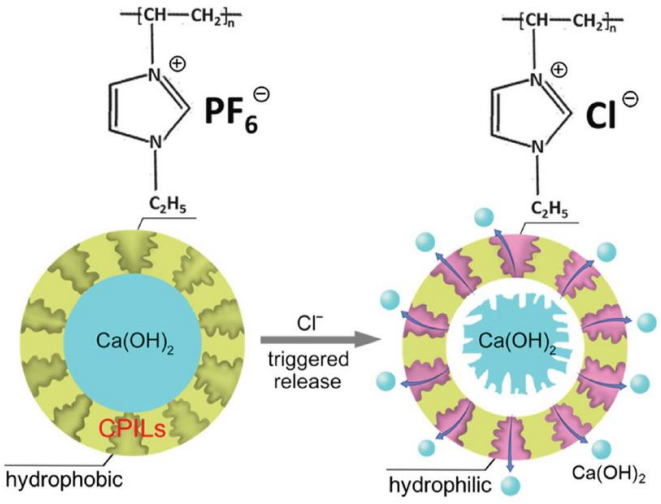

Figure 2.32 Schematic illustration of the release process of $Ca(OH)_2$ from the microcapsules triggered by Cl^- ions. (Liang et al., 2018)

As shown in Figure 2.32, the anions of ILs can be exchanged with other anions, such as the Cl^- ions, which enable the ILs to convert from hydrophobic to hydrophilic (Lv et al., 2016). With the responsiveness to Cl^-, ILs gained considerable attention in being used as the Cl^- responsive shell (Liang et al., 2018). Agents with low water solubility, such as $Ca(OH)_2$ could gradually permeate outside through ILs shell. In the work of Liang et al. (2018), they applied ILs in protecting rebar from corrosion; the steel was severely corroded in NaCl solution without micocapsules, while for the samples with ILs shelled capsules achieved promising results (Figure 2.33). The success of the ILs in this research demonstrated that ILs is able to improve the durability of reinforced concrete structures, and potentially being adapted for a wide range of applications. However, the supply of this specific type of ILs is restricted geographically, and synthesising process requires complex fabricating procedure and purification process (Marcilla et al., 2004; Detrembleur et al., 2011), which created high barriers in applying this technique.

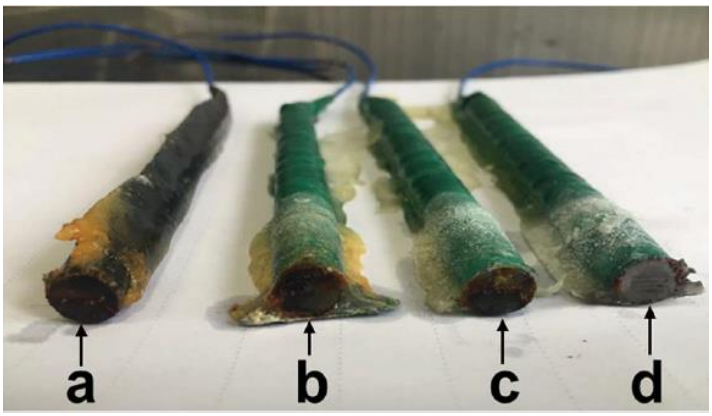

Figure 2.33 The digital photograph of the steel samples with different contents of IRs shelled coating in simulated seawater after 60 days, a-0g; b-0.5g; c-1g; d-1.5g. (Liang et al., 2018)

Alginate based shell

In the ion attack scenario, chloride ions are stable triggers in developing corrosion. Another facile method in responding to chloride ions is to generate shell materials that are able to react with chloride ions, such as metal ions, and thereby decomposing the shell materials. When these smart responsive shell materials contact with chloride ions, the metal ions will be extracted out to disintegrate the capsules and precipitated (Xiong et al., 2015).

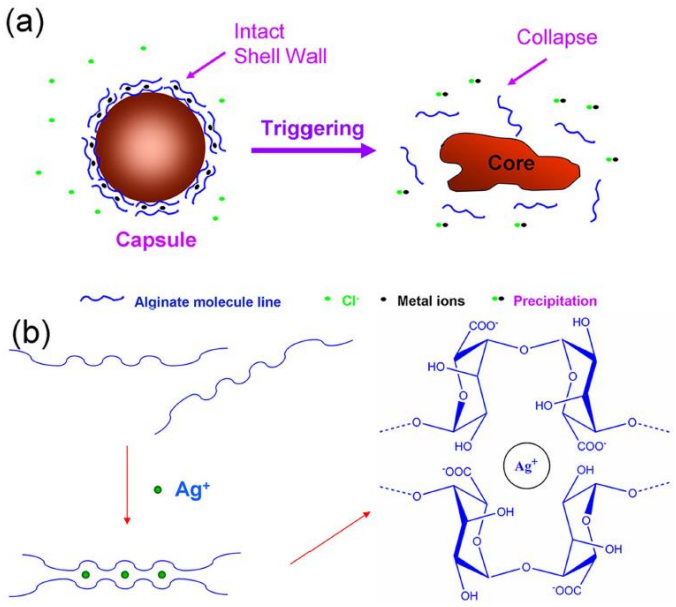

Figure 1. a) Schematic of capsules triggered by chloride ions b) The structure of alginate chelated with Ag^+

Figure 2.34 Schematic of capsules triggered by chloride ions and the reaction with metal cations (Xiong et al., 2015)

Xiong et al. (2015) selected sodium alginate as raw materials since it can be crosslinked with many metal ions to form the hydrogel. Ag^+ was chosen to be coordinated with alginate to form the wall materials of capsules, silver alginate (Ag-alg) can also form a characteristic "egg-box" structure (Paques et al., 2014). Each alginate molecular chain can be linked with other chains, causing the formation of a three-dimension gel network, which has enough strength to form the shell (Xiong et al., 2015). In their work, they successfully fabricated smart chloride ions responsive shell, silver alginate, and first introduce them into cementitious materials. As shown in Figure 2.35, shell materials were broken and successfully released agent core, and prove the capsules still can be triggered by chloride ions at low concentration of chloride ions, (seawater 3.5 wt%) in the concrete matrix.

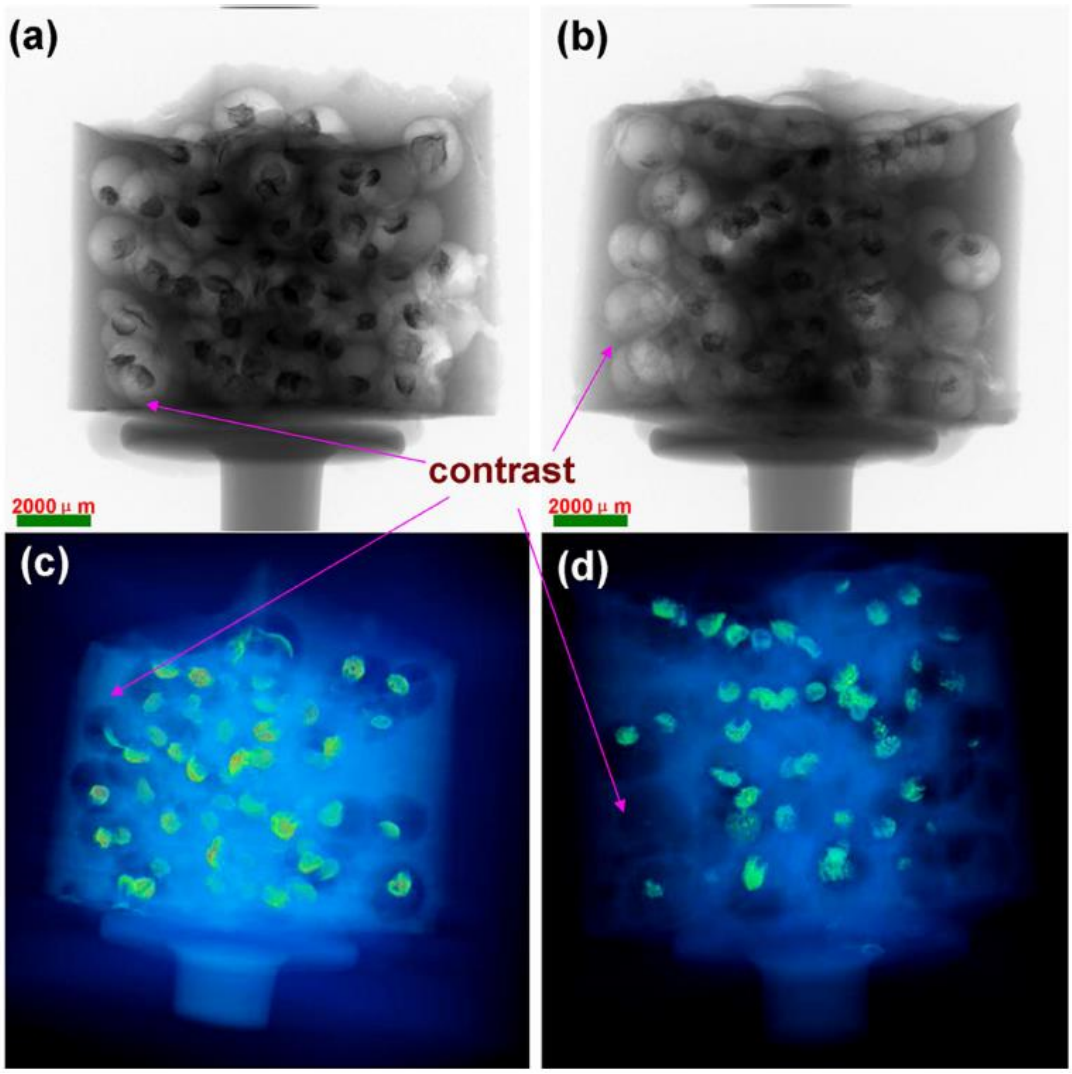

Figure 2.35 X-ray CT images of concrete specimen and X-ray CT test: without NaCl (a,c) and with NaCl (b,d)(Xiong et al., 2015)

This new method of self-recovery system is able to reduce the deleterious effect of chloride-attack and possesses high broken efficiency and sensitivity advantages. This is because chemical responsive shells can contact chloride ions, all shells will be broken. This can overcome the drawback in the mechanical triggered system, since it is difficult to ensure the shell can be broken under mechanical stress (Xiong et al., 2015). The second benefit of using a chemical triggered system is that chloride ions can penetrate into the concrete matrix through nano cracks and channels without micro-cracks formation, which had been proved by Xiong et al., the smart capsules can still be responsive to chloride ions without relying on cracks. These advantages made chemical triggered system an impressive candidate in responding to early-stage attacks.

In general, alginate-based chemical triggering from (Xiong et al., 2015) is by far the most promising technique due to the low entry barriers of fabrication compared with ILs

technique used by Liang and his co-worker, and with clear mechanism revealed. Polyols from Dry's work, however, has no followed up studies in recent years, which is mainly due to the uncertainty of polyol types she used in the 1990s.

2.7 Healing performance evaluation

The self-healing performance in cementitious material is primarily evaluated from the initiation of the self-healing process by the creation of cracks to characterise their performances after the healing process (Ferrara et al., 2018). Previous studies had adopted several methods and tests to describe the self-healing process and behaviour. The characterisation for self-healing systems is conducted for evaluating both healing efficiency and system reliability. Methods summarised by Van Tittelboom and De Belle for describing healing effectiveness and reliability could be broadly classified into three categories: (i) visualisation and determination, (ii) mechanical properties recovery and (iii) durability regaining. The related test approaches are listed in Table 2.6, which could cover the initiation of self-healing reaction, evaluation of self-healing efficiency, and monitoring of the healing process.

Self-healing mechanical performance is measured when the self-healing process initiated after a certain period of time. Specimens are normally reloaded to measure the strength, stiffness based on the stress-strain relations or force-displacement curves by three or four-point bending tests. Mechanical healing recovery can be evaluated by comparing the loading curves of untreated, and autonomously healing methods (Van Tittelboom et al., 2013). The peak load and the slope of the force-displacement curve are corresponding to strength and stiffness indications, respectively.

Three-point bending tests were mostly introduced to initiate a more controllable and comparable cracking event, which could create the preoriented crack in specimens, simultaneously monitor the self-healing process, and provide constant experimental results for numerical modelling (Selvarajoo et al., 2020a, 2020b; Joseph et al., 2010; Freeman and Jefferson, 2020). Three-point bending test is usually conducted with linear variable differential transformer (LVDT), which is attached at the bottom of the specimen to measure the crack width (Selvarajoo et al., 2020a, 2020b). Commonly, in order to control the crack propagation, a notch of the specimen was prepared before testing. On the other hand, four-point bending tests are able to induce multiple, random cracking

events, which could simulate real behaviour of a material used in a technical application (Sun et al., 2011; Harrop, 2018; Li et al., 2020). Since multiple cracks in the beam are normally induced by four-point bending tests, the width of each individual crack is approximately calculated though dividing the LVDT value by the total amount of cracks, when the elongation of the specimen is ignored (Van Tittelboom et al., 2016).

Digital image correlation (DIC) works together with Three-point bending/Four-point bending tests, by taking multiple images of the crack generation process, was used to measure the deformation of beams under load via tracking grey value patterns. However, this technique is greatly affected by resolution restriction, and its precision heavily depends on the camera and calibration analysis. Acoustic emission (AE) is another effective tool that is used to provide real-time cracking records in the matrix and was employed in determining self-healing performance (Van Tittelboom et al., 2012). This is a non-conductive method that collects the waves, ranging from a number of hits, amplitudes, velocity, frequency, to AE energy produced by and emitted within the material (Grosse and Ohtsu, 2008), thereby being recorded as AE signal.

Durability is one of the greatest challenges encountering by self-healing materials and promoting durability has become the primary goal. Water tightness is a direct way of evaluating and predicting the service life of cementitious materials and has become a typical durability test that is widely used by researchers (Van Tittelboom et al., 2015). Capillary absorption coefficient could provide accurate results to evaluate the durability of crack-healed specimens with single cracks (Van Belleghem et al., 2016). However, for the tests with multiple cracks, it is hard to evaluate the healing efficiency only based on sorptivity tests, and the water permeability of each crack is also difficult to be measured (Van Tittelboom et al., 2015; Van Tittelboom et al., 2016). In this case, visualised tools have been introduced to aid. Van Tittelboom et al. (2015) employed X-ray computed tomography and neutron radiography and firstly reported and analysed water absorption/distribution in self-healing samples.

Moreover, the visual observation was the most direct way to determine the width of sealed cracks. Microscopy techniques are usually employed to quantitatively analyse the width of the crack and visualise the distribution of the healing agent. Scanning electron microscopy (SEM) is also the commonly applied techniques to visualise the deposition and crystallinity of secondary crystal emerged in the cracks while requiring complex

preparation for testing (Alghamri et al, 2016; Formia et al, 2016). Emerging methods such as computed tomography (CT), could directly reflect the distribution of networks and cracks, will also be considered to be applied in the later stages (Fang et al., 2018). Similar to DIC, this technique is greatly affected by resolution restriction, so that Micro-CT was mostly applied to obtain relatively higher resolution images. However, visualised tools could only provide healing progression. It is worth remarking that understanding healing mechanism by introducing chemical and mineralogical characterisation methods is significantly meaningful in promoting self-healing performance (Ferrara et al., 2018). Powder X-ray Diffraction (p-XRD; Maes et al, 2016; Kanellopoulos et al, 2015; Qureshi et al., 2016), Infrared Spectroscopy (Alghamri et al, 2016; Qureshi et al., 2016) and Thermogravimetric Analysis (TGA; Van Tittelboom et al., 2010; Qureshi et al., 2016) were employed and suggested insights in selecting promoters for the healing process.

To conclude, methodologies introduced to assess the performance of self-healing technologies make it possible to provide a unified framework in conducting comparative studies among various research groups and also pave the way towards consistent incorporation of self-healing concepts to provide a feasible and reliable evaluation in analysing the life cycle of self-healing systems.

Table 2.6 Summary of tests for evaluation of self-healing performance (Ferrara et al., 2018; Van Tittelboom and De Belle, 2013; Xue et al., 2018)

	Technique	Application	Limitation
Visualisation and determination	Optical microscopy and image analysis	Visualisation crystal deposition and determination healing rate	Precision and efficiency depending on the microscope resolution
	Digital image correlation (DIC)	Crack patterns and strain distribution	Precision relies the camera and calibration analysis
	Scanning electron microscopy (SEM)	Visualisation crystal deposition	Expensive, only in grey scale depending on the atomic number of the element.
	Environmental scanning electron microscopy (ESEM)	Visualisation breakage of partially embedded capsule	unsuitable for fragile and large specimens, high cost
	X-ray tomography (CT)	Visualisation of release of encapsulated agent from embedded capsule in 3D	Extremely expensive, time consuming, with limited resolution
	X-ray diffraction analysis (XRD)	Determination of crystalline materials	Complex preparation
	Raman spectroscopy	Determination chemical composition	Complex preparation, highly depending on the spots detected
	Infrared analysis	Determination of precipitated products	Complex preparation and suitability of samples, moisture decreasing the accuracy; unavailable for minor deposition
	Chloride diffusion and penetration	Measurement of resistance against Chloride penetration; applicable for coastal structures or structures exposed to de-icing salts.	Rapid chloride ion permeability so far demonstrated only for specimens with w/c higher than 0.40

Durability Regaining	Sorptivity	Capillary water uptake by (healed) crack	Precision and efficiency depending on the crack states
	Water permeability	Water permeability coefficient can be determined by flow of water through healed cracks	Effectiveness is dependent on how the cracks were introduced
	Air permeability	Flow rate of air after healing has occurred measures the resistance against moisture/foreign substance penetration through (healed) cracks.	Very sensitive to the specimen composition: methanol can dissolve organic polymers used as healing agents.
	Ultrasonic pulse velocity (UPV)	Continuity of material	Precision and efficiency depending affected by metal reinforcement and transducer spacing
Mechanical property recovery	Tensile test	Regain in strength, stiffness and/or energy obtained when reloading healing specimen; formation of new cracks versus reopening of old cracks	Low accuracy, Influenced by parameters and curing condition of samples
	Three-point bending		
	Four-point bending		

2.8 Concluding remarks

Cement-based materials, the foundation of modern infrastructure, require improvements in enhancing durability without the need for repetitive and intensive maintenance work.

As discussed in section 2.1, durability and sustainability challenges in developed and emerging countries are still remaining. The value, therefore, lies in improving the quality of construction and the quality of materials used, in contributing to a more durable infrastructure, increasing its sustainability and reducing its cost. In reacting with the challenges of cost-effective, durability and sustainability encountered in the construction industry, it is necessary to continuously develop smart construction materials to be able to retain and repair the existing infrastructure and bring further sustainability to the next generation buildings. Thus, the idea of self-healing was facilitated into infrastructure, making cementitious materials that can heal themselves autonomously like our skin. As detailed in section 2.3, cementitious materials do possess some inherent autogenous self-healing capability due to the chemical contributions of continued hydration and carbonate formation. However, for effective autogenous healing, crack widths have a limit of 0.15mm and preferably are less than 0.05mm. Another approach is by autonomic healing. Researchers have been explored the use of engineered additions to further promote healing performance. To date, successful self-healing systems in cementitious materials had been based on the release of the limited amount of housed healing agents from microcapsules (Pelletier et al., 2011; Litina et al., 2014; Alghamri and Al-Tabbaa, 2016; Souza, 2017) as discussed in section 2.4. However, neither spherical capsules nor cylindrical-shaped capsules can provide unlimited healing agents for long-term repairing damage in the cementitious matrix. Damage scenarios require larger volumes of healing agents and the capability of dealing with repeated damage, therefore larger reservoirs are needed. A vascular system was therefore introduced in section 2.5. Since the vascular allows healing agents to be distributed from the healing agent reservoir throughout its structure to the damaged place. This process could continuously deliver healing agents and achieve repetitive repair, which is generally the most promising system that will help us go beyond conventional approaches to sustainable design to achieve resilient infrastructure. Applications of vascular networks in both polymer composites to cementitious materials were discussed, which had received promising results, especially

in more connected channel systems. Strategies of manufacturing vascular systems were discussed in section 2.5.3, which stated various approaches in creating complex channels in the matrix and their feasibilities. Finally, in section 2.6, chemical triggered shell materials were discussed in delaying the onset of corrosion and reducing the amount of total corrosion in saltwater environment. The relative novelty of chemical triggered self-healing cementitious materials only recently have self-healing concrete tests taken place.

In general, the main challenge in self-healing cementitious materials is efficiency and sustainability. Efficiency of self-healing is related with the position of the cracks and the size of the cracks. Most of the current solution such as intrinsic self-healing and capsule-based self-healing have been struggling in dealing with the large damage. The discrete distribution of self-healing capsules also limited the capability of diagnosing the cracks, in some cases, the cracks often went around the capsules instead of penetrating them. As for sustainability challenge, this is linked with long term performance after the self-healing materials being added. The amount of healing agent retained in cement or contained in capsules made it difficult for cementitious materials to heal multiple times, and some are unable to heal the damage a second time.

In reacting to these challenges, the vascular-based self-healing system was proposed to be the potential solution that is able to conquer the challenges, since it is a both interconnected and cyclic system. Interconnected structures have a great advantage over discrete capsule-based solutions in diagnosing cracks, which will drastically enhance their healing efficiency. Secondly, a vascular system also contains a healing agent reservoir, which enable it to continuously provide healing agents to the damage area, thereby achieving long-term healing.

However, to design and fabricate vascular-based self-healing system, there are technical challenges. More specifically, to promote the diagnose sensitivity of a vascular system, the design should be able to deliver healing potential without fracturing, or have built-in redundancy, thus maintaining its structural and flow continuity throughout the damage event-healing cycle. But in current designs (Joseph et al., 2010; Selvarajoo et al., 2020a; Harrop, 2018; De Nardi et al., 2020), the healing events were only triggered by physical cracks. Thus, connectivity and alternatively in designing vascular channels need to be considered to avoid potential blockages and leakages (Williams et al., 2008) in physical triggering systems. Other trigger mechanisms can be also considered to adapting in

vascular self-healing. When it comes to manufacturing, one of the biggest problems is scaling up since current additive manufacturing devices are limited by their enclosed printing workplace. This requires the next generation of the self-healing vascular system to equip with multiple functions and impart the restoration of both primary and secondary structural functionality simultaneously.

Overall, this literature review shows the significant progress made in self-healing cementitious materials field over the last two decades. The potential to use biomimetic vascular networks in this field has not yet been figured out, in terms of healing efficiency, failure mode and structure efficacy. So that, my PhD research aims to utilise biological principles to design biomimetic vascular structures for self-healing cementitious materials. Then, analyse the performance of this system by linking the findings from previous insightful studies.

Chapter 3

Methodology

This chapter introduces detailed description of the materials selected for study, sample preparation and experimental procedures associated with this research project. The chapter starts with presenting details of the various 3D printing and cementitious materials used followed by the materials preparations, testing techniques and procedures including both mechanical and microstructural as well as characterisation tests.

3.1 Materials

3.1.1 3D Printing Materials

Polylactic Acid (PLA)

PLA (polylactic acid, provided by Ultimaker®) was applied for generating vascular network using 3D printers. PLA filament technical information is given in Table 3.1.

Table 3.1 Polylactic Acid (PLA) Technical properties

Mechanical properties	Typical value	Test method
Tensile modulus	2,346.5 MPa	ISO 527 (1 mm/min)
Tensile stress at yield	49.5 MPa	ISO 527 (50 mm/min)
Tensile stress at break	45.6 MPa	ISO 527 (50 mm/min)
Flexural strength	103 MPa	ISO 178
Flexural modulus	3,150 MPa	ISO 178
Thermal properties	**Typical value**	**Test method**
Melt mass-flow rate (MFR)	6.09 g/10 min	ISO 1133 (210 °C, 2.16 kg)
Melting temperature	145 - 160 °C	ISO 11357
Diameter	**2.85 ± 0.10 mm**	
Max roundness deviation	**0.10 mm**	

* Data obtained from Ultimaker PLA TDS

Polyvinyl Alcohol (PVA)

PVA (polyvinyl alcohol, provided by Ultimaker®) is a water-soluble support material for multiextrusion 3D printing, with a good thermal stability. PVA in this work was used for creating hollow vascular network within cementitious materials, by utilising its water-soluble property. PLA filament technical information is given in Table 3.2.

Table 3.2 Polyvinyl Alcohol (PVA) Technical properties

Thermal properties	**Typical value**	**Test method**
Melting point / range	163 °C	ISO 11357
Thermal decomposition	> 210 °C	/
Melt mass-flow rate (MFR)	17 - 21 g/10 min	ISO 1133 (190 °C, 2.16 kg)
Ignition temperature	440 °C	/
Other properties	**Typical value/Description**	**Test method**
Density	1.23 g/cm3	/
Solubility in water	yes	/
Solubility in Dimethyl sulfoxide (DMSO)	yes	/
Diameter	**2.85 ± 0.10 mm**	
Max roundness deviation	**0.10 mm**	

* Data obtained from Ultimaker PVA TDS

3.1.2 Cementitious materials

This work included the testing of cement paste, mortar and concrete. High Strength Portland Cement (provided by Hanson®, CEM-I, 52.5) with a particle density of 2.7-3.2g/cm^3 and a specific surface area of 0.30-0.40m^2/g, was selected to conduct all the experiments in this project, complying with the requirements of BS EN 197-1. The chemical composition of the cement is presented in Table 3.3.

Table 3.3 Chemical composition of CEM-I cement

	Composition (%)						
Materials	CaO	SiO_2	Al_2O_3	Fe_2O_3	MgO	SO_3	LOI
Cement	63.60	19.50	4.90	3.10	0.90	3.30	2.10

* Data obtained from Hanson; LOI: loss on ignition

In the mortar and concrete mixes, the sand and gravel were obtained from Ridgeons Ltd, Cambridge, UK. Fine sand with a maximum particle size of 2mm was utilised. The gravel used in all concrete mixes had a maximum particle size of around 10mm. The particle size distribution (PSD) of both sand and gravel are given in Figure 3.1.

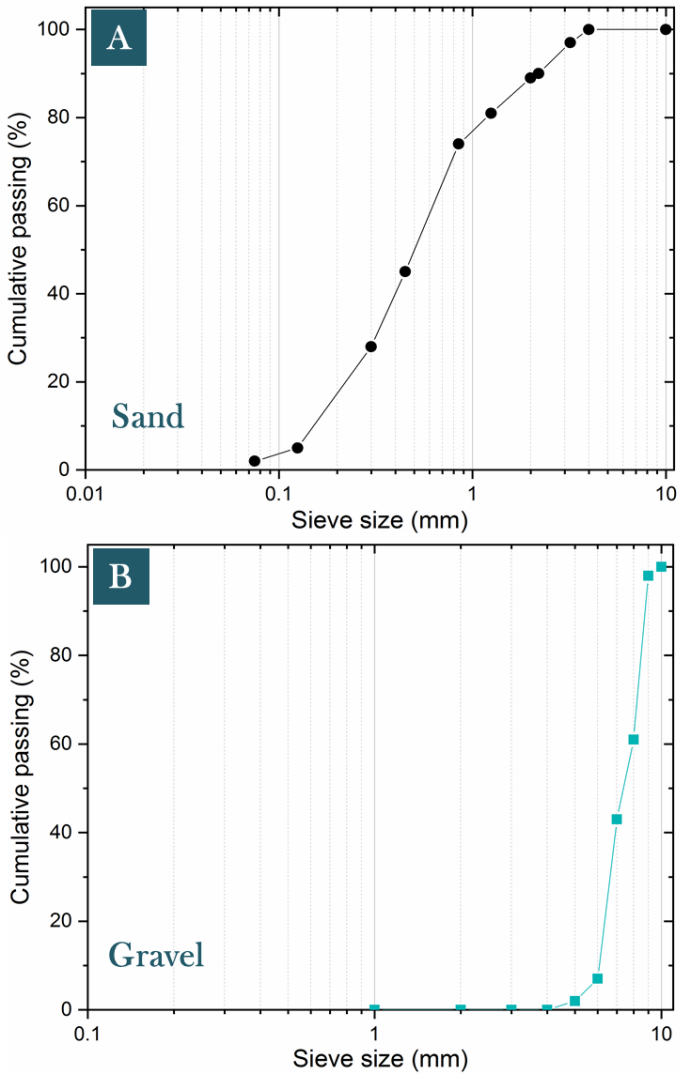

Figure 3.1 Particle size distributions of sand (A) and gravel (B) used in mortar and concrete mixes

3.1.3 Self-healing agents

Sodium Silicate (SS, Na_2SiO_3)

Healing agent Sodium Silicate was used during experiments for conducing self-healing tests, and this was obtained from Fisher Scientific®. Table 3.4 presents its physical and chemical properties.

Table 3.4 The chemical and physical characteristics of the Sodium Silicate

	Properties					
Materials	Formula	Mw ($gmol^{-1}$)	Density (20°C, g/mL)	Viscosity (20°C, cps)	pH	Melting point (°C)
Sodium Silicate	$Na_2O(SiO_2)_X \cdot XH_2O$	19.50	1.39	60.00	12.50	-1.00

* Data obtained from Fisher Scientific SDS

Tung Oil

Tung oil is a drying oil obtained from Tung tree (provided by Rustins®, density 0.932-0.937g/mL). Tung oil has been shown to reduce water sorption on concrete surfaces. So the Tung oil was use as sealing materials in this work.

3.1.4 Chemical triggering media materials

Sodium Alginate

To create a coating that can be triggered by certain chemicals, such as chloride ions, sodium silicate was used as a media material to be transferred into a chemical sensible coating. The sodium alginate was provided by Sigma-Aldrich®, UK.

Silver Nitrate Liquid (0.1M, $AgNO_3 \cdot H_2O$)

Silver nitrate was used to replace the sodium cations from sodium alginate by silver cations, and then form the chemical triggering coating. This was also purchased from Fisher Scientific®. Table 3.5 presents its physical and chemical properties.

Table 3.5 The chemical and physical characteristics of the Silver Nitrate

	Properties				
Materials	Formula	Molecular Weight	Solubility	pH	Vapor Pressure (20°C)
Silver Nitrate	$AgNO_3 \cdot H_2O$	169.87	Miscible	6.00	14 mmHg

* Data obtained from Fisher Scientific SDS

3.2 Vascular network fabrication

The vascular networks were designed in AutoCAD® and Creo® (Figure 3.2 A), then the designs were printed using Ultimaker® 3 Extended 3D printer (Fused deposition modelling system, FDM;) and Cura® software (Setting details: Nozzel type, 0.4 AA (for PLA) and 0.4 BB (for PVA); Cura input format, stl.; Layer resolution: 0.1 mm; Operational extruder temperature, 220°C; Operational bed temperature, 50-70°C; Print speed, 40mm/s; Travel speed, 120mm/s; Support, touching build plate, 25% density; Figure 3.2 B).

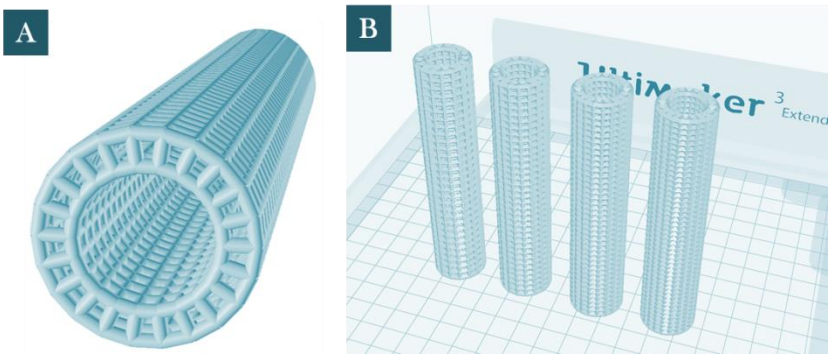

Figure 3.2 Vascular networks designed in AutoCAD (A) and prepared for printing (B) in Cura

FDM 3D printing is an additive manufacturing technique in which successive layers of print material are deposited on top of one another in order to create a 3D object (Sachs et al, 1995). The resulting layered print file was then transferred to the printer and used to direct the print head as to where to deposit a material layer of constant thickness in the x-y plane. Once a layer has been deposited the print bed moves down a distance equal to the material layer thickness and the next layer is deposited. Thus, a three-dimensional object was built up over time. Different 3D printed vascular structures were designed and fabricated using 3D printers. The design of vascular networks will be discussed in Chapter 4.

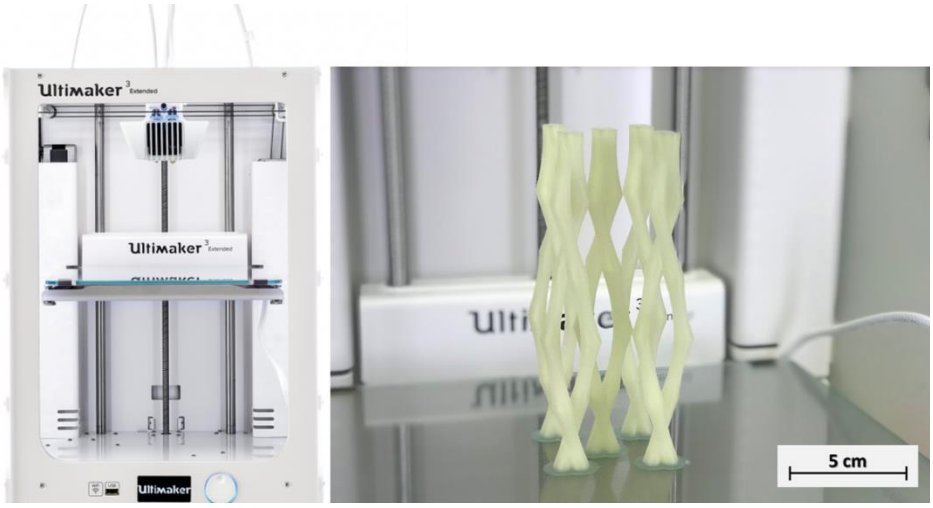

Figure 3.3 PVA vascular networks being printed in Ultimaker® 3D printer

3.3 Design, casting and curing of cementitious samples

3.3.1 General sample designs

Samples were designed for testing the feasibility of using PLA and PVA tunnel in cementitious materials. Then, healing behaviours and performance were evaluated by a

few measures such as crack closure tracking, water tightness and load recovery etc. To achieve this, standardised specimens were planned and conducted as shown in the Figure 3.4 below.

Both mortar and cement samples were considered in testing PLA vascular network for physical triggering use cases. Cementitious specimens were designed to test the behaviour and healing performance of 3D printed vascular networks in infrastructure. Cement and mortar-based beams were considered in this work to reflect the real structures. Concrete samples were not planned, since the current size of 3D prints would limit the dispersion of aggregate. Prismatic cement specimens were prepared for testing the viability of the 3D printed vasculature within cement matrix. The cement pastes were prepared use Ordinary Portland Cement (PC) (CEM-I, 52.5, supplied by Hanson) and water in a 0.4:1 ratio by weight. Mortar specimens were prepared for testing the survivability and healing behaviour of 3D printed vasculature within mortar matrix. The mortar mix was composed of water, sand and Ordinary Portland Cement (OPC) (CEM-I, 52.5 by Hanson) in a ratio of 0.4 :1.5: 1 by weight, in accordance with BE EN 196-1:2005. Detailed samples and designs can be found in Table 3.6.

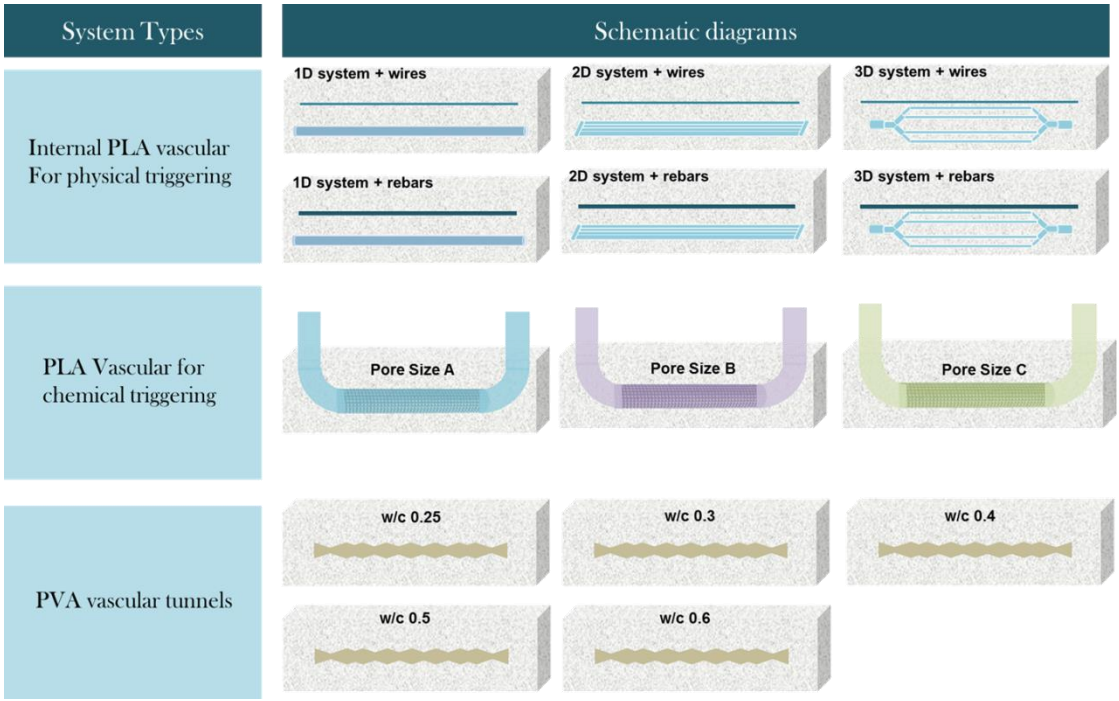

Figure 3.4 A schematic diagrams of different vascular specimens in this work

As for the vascular for chemical triggering, only cement paste was considered, with the aim of reducing the complexity of chemical composition. Specimens with Ordinary Portland Cement (PC) (CEM-I, 52.5 by Hanson) and water at water/cement (w/c) ratio of 0.4 were prepared. A similar set up was applied to polyvinyl alcohol (PVA) tunnel specimens due to the same reason. Prismatic specimens were prepared for testing the viability and performance of the 3D printed PVA vasculature within a cement matrix. The cement paste mix was prepared with Ordinary Portland Cement (PC) (CEM-I, 52.5 by Hanson) and water at water/cement (w/c) ratio of 0.25, 0.3, 0.4, 0.5 and 0.6 as the flowability of the cementitious mix will play an important role in the appropriate formation of the cement around the vascular structure.

Table 3.6 Summary of different types of samples conducted for internal PLA vascular systems

Test type	Sample type	Systems	Parallel tests	Pumping or encapsulated	Mould type (mm)	Curing condition	Healing condition
Compatibility	Cement beams	Plain	3	\	80×80×300	28 days	\
	Cement beams	1D/2D/3D	3	\	80×80×300	28 days	\
	Cement beams	1D/2D/3D+wires	3	\	80×80×300	28 days	\
Healing time	Cement beams	1D+wires	3	Pumping	80×80×300	28 days	7 days
	Cement beams	2D+wires	3	Pumping	80×80×300	28 days	7 days
	Cement beams	3D+wires	3	Pumping	80×80×300	28 days	7 days
Healing time/type	Cement beams	1D+wires	3	Pumping	80×80×300	28 days	28 days
	Cement beams	2D+wires	3	Pumping	80×80×300	28 days	28 days
	Cement beams	3D+wires	3	Pumping	80×80×300	28 days	28 days
Compatibility	Mortar beams	Plain	3	\	80×80×300	28 days	\
	Mortar beams	3D	3	\	80×80×300	28 days	\
	Mortar beams	3D+rebars	3	\	80×80×300	28 days	\
Healing type/time	Mortar beams	3D+rebars	3	Pumping	80×80×300	7 days	28 days
	Mortar beams	3D+rebars	3	encapsulated	80×80×300	7 days	28 days
	Mortar beams	3D+rebars	3	\	80×80×300	7 days	28 days
Healing type/time	Mortar beams	3D+rebars	3	Pumping	80×80×300	7 days	7 days
	Mortar beams	3D+rebars	3	encapsulated	80×80×300	7 days	7 days
	Mortar beams	3D+rebars	3	\	80×80×300	7 days	7 days
Healing type/time	Mortar beams	3D+rebars	3	Pumping	80×80×300	28 days	28 days
	Mortar beams	3D+rebars	3	encapsulated	80×80×300	28 days	28 days
	Mortar beams	3D+rebars	3	\	80×80×300	28 days	28 days
Healing type/time	Mortar beams	3D+rebars	3	Pumping	80×80×300	28 days	7 days
	Mortar beams	3D+rebars	3	encapsulated	80×80×300	28 days	7 days
	Mortar beams	3D+rebars	3	\	80×80×300	28 days	7 days

Table 3.7 Summary of different types of samples conducted for internal PVA tunnel systems

Test type	Sample type	Systems	Parallel tests	Water/cement ratios	Mould type (mm)	Curing condition	PVA Dissolve condition
Compatibility	Cement beams	Plain	3	0.25	40×40×160	7 days	\
	Cement beams	PVA structure	3	0.25	40×40×160	7 days	\
	Cement beams	Plain	3	0.3	40×40×160	7 days	\
	Cement beams	PVA structure	3	0.3	40×40×160	7 days	\
	Cement beams	Plain	3	0.4	40×40×160	7 days	\
	Cement beams	PVA structure	3	0.4	40×40×160	7 days	\
	Cement beams	Plain	3	0.5	40×40×160	7 days	\
	Cement beams	PVA structure	3	0.5	40×40×160	7 days	\
	Cement beams	Plain	3	0.6	40×40×160	7 days	\
	Cement beams	PVA structure	3	0.6	40×40×160	7 days	\
Feasibility	Cement beams	PVA structure	3	0.25	40×40×160	7 days	Water 25℃
	Cement beams	PVA structure	3	0.25	40×40×160	7 days	Water 40℃
	Cement beams	PVA structure	3	0.25	40×40×160	7 days	Water 70℃
	Cement beams	PVA structure	3	0.3	40×40×160	7 days	Water 25℃
	Cement beams	PVA structure	3	0.3	40×40×160	7 days	Water 40℃
	Cement beams	PVA structure	3	0.3	40×40×160	7 days	Water 70℃

Table 3.8 Summary of different types of samples conducted for PLA systems for chemical triggering use case

Test type	Sample type	Systems	Parallel tests	Mould type (mm)	Curing condition	Curing days
Feasibility	Cement beams	pore size A	3	40×40×160	water	7 days
	Cement beams	pore size B	3	40×40×160	water	7 days
	Cement beams	pore size C	3	40×40×160	water	7 days
Feasibility	Cement beams	pore size A	3	40×40×160	water	28 days
	Cement beams	pore size B	3	40×40×160	water	28 days
	Cement beams	pore size C	3	40×40×160	water	28 days
Feasibility	Cement beams	pore size A	3	40×40×160	air	7 days
	Cement beams	pore size B	3	40×40×160	air	7 days
	Cement beams	pore size C	3	40×40×160	air	7 days
Feasibility	Cement beams	pore size A	3	40×40×160	air	28 days
	Cement beams	pore size B	3	40×40×160	air	28 days
	Cement beams	pore size C	3	40×40×160	air	28 days

3.3.2 Sample casting

Cement, mortar and concrete specimens were prepared for different test series. Prism moulds 40 mm ×40 mm ×160 mm and 80 mm ×80 mm ×300 mm were used to prepare cement and mortar specimens.

Casting PVA samples

Stainless-steel moulds (40 mm ×40 mm ×160 mm) were used for preparing the prismatic cementitious beams. Firstly, prism moulds were cleaned and slightly lubricated with de-moulding oil. PC cement in dry conditions was stirred for 3 minutes, then water was added using a planetary type mixer at 120 rpm. Following the mixing, moulds were 50% filled with the cement paste before adding 3D printed PVA structures. Then the remaining parts of cement pastes were loaded into the moulds with PVA structures settled (Figure 3.5).

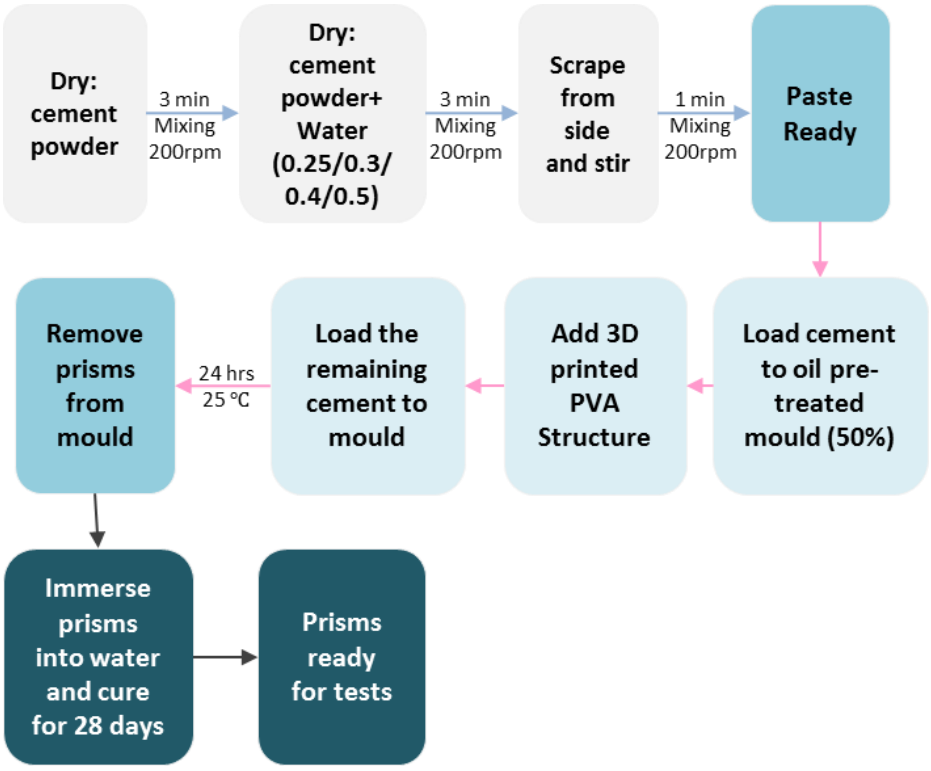

Figure 3.5 Specimen with 3D printed PVA structure fabricating workflow

Casting internal vascular PLA samples in cement paste

Stainless-steel moulds (80 mm ×80 mm ×300 mm) were used for creating prismatic cementitious beams.

Printed tubes were held by iron support stands to maintain their position in the moulds before and after pouring the cement mix. Cement mix was then poured into the moulds and vibrated at each stage to remove the air bubbles. Samples were submerged in water for curing for 28 days. Thin wires (Ø1.25mm) were used to simulate the cover placement of the network and to prevent complete failure of the prism upon cracking. Three prisms were prepared for each vascular network system.

Figure 3.6 Set-up for PLA vascular system in cement specimens

Casting internal vascular PLA samples in mortar

Prisms of 80 mm ×80 mm ×300 mm were used and the mortar mix was poured in two parts into the moulds. Each prism contained two 6 mm diameter straight steel reinforcement bars at 35 mm cover. The networks were positioned at the middle of each prism between the reinforcement bars anchored at the top so that the delivery tubes of the network lay in the cover region below the reinforcement bars (15mm cover). An example experimental set-up is shown in Figure 3.7. Control specimens were also cast to be used without any healing agent to compare the crack healing efficiency and the compatibility of the network with the matrix.

Figure 3.7 Set-up for PLA vascular system in mortar specimens

Casting cylindrical samples for rapid chloride permeability tests (RCPT)

For testing rapid chloride permeability, cylindrical specimens were required to be with a diameter of 100 mm and a thickness of 50 mm. So here a Polyvinyl Chloride (PVC) mould with a diameter of 100 mm and 200 mm length was used for casting mortar cylinders. 3D printed PLA disc (80 mm in diameter and 5 mm in thickness) containing coating materials were being placed at the marking point in the cylindrical mould, and then filled in with the cementitious mix. The mortar mix was composed of water, sand and Ordinary Portland Cement (OPC) (CEM-I, 52.5 by Hanson) in a ratio of 0.5: 3: 1 by weight, in accordance with NT BUILD 492. 50±2 mm slices were cut from the central portion of the casted cylinder.

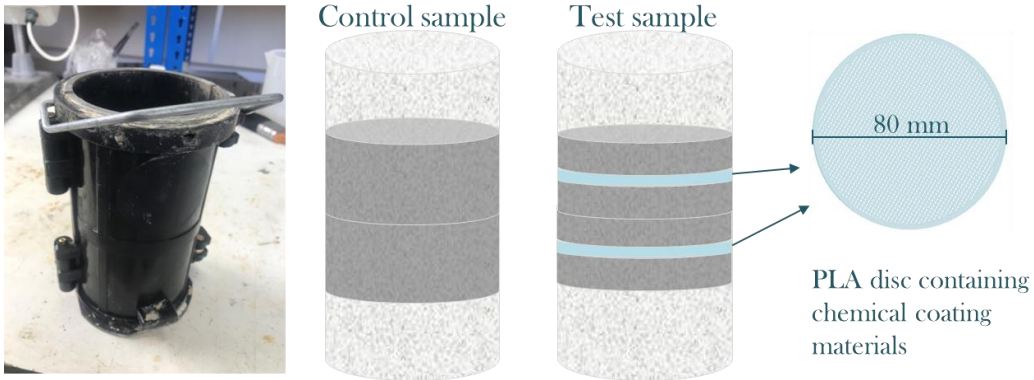

Figure 3.8 A schematic diagram of casting specimens for rapid chloride permeability tests

3.3.3 Sample curing

All samples were kept in the mould for 24 hours and were then demoulded and labelled. Prism samples were cured at 20°C in different conditions (submerged in water or in air) for 7 days and 28 days, according to the types of experiment they were designed for; while the cylindrical samples were cured at 20°C in water for 1 day, 7 days and 28 days adapted from NT BUILD 492 method.

3.4 Mechanical property designs

3.4.1 Cement and mortar specimens

After curing, the specimens were filled with healing agent and loaded in four-point bending. A Instron® 5500R-150kN testing frame was used with a quasi-static displacement-controlled rate of 0.25mm/min. The beams were put on two steel supports with the span of 240 mm. The upper surface of the beams was loaded through two steel rods with a span of 120 mm. A four-point bending test, conforming to ASTM Standard D6272-02, was applied to the prisms 7 days or 28 days after casting.

After cracking, the samples were allowed a healing period in a continuous pumping conditions to allow for crack recovery. The mechanical behaviour of specimens was tested again after the healing process.

Cement specimens

The prisms were placed on two steel supports with the span of 240 mm and the upper surface of the beams was loaded through two steel rods (50 mm in diameter) with a span of 120 mm (schematic in Figure 3.9). Tubes were centred (width: 30 mm before the edge, length: 20 mm before the edge), leaving 40 mm of artery tube in the air (50 mm below) for connecting the external pumping system.

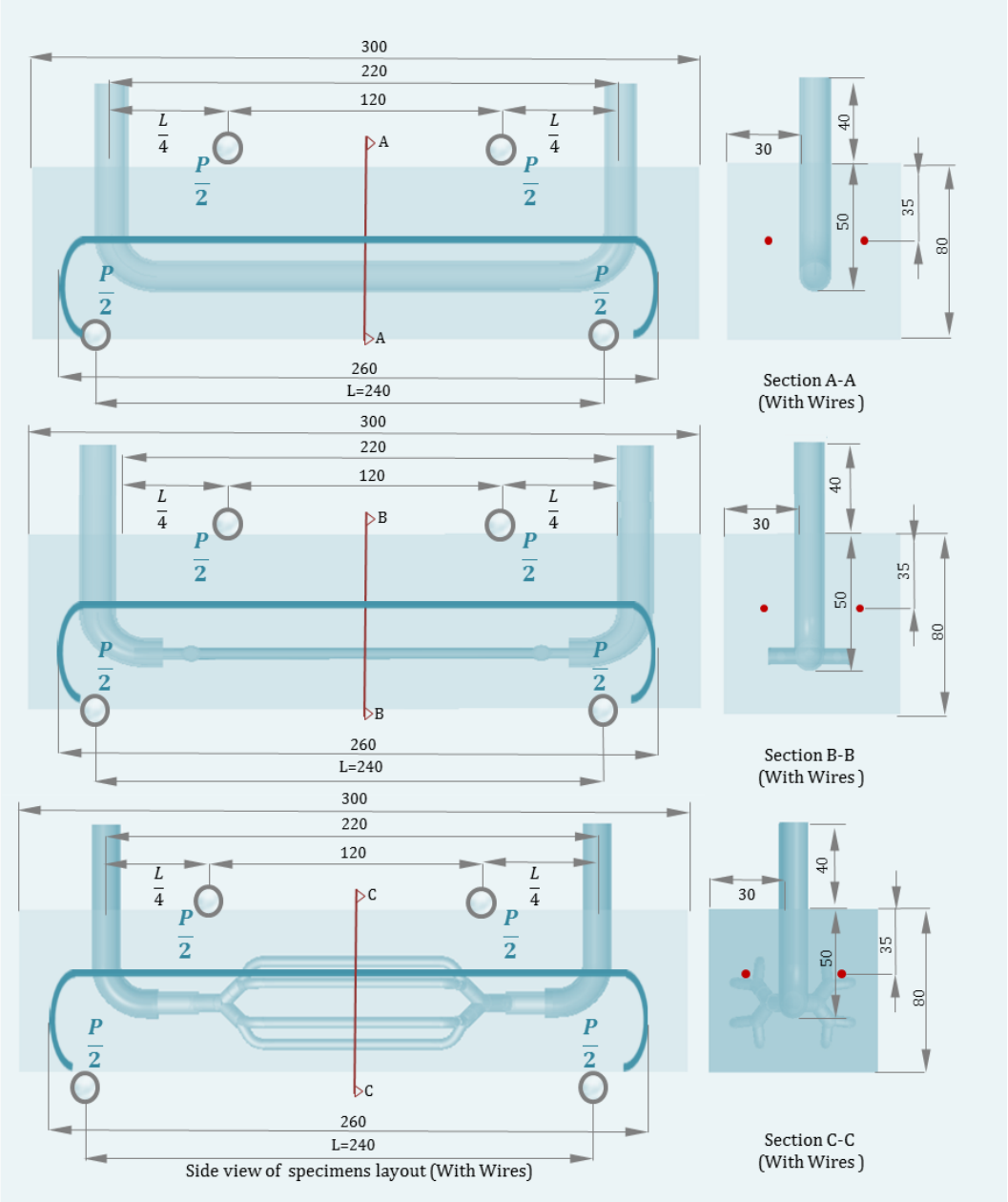

Figure 3.9 A schematic of the experimental setup for the four-point bending of specimens with the different internal vascular structures (a) 1D system, (b) 2D system and (c) 3D system

Mortar specimens

The printing layer of the PLA tubes is parallel with the crack plate. A Instron® 5500R-150kN testing frame was used with a quasi-static displacement-controlled rate of 0.25mm/min, and then this process stopped when the amount of load dropped more than 40% compared with its previous figure. The beams were put on two steel supports with the span of 240 mm. The upper surface of the beams was loaded through two steel rods with a span of 120 mm (Figure 3.10).

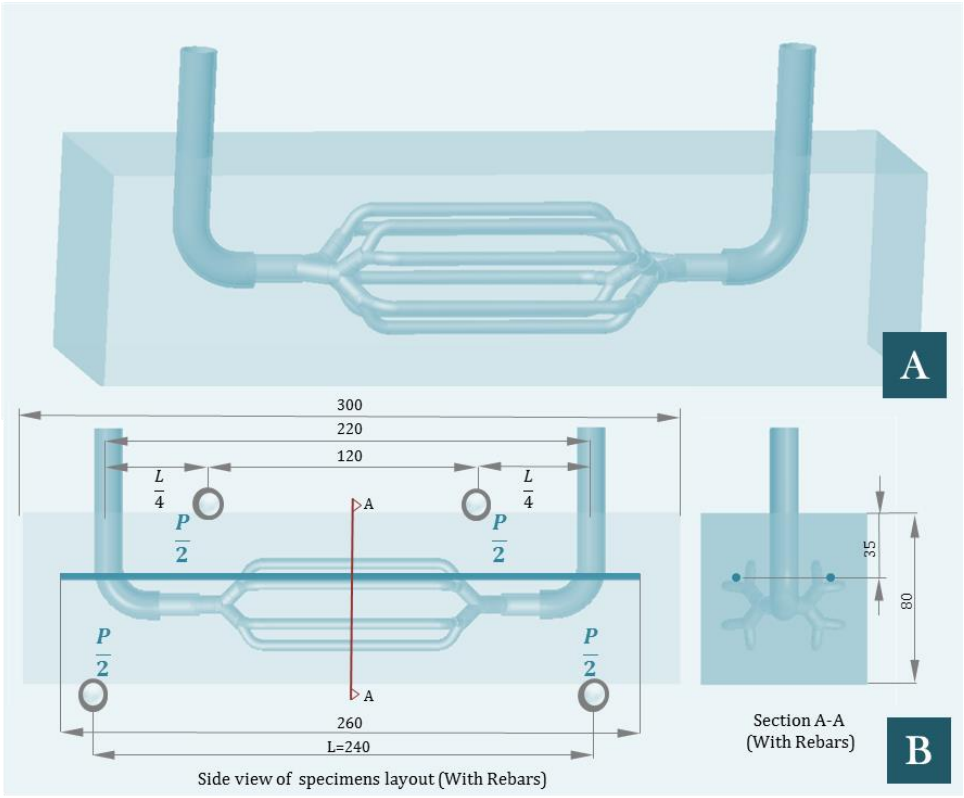

Figure 3.10 A designed diagram of vascular structure in mortar specimens and experimental setup for the four-point bending

After cracking and unloading, optical microscopy images were taken at multiple points along the induced crack to obtain a measure of residual crack width. Samples were then placed back into healing condition to facilitate the self-healing process for the longest duration of 28 days. During this time, samples were removed after 7, 14, 21 and 28 days to be tested for monitoring crack closure under a microscope. After the 28-day healing period, samples were completely separated, and material was extracted from the crack surface for microstructural analysis.

Flexural strength and strength recovery

The peak value of the loading curve, the point at which the cement sample failed under flexure and subsequently cracked, was extracted for flexural strength calculations (Figure 3.11). Specimens were cracked to evaluate their flexural strength using four points bending tests before and after healing. As described in the session above, flexural stress was calculated using equation 3.1 according to BS EN 12390-5:2009.

$$\sigma_f = \frac{3PL}{4bd^2} \qquad (3.1)$$

Where σ_f is the stress in the surface midpoint (MPa), P is the load (N), L is the support span (mm), b is the width (mm), and d is the depth (mm) of the specimen.

Thus, the strength recovery after healing process was calculated according to equation 3.2:

$$R_f = \frac{\sigma_1}{\sigma_2} \qquad (3.2)$$

Where σ_1 is the maximum stress of the original specimen and σ_2 is the maximum stress of the specimen after healing.

Bending stiffness and bending stiffness recovery

Bending stiffness can be derived from the equation of the beam deflection when it is applied by force:

$$\mathrm{K} = \frac{P}{w} \qquad (3.3)$$

Where P (N) is the applied force and w (mm) is the deflection. The bending stiffness (blue triangle in Figure 3.11) of the specimens were obtained and calculated from the Load-displacement diagrams (from Instron® machine) as illustrated below.

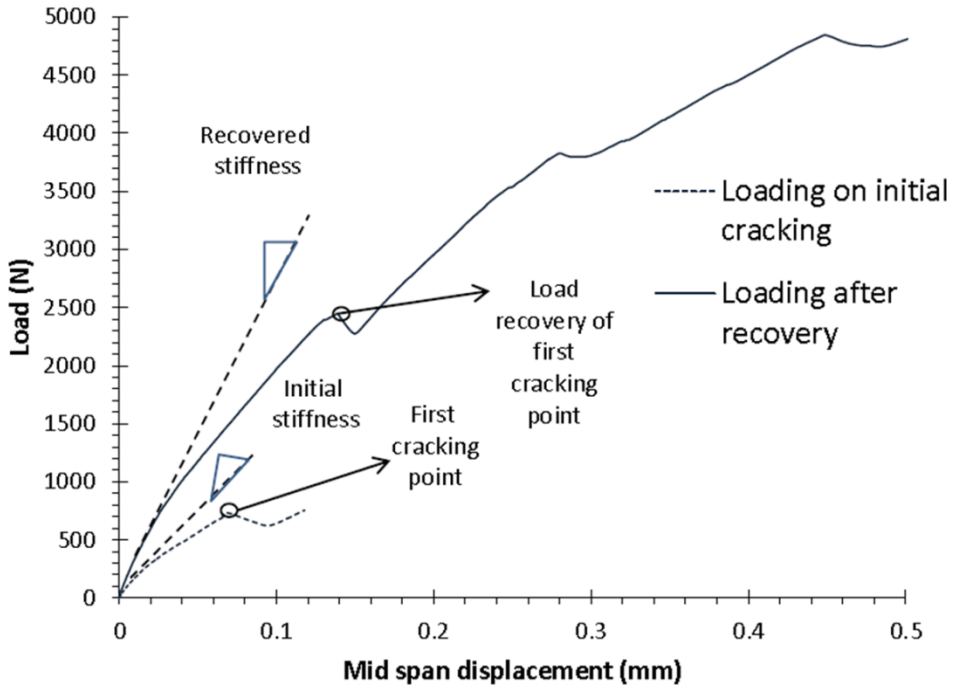

Figure 3.11 Terminology in a typical load vs displacement graph of restrained end prisms (Qureshi, 2016)

Thus the stiffness recovery after healing process was calculated according to equation 3.4:

$$R_K = \frac{K_1}{K_2} \qquad (3.4)$$

Where K_1 is the bending stiffness of the original specimen and K_2 is the bending stiffness of the specimen after healing.

3.4.2 3D printed vascular models

Similar setups were applied with the cement/mortar specimens in 3D printed plastic models, with the aim of better analysing and comparing their mechanical behaviours. Instron® 5500R-150kN testing frame was used with a quasi-static displacement-controlled rate of 0.25mm/min. Considering the length of 3D models, the models were put on two steel supports with the span of 200 mm. The upper surface of the beams was loaded through two steel rods with a span of 100 mm as shown in Figure 3.12. The loading process stopped when the amount of load dropped more than 40% compared with its previous loading figure.

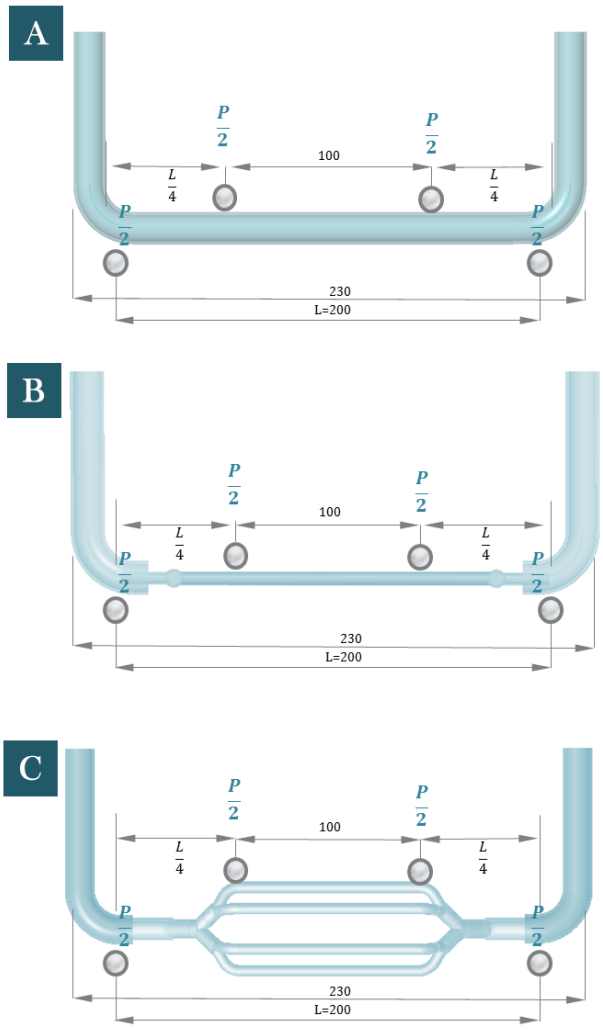

Figure 3.12 A schematic of the experimental setup for the four-point bending of different internal vascular structures (a) 1D system, (b) 2D system and (c) 3D system

3.5 Vascular network pumping system

3.5.1 Vascular network pumping system design

The reliability of the self-healing vascular network was considered by Williams et al. in 2008, which discussed what may cause self-healing system to be unable to achieve self-healing process after damage events. They believed that an ideal self-healing structure should include the following strategies to maximise its successfulness:

i. Fluid flow was pressurised by cylinder, ensuring system to achieve multiple healing events;

ii. Main tunnels connected with pump and main supply vessels were not designed to be ruptured;

iii. Small tubes of the vasculature were intended to be ruptured to release healing agents;

iv. Healing agents were required to initiate bleeding into any damage and cure reactions;

v. In a closed-looped network, both internal vascular structure and main apply vessels were favoured symmetric designs.

To compare the healing performance of pumping and non-pumping specimens, encapsulated non-pumping system and continuous pumping systems were designed and presented in Figure 3.13.

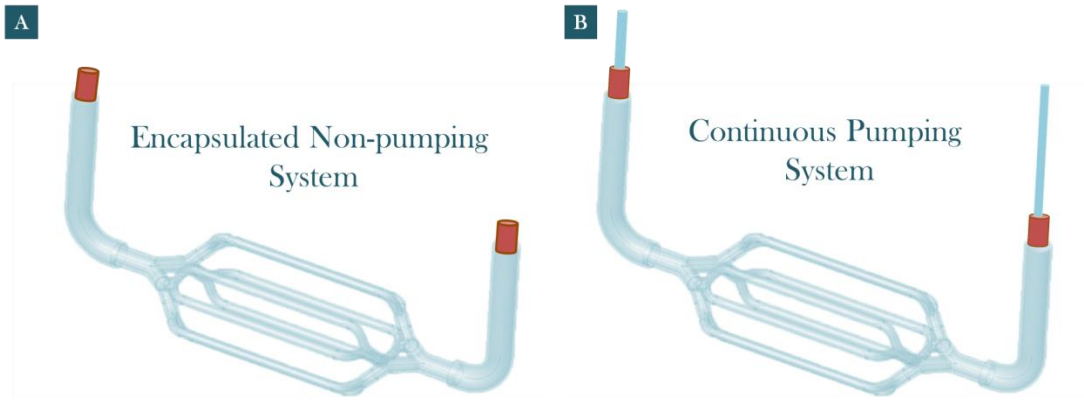

Figure 3.13 A schematic of the experimental setup for non-pumping system and continuous pumping system

For the pumping system, internal vascular networks will be connected with the main arteries and then linked to external pump and healing agent reservoir. Following the strategies mentioned above, the overall layout of the design could be seen in Figure 3.14. This figure gives an example of the real setting for internal vascular circulatory system. The input pipe of the embedded network was attached, via rubber tubing, to a peristaltic pump that transferred healing agent from a healing agent reservoir. The output of this network was piped back into the reservoir by another section of rubber tubing thus creating a complete circulatory system. The peristaltic pump circulated the fluid around the network at a volumetric flow rate of 60 ml/min by adjusting the voltage of a fluid velocity control.

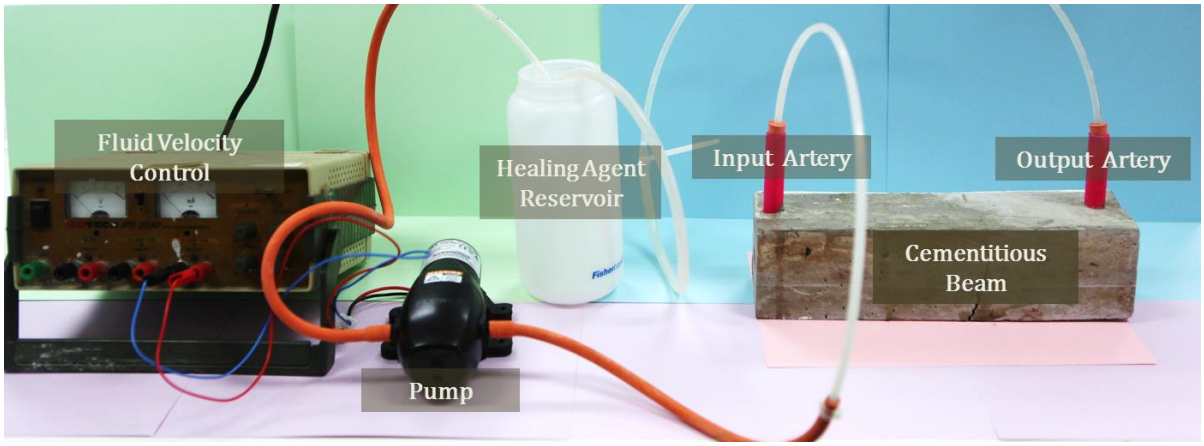

Figure 3.14 Experimental setup for the continuous pumping system

3.5.2 Channel resilience of vascular networks in pumping system

To compare the channel resistance difference in 1D/2D/3D structure, the engineered vascular matrix is connected to a recycling system for measuring the pressure changes, consisting of a peristalsis pump (Watson Marlow® 323, providing consistent pumping rate 60 mL/min), a reservoir (containing 500 mL sodium silicate), two pressure transducers (RS® Components, 249-3864, 1bar, 0-100mV), and connection tubing. Resistance of the designed 1D/2D/3D vascular systems was then calculated according to Akers (2006) and Choi et al., (2010), which the laminar incompressible flow of steady state inside a channel is described by:

$$Q = \frac{\Delta P}{R} \quad (3.5)$$

where Q (mL/s) is the volumetric flow rate, ΔP (kPa) is the pressure drop from one end of the channel to the other, and R (kPa • s • mL^{-1}) is the hydraulic resistance of the channel.

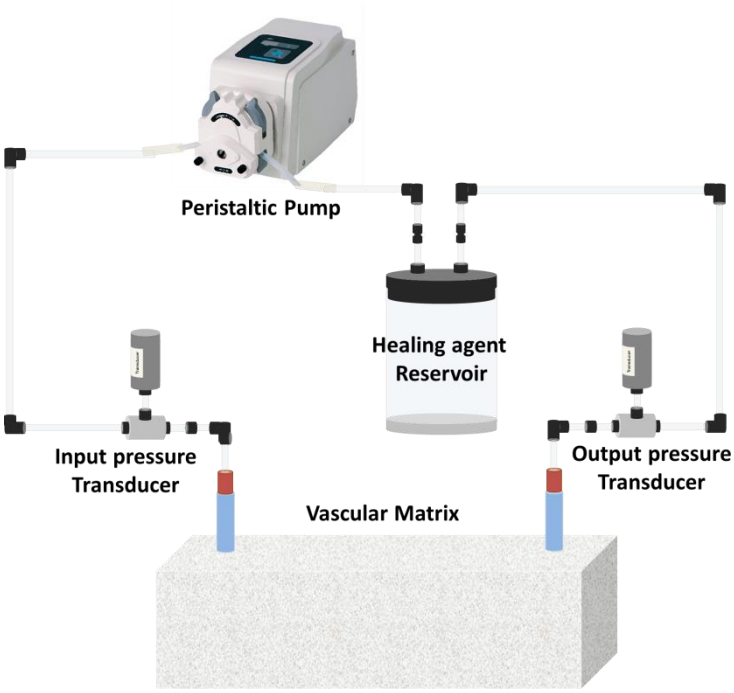

Figure 3.15 A schematic set-ups for measuring the pressure changes of the vascular system

3.6 Healing performance characterisation

3.6.1 Observation of cracks

Crack formation and healing products were observed using a DM 2700 M Leica® microscope equipped with LAS v4.6 software. Images during healing process were captured and monitored over time at 1, 2, 5, 10 and 28 days.

The progress of crack healing for large beams (80 mm ×80 mm ×300 mm) was monitored macroscopically through microscope observations of the cracks. Microscope images of cracks in large beams were captured and the morphology analysed via a GT Vision® GXCAM-1.3 microscope together with ImageJ® software. Crack size has been carefully measured using LAS v4.6 software and ImageJ® during observation. For a single main crack, at least 5 check points (when the width in the same crack varies drastically, more check points will be included) were marked using a blue/black marker. For each marked point, the width was measured 3 times and then recorded the average value.

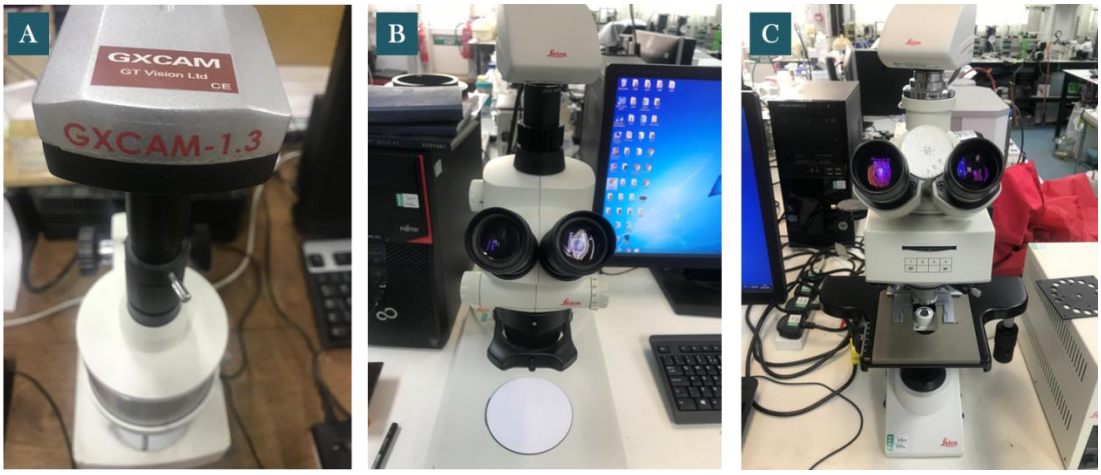

Figure 3.16 Observation of cracks and microstructures using (A) GXCAM-1.3 microscope, (B) and (C) Leica microscopes

3.6.2 Capillary water absorption

Evaluation of specimens' water tightness (before and after healing) was examined by capillary water absorption test, following ASTM C1585 (ASTM C1585 2013) and RILEM report (de Rooij et al., 2013). The beams were first dried in a vacuum chamber (25 °C) until the mass changes were less than 0.1% between 24 h periods. The specimens were then wrapped on the bottom and lateral dies with aluminium tape but the crack area was left uncovered for exposure to capillary water suction. During the sorptivity test, specimens were immersed in distilled water at a depth of 5 ± 1 mm. The water absorption was evaluated by measuring the mass changes (g) of specimens at 1, 4, 9, 16, 25, 36, 49, 64, 81 to 256 min, and normalised by the surface area (80 × 20 mm^2) and the density of water (1 × 10^{-3} g/mm^3), as shown in Equation 2.10 (Hall & Tse, 1986):

$$M_w = \frac{\Delta m}{A \cdot \rho} \quad (3.6)$$

$$M_w = \mathrm{C} + \mathrm{S}\sqrt{t} \quad (3.7)$$

where M_w is the water uptake quantity uptake per unit area of inflow surface (mm); Δm is the mass changes of specimens (g) during water absorption; A is the inflow area; ρ is water density (g/mm^3); S is sorptivity coefficient ($mm/h^{1/2}$) determined by the slope of $M_w - \sqrt{t}$curve.

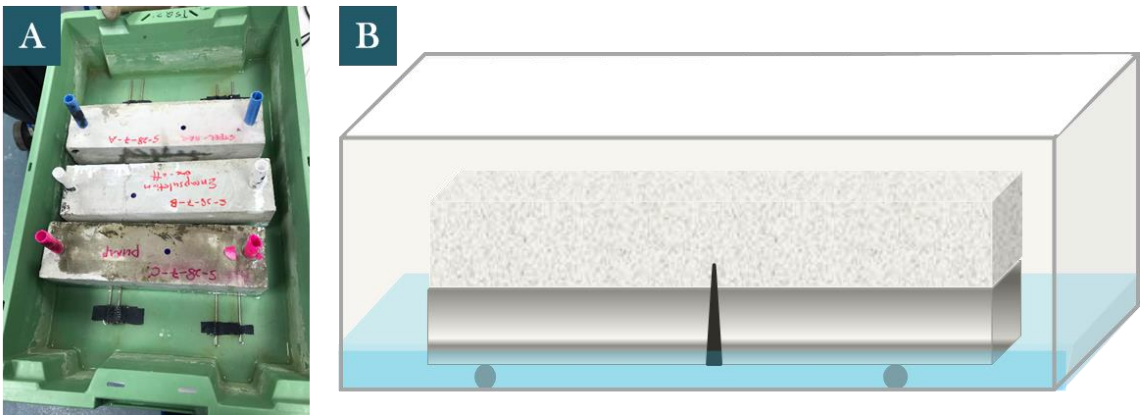

Figure 3.17 Illustration of the capillary water absorption setup and tests

Specimens were tested for their sorptivity before and after healing (after 7 and/or 28 days). This was done to observe the change in sorptivity throughout the 28-day healing period.

3.6.3 Morphology and composition analysis

The morphology and composition of the hydrated cement, self-healing materials and polymers was investigated using X-ray diffraction (XRD), Fourier Transform Infrared Spectrometer (FT-IR), Thermogravimetric analysis (TGA) and Scanning Electron Microscopy-Energy Dispersive X-ray spectroscopy (SEM-EDX) analyses. Samples from specimens were collected using a knife and then being ground to pass through a 40 μm sieve before being tested using X-ray diffraction (XRD) and thermogravimetric analysis (TGA).

X-ray diffraction (XRD)

X-ray diffraction (XRD) analysis was utilised to detect the crystallinity of mineral and polymer samples. Samples were mounted on a smooth glass surface attached to a flat holder and examined using a Siemens® D500 X-ray diffractometer with a Cu-Kα radiation source. The diffractometer was operating at 40 kV and 40 mA, and emitting radiation at a wavelength of 1.5405 Å. Scanning ranged between 10-60°(2θ) at a rate of 1s/step and a scanning resolution of 0.02°/step. Following the scanning, the diffraction raw data was searched in the PDF-2004 database using the Jade® software in order to identify the material peaks in the graph.

To analyse the cement based samples, both healing products and cementitious background samples were obtained by a curve knife and then collected in sealed glass bottles for further grounding. All the samples were ground to pass a 40 μm mesh sieve. Powder samples were placed in a transparent plastic disc container right before testing.

Polymers were collected by tweezers and then collected in sealed glass bottles. Samples were placed in an aluminium disc and glued by Bow Corning® gel for XRD tests.

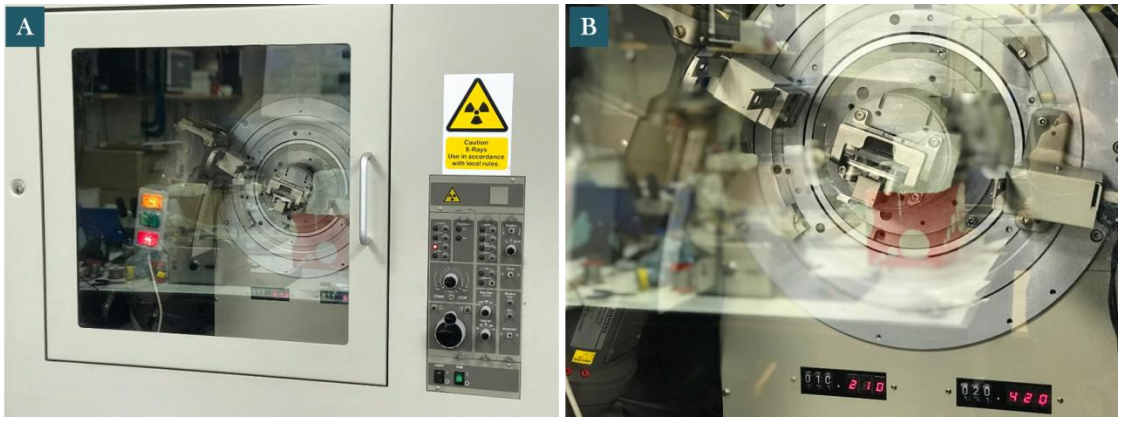

Figure 3.18 Powder X-ray diffraction (XRD) analysis using a Siemens® D500 X-ray diffractometer

Fourier Transform Infrared Spectrometer (FT-IR)

Infrared spectroscopy was used to further characterise polymer structure in terms of fundamental vibrations and associated rotational-vibrational structure behaviour. A mid-infrared (4000-400 cm^{-1}) ranged PerkinElmer® FT-IR Spectrometer *Spectrum Two* was used to perform this test. Spectra were collected in the transmittance bands between 4000 and 400 cm^{-1} at a resolution of 1cm^{-1}. The powder sample was pressed against the face of a single crystal. The infrared light passes through the crystal and only interacts with the sample at the interface between the two materials.

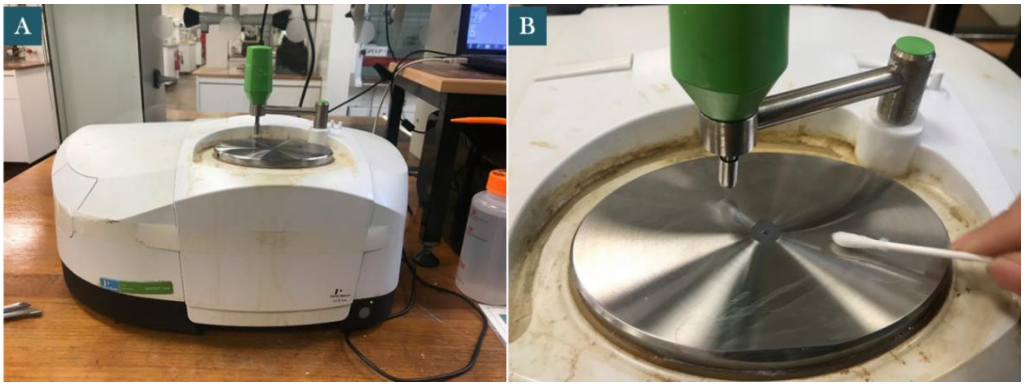

Figure 3.19 Fourier Transform Infrared Spectrometer (FT-IR) analysis using a PerkinElmer® Spectrometer

Scanning Electron Microscopy- Energy Dispersive X-ray spectroscopy (SEM-EDX)

SEM was used to characterise the surface morphology of the mortar, healing materials and healing products. Combined with EDX, the elemental composition of materials was further studied. SEM-EDX was carried out using Phenom® (Pro G2, Netherlands). An electron beam energy of 15 keV with a short working distance (~6-8 mm) was used for all imaging. The samples were then mounted onto aluminium stubs using adhesive carbon tape and silver patching. Samples were coated with gold film (2-3 nm) using a K550 Emitech sputter coater to avoid charging and improve the secondary electron signal required for topographic examination in the SEM.

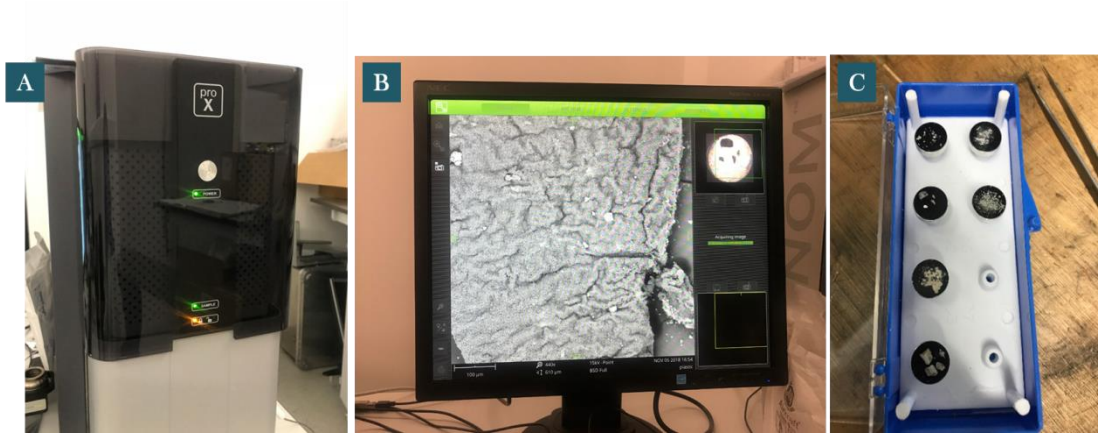

Figure 3.20 (A) Phenom® Pro G2 instruments for SEM-EDX analysis, and (B) analysis software and (C) sample prepare process

Thermogravimetric Analysis (TGA)

Thermogravimetric analysis (TGA) was applied to characterise the composition of the coating materials and healing products after the healing process. TGA analysis was carried out using PerkinElmer® STA6000 and ceramic crucible under air atmosphere within the range of 30 to 800 °C at a rate of 10 °C /min with ~10 mg of dried powdered samples. Differential thermogravimetric calorimetry (DTG) curves are obtained by differentiating plots of normalised sample weight (%) vs. sample temperature (°C).

Figure 3.21 PerkinElmer® STA6000 instruments for thermogravimetric analysis

3.6.4 In-situ structure analysis

Computational Tomography (CT)

Computational Tomography was used to obtain 3D maps of the internal infrastructure indicating the healing agent distribution and the relationship between vascular tubing designs and crack healing area.

The cement samples were scanned by a Nikon® X-Tek H 225 ST CT-scanner. Reconstruction of the original CT images were produced 1300 slices (oriented obliquely through the specimen) composed of isometric voxels with a resolution of 0.089579 mm/voxel; CT scans were processed using the 3D visualisation software package Mimics® v.14.0 (Materialise HQ, Leuven, Belgium) on a 64-bit Dell Inspiron 15R laptop with 8 GB RAM.

The CT images of the samples were obtained by Mimics®, and their CT values were measured, and the theoretical volume and CT value of the samples were automatically generated by 3D reconstruction. By using this function, the volume of the crack section, healed parts, tubing area etc, can be therefore calculated.

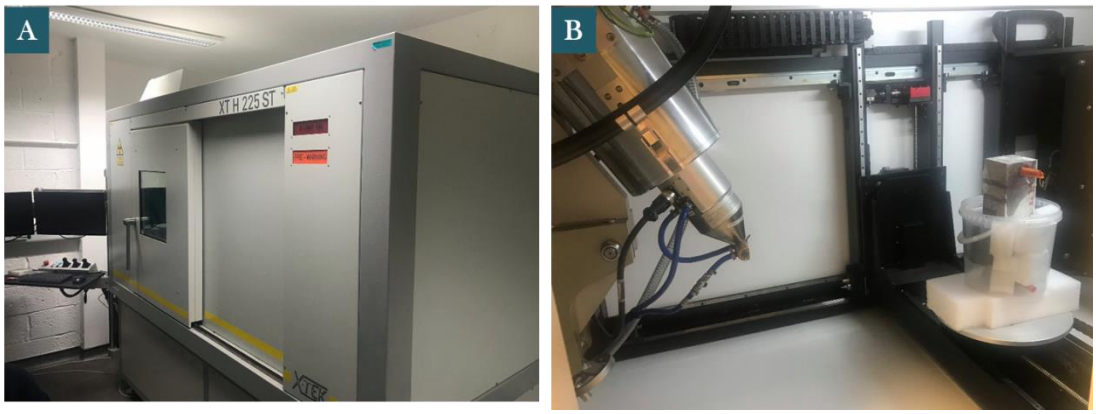

Figure 3.22 Nikon® X-Tek H 225 ST CT-scanner for computational tomography analysis, (A)CT-scanner and (B) X-ray source and sample placement

3.7 Chemical triggering materials and performance

3.7.1 Coating material synthesis

Coating material for chemical triggering use case was synthesised according to Xiong et al., 2015. A schematic process for synthesis of silver alginate is given in Figure 3.23. Sodium alginate was completely dissolved in deionised (DI) water. After stirring for 10 minutes, the sodium alginate mixture was placed on shaking table with 200 rpm for 24 hours. Then silver nitrate was added to the dissolved sodium alginate solution. The mixture with silver nitrate and sodium alginate was again placed on shaking table with 200 rpm for 3 hours. The resulted silver alginate gel was separated by a separating funnel with 0.22 µm filtering paper. This is followed by a few washing procedures using DI water.

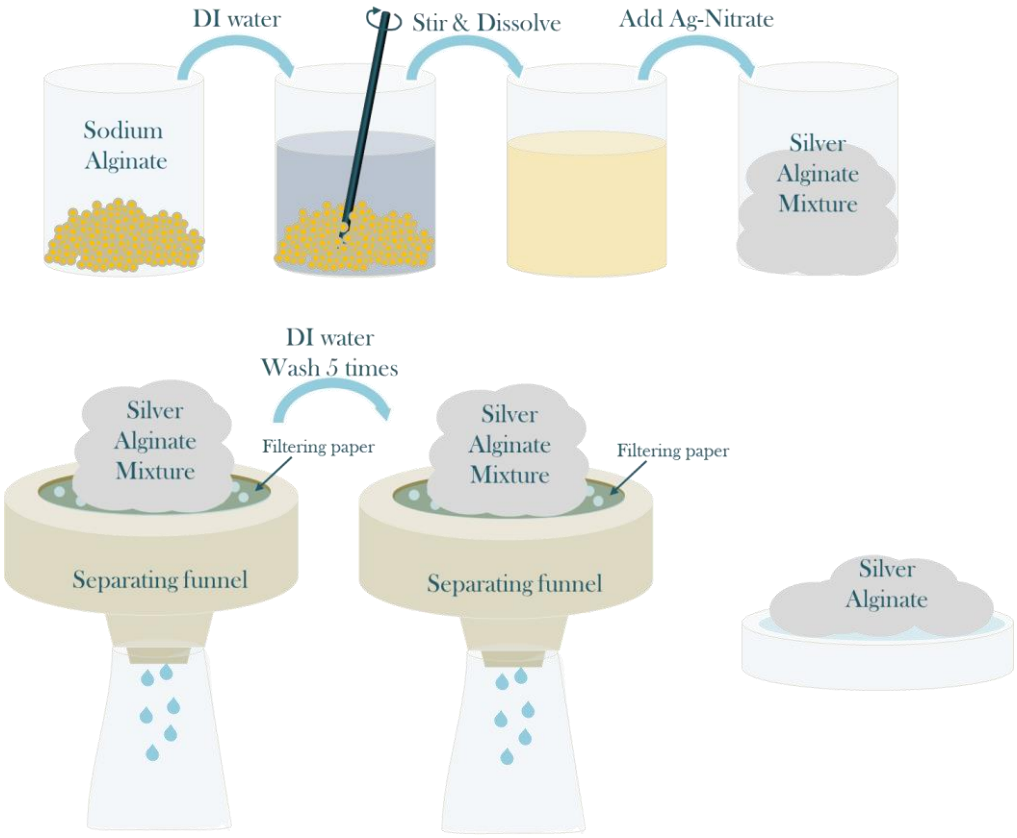

Figure 3.23 A schematic diagram of coating material synthesis process

3.7.2 Rheological properties of coating materials

A Brookfield DV3T Rheometer (Figure 3.24) was used to measure the viscosity of chemical sensitive materials with different component ratios. The shear testing profile was adapted (seen in Figure 3.25) from Nanthagopalan and Santhanam (2009).

The SC4-27 spindle was inserted into the sample cup containing the coating materials before starting the tests.

The viscometric testing scheme used was adapted from Soukoulis et al. (2016). All the measurements were performed at 20°C. Before the tests start, a pre-conditioning process was carried out on the sample for 3 mins at a speed of 200 rpm under 20°C.

The measurements were taken at 20 different shear rates, and steady state shear flow measurements applying upward-downward ramp shear rates ranging from 200 to $10s^{-1}$ was used to obtain the curve.

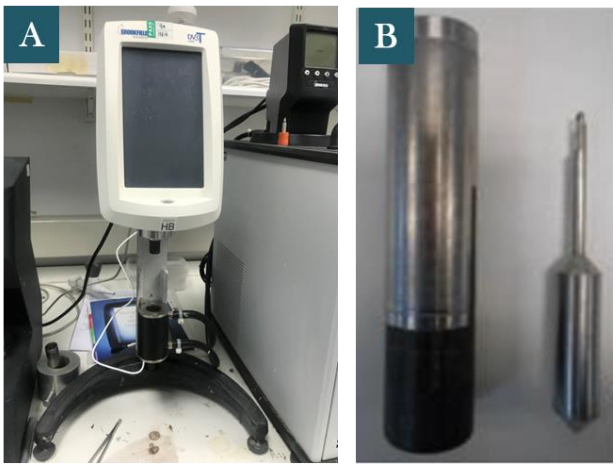

Figure 3.24 Brookfield DV3T Rheometer used to obtain the viscosity of coating materials; (A) Desktop view and (B) sample container and SC4-27 spindle

Alginate upward ramp shear stress (τ) – shear rate data (γ) were fitted to Herschel-Bulkley model:

$$\tau = \tau_0 + K\gamma^n \qquad (3.8)$$

where: τ_0 equals the yield stress (Pa), K is the consistency coefficient (mPa • s^n) and n is the rheological behaviour index (dimensionless). And this Herschel-Bulkley model was chosen on the program software while taking the measurement.

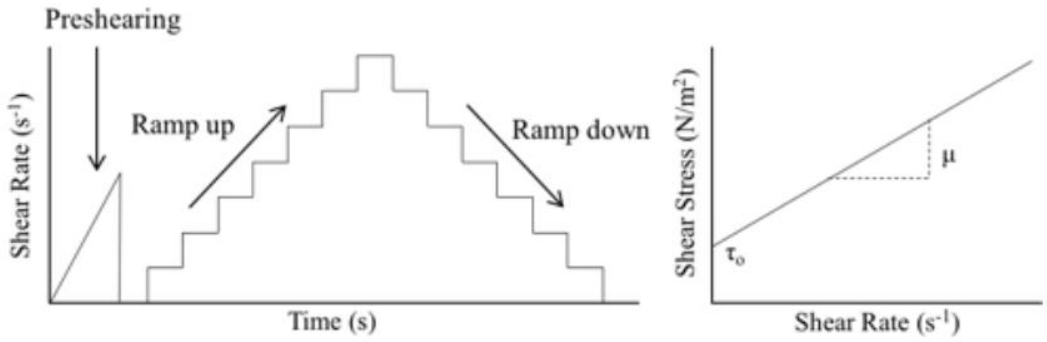

Figure 3.25 Shear testing profile used to obtain viscosity of samples (Nanthagopalan and Santhanam, 2009)

3.7.3 Visualisation device design

A visualisation device (Figure 3.26) was designed to observe the agent releasing behaviour of porous vascular structures. The device consists of three main parts: (i) agent injection part (left side controlled by a valve); (ii) observing part, which is a transparent vessel that are able to connect with testing vascular structures; (iii) discharging part, where fluids can be removed from the main observing part.

To use this device, the valve should be firstly closed to add background solution (normally DI water). The cap of the observation part should be removed to fill in background solution as shown in Figure 3.26. Then the target vascular structure can be attached to the cap and dipped into the background solution. Locker of the cap should be turned on before injecting agent solution. After the test, the locker should be turned off to release the liquid.

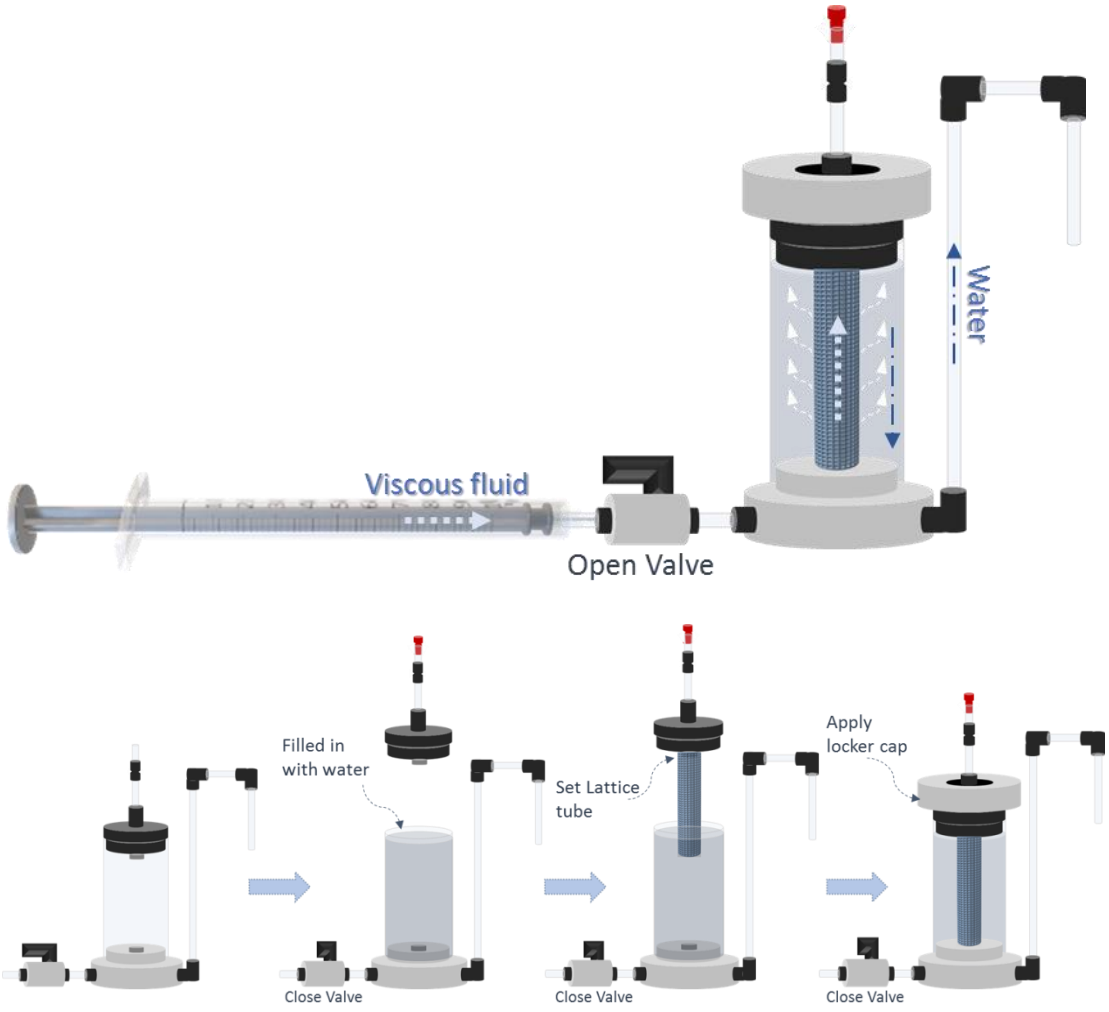

Figure 3.26 Schematic diagrams of the visualisation device and the instruction for testing

3.7.4 Solution composition analysis

The solution collected to detect chemical triggering reaction was investigated using Inductively Plasma-Optical Emission Spectrometry (ICP-OES), Ultraviolet-Visible Spectroscopy (UV) and Ion Concentration (EDT) analyses.

Ultraviolet-Visible Spectroscopy (UV)

Reacted samples were collected for testing Ultraviolet-Visible Spectroscopy (UV). The UV-Vis diffuse reflectance spectra (UV-Vis DRS) of the samples were recorded by using a PerkinElmer® Lambda 35 UV-Vis spectrometer.

Figure 3.27 PerkinElmer® Lambda 35 UV-Vis spectrometer for testing solution

Ion Concentration pH meter

Solution (before and after chloride reaction) was mixed on a shaking table (KS501 digital, IKA®) with a 100 rpm shake rate for 24 hours, and then passed 0.22 μm filters before being collected for testing. Chloride concentration was detected using Ion concentration pH meter DR359TX, together with Chloride half-cell ISE-1261, provided by EDT directION®. Ion concentration meter which automatically calculates the relationship between two or more concentration standards and stores this in memory allowing unknowns to be read directly. Anion/cation recognition is automatic and up to 5 calibration points may be entered, enabling the user to cover a wide dynamic measurement range with just one calibration.

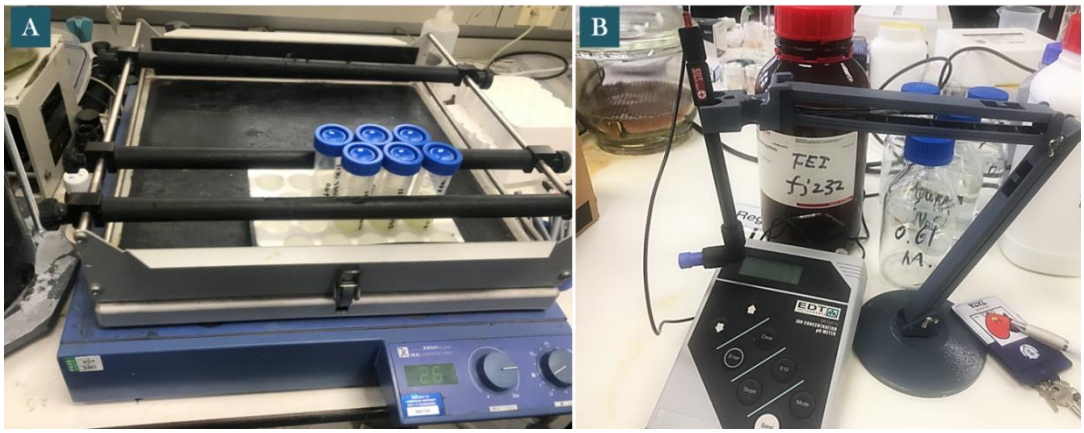

Figure 3.28 (A) Shake table and (B) EDT Ion concentration pH meter

3.7.5 Rapid Chloride Penetration tests (RCPT)

Cylindrical slices (Ø100 × 50 ± 2 mm) were casted and cured as described in section 3.3. When the surfaces of cylindrical slices were dried, they were then placed in the vacuum container for vacuum treatment (1–5 kPa).

Figure 3.29 (A) Vacuum container; (B) reaction cells connecting with the power supply; (C) general setup and (D) Proove it software

Both end surfaces must be exposed in the vacuum container (Figure 3.29 A). Maintain the vacuum for three hours and then, with the vacuum pump still running, fill the container with the saturated $Ca(OH)_2$ solution (by dissolving an excess of calcium hydroxide in distilled or de-ionised water) so as to immerse all the specimens. Maintain the vacuum for a further hour before allowing air to re-enter the container. Keep the specimens in the solution for 18 ± 2 hours.

After the pre-treatment process, rubber sleeves were fit on the specimens and secured with two clamps. The end surfaces of specimens were to be exposed to the chloride solution (catholyte, 10 % NaCl) and sodium hydroxide (anolyte, 0.3 N NaOH). Reservoirs of the cells shown in Figure 3.30 B were filled in with approx. 200 mL of 10 % NaCl and 0.3 N NaOH. The cathode was connected to the negative pole and the anode was connected to the positive pole of the power supply (PROOVE it®, Germann Instrument).

After the tests, 0.1 M silver nitrate solution was sprayed on to the freshly split section. White silver chloride precipitation on the split surface is clearly visible (after about 15 minutes), and then the penetration depth can be measured, with a suitable ruler, from the centre to both edges at intervals of 10 mm (NT BUILD 492).

3.8 Concluding remarks

In this chapter, materials, experimental setup and characteristic methods used in the subsequent research work was provided.

The principal types of materials used in this work were 3D printing plastics, healing agents and coating materials. Large cement specimens (80 mm ×80 mm ×300 mm) with different mix proportions were prepared for investigating self-healing systems with different vascular dimensions. Large mortar prisms (80 mm ×80 mm ×300 mm) with 3D vascular networks were prepared to investigate the healing behaviours in different healing conditions. Small cement paste samples (40 mm ×40 mm ×160 mm) were embedded with PVA network and chemical triggering vasculatures, with the aim of exploring the feasibility of creating connected tunnels and exploring the workability of generating a chemical controlled releasing system.

First, the 3D prints were invested by testing their tunnel resilience and flexural properties. Then self-healing performances of the large specimens were assessed through three measures: load recovery under a four-point bending test, crack sealing efficiency using a digital microscope, and durability improvement using water sorptivity and computational tomography. The micro-structures of the cementitious materials and self-healing compounds formed in the cracks were investigated using FT-IR, XRD, TGA and SEM-EDX.

Chemical triggering coating materials and vascular structures were synthesised and fabricated. Reaction between coating materials and chloride solution, mimicking chemical attack events, were evaluated by EDT, UV and RCPT.

The results of these experiments and associated discussion are presented in Chapter 4, 5 and 6 accordingly. As shown in Figure 3.40, physical triggered vascular system based

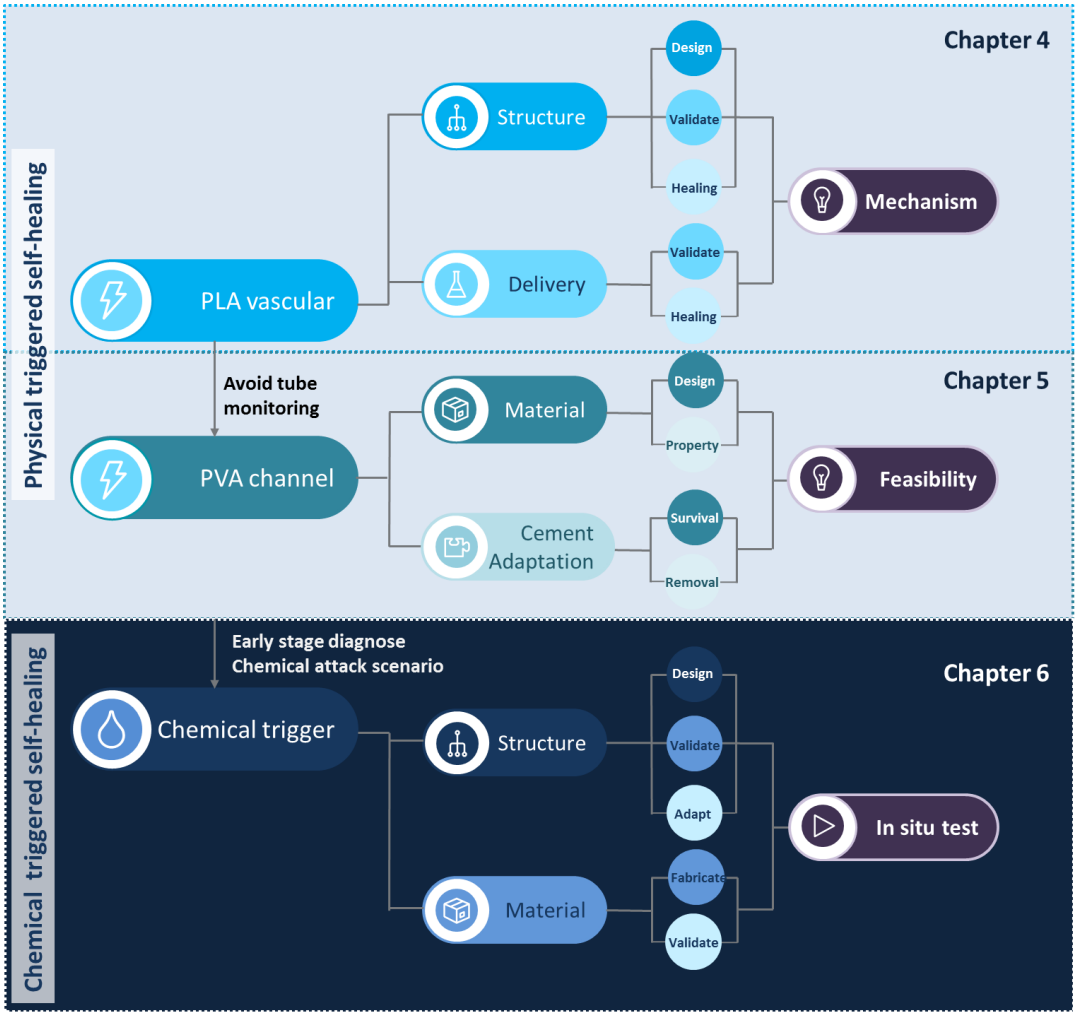

Figure 3.40 Schematic of work carried out for Chapters 4, 5 and 6 of the thesis.

on PLA and hollow channels created by PVA are exhibited in the first two result chapter, namely Chapter 4 and Chapter 5. Chapter 4 presents findings relating to the design of a biomimetic vasculature and their self-healing performances under different orientations and healing agent supply methods. To avoid long term tube monitoring and enables multi-scale healing over time, in Chapter 5, PVA was applied as a sacrificial material to create hollow channels in cementitious material. This chapter presents findings relating to the feasibility of creating hollow connective tunnels in cement via a water soluble PVA material. In chapter 6, instead of physical triggering, the proposed vascular self-healing technology further expanded to chemical triggering, using chloride ion triggers to release healing agents. The results of a chemical sensitive coating materials, and chemical triggering viability between coating materials and chloride solution are presented in Chapter 6.

Chapter 4

3D self-healing vascular model design & performance in cementitious materials

In this chapter, a biomimetic vascular network was designed and tested in two different types of cementitious materials, namely cement-based and mortar-based matrix. In the first scenario, healing performance of biomimetic vasculatures were compared with that of non-biomimetic systems (including one dimensional vascular and two dimensional vascular networks) in cement paste based samples. Comparison between the vascular systems with their mechanical properties and healing performance was used to shed light on their design suitability for vascular self-healing in cementitious systems. Details of the vascular designs are provided in section 4.2. Then, a further study of this 3D vascular system in mortar matrix was followed, with the aim of better understanding its feasibility in being utilised in real case scenarios followed by in-depth characterisation. Pumping (closed) system and non-pumping (open) systems were applied to investigate the healing efficiency of the amount of agent provided over time. A thorough investigation into the effect of healing agent providing methods on the mechanical properties, the healing performance as well as their mechanisms during the healing process is presented. Results presented in this chapter have been published in Li et al. (2020).

4.1 Design of vascular networks for physical triggering

4.1.1 Aim of the biomimetic design

The design of PLA (Polylactic acid) vascular networks for physical triggering was required to be robust to withstand casting whilst having sufficient amount of daughter branches to cover the beam, thereby enabling the vascular systems to have fast diagnosis and releasing

of healing agent to the crack areas. PLA was chosen as printing material to build up the vascular network, because of its brittleness, lower carbon-footprint compared to other plastics, biodegradability and good compatibility with the matrix. Good compatibility ensures the cracks penetrating through the vascular structure, instead of going around it.

In some cases, such as Heywood(2015) and Thao (2011), healing agents would not fully cover the whole crack plane area due to low tube coverage. To achieve higher coverage, more daughter branches are necessary to cover more area. But if the number of daughter branches increases and if the diameter is not small, most of the cement will be replaced by plastic and empty space within the tubes. This would also weaken the overall structure. To avoid weakening the cement matrix, smaller diameters were used for each daughter branch to avoid occupying excessive space in cement. In addition, when Murray's law is obeyed (Murray, 1926a), the angle between parent-daughter branches can minimise the turbulence which means that the healing agent will not be concentrated near the junction areas.

Thus a relevant biomimetic design aims at (i) increasing vessels coverage; (ii) avoiding weakening the cement matrix; (iii) ensuring strong bonding between the walls and cementitious materials and (iv) avoiding blockage while the healing agents pumping throughout the system, thereby achieving rapid physical triggering response and effective healing process. Furthermore, the printed structures should be strongly bonded with the cement prisms to assure physical triggering of the tubes.

4.1.2 Theoretical background of the biomimetic design

Three main aspects are important while designing vascular structures: the optimal diameter, length and angle relationship between the daughter and parent branches (Murray 1926a, b). Previously, researchers rarely consider combining all these elements in designing vascular structure. Here, I have adapted and merged the theorical concepts on designing the shape and defining parameters of a biomimetic vascular structure.

Lengths & Diameters

We consider a cylindrical tube, highlighted in yellow in Figure 4.1, where the diameter is D and length is L.

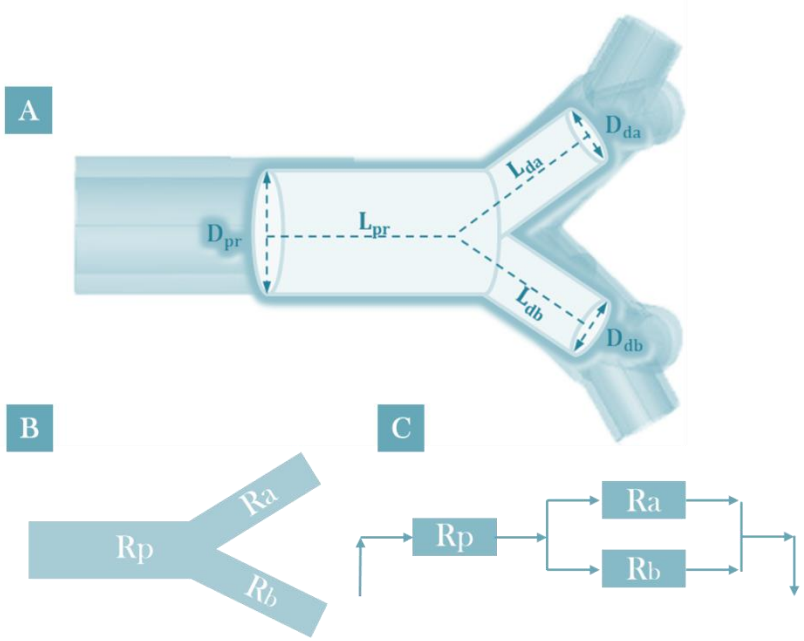

Figure 4.1 Fluid dynamic diagram adapted in the PLA vascular network for physical triggering (A), Resistance from vascular branches (B), and analogical resistance from electricity (C)

The total flow volume of the tubes in Figure 4.1 A is explained in equation 4.1, where V_{pr} (volume of parent branch) and V_{da} (volume of daughter branch a) and V_{db} (volume of daughter branch b):

$$V_{Total} = V_{Pr} + V_D \qquad (4.1)$$

$$= \frac{\pi}{4} D_{Pr}^2 L_{Pr} + \frac{\pi}{4} (D_{da}^2 L_{da} + D_{db}^2 L_{db})$$

Based on a fluid-dynamic interpretation, for energy to be minimised, the sum of the energy used to overcome friction due to shear stress (Rodbard, 1975) on the walls. Similar to electricity (Figure 4.1C), the total flow resistance of the tubes is explained in equation 4.2, where R_{pr} (resistance of parent branch) and R_{da} (resistance of daughter branch a) and R_{db} (resistance of daughter branch b):

$$R_{h,Total} = R_{pr} + \left(\frac{1}{R_{da}} + \frac{1}{R_{db}}\right)^{-1} \qquad (4.2)$$

In order to establish relations for the sizes of tubes that provide easier access to flow. Maximum flow access means minimum resistance under constraints (Lewins, 1994). To this end, we have to minimise the cost function R_λ^*:

$$R_\lambda^* = R_{h,Total} + \lambda V_{Total} \quad (4.3)$$

where λ is the Lagrange multiplier and C is the constraint function, with respect to the independent variables.

In order to find the relationship between the length (L) of daughter branches and parent branches, the flow resistance R_h is represented by D and L based on fluid dynamic interpretation as shown below (Miguel, 2016):

$$R_h = \frac{\Delta p}{Q^\omega} = \frac{4M[8\left(\frac{1}{\omega}+3\right)]^\omega L}{\pi^\omega D^{3\omega+1}} \quad (4.4)$$

where Δp is times the pressure drop, Q ($Q = \frac{\pi D^3}{8(\frac{1}{\omega}+3)}\left(\frac{D}{4M}\frac{\Delta p}{L}\right)^{\frac{1}{\omega}}$) is volumetric flow rate and defined as the product of axial velocity and the cross sectional area of the tube, ω is the fluid behaviour index (or the power-law exponent) and M is the fluid consistency index (represents viscosity).

Considering a symmetrical system with 2-branches, all the daughter branches diameter, D_{dg}, are the same, so $D_{da} = D_{db} = D_{dg}$. The same applies to the length L_{dg}, where $L_{da} = L_{db} = L_{dg}$. Thus $R_{h,Total} = R_{pr} + \left(\frac{2}{R_{dg}}\right)^{-1}$, $V_{Total} = \frac{\pi}{4}D_{Pr}^2 L_{Pr} + \frac{\pi}{2}D_{dg}^2 L_{dg}$.

In this case, equation 4.3 can be thereby rewritten as:

$$R_\lambda^* = R_{Pr} + \left(\frac{2}{R_{dg}}\right)^{-1} + \lambda\left(\frac{\pi}{4}D_{Pr}^2 L_{Pr} + \frac{\pi}{2}D_{dg}^2 L_{dg}\right) \quad (4.5)$$

$$R_\lambda^* = \frac{4M[8\left(\frac{1}{\omega}+3\right)]^\omega L_{Pr}]}{\pi^\omega D_{Pr}^{3\omega+1}} + \frac{4M[8\left(\frac{1}{\omega}+3\right)]^\omega L_{dg}]}{2\pi^\omega D_{dg}^{3\omega+1}} + \lambda\left(\frac{\pi}{4}D_{Pr}^2 L_{Pr} + \frac{\pi}{2}D_{dg}^2 L_{dg}\right) \quad (4.6)$$

According to Fermat's theorem, if a function has a first derivative at an interior point where there is a local extremum, then the derivative must equal zero at that point. In

addition, if the second derivative exists a dispositive (concave up), the function has a local minimum value. By considering constructal law (Bejan, 1996), maximising flow access means minimising resistance under constrains. In the pursuit of achieving local minimum resistance, so the boundary conditions for equation 4.6 are:

$$\frac{\partial R_\lambda^*}{\partial D_{Pr}} = 0 \qquad (4.7)$$

$$\frac{\partial R_\lambda^*}{\partial D_{dg}} = 0 \qquad (4.8)$$

$$\frac{\partial^2 R_\lambda^*}{\partial D_{Pr}^2} > 0 \qquad (4.9)$$

$$\frac{\partial^2 R_\lambda^*}{\partial D_{dg}^2} > 0 \qquad (4.10)$$

Thus equation 3.7discribing parent branches can be rewritten as below:

$$\frac{\partial R_\lambda^*}{\partial D_{Pr}} = \frac{\partial}{\partial D_{Pr}}\left(\frac{4M[8\left(\frac{1}{\omega}+3\right)]^\omega L_{Pr}]}{\pi^\omega}\cdot\frac{-(3\omega+1)D_{Pr}^{3\omega}]}{D_{Pr}^{6\omega+2}} + 2\lambda\frac{\pi}{4}D_{Pr}L_{Pr}\right) = 0 \quad (4.11)$$

$$\frac{-\{4M[8\left(\frac{1}{\omega}+3\right)]^\omega(3\omega+1)\}}{\pi^\omega}\cdot\frac{1}{D_{Pr}^{3\omega+2}} + \lambda\frac{\pi}{2}D_{Pr} = 0 \qquad (4.12)$$

$$\frac{-\{4M[8\left(\frac{1}{\omega}+3\right)]^\omega(3\omega+1)\}}{\pi^\omega}\cdot + \lambda\frac{\pi}{2}D_{Pr}^{3\omega+3} = 0 \qquad (4.13)$$

$$D_{Pr}^{3\omega+3} = \frac{8M[8\left(\frac{1}{\omega}+3\right)]^\omega(3\omega+1)\}}{\pi^{\omega+1}\cdot\lambda} \qquad (4.14)$$

$$D_{Pr} = \frac{(8M)^{\frac{1}{3\omega+3}}[8\left(\frac{1}{\omega}+3\right)]^{\frac{\omega}{3\omega+3}}(3\omega+1)^{\frac{1}{3\omega+3}}}{\pi^{\frac{\omega+1}{3\omega+3}}\cdot\lambda^{\frac{1}{3\omega+3}}} \qquad (4.15)$$

Similarly, for the daughter branches, equation 4.8 can be rewritten as below:

$$\frac{\partial R_{\lambda}^{*}}{\partial D_{dg}} = \frac{\partial}{\partial D_{Pr}}\left(\frac{-4M[8\left(\frac{1}{\omega}+3\right)]^{\omega}\cdot(3\omega+1)L_{dg}}{2\pi^{\omega}}\cdot\frac{1}{D_{dg}^{3\omega+2}}+\lambda\pi D_{dg}L_{dg}\right) = 0 \quad (4.16)$$

$$\frac{-\{2M[8\left(\frac{1}{\omega}+3\right)]^{\omega}\cdot(3\omega+1)\}L_{dg}}{2\pi^{\omega}}+\lambda\pi D_{dg}^{3\omega+3}L_{dg}=0 \quad (4.17)$$

$$D_{dg}^{3\omega+3} = \frac{2M[8\left(\frac{1}{\omega}+3\right)]^{\omega}\cdot(3\omega+1)}{\pi^{\omega+1}\cdot\lambda} \quad (4.18)$$

$$D_{dg} = \frac{2M^{\frac{1}{3\omega+3}}[8\left(\frac{1}{\omega}+3\right)]^{\frac{\omega}{3\omega+3}}\cdot(3\omega+1)^{\frac{1}{3\omega+3}}}{\pi^{\frac{\omega+1}{3\omega+3}}\cdot\lambda^{\frac{1}{3\omega+3}}} \quad (4.19)$$

So that the relationship of diameter in this symmetric branching system (4.15/4.19) is given by:

$$\frac{D_{dg}}{D_{Pr}} = 2^{\frac{-2}{3\omega+3}} \quad (4.20)$$

Facilitate equation 4.20 to equation 4.2 can get the relationship of length in this symmetric branching system as:

$$\frac{L_{dg}}{L_{Pr}} = 2^{\frac{-3\omega+1}{3\omega+3}} \quad (4.21)$$

Sodium silicate was used as a model mineral healing agent is this study, as its reactions with the cementitious matrix can recover the original properties. As sodium silicate is a Newtonian liquid, ω=1 and Equation 4.20 and 4.21 yields $\frac{D_{Daughter}}{D_{parent}} = 2^{\frac{-1}{3}}$ and $\frac{L_{Daughter}}{L_{parent}} = 2^{\frac{-1}{3}}$.

Thus, the design of lengths and diameters of daughter and parent branches in a ratio of $2^{\frac{-1}{3}}$ was applied in this study.

Branching Angles

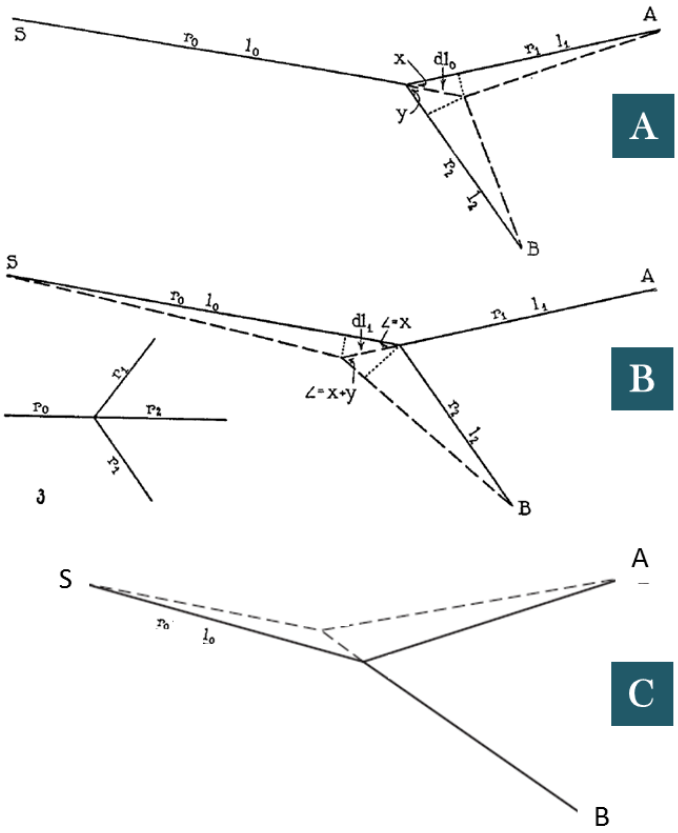

Figure 4.2 Murray's original drawing for branching angle rule (A, B) (In the notion of his paper, r_0, r_1, r_2 are the radii of the arteries; l_0, l_1, l_2, the lengths, and x and y are the angles) (Murray, 1926); the third scenario missing from Murray's diagram and drawn in Adam et al. (2011)

Murray (1926b) also provided an original formula for the angle of branching, giving the idea of treating non-symmetric branches and trifurcations.

Here we consider the most efficient branching in allowing for the distribution of energy from a point S to two points, A and B. r_0, r_1, r_2 are the radii of the arteries; l_0, l_1, l_2, the lengths, and x and y are the angles, to be determined, which the branches make with the line of direction of the parent branch proceeding from S (Figure 4.2 A). The dotted lines show the triangles constructed in order to arrive at this result.

According to each scenario (Figure 4.2 A, B and C), we could obtain equations for each of the three constructions as below:

$$\mathrm{d}l_0 r_0^2 = \cos x \mathrm{d}l_0 r_1^2 + \cos y \mathrm{d}l_0 r_2^2 \qquad (4.22)$$

$$\mathrm{d}l_1 r_1^2 = -\cos(x+y)\mathrm{d}l_1 r_2^2 + \cos x \mathrm{d}l_1 r_0^2 \qquad (4.23)$$

$$\mathrm{d}l_2r_2^2 = -\cos(x+y)\mathrm{d}l_2r_1^2 + \cos y\mathrm{d}l_2r_0^2 \qquad (4.24)$$

The "cost" of the section l_0 is now increased by the increment $\mathrm{d}l_0r_0^2$ and the costs of the branches are decreased by $\cos x\mathrm{d}l_0r_1^2$ and $\cos y\mathrm{d}l_0r_2^2$ respectively. The left part of formula (in equation 4.22, 4.23 and 4.24) represents the cost increase, whilst the right part (in equation 4.22, 4.23 and 4.24) shows the cost decrease.

According to equation (4.22, 4.23 and 4.24), the correlation between branching angle and the radius ratios can be obtained as:

$$cosx = \frac{r_0^4 + r_1^4 - (r_0^3 - r_1^3)^{\frac{4}{3}}}{2r_0^2r_1^2} \qquad (4.25)$$

$$cosy = \frac{r_0^4 + r_2^4 - (r_0^3 - r_2^3)^{\frac{4}{3}}}{2r_0^2r_2^2} \qquad (4.26)$$

$$\cos(x+y) = \frac{-r_1^4 - r_2^4 + (r_1^3 + r_2^3)^{\frac{4}{3}}}{2r_1^2r_2^2} \qquad (4.26)$$

Considering our study is a symmetric splitting:

$$cosx = cosy = \frac{1 + \delta_1^4 - (1 - \delta_1^3)^{\frac{4}{3}}}{2\delta_1^2} \qquad (4.27)$$

In this case, $\delta_1 = \frac{1}{\sqrt[3]{2}}$

Which provides $x = y = 37.5^\circ$.

The designed model and its parameter

As a result, a branch-like distribution of the healing agent is achieved while minimising the space occupied by the vascular network and preventing blockages in junction areas. A schematic representation of the vascular network and its main parameters is presented in Figure 4.3.

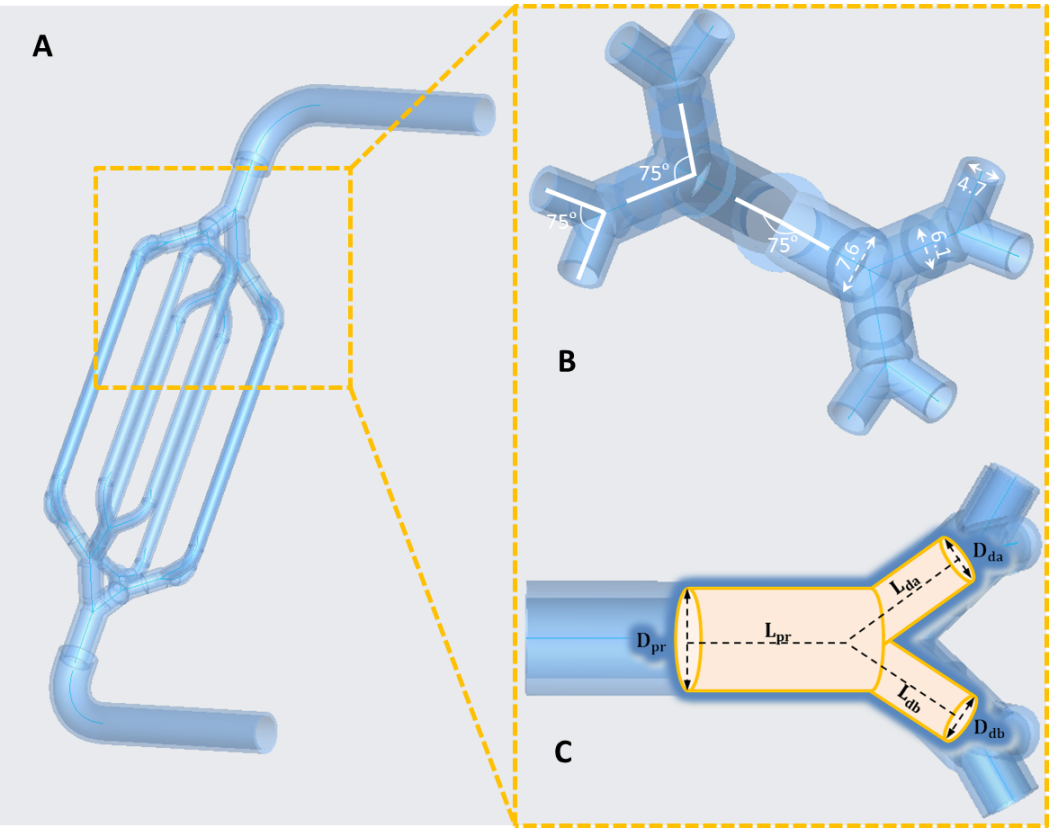

Figure 4.3 A biomimetic design of 3D vascular network; (A) designed model following Murray's law; (B) parameters considered in the model; (C) fluid dynamic diagram adapted in this model.

Detailed figures for vascular dimensions could be found in Figure 4.3 B. The artery connecting to the pump was limited to the fitting to the pump tubing and defined as 13.6 mm outer diameter (OD) and 11.6 mm inner diameter (ID). Then, the first parent branch was adapted to 11.6 OD and 9.6 mm ID in order to be snug to the artery. Thus the daughter branches ID were calculated from Equation 3.3 as 7.6, 6.1 and 4.7 mm, as shown in Figure 4.3 B. Formia et al. (2015) found that viscous healing agents, such as sodium silicate cannot be released from the tube smaller than 2 mm in diameter. Adapting this factor, the minimum inner diameter of the daughter branchs were 4.7 mm and were sufficient enough for delivering sodium silicate for this study.

In addition, the design of the length for each generation daughter branch was limited by angle (3.8), length relationship (3.4) and cement beam parameters (length 300mm, width or height 80 mm). Then, the first parent branch was adapted to 26.0 mm. Thus the daughter branches were calculated from Equation 3.3 as 20.6, 16.3 and 12.9 mm.

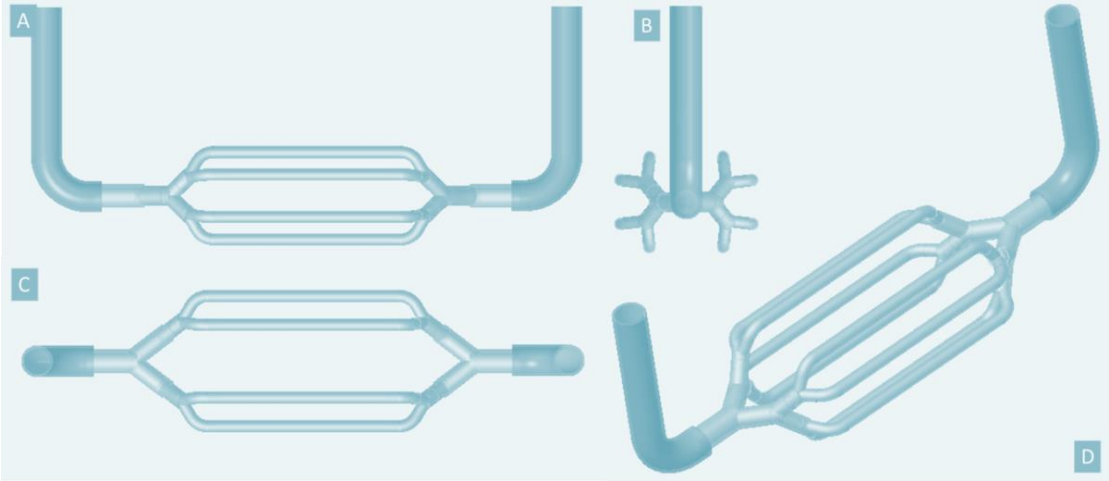

Figure 4.4 Designed vascular model for cement specimens, bifurcation system; A, front version; B, left version C, top version; D, general look.

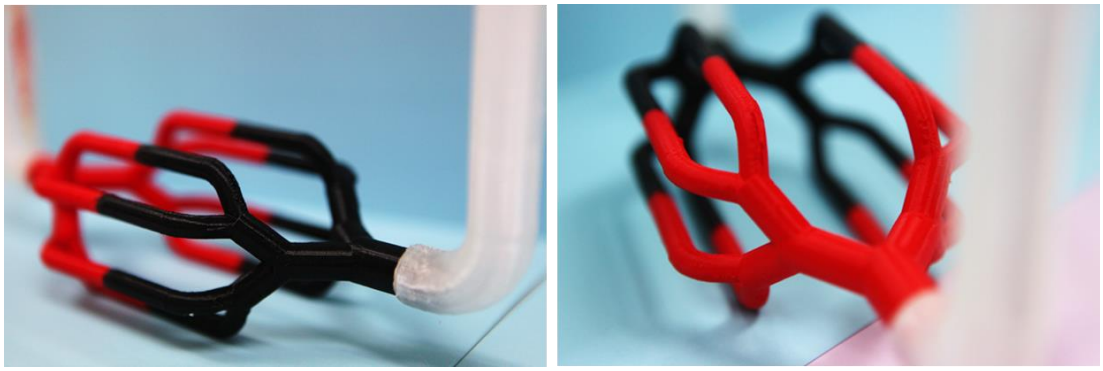

Figure 4.5 Photography of printed model in Figure 4.4

The designed network was manufactured by 3D printing to allow the precise control and tailoring of diameters and complexity of the structure. The printed work is shown in Figure 4.5. All networks were designed with a constant volume capacity of 65 ml. This allowed the comparison with 1D and 2D orientations of the tubes and assessment of healing efficiency.

4.2 Comparable vascular network designs for physical triggering

4.2.1 One-dimensional (1D) vascular network for physical triggering

In Figure 4.6, both designed and final fabricated structures were presented. The arrows indicated the sodium silicate flow through the systems. A volume of 65 ml was designed for all 1D structures with the aim of controlling the same amount of healing agents passing

through during the healing process. The volume of each fabricated structure had been further measured and confirmed by connecting the printed structures with a scaled container.

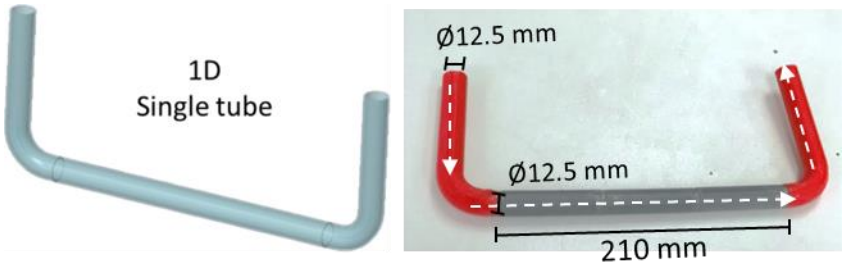

Figure 4.6 Designed model and photography of printed 1D model

4.2.2 Two-dimensional (2D) vascular network for physical triggering

As for the 2D structure, both designed (Figure 4.7) and final fabricated structures were presented. Four parallel daughter branches were designed to equal to the four sub-branches (2nd daughter branches) from 3D biomimetic model mentioned in section 4.1. In the 2D design, these four parallel branches are also 2nd daughter branches. Whilst the 3rd daughter branches in 2D model was not designed mainly due to the feasibility of designing a 2D system with 8 parallel tubes with 65 ml in volume in total. The model would have taken too much room of the cement locally. So here, the 2D model was designed in a 2D shape, and the daughter branches were designed paralleled. The arrows indicated the sodium silicate flow through the systems. Same with 1D structures, a volume of 65 ml was designed for all 2D structures with the aim of controlling the same amount of healing agents passing through during healing process. The volume of each fabricated structure had been further measured and confirmed by connecting the printed structures with a scaled container.

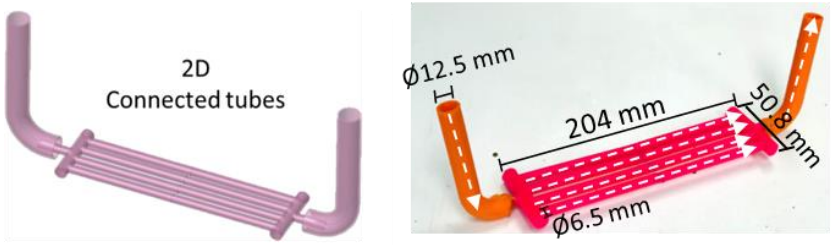

Figure 4.7 Designed model and photography of printed 2D model

4.3 Prints accuracy and vascular networks properties

4.3.1 Printing accuracy and surface morphology

Print accuracy and morphology were studied in this work. The intention of this test is to provide convincible accuracy of different geometrical characteristics of the prints. As shown in Figure 4.8 D and E, the designed lengths and actual printed length of try-out columns were compared, and showed the lengths between 1 and 10 mm have an accuracy of 97.31% (slope of the curve in Figure 4.8 D). Larger lengths between 12 and 24 mm have a higher accuracy of 98.99%. Similar results were found in Kacmarcik et al.(2018), who stated a maximum dimensional deviation range at 3.377% in an Ultimaker® 3D printer.

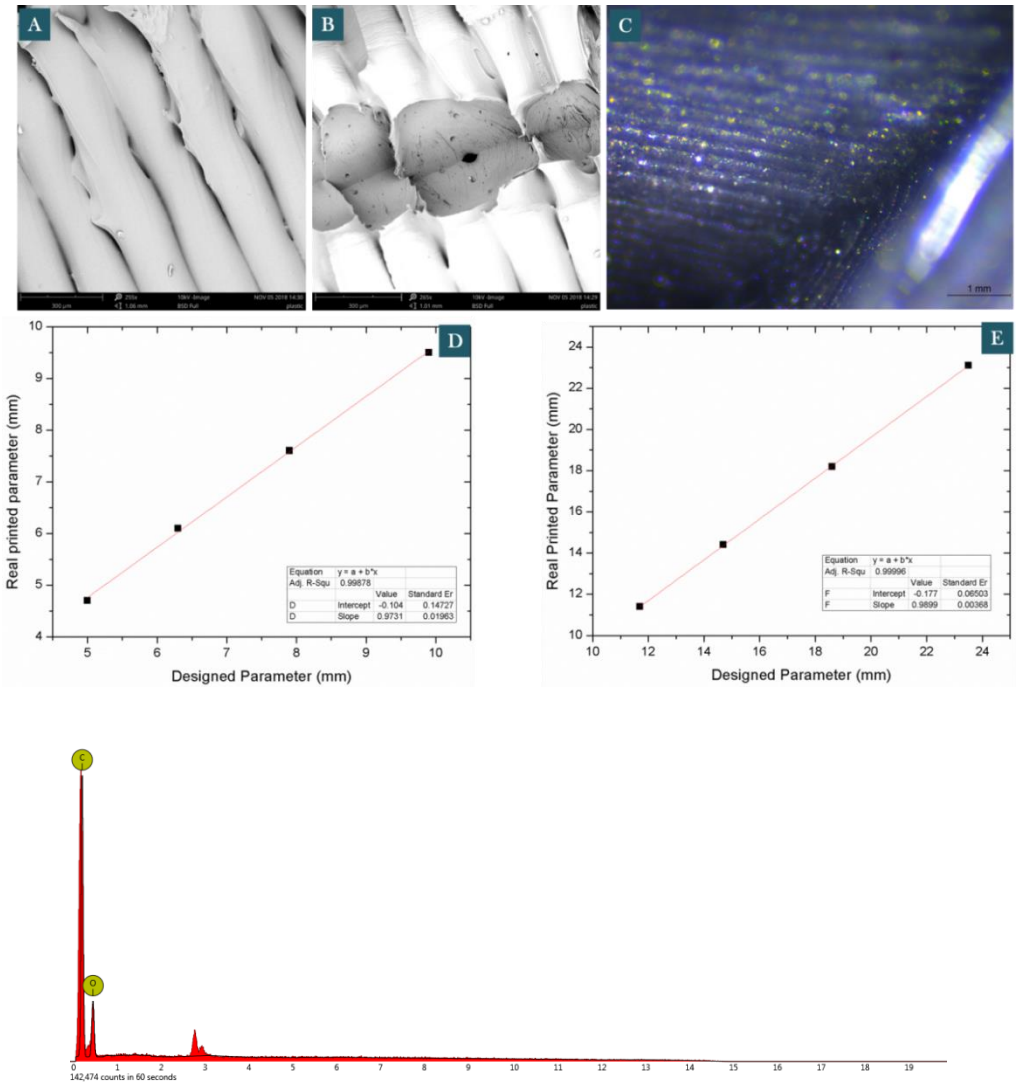

Figure 4.8 Morphology of printed models (A) and (B) under SEM, and (C) under microscope. Printing accuracy diagrams (D and E), and the EDX pattern of PLA plastic.

Small layer gaps between printed layers were observed from both microscope and SEM. The layer gaps were as small as 1 μm under SEM images, and the material of the plastic was again been proved by EDX, which showed sharp peaks carbon (C) and oxygen (O) element in the EDX pattern. The small peaks beside were the coating material for SEM-EDX pre-treatment with the aim of improving conductivity.

4.3.2 3D printed biomimetic 3D vasculature under CT

Computed tomography was used to examine 3D prints accuracy within the channels, thereby avoiding any blockage in the channels created by unexpected printing errors.

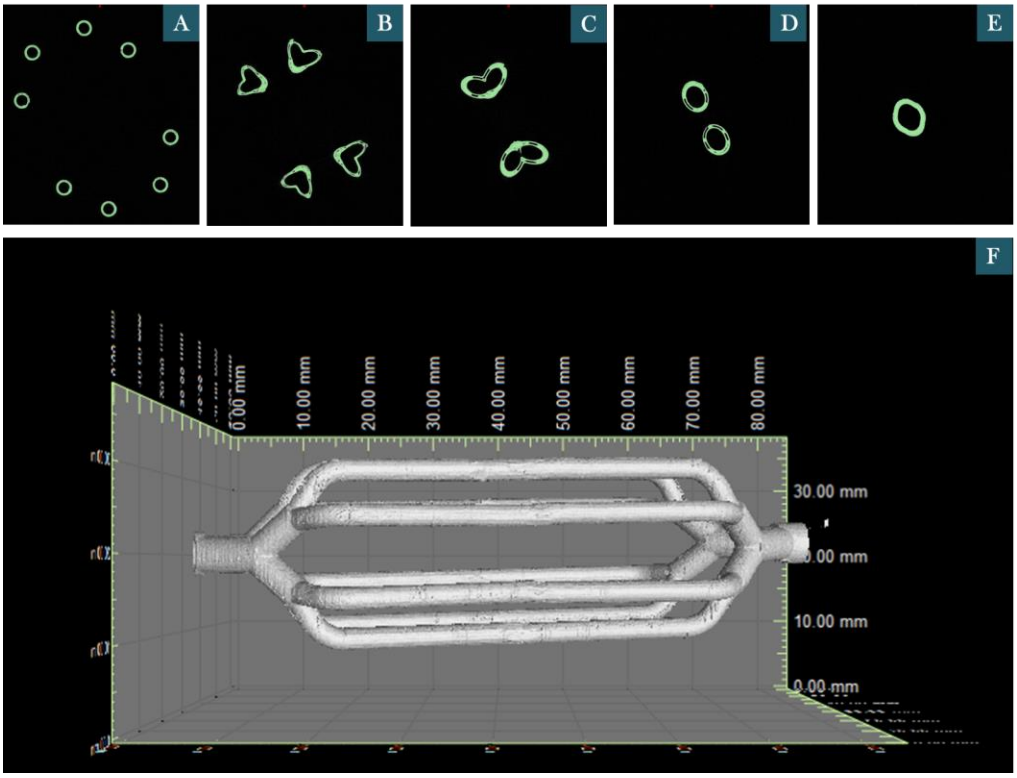

Figure 4.9 Reconstructed image of 3D printed biomimetic 3D vasculature, sliced section from the third daughter branches (A), joint between third daughter branches and second daughter branches (B), joint between second daughter branches and first daughter branches (C), first daughter branches (D), parent branch (E) and the who construction image of the printed model (F)

All channels of the vasculature were printed as designed. Occasional printing errors were a concern, as they may block the joint or other parts of the channels, hampering the flow and disruption of healing agents to smaller daughter branches. According to Figure 4.9 B and C, there were no accidental blockages being made at the jointing areas between different sized branches. This further confirmed the accuracy of the printing process

using Ultimaker®, and built up the confidence of using the printed 3D models in the following tests.

4.3.3 Assessment of mechanical properties of vascular networks

The fractural response of 3D printed structures was also examined before embedding into cement. Structures were loaded to failure under bending. Five parallel tests were carried out in each vascular type, with the aim of avoiding accidental error.

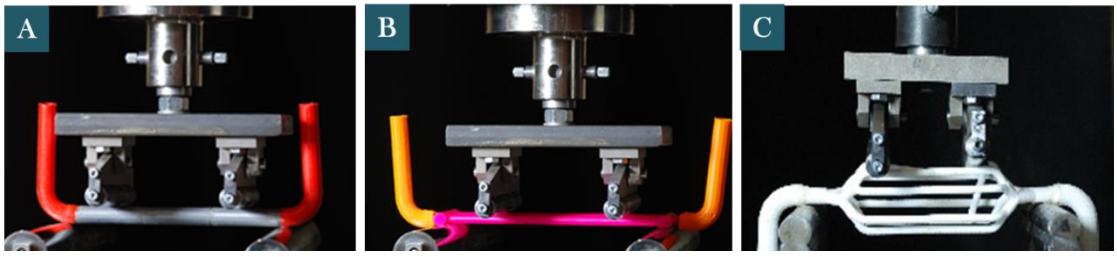

Figure 4.10 Photographs during loading process of the 1D (A), 2D (B) and 3D (C)

Results showed that single tube (1D structure) showed the lowest bending strength, at around 71 N. 2D and 3D on the other hand, had a relatively higher figure, at 129 N and 134 N respectively. It is obvious that 2D and 3D networks demonstrated higher capacity than 1D structure, as they have more supporting structures to distribute forces rather than concentrating on one single tube. Similarly, Heywood (2015) reported that a thinner (with 4 mm inner diameter and 5mm outer diameter, 188mm in length) single PLA tube failed at 27.5 N during the test (loading rate 0.125 mm/min). This is much lower than the 1D structure (with 12.5 mm inner diameter and 15 mm outer diameter, 210 mm in length) in our study. Loading response difference relates with loading rate, bending methods (three points, four points), and the tube thickness in this case. The thickness of the tube was one of the main reasons that resulted in different load response for a single tube, as the same commercial PLA was used for printing. As a result, all 3D printed PLA structures failed below 200 N, which indicated that they required low energy to crack and release healing agent, making 3D printed PLA structure an ideal option for self-healing structures.

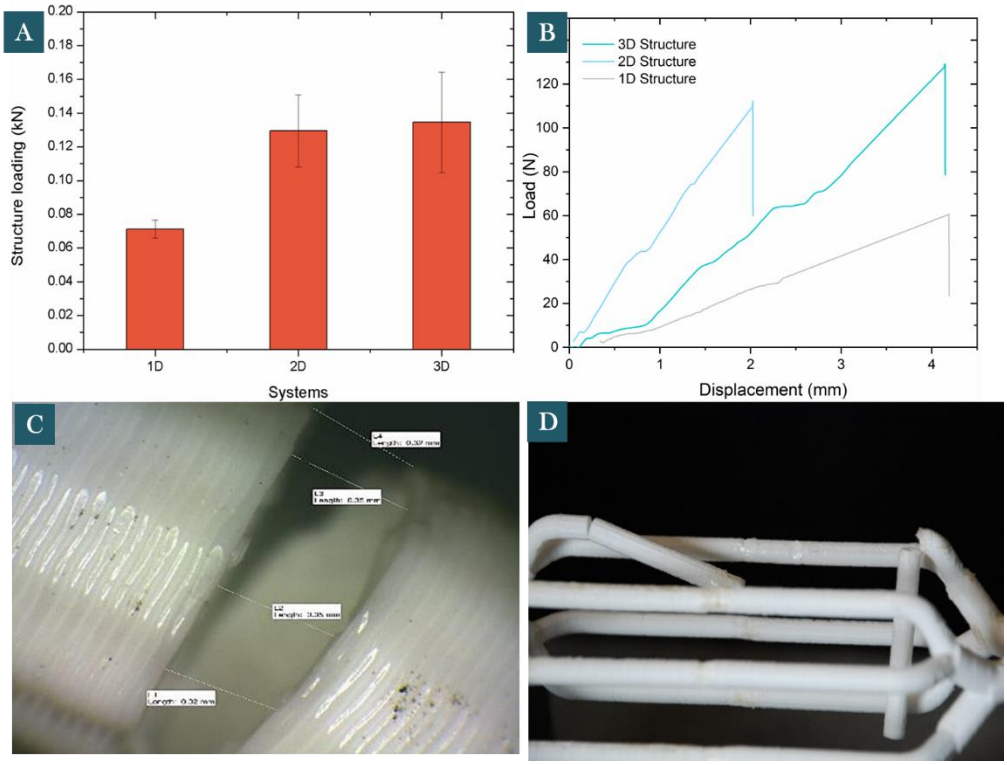

Figure 4.11 Load response of 1D/2D/3D printed structures (A) and typical load-displacement curves of 1D/2D/3D structures (B), photography of the damage part (C) and the general image of the structure after loading (D)

Interestingly, the soldering part was not broken as expected, but the part slightly away from the soldered part was damaged (Figure 4.11 B and C). This phenomenon proved that the soldered part was not the weakest area of the vascular structure. This is because layer-by-layered 3D printing process created weak gaps between layers (as shown in Figure 4.8 A), while the soldering process erased this layered structure and somehow acted as further bracing strengthening the tube locally. Multiple tests were examined to ensure the consistency of the PLA models load response, showing the 1D model has the lowest load response, while 2D and 3D having similar figures with relatively larger error bars.

4.3.4 Assessment of channel resilience properties of vascular networks

To compare the channel resistance difference in 1D/2D/3D structure, the engineered vascular matrix is connected to a recycling system (consisting of a peristaltic pump, a sodium silicate reservoir and two pressure transducers) for measuring the pressure changes. The connection details and resistance calculation were explained in Chapter 3. Large pressure difference between the inlet and outlet transducers means large resistance

within the channels, which would request relatively higher energy to pump the healing agents. There was around 2.5 kPa pressure difference in the 1D system, which correlated its total resistance was 2.5 kPa • s • mL^{-1}(Figure 4.12). In the 2D system, secondary channels were designed with 90-degree branching angle. The figures of both pressure change and resistance increased to approximately 7.6 kPa and 7.6 kPa • s • mL^{-1}.

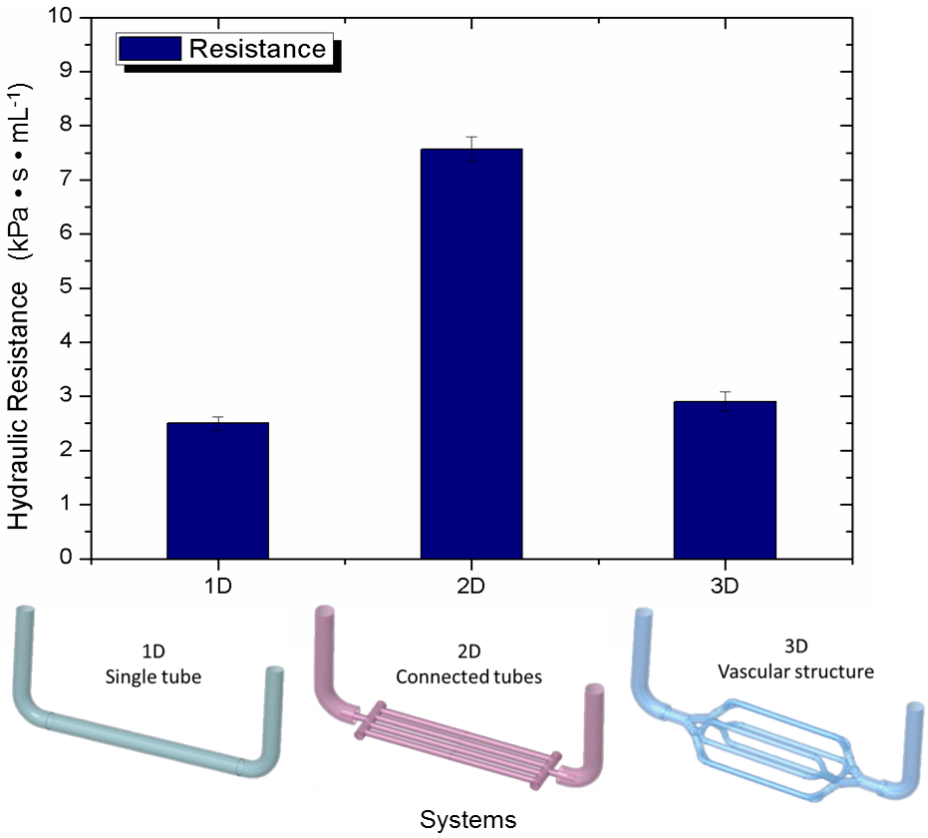

Figure 4.12 Hydraulic resistances of 1D/2D/3D models

The channel complexity, cross-sectional areas and branching angles can affect the growth of hydraulic resistance (Razavi et al., 2014). In the case of 3D structure, hydraulic resistance was only 2.9 kPa • s • mL^{-1}. This demonstrated that the design of fluidic channels which obey Murray's law improves fluidic control (Lim et al., 2003).

4.4 Compatibility of cementitious vascular system

4.4.1 Characterisation of vascular networks in cement

In initial investigations, cement samples with 3D printed PLA vasculatures were cast (80mm x 80mm x 300mm). Samples were cast and cracked after a period of time (7

days/28 days) of curing. The interface of cement and PLA prints could be observed on cracked cement surfaces with the naked eye.

3D printed pattern on the tubes provided a rough surface compared with smooth PU tubes applied in Davis et al (2015), which could be easily pulled out after cement beam were cured. The pattern increased friction between 3D printed structures and cement matrix (Figure 4.13). As shown in Figure 4.13 C, 3D printed tubes clearly retained their pattern on cement pastes, which created a rough surface on the cement side, and thus enhanced the bonding between vascular structures and cement beams.

All different 3D printed structures did not debond from the cementitious matrix confirming the strong adhesion between them and the brittleness of PLA which enabled its fracture. This means 3D printing patterns and PLA materials are suitable for producing vascular structures and are bonded well with cement specimens.

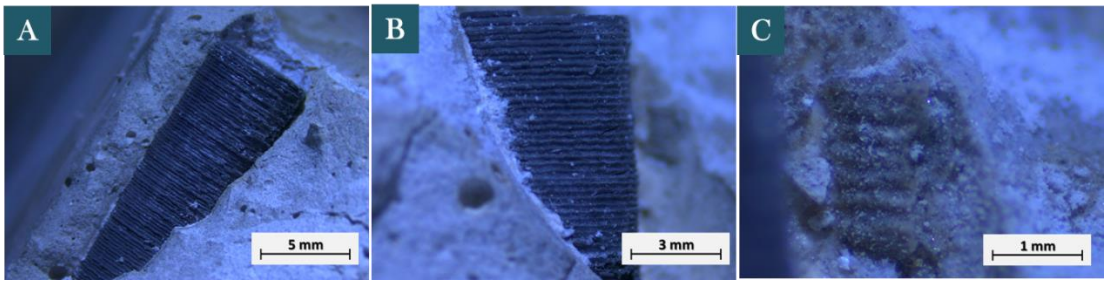

Figure 4.13, microscope image of the connection between individual tube and cement beams, boundary between vascular structures and cement matrix (A); minerals between PLA tube and cement matrix (B); pattern remained after tube was manually separated from cement (C)

4.4.2 Mechanical performance

Four-point bending tests were applied to form cracks in the samples embedded with the fabricated 1D, 2D and 3D vascular networks and the results are shown in Figure 4.14. Plain cement beams showed the least flexural strength, at around 2.3MPa, compared with specimens with PLA tubes added. Specimens were held by the embedded wires that prevent complete sample separation (as discussed in Chapter 3). An increased load was necessary to crack the samples embedded with the vascular networks once compared with the plain beam samples (Figure 4.14), hinting the physical triggering or the PLA tubes.

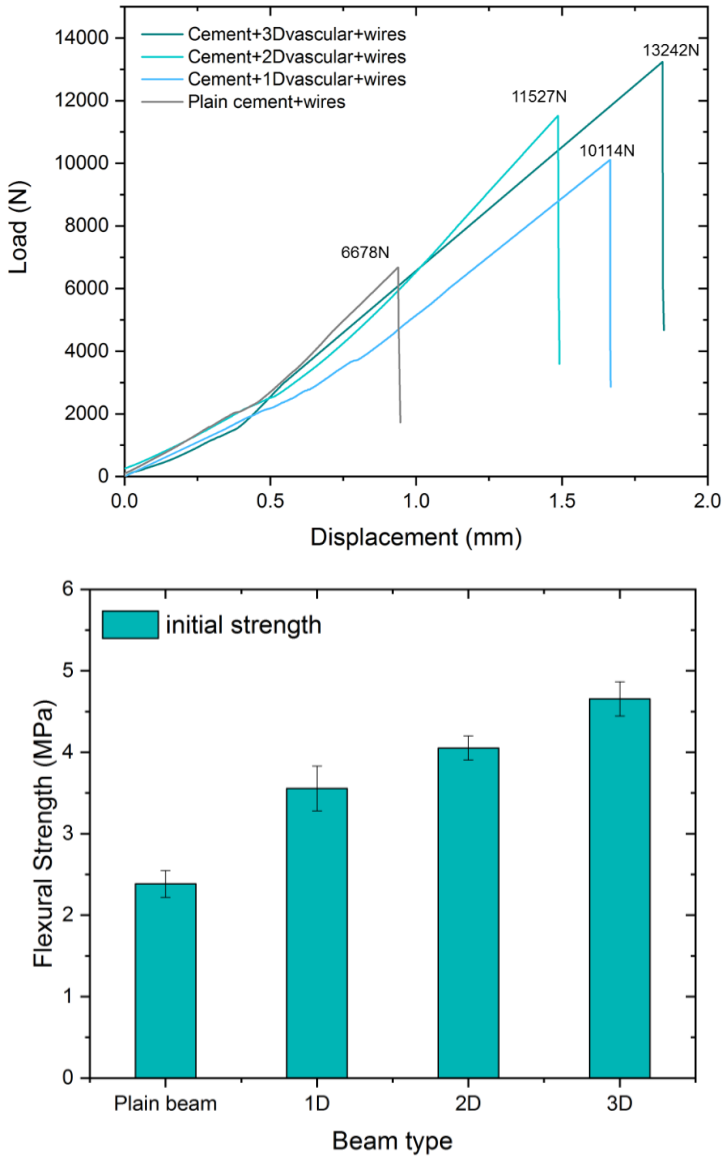

Figure 4.14, Typical Load-displacement curves (Top) and initial flexural strength of the plain/1D/2D/3D specimens (Bottom)

The effect of vascular tubes addition on the mechanical properties of cement pastes is influenced by various parameters. Firstly, the effect will be dependent on the properties of the incorporated tubes themselves. If the PLA tubes possess superior properties to that of the matrix, there is the potential for their addition to enhance the composite's mechanical properties. As demonstrated in section 4.3.3, the tubes themselves could only bear a load less than 200N, it is unlikely that the tubing structure itself contributed to load-bearing directly. Instead, the plastic tubing structure acts as a reinforcement (Kim and Han, 2017) of the cement beams and assisted in distributing and transferring stress in the matrix(Yuhazri et al., 2017).

4.5 Self-healing performance and efficiency in 1D/2D/3D systems

4.5.1 Effect of vascular networks on the mechanical properties of cement

Strength recovery and stiffness recovery after healing were used to evaluate the mechanical triggering and healing efficiency of the vascular system. To isolate the contribution of autogenous healing and clearly identify the effect of healing agent, a series of tests were completed without any healing agent.

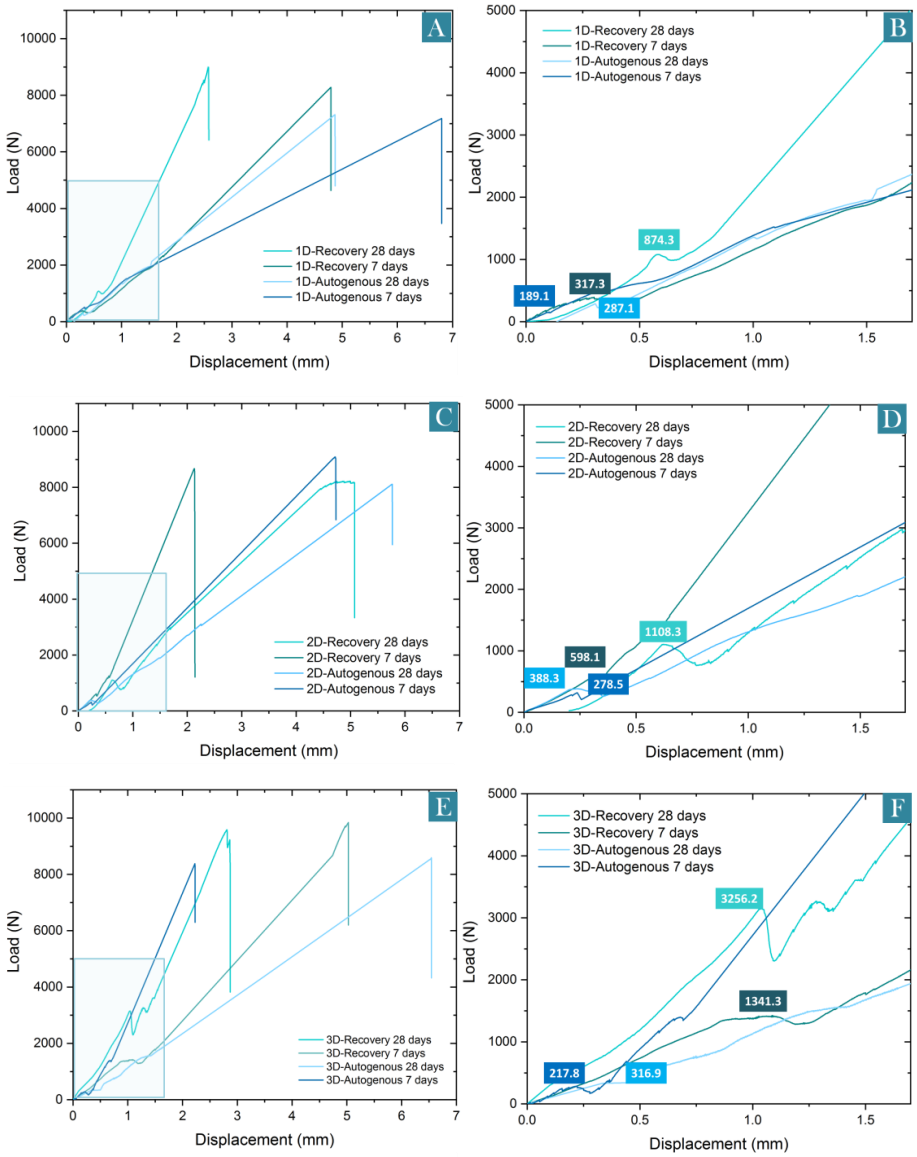

Figure 4.15, Typical Load-displacement curves under four-point bending testing of 1D vascular samples (A, B(zoomed in from A)) cracked after 7 days and 28 days of healing; 2D vascular samples (C, D(zoomed in from C)) cracked after 7 days and 28 days of healing; 3D vascular samples (E, F(zoomed in from E)) cracked after 7 days and 28 days of healing; load recovery of first cracking points are marked in coloured box.

In Figure 4.15 and 4.16, autogenous healing was observed in the controlled beams, which received an approximately 1 to 3% of strength recovery. For the treatment groups, the sodium silicate solution was pumped into the systems continuously for 7 days or 28 days at 60 mL/min. The sodium silicate solution promotes self-healing through a reaction with calcium hydroxide, a product of cement hydration, to produce calcium silicate hydrates (C–S–H) gel which allows some recovery of strength (Kanellopoulos et al., 2015; Alghamri et al., 2016).

Although autogenous healing may have participated in all samples, this effect would be less significant as the cracks were all wider than 600 μm. And the controlled specimens with no additional agents introduced showed minimal strength recovery after 28 days. Thus, this is less likely to have an effect on the healing time of 28 days. The best strength recovery was observed in samples with 3D biomimetic vasculature. This may be due to an increase in the crack face coverage by the healing fluid and hence crack faces were analysed further to see how healing agent penetration across the crack faces varied with different geometries.

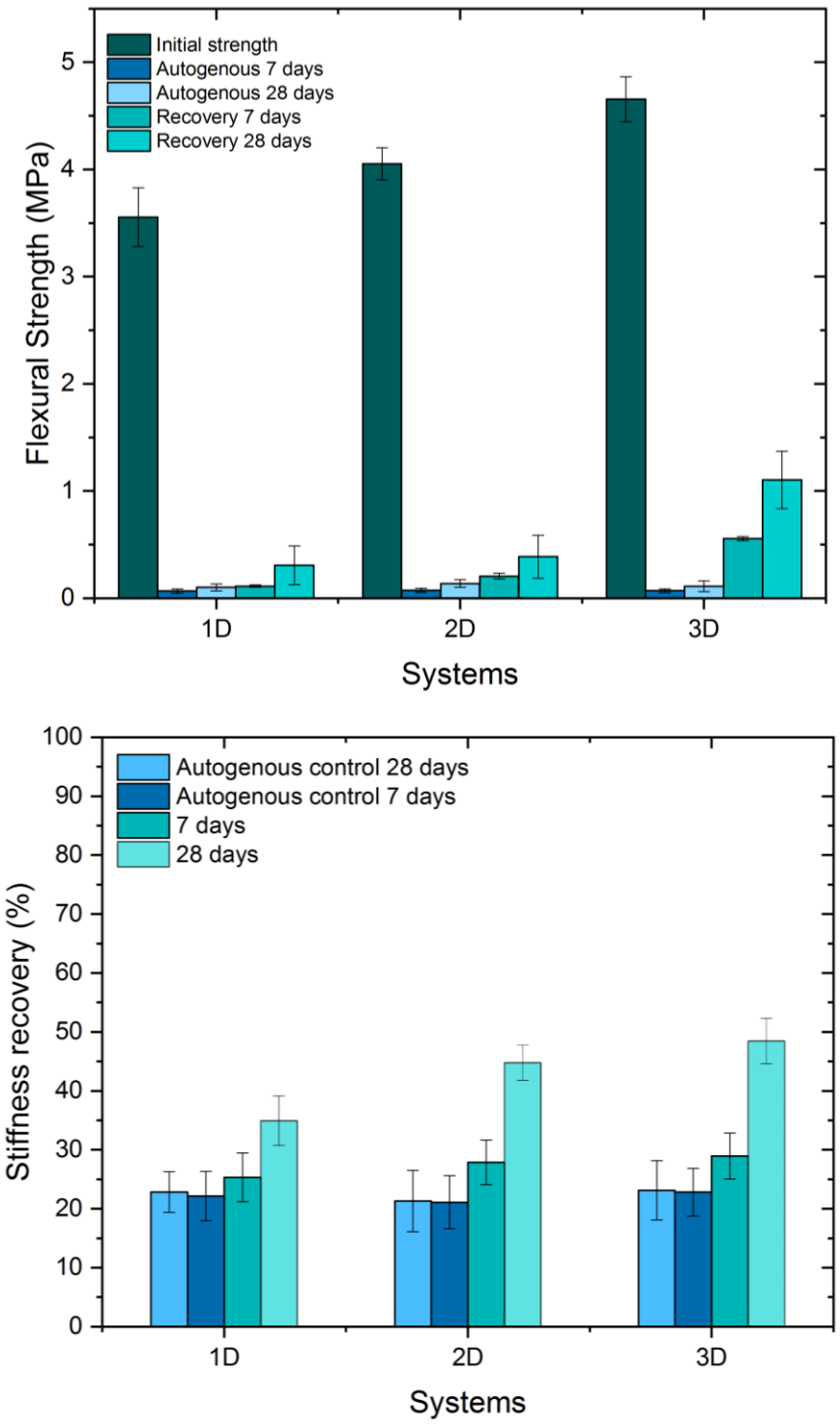

Figure 4.16, Flexural strength of the specimens before (initial strength of 1D/2D/3D system) and after 7 days and 28 days of healing process (recovered strength of 1D/2D/3D system), and the strength of autogenous healing specimens (samples with PLA tubes embedded but with no healing agent introduced); note that error bars represented 3 duplicated samples tested in one experiment (Top);Stiffness recovery of the specimens of 1D/2D/3D systems after 7 days and 28 days of healing process (Bottom)

Stiffness improvements were found increasing with the large daughter tube distribution of the systems (Figure 4.16). This is correlated with the findings from the strength

recovery. Stiffness recovery in the samples with healing agents being pumped for 7 or 28 days were significantly improved due to the amount of healing agents bonded between the crack faces. Additionally, there was an improving trend from 7 days to 28 days stiffness. On the other hand, small load and stiffness recovery was expected in controlled samples (autogenous healing) due to the crack width and mineral based-bonding between two crack faces.

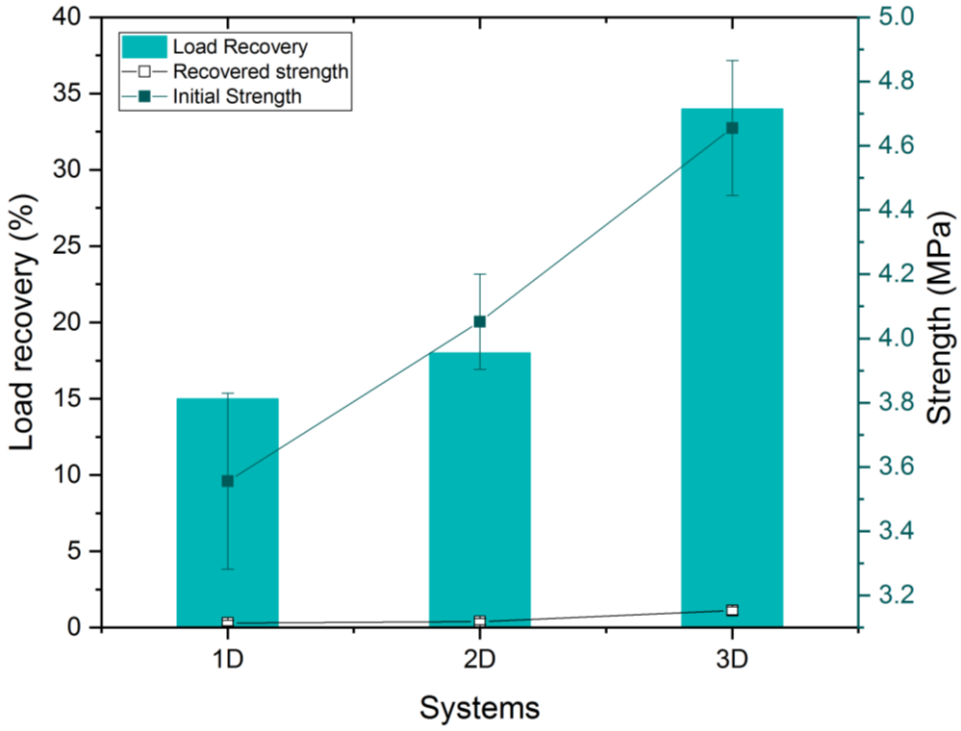

Figure 4.17, Load recovery and strength of the specimens of 1D/2D/3D systems after 28 days of healing process

Load recovery of 10%~20% was observed for 1D and 2D-structures while 3D vascular network specimens reached 34% after 28 days of healing agents pumping (Figure 4.17), compared with the initial load. A previous investigation of self-healing performance using sodium silicate encapsulate in sodium silicate in glass vials reveals similar results to the 1D and 2D-systems, with a load recovery rate of ~20% (Kanellopoulos et al., 2015). And Heywood (2015) achieved a ~10% of load recovery in a 2D vascular system with colloidal silica introduced. The increased load recovery of the 3D vascular network was attributed to the delivery of healing agent at multiple points at the surface of the crack, thus enhancing the healed surface.

4.5.2 Assessment of transport property recovery (Sorptivity)

To evaluate the recovery in water tightness, capillary water absorption for the cracked concrete specimens with and without healing was also measured. The durability of concrete depends predominantly on the ease with which fluids enter and move through the matrix and sorptivity is an indicator of concrete's ability to absorb and transmit liquid through it by capillary suction.

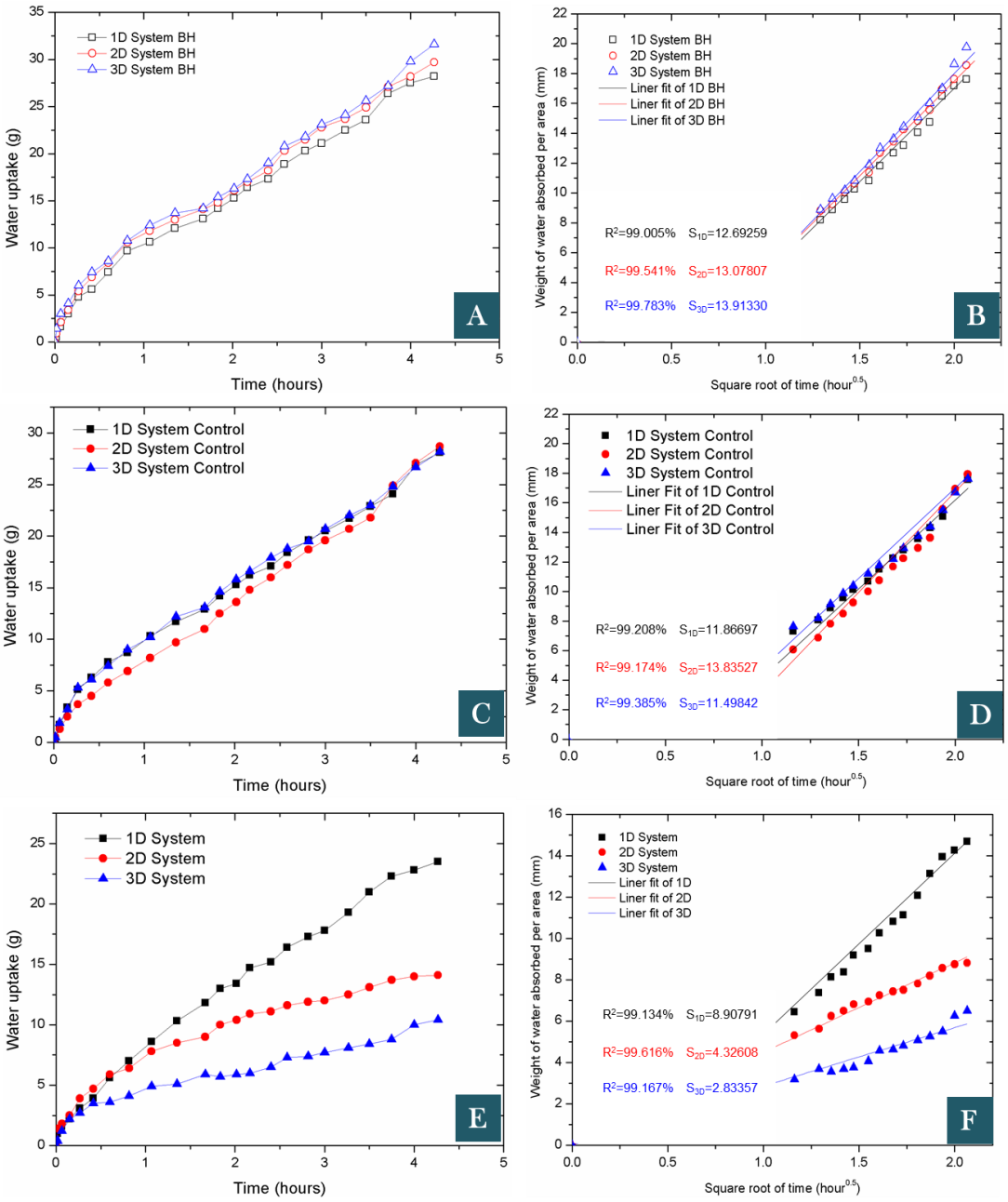

Figure 4.18, Water uptake process over time before healing (A), control group (without healing agent pumping) after healing (C) and treatment group (with healing agent pumping) after healing (E); Water sorptivity of specimens vs the square root of time before healing (B), control group after healing (D) and treatment group after healing (F)

Figure 4.18 plots the water uptake process and the capillary water absorption through cracks before and after 28 days sodium silicate pumping from inducing the 0.7 mm width cracks in comparison with control group samples. No significant difference in the water uptake was observed in the control samples after healing (Figure 4.18 C) compared with the samples before healing (Figure 4.18 A). The results indicate that autogenous healing in air condition barely contributed to enhancing the water tightness. Besides, it is noteworthy that, the 1D/2D/3D network did not provide any preferential flow path in cement. Figure 4.18 E shows the water uptake after healing, where the preferential water flow path is blocked by the healing products, and the water absorption by capillary action and the overall sorptivity is reduced. The mean sorptivity coefficient values for the 1D/2D/3D vascular-cement of cracked samples before healing are 12, 13 and 13 ($mm/h^{1/2}$) and 9, 4 and 3 ($mm/h^{1/2}$) after healing. Thus, the reduction ratio of initial sorptivity is 25, 69 and 77% for the 1D, 2D and 3D vascular-cement, respectively. This is because capillary flow within cracks is mainly influenced by crack width and depth. When solidified sodium silicate gel blocked the crack, the crack length and depth were shortened, thereby slowing down water uptake (Alghamri et al., 2016) and then reducing water sorptivity. In this case, the 3D vascular system was able to block more crack area compared with the 1D and 2D systems.

Figure 4.18 shows the changes in the water absorption of the three vascular beams over time before and after healing. As shown in Figure 4.18 B and D, the water absorption in all specimens was proportional to the square root of time after 1 h. The reason of choosing data for linear analysis after 1h is because (1) water uptake at an early stage could be affected by the accuracy while measuring in a short time of period; (2) few unstable sodium silicate gels would be dissolved by water at an early stage. From the slope of the graph of water absorption vs square root of time, and is calculated using Equation 3.7 from Chapter 3.

It is clear from Figure 4.19 that specimen in which healing agent was released show lower sorptivity coefficient than equivalent controls. There is a significant trend between the geometry of the systems and water sorptivity coefficient, which indicated that systems with more tube coverage within the matrix have better water permeability, due to the sufficient cracks faces were covered. Further to this the healing process is accelerated by the presence of the healing agent – healing from 7 to 28 days in 3D vasculature systems showed a decrease in sorptivity coefficient from 12.9 to 11.5

($mm/h^{1/2}$) and 9.5 to 2.8 ($mm/h^{1/2}$) for healed and control samples with tubes respectively.

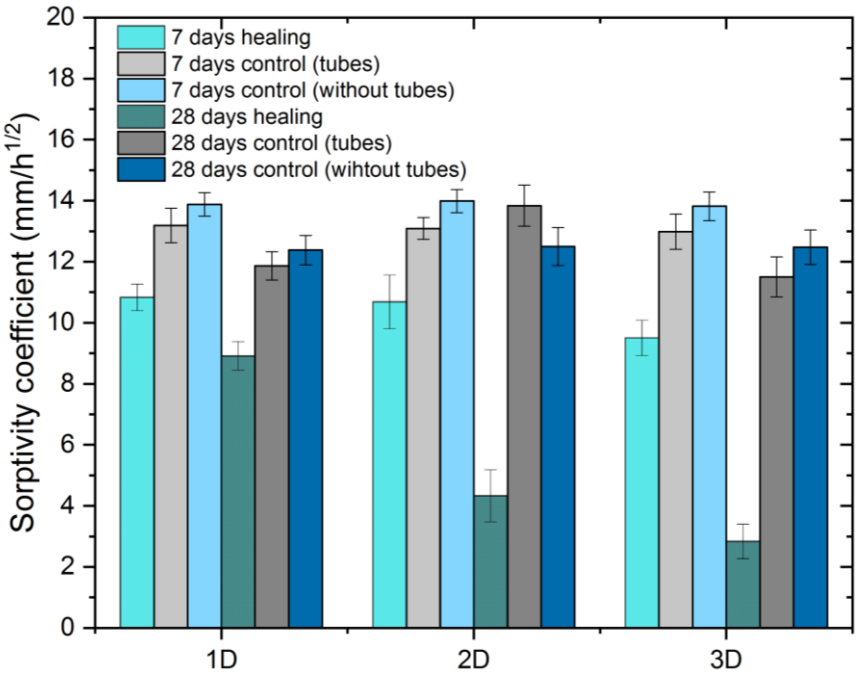

Figure 4.19, Sorptivity coefficient of the 1D/2D/3D systems together with their controlled specimens

Control samples with and without tubes showed barely variation in sorptivity and sorptivity reduction over healing time, which suggested the presence of the tubes within the specimen has little effect on the healing.

4.5.3 Crack width and closure

In addition to showing recovery in mechanical and transport properties, the surface crack area also decreased as time went on for the 1D/2D/3D vascular-cement systems. Optical microscopy was used to quantify crack the initial crack width and the final crack closure after healing. The four-point bending test was set to stop after the load dropped more than 40%, thus resulting in the widest part for each crack is ranging between 600 to 800 μm in all vascular systems before healing. Crack location was random in between loading spans as expected since four points bending method allows for uniform moment distribution between the two loading noses (Figure 4.20).

Crack patterns of vascular beams showed a gradual type of failure. This is because the holding wires will also act as a backbone to the cement beams as it tends to support the entire load of the cement and connect the crack surface so the beam does not

fracture into two sections. The shape of vascular structures did not affect the pattern significantly, and there was no specific pattern propagation trend in 1D/2D/3D beams. This indicated that the PLA prints and cement were well bonded offering light reinforcement that improves slightly the bending strength as discussed in the previous section, and they are not creating any preferential crack paths for cracking to happen. Moreover, the microstructure of 3D printed PLA in Figure 4.8 also revealed that the layer of 3D printed PLA tube have significant gaps where the print head finishes one layer and moves on to the next. These imperfections between layers act as a crack within the material and make it far more brittle than a solid PLA tube when cracks were initiated (Heywood, 2015).

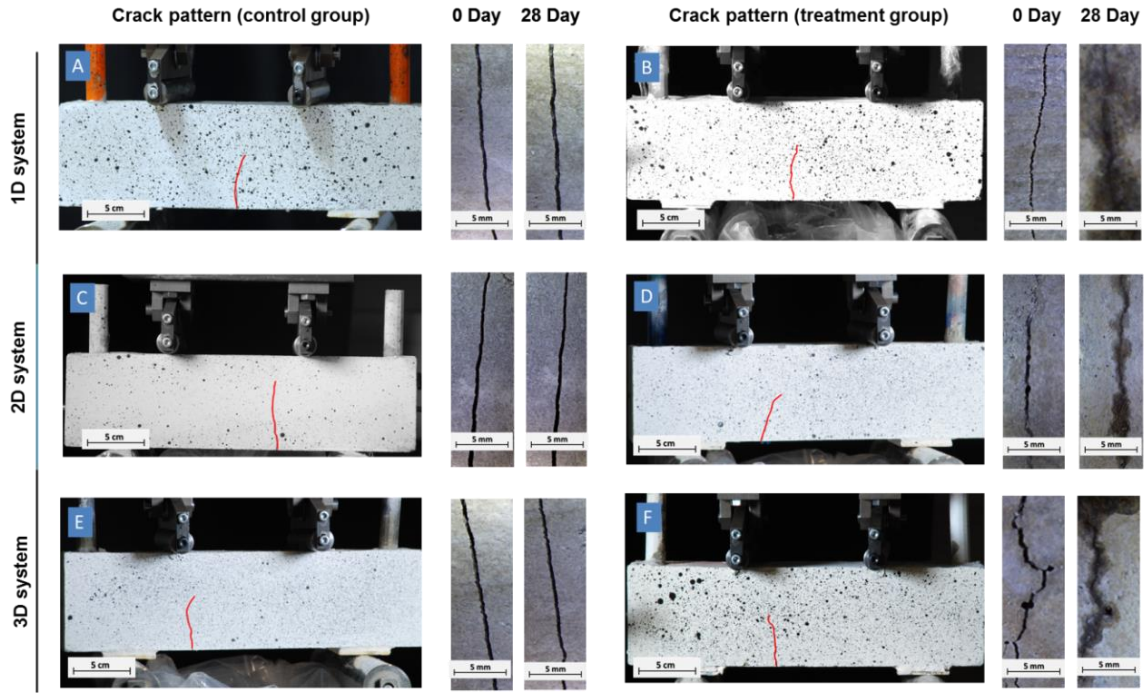

Figure 4.20, Photography of vascular beams crack pattern and microscope images of the main crack healing process in three different vascular systems after first Four-point bending test; controlled group (without healing agent) A, C and E; treatment group (with healing agent pumping) B, D and F.

After 28 days of pumping, sodium silicate was released from the tubes, a dark area around the cracks showed fresh healing agents were filled in cracks in all vascular systems. In most of the microscope images, solidified gels were then found both inside and around cracks systems after 28 days due to long term pumping (Figure 4.20). However, there was no significant crack closure observed in all controlled samples, which coincided with the low mechanical recovery result.

Crack widths at before and after 28 days healing were plotted in the diagram in Figure 4.21. In Figure 4.21 A, the yellow area illustrates the region covered by plotting the crack width after 28 days versus the original crack for the control samples (1D/2D/3D) without healing agents pumped in. This indicated that there was few crack closure observed after autogenous healing process exposed in the air. However, this case changed in the treatment group. The grey area in Figure 4.21 B illustrated for the 1D vascular-cement system. The upper boundary of the grey area correlates with unhealed cracks and indicates cracks with none and/or little crack width reduction in 28 days. At the same time, the lower boundary of the grey area indicates cracks with a significant reduction in width due to the deposition healing products. For the 1D vascular-cement system, the wide range of data indicating healed and unhealed cracks was attributed to a single-sourced distribution of the healing agent. Once the crack part near to tube area was healed, it stopped the healing agent distribution to the further crack surface. Alternatively, the 2D vascular-cement system, represented by the red area, shows a drop in the upper boundary, indicating the growing in healed cracks. The lack of variation from the 3D-vascular cement system collected is indicated by the narrow blue area, thus demonstrating that most of the crack widths were healed after 28 days. In this case, the vascular pumping systems have significantly improved the healing potential and could heal cracks with a width of around 700 μm.

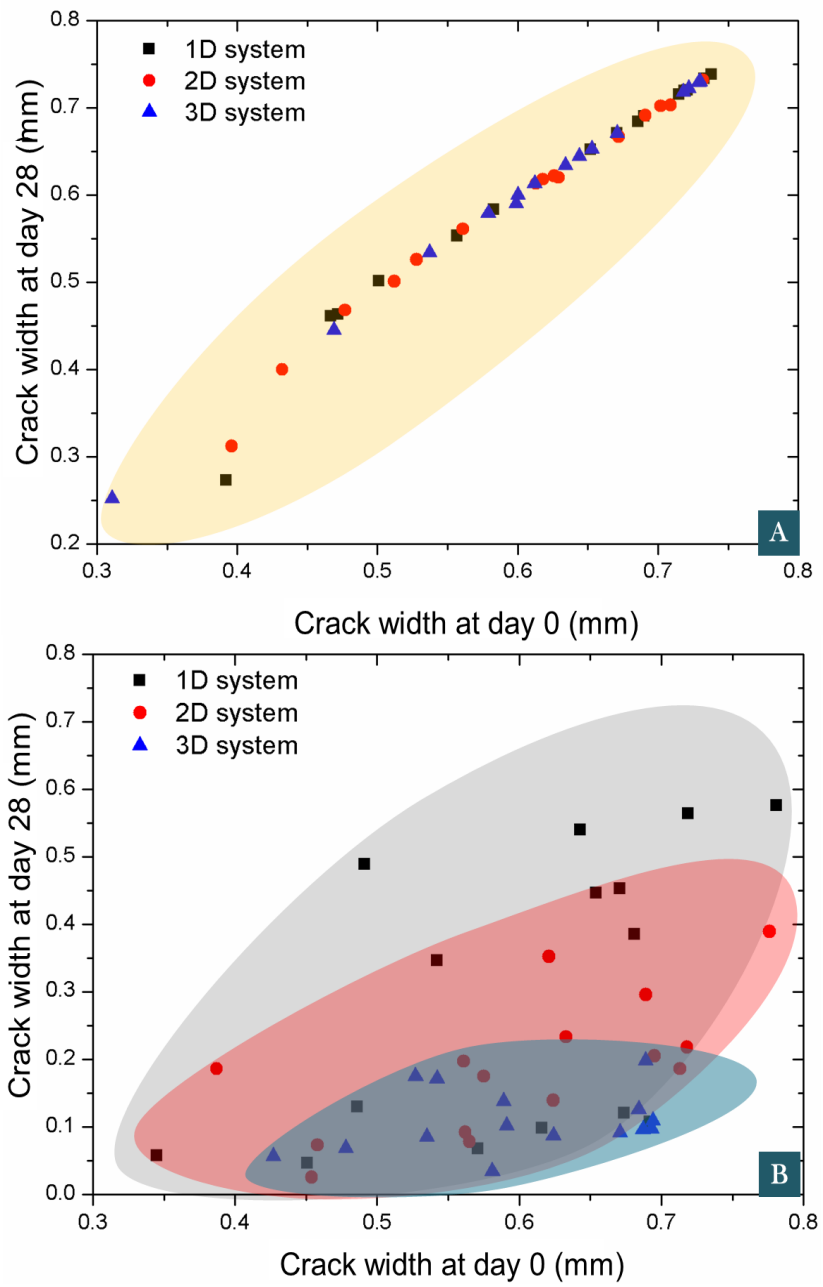

Figure 4.21, Crack closure diagram of 1D/2D/3D vascular systems control group (A) and treatment group (B) before and after 28 days of healing

The healing performance showed an increasing trend with the increasing dimensions of vascular designs. Quantitatively, crack closure rate from microscope images was evaluated by the percentage of healing area closure (CA, %) using following equation:

$$\mathrm{CA}(\%) = \frac{CA_0 - CA_t}{CA_0} \times 100\% \qquad (4.28)$$

Where CA_0 (mm^2) is the crack cross-section area after cracking and CA_t (mm^2) is the crack cross-section area after healing time *t*. The crack cross-section areas were calculated via Image J software. In Figure 4.22, it is clear that the closure percentages of 3D vascular specimens were up to 81%, followed by the figure of the 2D system, at around 69%. 1D system held the lowest closure percentage, at around 52%. As for 7 days, the figures were dropped, whilst the trend of CA% decreasing in higher dimensions systems remained. The little CA difference between 7 days and 28 days indicated the sealing process on the crack surface happened mostly in the first week, and this process cannot be significantly improved by extending pumping time, as the healed part of crack would block healing agent release from tubes.

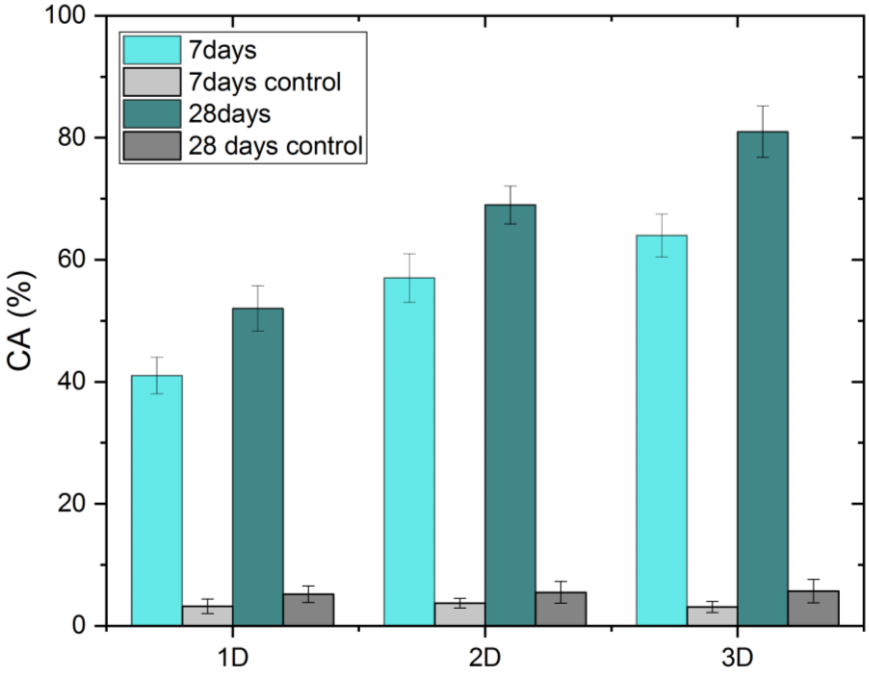

Figure 4.22, Crack healing CA(%) diagram of 1D/2D/3D vascular systems control group after 7 days and 28 days of healing

A previous investigation on 1D and 2D vascular-cement system reveal a ~45% of crack closure for 1D system and ~72% when more parallel tubes were added when a similar mineral healing agent was used (Heywood, 2015). This indicates the importance of multiple sources of healing agent delivered at the crack surface by the vascular network on enhancing the crack closure.

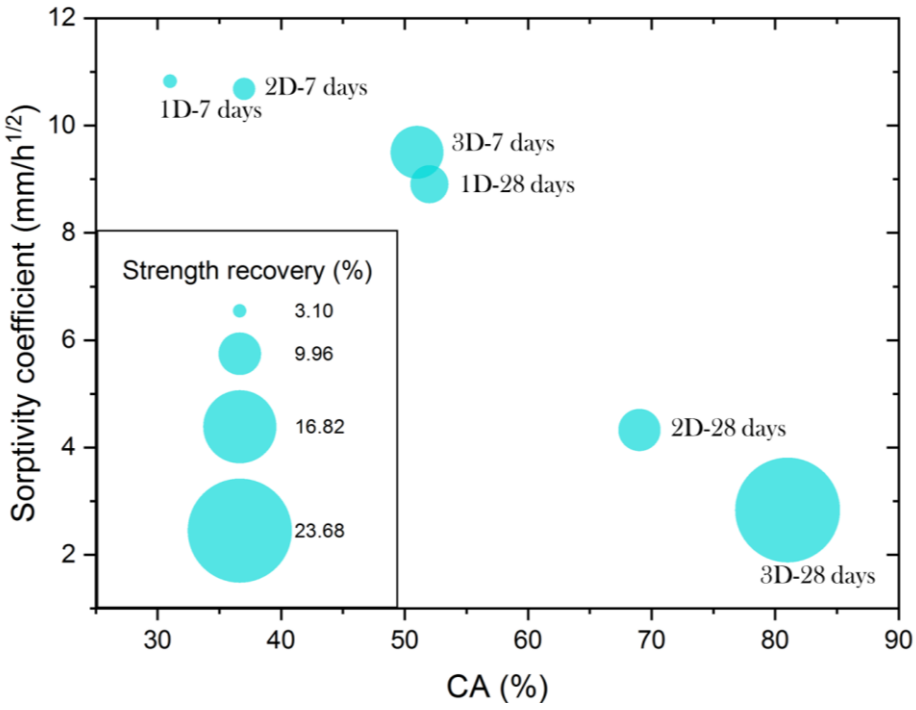

Figure 4.23, Sorptivity, CA and mechanical strength recovery with the 1D/2D/3D samples after 7 days and 28 days of healing

The correlation between overall self-healing parameters is shown in Figure 4.23. All three self-healing recovery parameters (CA %, Strength recovery % and sorptivity coefficient) were proportionate with the strength recovery results (bubble size) and plotted against the corresponding CA % and sorptivity coefficient.

A similar correlation can be seen between CA % and strength recovery in the samples from Figure 4.23. Both CA % and strength recovery show an increasing trend with the increase days of healing. Thus, the efficient crack sealing resulted not only in a higher load recovery and stiffness improving trend, but also showed improvement in durability parameters i.e. a decrease in the sorptivity coefficient.

However, the trends plotted in the diagram were not liner due to samples wide cracks wider cracking, indicating that the 1D/2D systems performed even worse in short term healing. Whilst 3D system was able to dramatically increased the mechanical performance, water permeability and CA %.

Therefore, based on different vascular systems functionality and the healing period, the desirable self-healing performance could be optimised based on daughter tube coverage design, sealing efficiency and strength improvement.

4.5.4 Mechanism of self-healing

SEM-EDX

Gel-like healing product was found in all three systems. The SEM characterisation of the healing products after the sodium silicate was delivered using a vascular network shows the presence of plate-shaped materials (Figure 4.24).

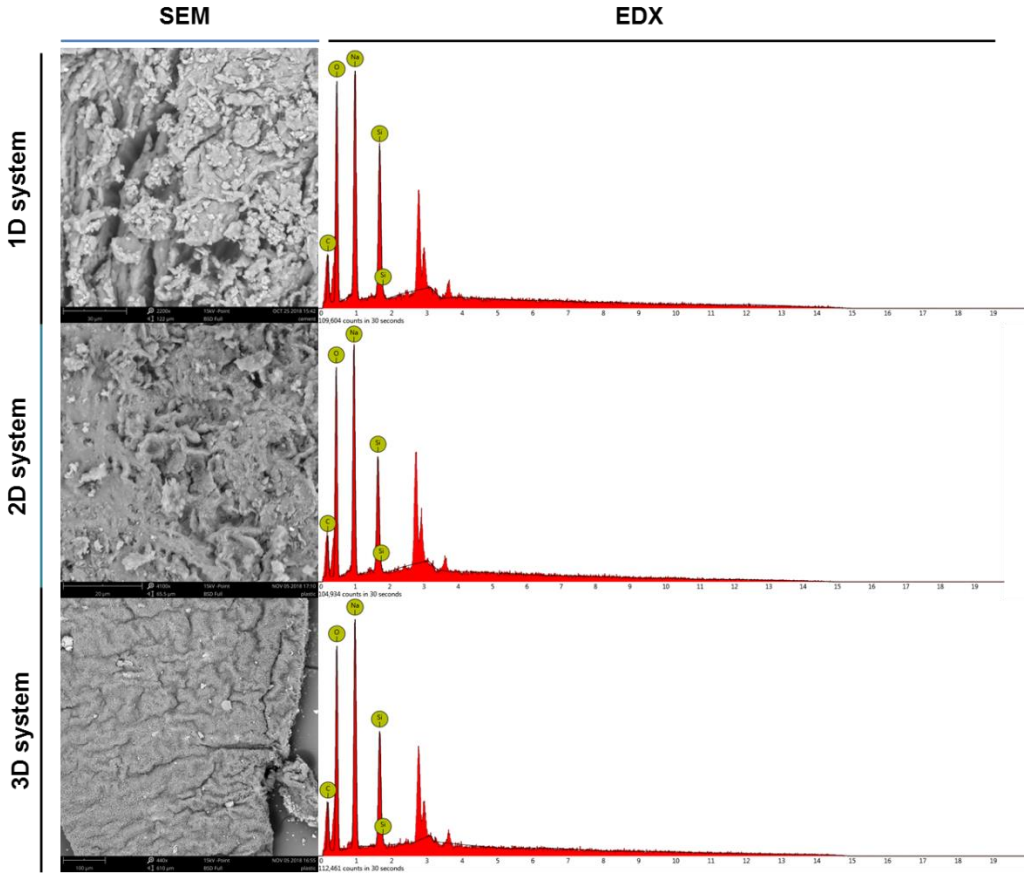

Figure 4.24, SEM/EDX morphology and elemental analysis of healing product extracted in cracks after 28 days of healing in 1D/2D/3D vascular systems

EDX analyses conducted on them revealed that chemical composition of the product consists mainly from O (44.87%), Na (41.72%), Si (10.42%) and C (3.00%) elements by weight. These elements were attributed to the reaction between Na_2SiO_3 and CO_2 (air) in presence of water vapour at temperatures at low temperature (<60 °C) (Rodríguez-Mosqueda and Pfeiffer, 2013):

$$Na_2SiO_3 + 2CO_{2(g)} + H_2O_{(v)} \rightarrow 2Na_2HCO_3 + SiO_2 \quad (4.29)$$

This explains the presence of Carbon in solidified gel materials. And the crystallinity of Na_2HCO_3 at 25 °C is also plate-shaped as shown in Figure 4.24. This healing material is

different compared to calcium-silicate-hydrate and calcium hydroxide reported by Giannaros et al. (2016) and Kanellopoulos et al. (2015). In this case, the pumping system for all vascular networks provided excessive sodium silicate. Most of which was exposed to air and reacted with CO_2 and water vapour, thereby forming the glue-like Na_2HCO_3 and silica mixed gel.

Computed tomography reconstruction (CT)

CT-scan was used to obtain a 3D maps of the internal infrastructure indicating the healing agent distribution and the relationship between vascular tubing designs and crack healing area. It revealed that in both 1D and 2D systems, only the cracking area below and around tubes were healed, as shown from the reconstructed cross section diagrams in Figure 4.25. The volume fractions of PLA presented were similar in all 1D, 2D and 3D systems (1D: 2.24%; 2D: 2.42%; 3D: 2.38%), which indicated that the increasing loading trend is mainly related with geometry shape rather than PLA volume fractions.

As for the 3D vascular specimen, crack successfully triggered 6 tubes (out of 8), which all released sodium silicate gels to the crack, covering most of the cracking area. On the top of Figure 4.25, the grey level images of specimens incorporating 1D/2D/3D vascular networks show the light grey parts represents the cement matrix, as cement had a relatively high density and elements atomic number, compared with the dark parts indicate PLA tubes, gel and cracks. Cracks and bubbles within cement were represented by black, indicating empty space. The grey level of the healed crack is similar to that of silica gel. PLA tubes had low density, and were presented as dark grey parts. Cement, gels, tubes and empty space were then separated by using Mimic software and reconstructed in a three dimensional images showed in the bottom of Figure 4.25.

The diffusion distance from the tubing to the cracks varied in different systems. The healing agent needed to travel 36 mm (maximum) to reach the cracking area in the 1D system, which significantly reduced the healing efficiency. In the 2D system, the maximum distance of the diffusion path reduced to around 28 mm, due to a larger tube coverage. This figure was again decreased to 21 mm in the 3D system, owing to its highly connected network and large tube coverage.

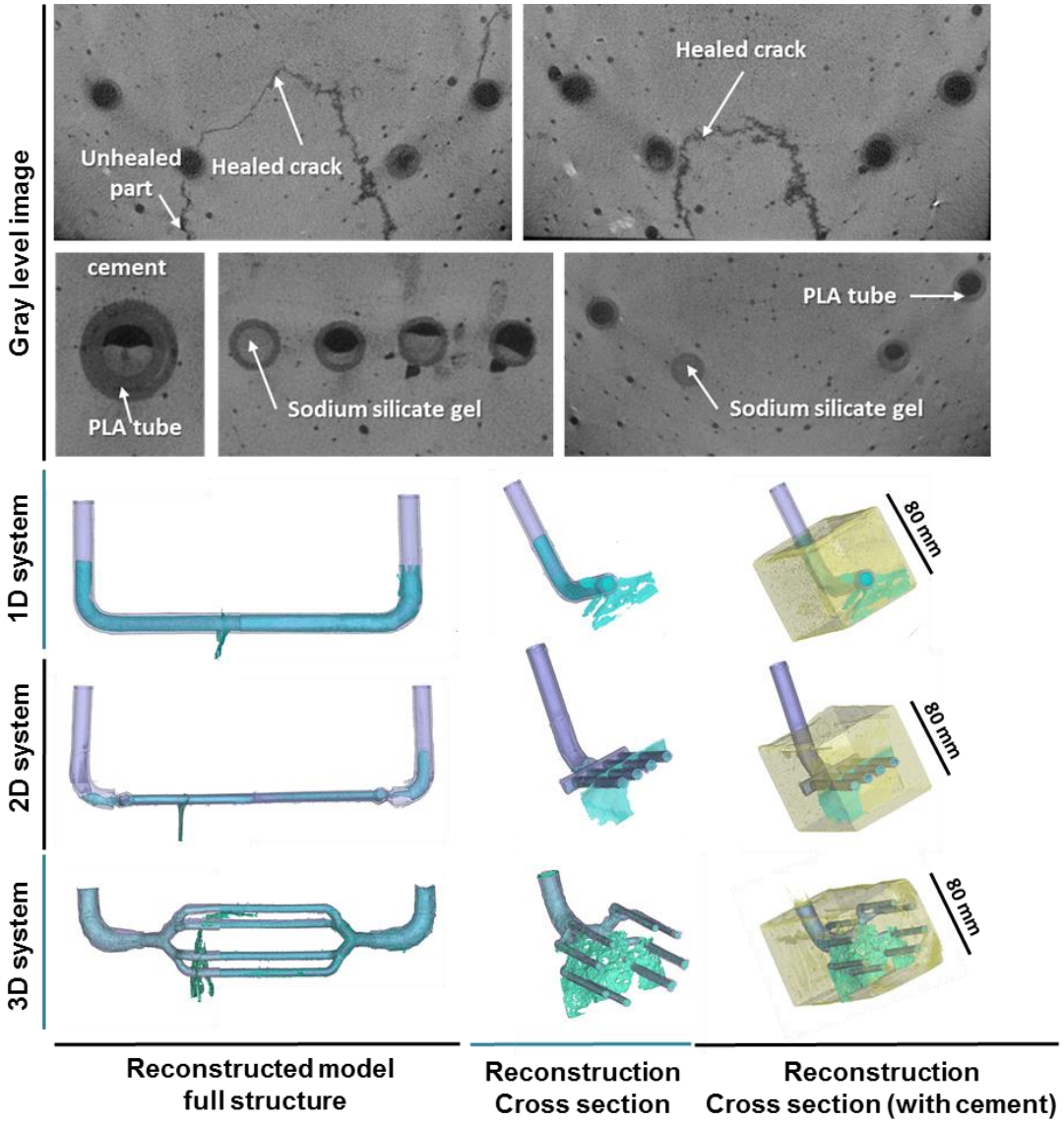

Figure 4.25, CT gray level image and reconstructed image of 1D/2D/3D vascular specimens, where the yellow coloured part represents cement beam; violet coloured part represents PLA vascular structure; blue coloured part represents sodium silicate gels; light blue (1D/2D) /green (3D) coloured part represents gels filled in crack

Here we adapted Shim et al (2018) the definition describing crack healing ratio (H_r), by comparing origin crack volume before healing percentage (V_{crack}, mm^3) with the percentage of gels healing volume (V_{gel}, mm^3) from CT reconstructed model as:

$$H_r = \frac{V_{gel}}{V_{crack}} \quad (4.30)$$

The healing ratio of 3D vascular specimens was around 72%, which is followed by 49% in the 2D system. The lowest healing ratio was observed in the 1D system, at around 36%. This shared a similar trend with crack closure percentage data, suggesting that 3D vascular

system had sufficiently covered the cracking area and had the best healing ratio compared with that in 1D and 2D systems. The increased crack healing ratio in the 3D vascular-cement systems contributed to the improvement in the load recovery of the specimens, where the 3D vascular beam reached 34% after healing and positively correlated with water tightness.

The delivery of healing agents to the crack using vascular network relies on a two-step process: first the sodium silicate was delivered into the crack surface, where the main distribution forces were the pumping and gravity. After the solidification of the sodium silicate, the healing products were deposited around the vascular tube, minimising the dripping of healing agent but also decreasing the spreading around the crack surface. As a result, only partial healing occurred within the crack, even after 28 days of pumping healing agent. The partial healing is most pronounced in the 1D- and 2D-vascular cement system, where the tubes were positioned below the central crack zone, resulting mostly in healing around the tube and at the crack mouth. In addition, at a crack width of 700-800 μm, the capillary force is not strong enough to drive the healing agent up and fill in the crack tip (Thao, 2011). As a result, both 1D and the 2D system failed to deliver healing agents in the crack tip area, as shown in Figure 4.25. Similar results were also found in Heywood (2015), reporting 38% and 60% of the crack area, was covered by 1D and 2D systems, respectively; and the crack tip zones were not covered by any healing agents. In contrast, the 3D-vascular cement system provides multiple sources of the healing agent to the crack surface, maximising the delivery of healing agent before the solidification of the sodium silicate heals the area around the tube.

Mechanism

The distribution of healing agent using the 1D, 2D and 3D-vascular cement system is schematically represented in Figure 4.26. For the 1D-vascular cement system, most of the crack mouth is filled in with healing agents since the capillary force is not strong enough to suck healing agent to fill the above space. This filled area is also limited by continuous healing agent supply, as the sealed crack mouth would block further agent supply. Thus, the healing area in 1D system is only located around the tube. A similar scenario is found in 2D system (Figure 4.26 B), healing area is also restricted around the crack mouth. While, parallel interconnected tubes enable larger tube coverage in the crack plate, providing alternative channels for healing agents to travel to the crack area, thereby enlarging healing area at crack mouth zone. In 3D system (Figure 4.26

C), a 3D vascular network is designed to provide more tube coverage at the crack plate compared with 1D and 2D structures.

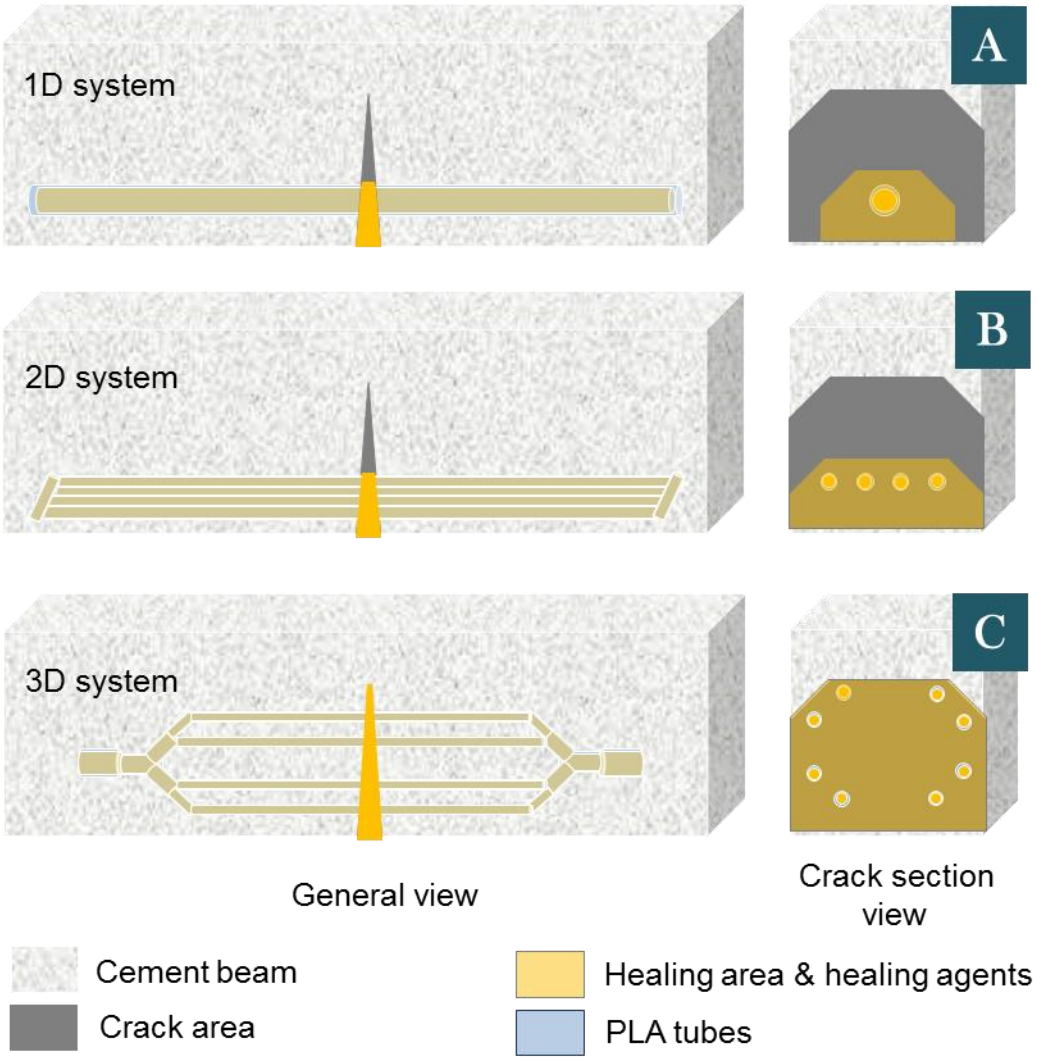

Figure 4.26, Healing regimes and applications in 1D (A), 2D (B) and 3D (C) systems

Single tube (1D) or paralleled tubes (2D) were restricted by their geometry shapes to increase their tube coverage at crack sections. As they cannot enlarge their volume indefinitely to increase tube coverage, as it weakens the cement matrix. To achieve large tube coverage area at a crack section, branching tubes should be assigned in three dimensions. Upper branching tubes above the tension zone perfectly solve the problem of insufficient capillary forces, ensuring healing agents filling in both crack mouth and tip zone. The 3D vascular network has a shorter diffusion path (from the PLA tubing to the cracks), by having a larger tube coverage in the cement matrix compared with the 1D and 2D systems. This significantly improved healing performance. Eight alternative channels secure continuous healing agent supply during

the period of healing. This 3D design resulted in a 72% of healing ratio compared with 36% and 49% in 1D and 2D systems. This suggested that partial healing could be drastically reduced by applying a 3D vascular structure, which contains more connected daughter tubes and enables large tube coverage. This is because an increase in the number of interconnected tubes could ensure healing agents supply since more alternative options are provided for agents to reach cracking area over time. Besides, larger tube coverage area in crack section solves the problem when capillary force is not strong enough to absorb healing agents to crack tip from tension zone.

4.6 Investigation on agent delivery supply

As discussed in the previous sections, the 3D biomimetic system showed great potential in boosting long term healing process and presented with relatively better healing in strength, stiffness recovery, water permeability and crack sealing abilities. The orientation of the network provided good exposure of the crack planes, but further validation on whether a continuous supply of healing agent will improve healing performance is still not clear. Therefore a further study of this 3D vascular system in the mortar matrix was followed, with the aim of further investigating the influence of supply of healing agent and understanding its feasibility in being utilised in real case scenarios.

4.6.1 Closed & Open mortar system in investigating agent supply strategy

Pumping (closed) system and non-pumping (open) systems were applied to investigate the healing efficiency of the amount of agent provided over time. For the closed system, it is connected with a healing agent reservoir, pump and connective tubes, building up a closed healing agent recycling pumping system. As for the open system, the healing agents were encapsulated once before cracking, with no additional healing agents pumped after the cracks initiated. Specimens were prepared for testing the survivability and compatibility of 3D printed vasculature within the mortar matrix. The networks were positioned at the middle of each prism between the reinforcement bars anchored at the top so that the delivery tubes of the network lay in the cover region below the reinforcement bars (15mm cover). Control specimens were also cast to be used without any healing agent to compare the crack healing efficiency and the compatibility of the network with the matrix. A detailed explanation can be found in Chapter 3.

4.6.2 Characterisation of 3D biomimetic structure in mortars after healing

Similar with the cement-vascular systems mentioned in section 4.4, mortar-vascular systems received strong adhesion between PLA tubes and mortar matrix.

Healing products between the PLA tubes and the surrounding matrix were found in all specimens after healing. The purple-blue coloured dye was added into sodium silicate to mark the position of the healing agents. This purple-blue coloured zone was not found in the fresh cast beams, meaning this penetration process required a relatively long time for the agent to travel.

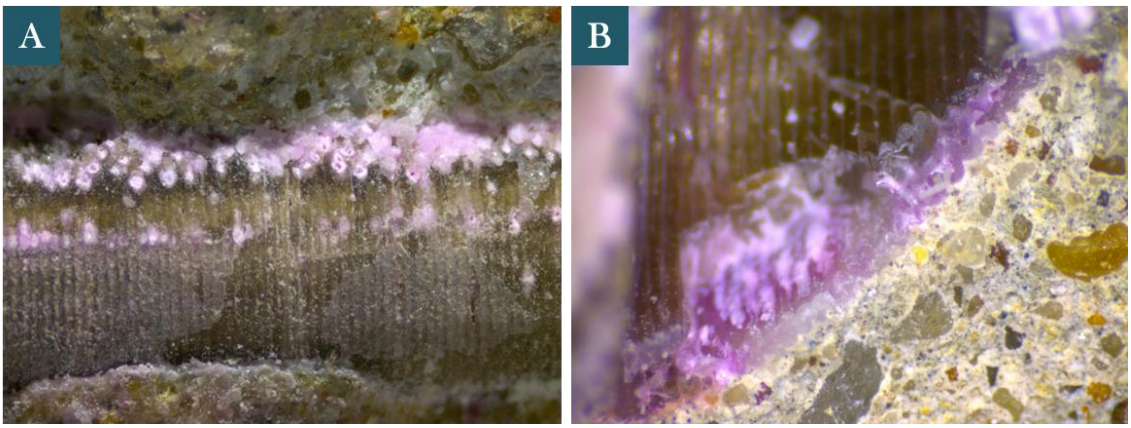

Figure 4.27, Photography of (A) secondary mineral layer between the tubes and the mortar matrix (A) and the inner look of the PLA tubes

As shown in Figure 4.27, healing agents formed a layer in between the PLA tubes and the matrix. This is because the tiny gaps between the printed patterns (also shown in section 4.4) would allow slow penetration from the tubes to the matrix. Specifically, the mortar mix contains various sized particles which accidentally created tiny cavities at the edge area while casting the vascular models. On the contract, cement paste is more uniformed and with fine particle size, which adapted well with the 3D printed vascular surface.

This penetration in mortar system did not travel far as the sodium silicate interacted with the matrix and formed a white coloured mineral layer in Figure 4.27A. This layer actually strengthened the bond between the tubes and matrix, as the bonding was formerly strengthened by the 3D printing pattern before agent introducing.

4.7 Agent supply & healing potential

4.7.1 Mechanical differences after healing

The cracking strength and stiffness recovery of prism samples were measured using a four-point bend test. The healing period affected the load recovery for the mortar specimens. Both encapsulated and pumping systems obtained a significant improvement in load response after 28 days of healing with the closed system achieving a 37% of load recovery compared to 16% for the open system. However, the healing potential is significantly reduced when a shorter healing period is adopted with closed/open specimens achieving a 17% and 5% of loading recovery, respectively. Control specimens were used to identify the autogenous healing contribution which was almost negligible.

Cracking strength and stiffness recovery after healing using Equation 3.1 and Equation 3.3 from Chapter 3 and are presented in Figure 4.28. Post healing strength in the controlled samples had minimal recovery after 28 days, whereas the closed systems and open systems were cracked at around 3 MPa and 2 MPa respectively.

The effect of continuous closed circulation of the healing is better seen in Figure 4.28. All the Closed network specimen held a relatively high strength recovery compared to Open network within the same healing period. Specimens that were pumped 7 days even had a better performance than the one being healed for 28 days without pumping. So, the amount of healing agent is highly influencing the healing efficiency confirming previous findings (Formia et al., 2015). Moreover, the results underline the importance of sodium silicate volume being available during a set healing period.

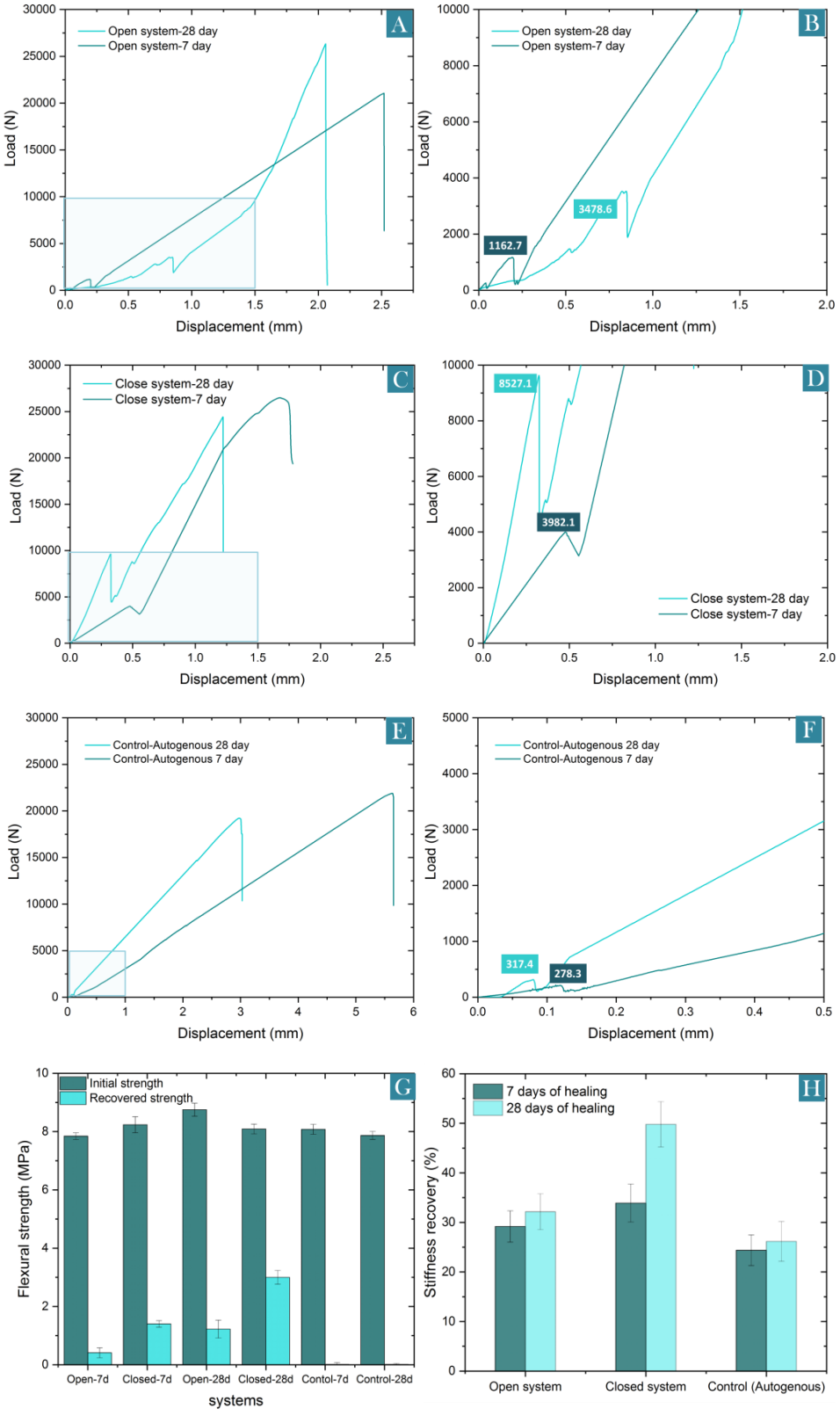

Figure 4.28, Typical Load-displacement curves under four-point bending testing of both closed (A, B(zoomed in from A)), open (C, D(zoomed in from C) system and controlled system (E, F(zoomed in from E)); flexural strength (G) and stiffness recovery (H) after 7 days and 28 days of healing

Healing products were expanding in the crack zone and mortar matrix through either a re-hydration process or forming a glue-liked bonding relationship between crack faces, which makes the samples stiffer over time. Hence, in most cases, the higher proportions of the healing products and longer healing period resulted in a better stiffness recovery. Relatively small flexural strength and stiffness recovery were expected in open systems compared with closed systems as sodium silica does not act as a glue bonding the two crack faces back together but reacts with calcium hydroxide at the crack faces to form C-S-H. This will be further discussed in the following section.

4.7.2 Assessment of transport property recovery (Sorptivity)

Figure 4.29 presents the water sorptivity results of the specimens before and after healing. The representative plots of cumulative water absorption over the testing time of the Closed and Open network specimen are given in Figure 4.29 B and D.

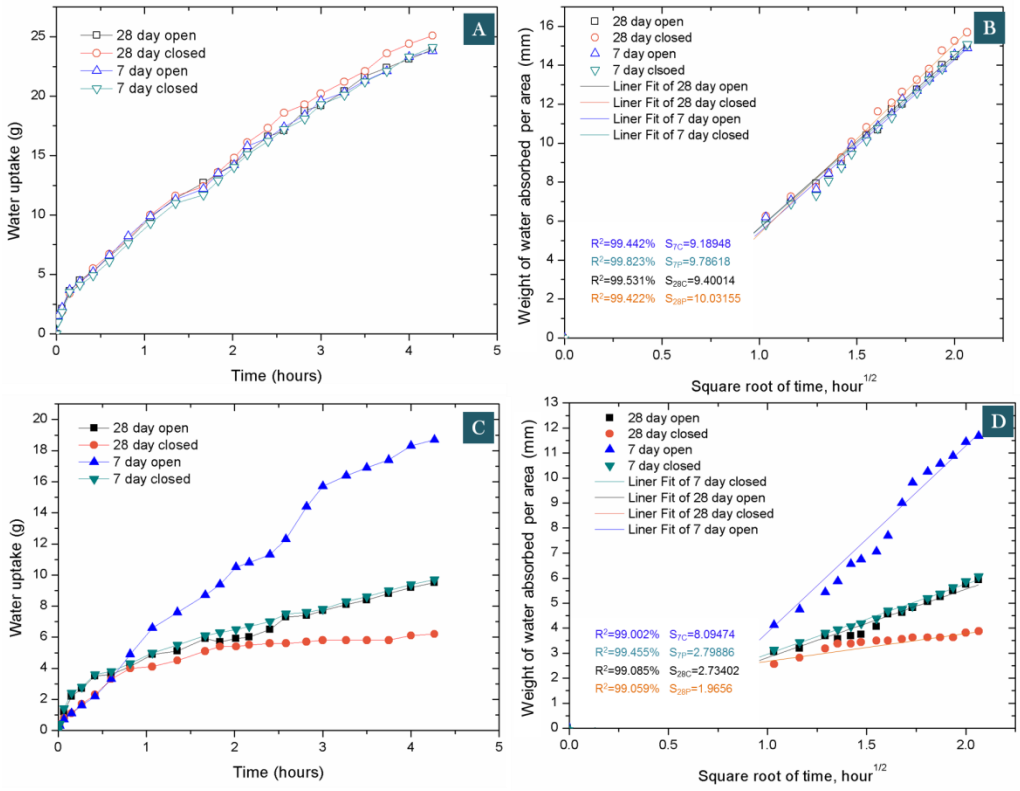

Figure 4.29, Water uptake process over time before healing (A) and after healing (C), water sorptivity of specimens over the square root of time before healing (B) and after healing (D)

The corresponding sorptivity coefficients are the slope of each linear fit line in Figure 4.29 A and C, which revealed that the water uptake by capillary absorption through the cracks was substantially reduced in the post-healing samples, compared with that before healing. This indicated a recovery in water tightness after healing.

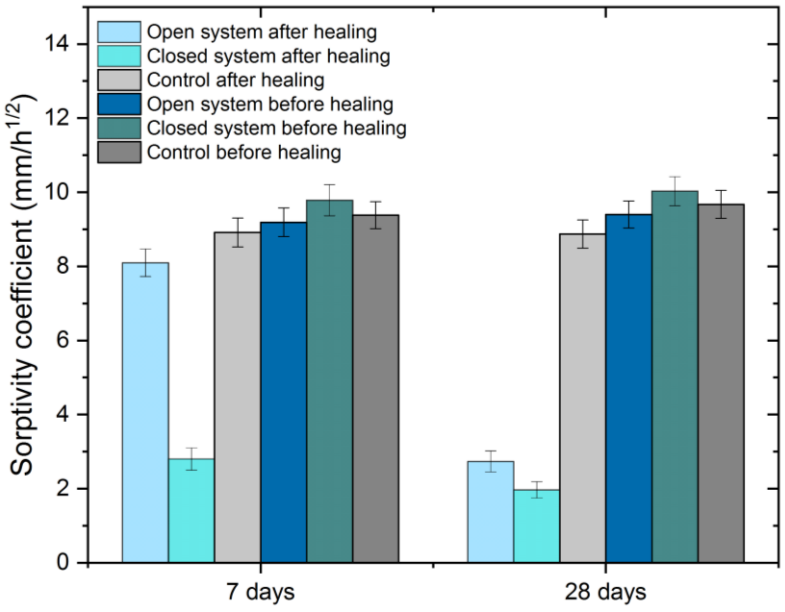

Figure 4.30, Sorptivity coefficient of the open/closed systems together with their controlled specimens

The largest reduction was observed in the samples healed with sodium silicate in closed system which showed a massive reduction in the sorptivity coefficient compared with the control cracked samples and a very similar response to the samples before healing (Figure 4.30). These results suggest that the healing products formed at the crack are not limited in close proximity to the crack opening but extend deeper in the crack forming a barrier that drastically decreases the absorption process. If the formed healing materials were located only close to the crack mouth area, it would have been easier for the water to penetrate and yield larger sorptivity values than the ones recorded. On the other hand, the water coefficient of the open system with 7 days of healing period showed a high sorptivity coefficient, which indicates a thin and permeable localised layer formed within the crack, allowing a relatively easier capillary absorption.

The sorptivity coefficient values of the closed network samples were consistently lower than the open network beams. This suggested that the water tightness was improved more in pumping systems after the same healing days. Interestingly, sorptivity coefficients of 28 days of the open networks and 7 days of the closed network specimen shared similar trend. It makes sense that the pumping system will provide better healing than the one-off system due to a larger available quantity of sodium silicate that has the potential to react and heal the cracks. This is the evidence linked with loading

recovery findings, which proved that the amount of sodium silicate had a more significant role than the length of healing time.

The results presented here suggest that the amount to healing agents introduced over time can be the largest factor to improve the water permeability of the mortar matrix. In addition, the results indicate that the healing products formed in the cracks of all the specimens play a significant role in the overall reduction of the sorptivity coefficient.

4.7.3 Crack width and closure

Crack closure was observed in all systems; whereas healing materials differed. Microscope images provided a general impression that gels were the dominant healing product that filled in cracks in closed networks (Figure 4.31 C and D). On the other hand, crystallised minerals were found in all the Open network specimen (Figure 4.31 A and B).

Crystals formed in the outer periphery of the cracks. Surface crack healing in both pumping and non-pumping caused the decrease of water passing through the cracks, as showed in the water sorptivity tests. The healing performance was improved significantly and positively linked with the increasing volume of sodium silicate. Initial crack mouth widths (between 500-700 μm) were gradually decreased over the healing period. It was also found that the longer the healing time frame the better the healing closure. Closed network systems were observed to have 83% and 47% Crack closures after 28 days and 7 days, respectively. As for the Open systems, the crack closure percentages were relatively lower, at around 71% and 34% after healing 28 days and 7 days.

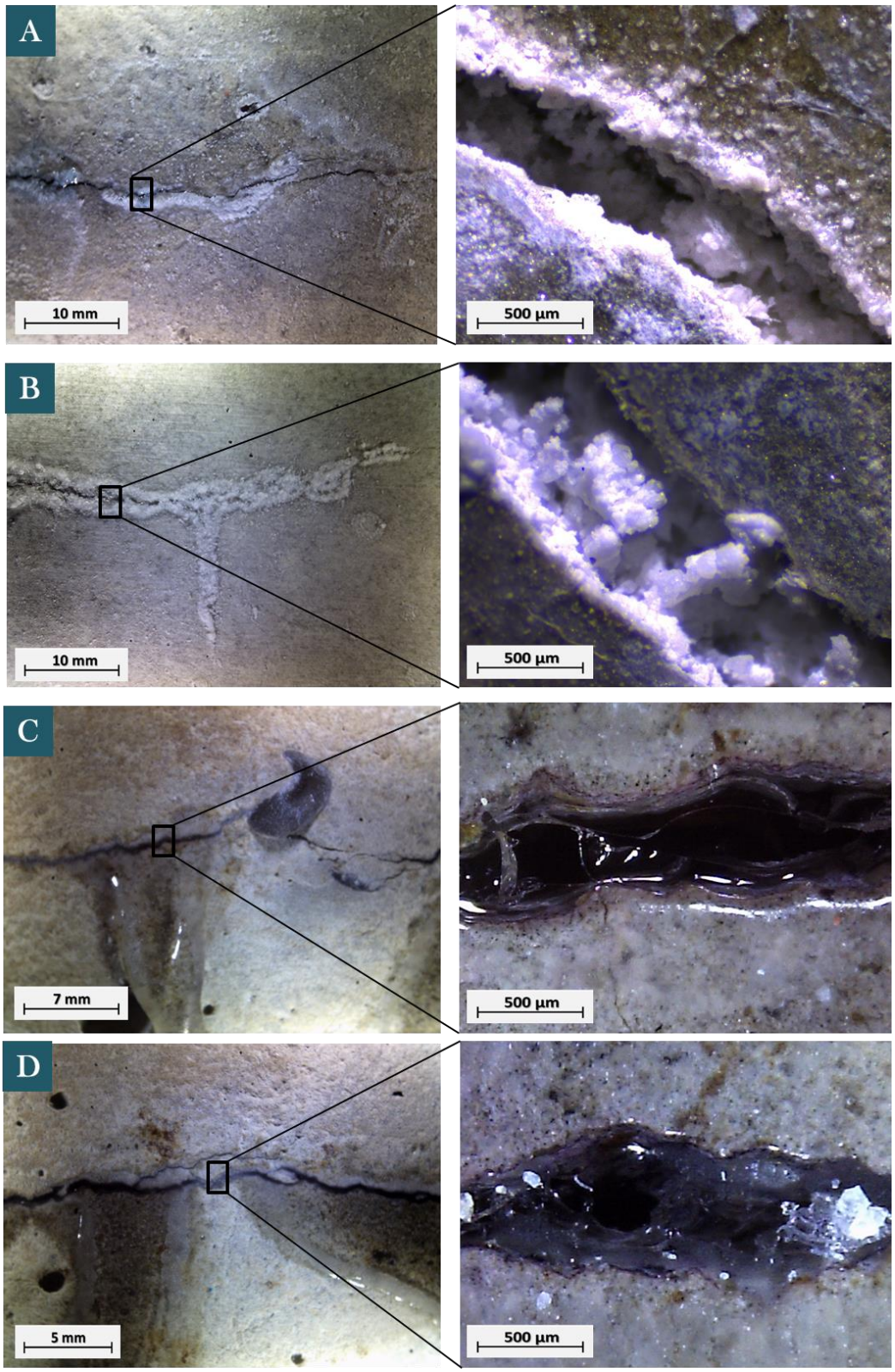

Figure 4.31, Morphology of crack healing in different systems. Open network specimen after (A) 7 days and (B) 28 days of healing; Closed network specimen after (C) 7 days; and (D) 28 days of healing.

Additionally, the results from the microscope images also supported that it is plausible that the healing products observed on the crack walls has acted as an additional barrier on the water diffusion in the material.

4.7.4 Healing mechanism under different agent supply system

XRD

Healing products from both systems were extracted and their microstructure characterised using XRD and analysed via Jade® software. Both initial curves and confirmed materials PDF patterns were presented in Figure 4.32. PDF patterns of the materials were automatically identified from Jade® according to the initial curves with the background line removed.

Mineral interaction influence on the open system healing products was found as the strongest intensity for the major calcite ($CaCO_3$) peaks at 23.1°, 29.5°, and 35.6°, and C-S-H (sodium carbonate hydrate) peaks at 29.6°, 33.5° and 47.7°. The domination of calcite was related to the exposure of the specimens during the healing process to the atmospheric condition accelerated the carbonation rate (Huang et al., 2014), which coincides with Tittelboom et al. (2012) preliminary findings on calcite healing compounds.

Weaker peaks for different phases of calcium silicate ($CaSiO_3$), calcium hydroxide ($Ca(OH)_2$), minimal sodium hydrogen hydrate ($NaHCO_3 \cdot H_2O$) and silica (SiO_2) were also detected from the curves. Normally, calcite and silica along with cement rehydrated products such as portlandite ($Ca(OH)_2$), calcium with silicon and sulphate phases (C-S-H and Ettringite) peaks were detected in the XRD with different intensities (Qureshi, 2016).

The XRD peaks from the pattern clearly indicate the presence of C-S-H and calcite in all open network systems and the intensity of diffraction peak increases as C-S-H and calcite increased over healing time. It is clear that the addition of sodium silicate led to production of C-S-H over time. These observations are consistent with findings from Irico et al. (2017) where the authors reported a widening of the tobermorite region at around 30° when adding sodium silicate. However, these C-S-H were barely found from all the closed systems, which indicated a completely different healing mechanism happened in the pumping process.

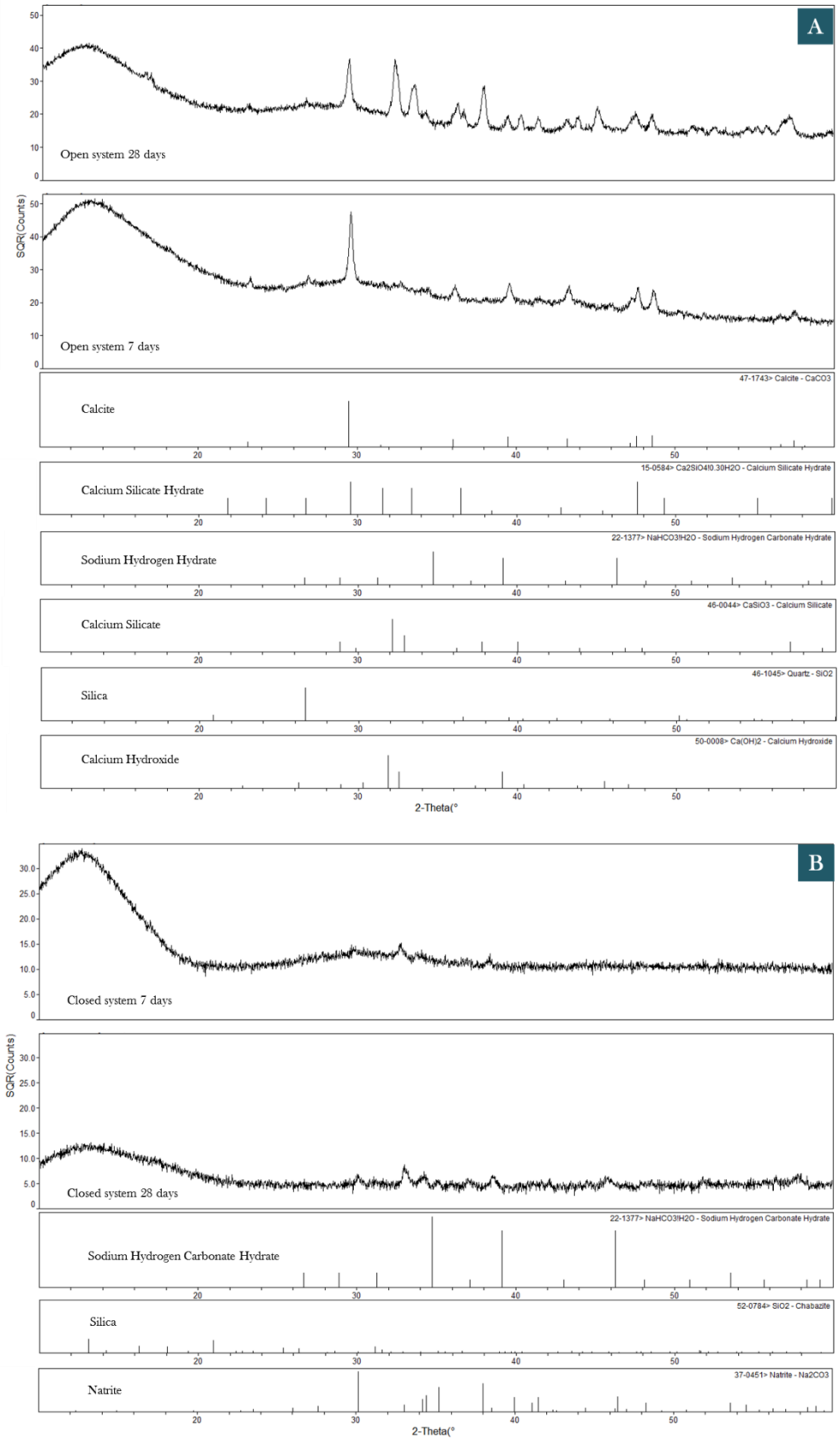

Figure 4.32, XRD diagrams of the infill gels in Open systems for 7 days and 28 days (A), infill materials in Closed systems for 7 days and 28 days (B).

Conversely, in closed systems, reacted gel (35.2° and 38.7°, $NaHCO_3$) was expected as the dominant product as discussed in section 4.5.4. The low intensity of these peaks could be attributed to the low crystallinity (gel-like) nature of the formed product.

Sodium silicate is a colloidal Newtonian liquid until the viscosity rises during the healing process, due to neutralisation of the SiO_2-Na_2O bond and reaction with CO_2 in the air. SiO_2 tend to precipitate by polymerisation in form of silici acid (H_2SiO_4) (Garba, 2012). This is due to its ability to form a cohesive substance consisting of countless individual colloidal particles. Sodium silicates here in the closed system act as binders considering its ability to form silica based gel and crystalline compounds that form a new hardened material (Tognonvi et al., 2010).

The Si-O-Si bonds within silica and silici acid are far stronger bonds, which gives rigidity to the bonded material (Greenberg & Sinclair, 1955). This was also correlated with the findings in stiffness recovery and strength recovery in mechanical tests, where the closed system with silica gel products received a much higher recovery compare with the open systems.

TGA

Composition of healing products in both systems was further confirmed by TGA diagrams (Figure 4.33 A and B). This showed major weight loss in 7 days for the Open network specimen at around 120 °C and in the temperature range of 640-670 °C. These can be attributed to (C–S–H) the decomposition of calcite respectively (Bazaldúa-Medellín et al., 2015). A similar trend can be seen after 28 days of healing.

As for the closed network system, crystallised minerals were barely found whilst primary weight loss can be seen around 150 °C. This was attributed to the decomposition of sodium carbonate hydrate and sodium silicate (Nurudeen et al., 2014). Overlapping peaks of sodium carbonate hydrate and sodium silicate have resulted in more intense peaks as shown in that region TGA (Figure 4.33 C and D). This further confirms the initial assessment through XRD and visual observations.

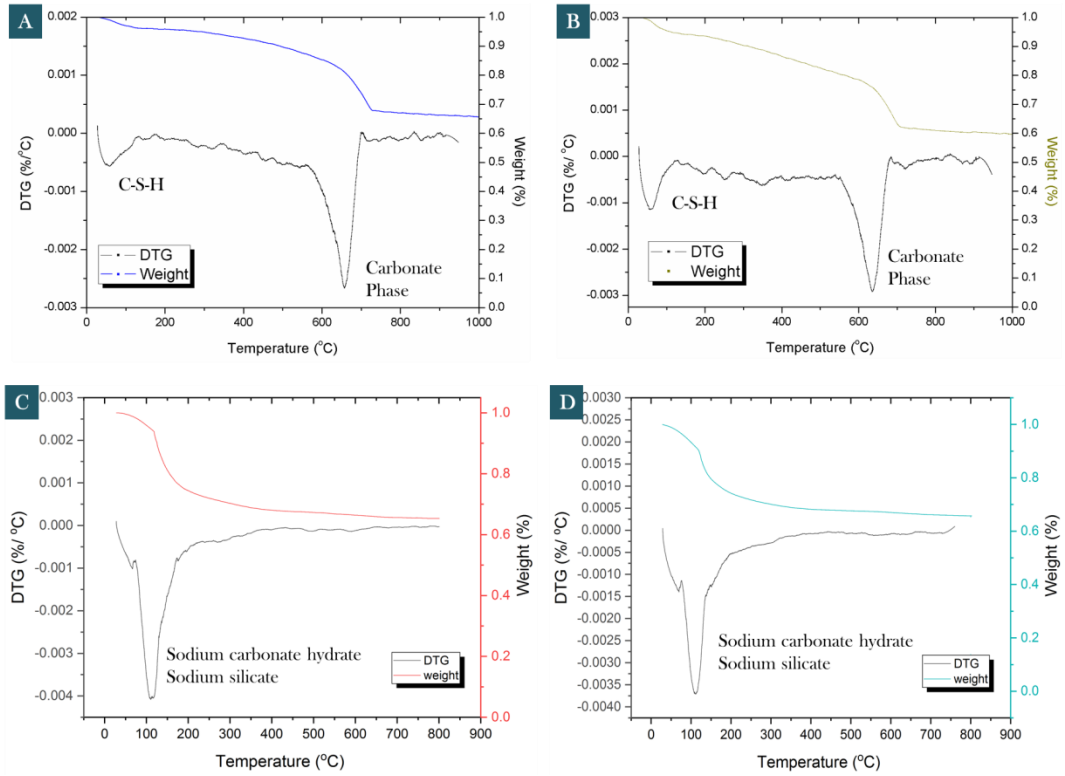

Figure 4.33, TGA diagrams of the infill materials in Open systems (A) for 7 days and (B) 28 days; infill gels in Closed systems (C) for 7 days and (D) 28 days (Note that the closed system had a TGA temperature up to 800 C, due to its polymerised texture and the potential effects to the crucibles).

SEM-EDX

SEM/EDX was also applied to further confirm products from cracks. The ternary diagram (Figure 4.34) suggested that one-off sodium silicate application increased the calcium based product formation, namely calcite and calcium carbonate hydrate. The existence of calcite and calcium carbonate hydrate was confirmed by crystallinity and morphology in SEM.

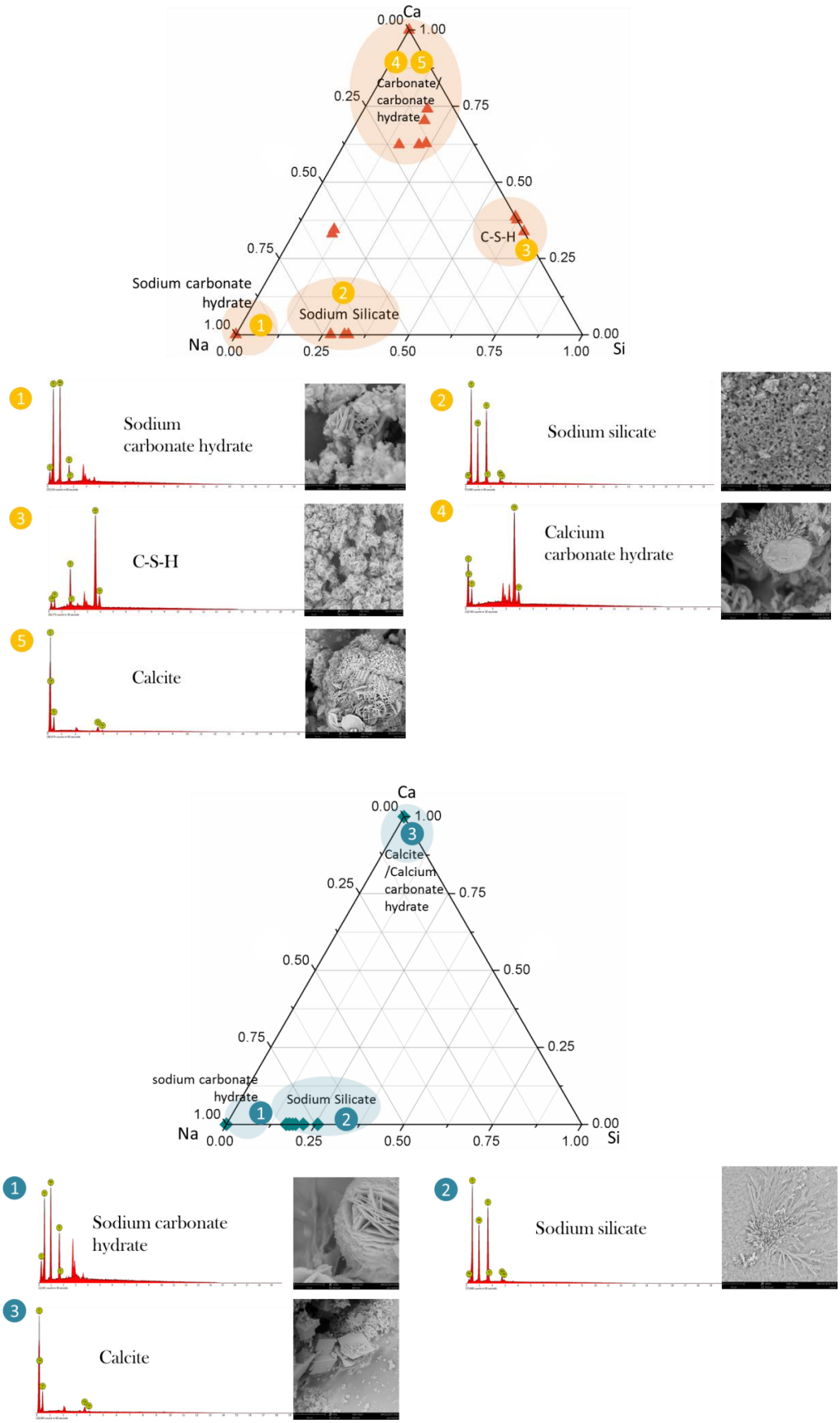

Figure 4.34, Atomic mass percentage correlations of healing materials in open (red) and closed (blue) systems in ternary Ca-Na-Si diagrams

As calcite precipitated and appeared in a layered and rhombohedral shape in room temperature (Al-Omari et al., 2016). C-S-H was confirmed by both TGA and SEM/EDX. Sodium silicate, and sodium carbonate hydrate were also found according to SEM/EDX. As Ca^{2+} had more actively participated in the secondary hydration of the cement for self-healing (Qureshi and Al-Tabbaa, 2015), it is observed that several calcium based minerals were generated from Figure 4.32.

In Closed systems, however, infill products were dominated by sodium carbonate hydrate and sodium silicate gel, while minor calcite formation was also observed (Figure 4.34). This indicated that sodium silicate in continuous pumping systems reacted with open air and formed silica-sodium carbonate hydrate gels in the cracking area.

CT

Microstructural observations confirmed mechanical and durability indicators recovery identifying the closed network system as the optimum circulation condition. In this case, computed tomography was introduced to reveal how the healing agent was being delivered to target cracking area and visualise the healing products in a closed system. The crack volume reduction was calculated similarly to Shim et al. By comparing the original crack volume before healing with the volume occupied by gels in the crack from analysing the CT reconstructed model it was shown that after 28 days of pumping, 87% of the crack volume was healed by solidified sodium silicate. High healing product volume calculated here coincides with high load recovery and low water sorption in the closed network systems.

Figure 4.35 shows X-ray CT reconstructed images of specimens incorporating vascular network after 28 days of the pumping process. As expected, that most of the daughter tubes (6 out of 8) were triggered upon crack initiation, with healing agents flowing through. The lower part of the crack was healed first in this sample. This is attributed to a pressure drop in the system due to the crack opening rendering a preferential path for the viscous liquid through the lower tubes initially. Healing agents continued to be pumped to higher tubes when the lower part of crack was healed and the lower tubes were blocked for further agent release. This can be observed and proved by the minor

liquid remaining in higher tubes after healing.

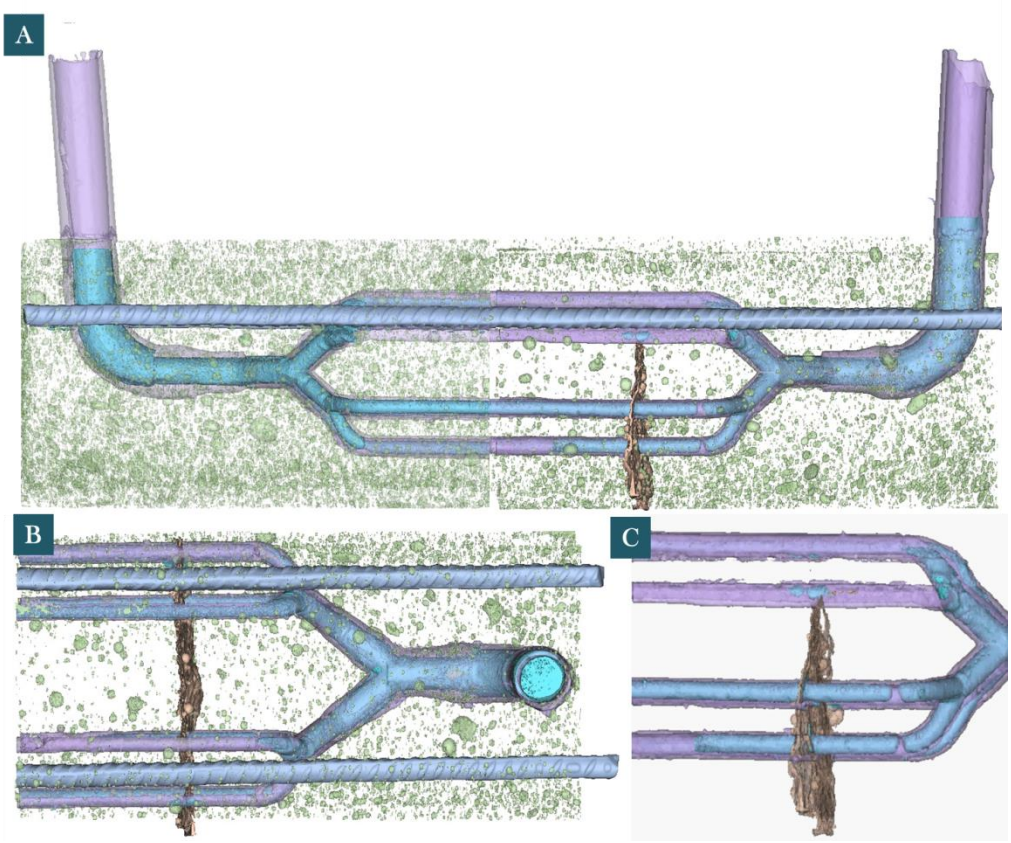

Figure 4.35, A computed tomography diagram of the Closed network system after 28 days (A), top view of the healed side beam (B) and (C) a closed view of healed crack, where the green coloured part represents mortar; purple coloured part represents steel rebar holders; violet coloured part represents PLA vascular structure; blue coloured part represents sodium silicate gels; yellow coloured part represents gels filled in crack

Mechanism

The mechanisms can be described from a conceptual schematic of the processes taking place in both Closed and Open systems from Figure 4.36. In the former system, healing products were dominated by gels, which were sodium carbonate hydrate and unreacted sodium silicate. This is because healing agent sodium silicate was excessive over time, causing the insufficient reaction between sodium silicate and calcium cations at crack areas, thereby resulting to most of the sodium silicate primarily reacting with air (CO_2) and solidifying as gels. Only some sodium silicate closer to crack face reacted with Ca^{2+}. On the other hand, the limited amount of sodium silicate in the Open systems, allowed the reaction with surrounding cations and air (CO_2) contributing to further hydration processes, resulting in calcium-based healing products such as C-S-H, Calcite, and other related carbonates. Nevertheless in Closed systems, healing products acted as glues,

forming stronger bonds with mortar, showing improved load recovery and low water transportation.

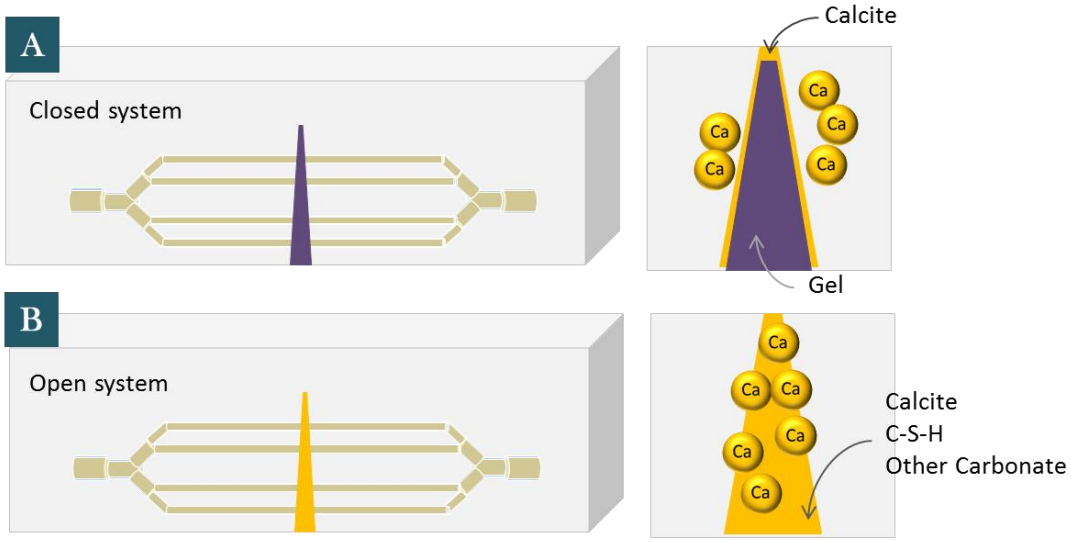

Figure 4.36, Healing mechanisms of both Closed (A) and Open network systems (B)

4.8 Concluding remarks

State of the art findings identified the use of biomimetic vascular networks as a powerful source of innovation that would help us go beyond conventional approaches to achieve resilient cementitious structures.

Herein, vascular networks were designed and manufactured by 3D printing and embedded into specimens to assess their healing potential (Figure 4.37).

In the first part of this chapter, the biological concept—Murray's Law, was used to develop an interconnected structure for delivering healing agents in the cementitious material. For the first time, a 3D-vascular network based on a biomimetic design that follows Murray's Law was developed, 3D-printed and compared with corresponding 1D and 2D networks for use in the self-healing of cementitious materials. Murray's law was obeyed during the design of the 3D-vascular network, aiming at minimising turbulent flow at junctions while also broadening the distribution of healing agents. The biomimetic three-dimensional design was then 3D-printed using polylactic acid (PLA) for the production of the vascular network. PLA structures presented brittle fractural response and suitable interfacial bond for mechanically triggered use in self-healing.

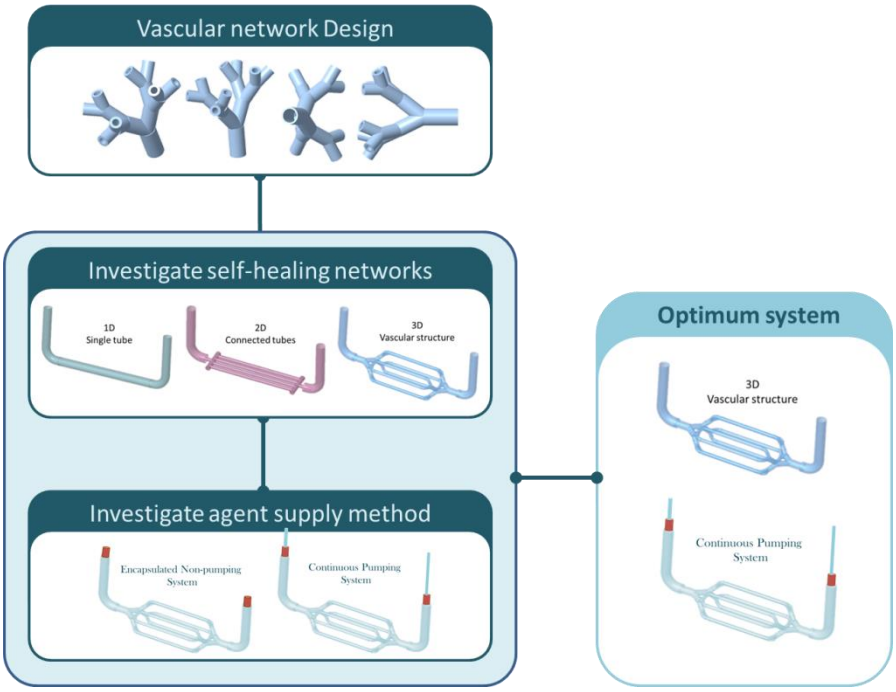

Figure 4.37, Schematic diagram of the investigation process in identifying the optimum self-healing vascular system

Then, 1D and 2D structure were introduced to investigate whether geometry and orientation of vascular structure would affect healing performance under a continuous agent pumping scenario. Notably, the increased load applied to crack the samples embedded with 1D, 2D and 3D vascular network indicated that the plastic tube acted as a reinforcement of the cement beams. All the 1D/2D/3D vascular network were effective in delivering healing agent (sodium silicate). Initial cracks (between 600 to 800 μm) from all systems were observed to be healed over 28 days. A recovery in mechanical properties of ~20% for 1D and 2D-structures and 34% for 3D vascular network specimens were attributed to self-healing. Additionally, sorptivity tests were performed to evaluate the recovery in water tightness. The inclusion of 1D, 2D and 3D vascular network led to around 25, 69 and 77% reduction of the sorptivity index values in comparison with the values of the cracked control specimens. The crack mouth opening was non-uniformly closed in the 1D vascular-cement system, resulting in healed and unhealed cracks. Alternatively, an increased number of healed cracks were observed in the 2D vascular-cement system and virtually all the crack mouth opening was reduced in the 3D vascular-cement system. The crack closure efficiency was 52, 69 and 81% for the 1D, 2D and 3D vascular networks specimens, respectively. The circular pumping of sodium silicate for 28 days provided excessive sodium silicate in the three networks. Through SEM-EDX, Na_2HCO_3 and silica mixed gel were proposed as healing products as the sodium silicate

was exposed to air and reacted with CO_2 and water vapour. The volume of healed crack was investigated using CT-scan and calculated as 36%, 49% and 72% for the 1D, 2D and 3D vascular networks specimens, respectively. In this case, partial healing could be drastically reduced by applying a 3D vascular structure, which contains more connected daughter tubes and enables large tube coverage. The systematic improvement in the healing performance of the 3D vascular networks specimens was attributed to the design obeying Murray's law and therefore broadening the coverage of healing agent distribution while reducing the energy required for pumping.

After the optimum vascular structure was identified, the third part of this chapter was to evaluate the agent supply method and the healing potential under different agent providing systems. Rather than cement paste, mortar matrix was introduced in this part of experiments, with the aim of further investigating the influence of supply of healing agent and understanding its feasibility in being utilised in real case scenarios.

Different healing agent delivery approaches were considered; an Open and a Closed network system. In the former continuous circulation of the healing agent was achieved through pumping while in the latter a fixed amount of healing agent was enclosed while the system remained open to the environment. These achieved healing through different healing mechanisms. The former was found to react with calcium hydroxide leaching from the matrix to generate C-S-H and hydration products to fill in cracks. However, the later reacted with open air to form silica-based gels in the cracking area. This approach, of pumping a large volume of sodium silicate was identified as the ideal choice to improve the self-healing of a cementitious matrix as it was able to not only react with the calcium hydroxide in the cementitious matrix but the gelled excess healing agent acted like glue, allowing better loading recovery and water sorptivity ability than encapsulating limited amount of sodium silicate. These results confirm not only the great potential of the vascular network but also of a mineral-based healing agent to deliver consistent healing offering a pragmatic solution to the demands for prolonged and long-term damage management.

In conclusion, the healing mechanism can differ not only because of the orientation of the tubes but also conditions of supply. Biomimetic 3D structures contain more connected daughter tubes and enable large tube coverage, which is able to avoid partial healing. Gel-like healing product from the continuous agent supply system drastically improved healing performance. Applying both 3D biomimetic vascular structures and

with a continuous healing agent providing method was demonstrated as the optimum system in promoting healing potential and bringing great potential in long term damage management. According to the results we collected, ideal healing agents for this type of vascular system have to fulfil a few requirements: (i) with no chemical reaction with PLA structure; (ii) able to flow within the system; (iii) able to remain stable within the reservoir for a long duration. In this case, silica-based agents are more ideal for this system for future research. However, if the polymer-based agents (i.e. epoxy, PMMA etc.) has its functional removing/washing solutions, it is also can be considered to use for this long-term process. Compatibility between healing system and the cementitious materials has been always a challenge in most of the capsule based self-healing systems. However, by using 3D printing technique, this could be fundamentally solved due the unique 3D printing pattern (acting as an anchor), and the large surface area attached to the cementitious materials. For future designs, the surface of the vascular network could be designed to be rough, and also the shape of the vascular could be more interconnected.

Chapter 5

Feasibility of creating PVA (Poly-vinyl alcohol) channels

This chapter mainly discusses the feasibility of using PVA (Poly-vinyl alcohol) as a sacrificial material to create hollow channels within cementitious materials. This is because a hollow vascular channel for self-healing system could avoid long term tube monitoring and enables multi-scale healing over time. Complex channel structures could be design and printed using PVA, which will be dissolved to create hollow channels within the cement matrix. To validate its workability, the printability of PVA was firstly investigated. Then, a few interconnected vascular channel models were designed coordinating with PVA printing behaviour. A double twisted channel design was selected due to its stablility during the 3D printing process and its potential to be used to deliver two-part healing agents. The following section discusses the dissolution behaviour and duration of 3D printed PVA structures in water. The survival behaviour of the 3D-printed structures during the curing of cement paste at different water content was investigated via computed-tomography (Micro-CT). Then, PVA removal tests were conducted under different water-bath temperatures. The research focuses on the potential of PVA to be used as a sacrificial material to create hollow tunnels in the cementitious material to promote self-healing. Results presented in this chapter have been published in Materials (Li et al., 2019).

5.1 PVA channels design and properties

There are two main ways of creating vascular structures in cementitious materials: remaining glass/plastic tubes in-situ and removing the none-cementitious tubes after

pastes are cured. The first method, which is the most commonly used, has been discussed in Chapter 4. For the second method, it avoids long term tube monitoring and enables multi-scale healing over time. Studies (Davies et al., 2015) currently apply polyurethane (PU) tubes and pull them out after cementitious pastes are cured as PU tubes will shrink after heating. This removable 2D PU structure provided a way of maintaining multi-use networks that can be re-used over the lifetime of a cementitious structure to enhance and enable multi-scale healing. However, this is only for 1 and 2 dimensional (1&2D) vascular structures. On the other hand, three dimensional (3D) networks are more complicated and consist of interconnected structures, which are capable of transporting healing agent to the damaged areas across the specimen's volume.

However, it is also hard for 3D vascular structures to monitor glass/plastic tubes after several healing cycles. To overcome this limit, a three-dimensional hollow internal tunnel structure is therefore requested to be created. Removable PU tubes can only be used in simple structures like single channels or 2D grid structures. This is because they cannot be bent to a high curvature to create complex or biomimetic structures. Besides, such complicated structures would make it even harder for pulling PU tubes out after pastes are cured. These problems can be solved by using sacrificial materials combing 3D printing technique. Developers could fully control the model designs in fulfilling certain required tubing size or coverage area in the matrix. In this case, desirable sacrificial materials that (i) could be printed in a solid model, (ii) able to hold the designed shape during the concrete curing process, and finally (iii) could be dissolved via solvent are very much preferred.

Herein, polyvinyl alcohol (PVA) was chosen as a sacrificial material to create 3D internal tunnels in cementitious system. The advantages of such an approach are: (i) it uses commercial 3D printing material and can be print complex 3D structures; (ii) PVA is water soluble and therefore could be easily removed from prisms using water.

5.1.1 Printability of PVA

PLA has been widely used in industry, its lower printing temperature is easier to print with and therefore better suited for parts with fine details and flexible in sizes. Unlike PLA, PVA was a new commercial printing material being introduced to 3D printing. It was invented as supporting materials for the main 3D prints (usually being printed by PLA, ABS etc.) that can be further dissolved by water, saving time and commitments in

removing the supporting materials manually. This water soluble property makes PVA a potential candidate as a sacrificial material to be used in creating hollow channels in cementitious materials.

The quality of PVA supports in the 3D printing was not usually set as a priority, since the PVA supports will be dissolved eventually. Previously, PVA was used as supporting material in some PLA vascular models during 3D printing process. The PVA supporting structures with thin layers (~0.1mm) were often seen broken or damaged by the hitting of printing nuzzles. These small damages in the supporting structure wouldn't affect the main PLA structure, as the forces were distributed to the larger supporting structures with no damage, and the PLA structure itself would also bear most of its weight. However, this raised the concerns of using PVA as main materials for generating structures. Thus, the printability and printing accuracy were examined firstly before the designs being made.

Printability

Printability was quantified by printing single columns with different diameters. Their target height was 200 mm due to the size limit of the 3D printer. Columns were designed to stand vertically with their bottom attach to the plate only. Ten paralleled tests were taken place for each sized column with the diameters chosen ranging from 2 mm to 10 mm. Tubes printing (without support) was once considered, but all the prints failed to reach 200 mm, indicating the brittleness of PVA.

As shown in Figure 5.1, columns below 4 mm were unlikely to achieve their half-target height. As the diameter increases, their chance of reaching target height surged.

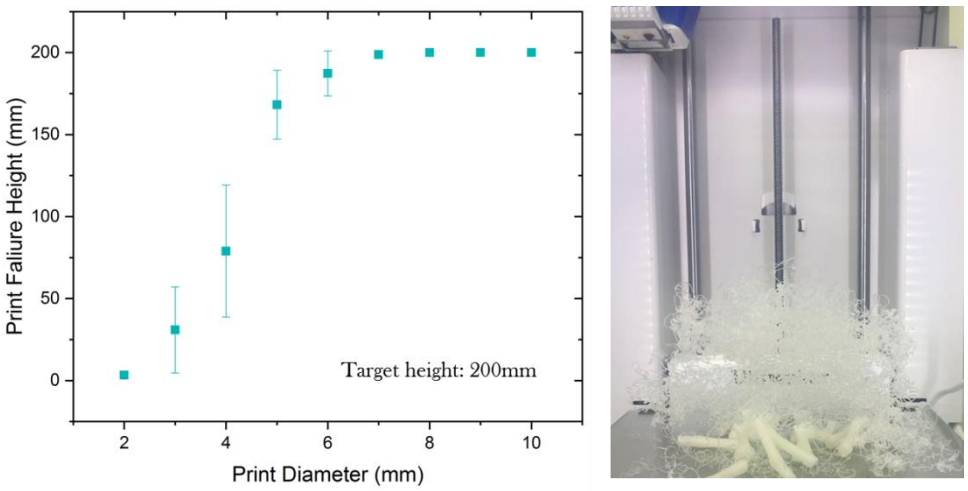

Figure 5.1 Printability of PVA with the target height of 200 mm (Left) and photography of print failure (original design of the model has been partly/full collapsed) (Right)

The diameter of 7 mm became a critical point where all the printed columns with larger diameter achieved their target height. Additionally, the columns with a diameter between 5 mm and 6 mm have a roughly 80-90% chance to succeed. These findings indicated that the minimum diameter of the design be large than 7 mm if the target height is 200 mm. And if the target height reduces to between 100 mm and 150 mm, the diameter could be further decreased to 4 mm. Thus, a suggested target height for the PVA design would be below 150 mm and with the diameter larger than 4 mm.

Printing accuracy

After knowing the printability boundary of PVA, the printing accuracy of this material became a priority to be investigated. To test the printing accuracy of PVA, this has been further segmented into width accuracy and height accuracy, due to the pattern and printing pathway differences in Figure 5.2 C and D.

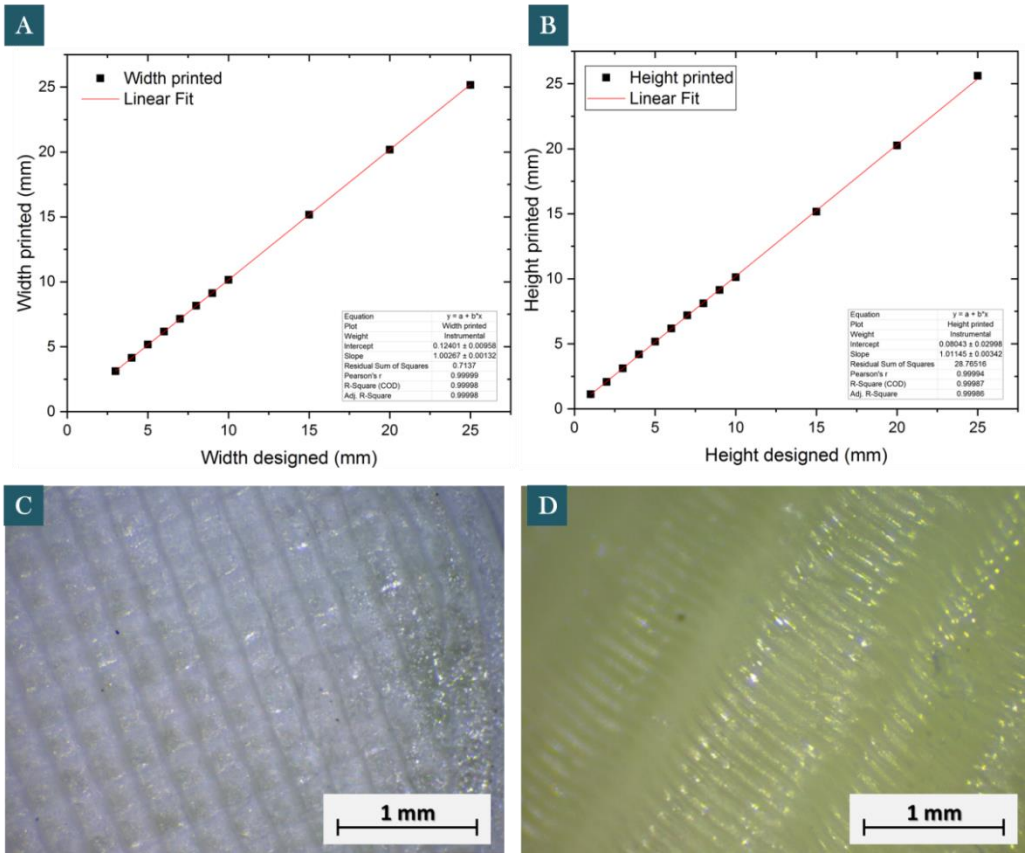

Figure 5.2, Printing accuracy of the PVA diagrams, width (A) and height (B), and the morphology of printed models (C) and (D) under microscope.

As shown in the figure, the 3D printer nozzle travelled in a gridded path when printing the same layer. However, the layers between each other were added up in a parallel way.

By comparing the measured printing width with the value set in CAD (from 3 mm to 25 mm), we observe a deviation of less than 1%. We explain this excellent agreement by the fact that the printed channel width is mainly determined by two accurately adjustable printer properties: the printer nozzle temperature and the feeding rate of the filament into the 3D printer (Dizon et al., 2018). By tuning these parameters to their optimum, the agreement in scaffold width can be achieved without changing other printer settings.

In terms of the height accuracy, we must remove the height of the base layer (±5 μm). It is a functional layer for all 3D printing models, aiming to stabilise the prints, and will be automatically added into G-Code for printing. This height positioning (together with the functional layer) can contribute up to 2.6 % of the height deviation. And this imperfect in terms of the building plate were further being removed from the actual printing height. To compare the printed value to the height set in CAD (from 1 mm to 25 mm), we must also consider that heat-treating the printing scaffold transforms its geometry from rectangular into semi-elliptical, without changing the layer width. Surprisingly, this has been correlated well with the 3D printer and resulted in a similar deviation value with the width accuracy.

5.1.2 PVA channel design

The idea of designing an interconnected hollow channel system in cement is to avoid further monitoring the plastic/glass based tubes. There were two types of designing approach by considering the healing agent types.

Interconnected structure with air/catalyst triggered healing agent

For the first and more ideal type, a design should be with a number of connected joints and alternative channels to be able to reach certain areas. The healing agent for this type should be the air/catalyst triggered agents, which would only happen to be hardened when the cracks appear, but with no interactions with cementitious materials. However, more connected joints and channels mean more space in cement are being taken. Considering the printability of PVA, it is quite challengeable to achieve a well-performed design. The initial design regarding the interconnected channels was inspired by the bone structure (Figure 5.3).

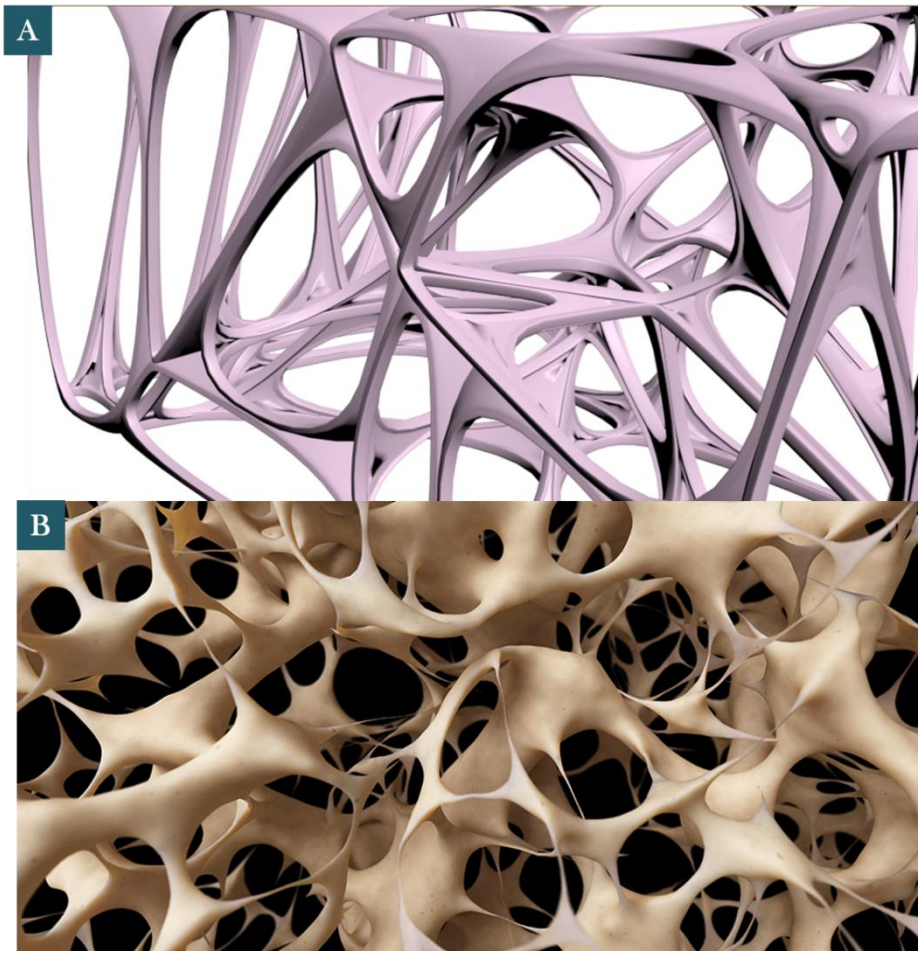

Figure 5.3 Designed bone structure using topology in Autodesk (A) and bone structure in real (B)

The whole structure was designed according to the size of the targeted beam (40 mm × 40 mm × 160 mm), with a length of 145 mm, a height of 30 mm and a width of 30 mm. The ploy in the design was firstly divided into 30 parts and applied topology after that. Then the sub-polygons were shelled to form the shape as shown in the Figure 5.4. Initially a shell thickness of 1 mm was selected since it would take the lowest volume in the matrix. Due to more connections added in this structure, it might be possible to be successfully printed in the 3D printer. However, it failed after its first layer being printed as the PVA shell was too weak to be able to hold the entire structure. Then, the parameter was further changed into 2 mm, 3 mm and 4 mm as shown in Figure 5.4.

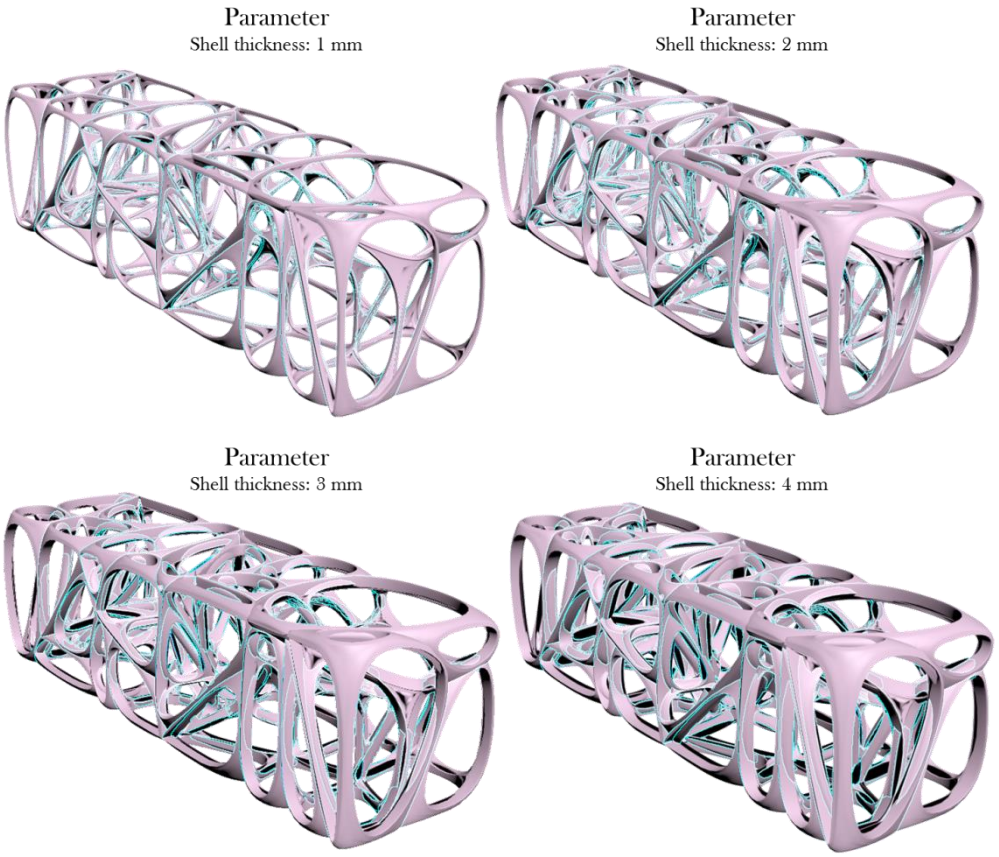

Figure 5.4 Designed bone structure with various parameters

3D printing was attempted for each model, but even the model with a shell thickness of 4 mm failed to be successfully printed due to its brittleness. Both vertical and horizontal positions were set and tried in 3D printing, but none of these worked.

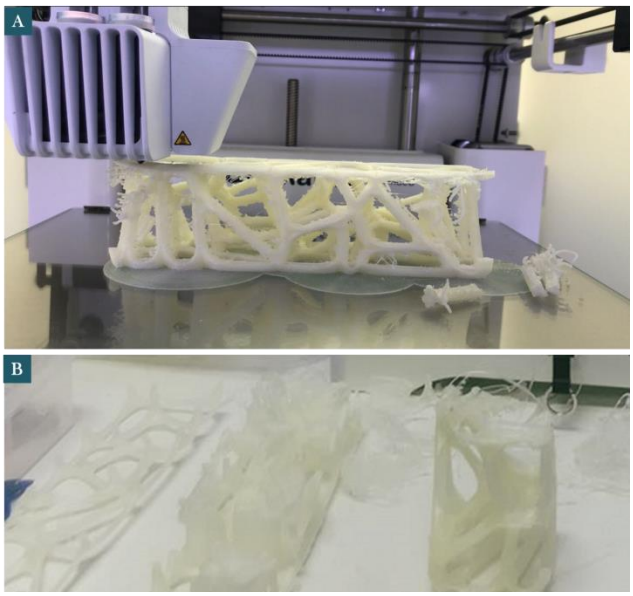

Figure 5.5 Printing process of PVA bone structure, (A) failure in 4 mm model, and (B) failure of 2 mm (left), 3mm(middle) and vertical positioned 4 mm model (right)

Supporting structures were not added in the 3D printing program, since the removal process (manually) will also destroy the main PVA prints according to the preliminary trials.

Further parameters have not been tried, since the 4 mm model already taken an over 38% of volume from the cement matrix, and the matrix will be greatly weakened by the time the PVA structure is removed. In this case, the bone structured channel system is unlikely to be achieved unless the brittleness of PVA filament can be significantly improved.

Dual-channel with two part healing agent

As for the second type, separate channels were designed to fit with two part healing agents. Hardener itself or epoxy itself wouldn't be able to block the cracks, and can be continuously provided through the channels. Ideally, separate hardener and epoxy inputs, as well as individual outputs should be designed and printed. However, considering the printability of PVA, both the inputs and outputs were united to create a more stable structure in the 3D printing process (Figure 5.6, connected area). Since the sacrificed PVA material will be further removed after cement matrix cured, united input and output can be separated by plugging in with separate connected tubes from outside.

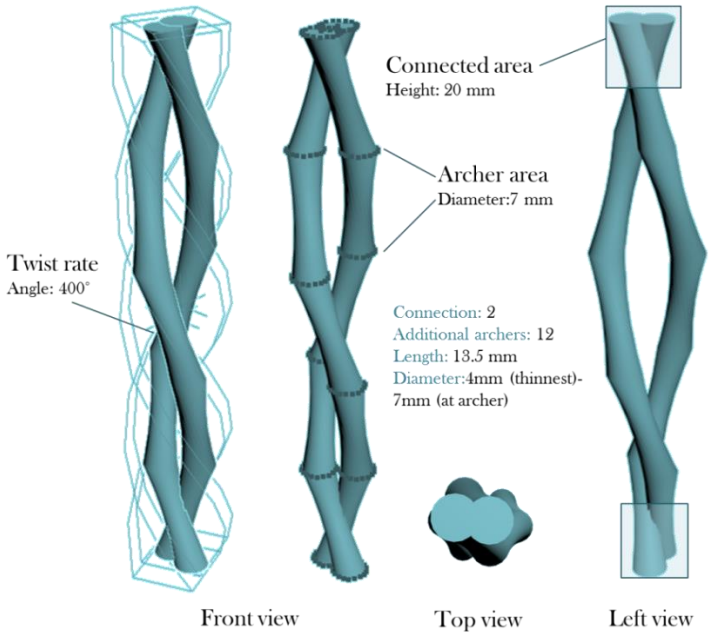

Figure 5.6 Dual-channel design for PVA channels creation

As shown in Figure 5.6, separate channels for both hardener and epoxy were designed with a few archer areas, similar to the joints in bamboos. These were designed to have

better compatibility with cement matrix during the curing process, considering the PVA water-soluble property. An angle of 400 of twisting rate was added to ensure the channels were symmetrically distributed in the cement matrix within the 30 mm width of the model size.

The Dual-channel system design was successfully printed via Ultimaker®, and a set of five models were printed all together in roughly 50 hours (Figure 5.7).

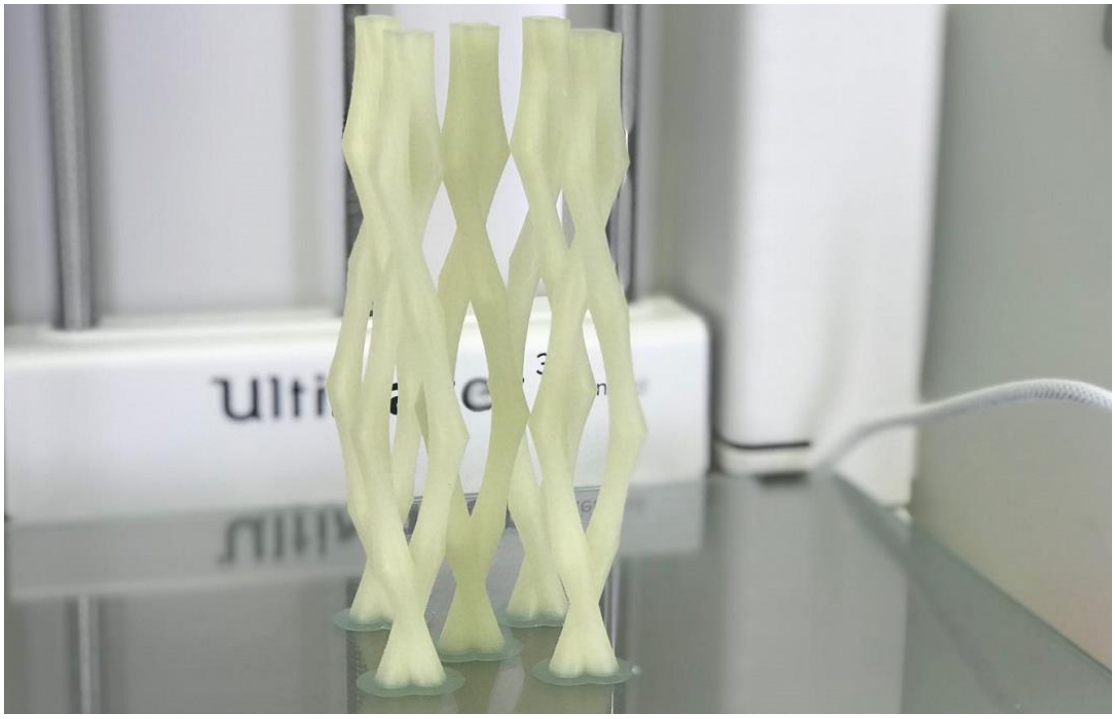

Figure 5.7 Dual-channel design printed in Ultimaker®

5.2 PVA dissolution behaviour tests

5.2.1 PVA 3D printing filament analysis

As PVA was selected as a sacrificial material in this study, its water soluble property was requested further investigation over time and in different conditions before being embedded in the cement matrix.

The non-disclaimed PVA compound filament was investigated to be extruded in a commercial 3D-printer. PVA is widely used in the 3D printing field as a supporting and break-out material due to its brittleness and ability to dissolve in water (Ni et al., 2017; Salentijn et al., 2017). However, it is less popular and has limitations in terms of different

nozzle requirement compared to other traditional 3D printing materials such as polylactic acid (PLA) and acrylonitrile butadiene styrene (ABS). Heating the PVA in the same PLA/ABS extruding print resulted in bubble formation and clogs in the extruder (Jamróz et al., 2017). Thus, the chemical properties of the non-disclaimed PVA provided before and after the extrusion were first compared and then the dissolution behaviour of the former investigated.

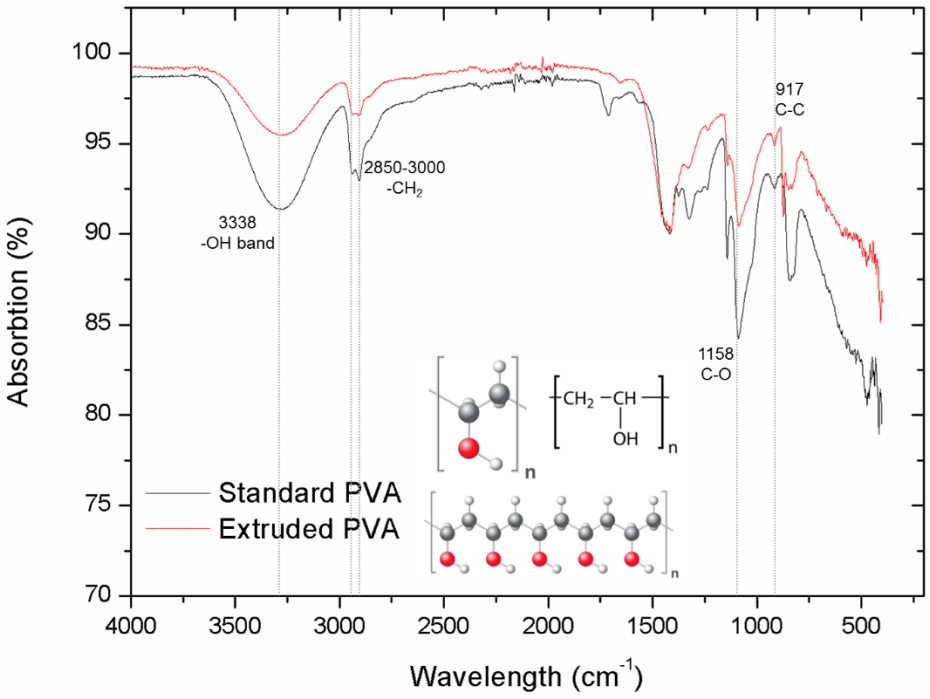

Figure 5.8 The FT-IR analyses of the 3D extruded and standard PVA materials

The chemical functional groups in PVA before and after 220° C extruding were compared using FTIR (Figure 5.8). The sharp peaks at around 2850 and 3000 cm^{-1} are assigned to the CH_2 stretching modes (Mansur et al., 2004, 2008). Also, hydroxyl group contribution was seen with absorption at around 3338 cm^{-1}. Important peaks at around 1158 cm^{-1} were verified as C-O bond. C-C bonds with a frequency at around 917 cm^{-1} were identified previously in FTIR data (Zheng et al., 2008). Extruded PVA showed different peak intensities compared to the original PVA whereas the peak wavelengths remained the same. Peak intensity differences were mainly affected by the crystalline portion of the polymeric chains. Besides, the peak at 3338 cm^{-1} broadened indicating the intramolecular hydrogen bond is formed between two neighbouring OH groups (Mansur et al., 2008). This means that the extrusion process involved in 3D printing slightly

changed its crystallinity. And the main functional groups remained unchanged. In this case, there was no significant difference between standard PVA and extruded PVA, so that standard PVA behaviours are also applicable for the extruded PVA.

5.2.2 PVA column unit dissolution

The dissolution of PVA was investigated by 3D printing PVA cylinders (1 mm in length and 1 mm in diameter, 1 g) and measuring it weight variation while submerse in water, as shown in Figure 5.9.

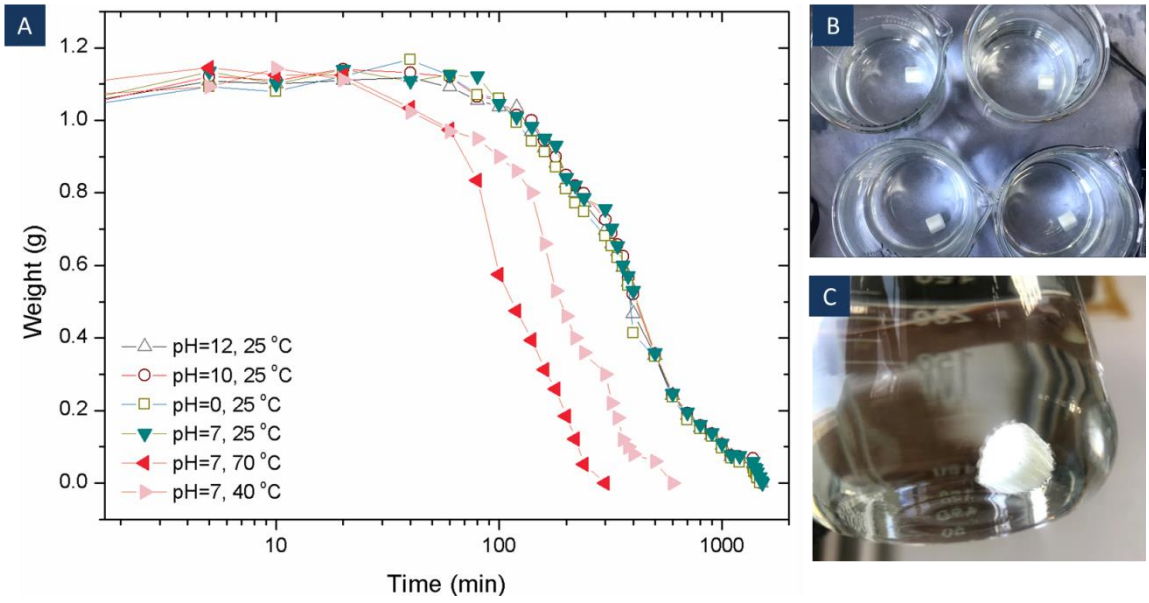

Figure 5.9 3D printed PVA cylinders dissolving behaviour in different temperatures and pH (A), photograph of 3D printed PVA cylinder dissolving in different pH solution (B), photograph of 15 mins dissolving, expansion layer appears (C)

The samples were tested at 25°C at pH 0, 7, 10 and 12 and also tested at increased temperatures of 40°C and 70°C for samples at pH 7. The weight of each cylinder was measured every 5 minutes for the first 30 minutes, and every 15 minutes till fully dissolved (Danner and High, 1993) and the results are presented in Figure 5.9. The results show that all the 3D printed PVA cylinders presented an increase in weight at the early stage of the test before the weight started to reduce, which were normally happening in the first 100 mins. This is due to water uptake by the PVA which enables water molecules to penetrate its polymeric chains, thereby weakening the -OH bonds and then dissolving PVA (Park et al., 2018). It is clear from the image that the pH does not have an effect on PVA dissolution or timescales. This showed that the highly alkaline environment of the

cement paste or any changes in the pH would not affect the dissolution of the PVA, and the main PVA units can survive in the cement paste during the curing process. The temperature on the other hand was found to accelerate the dissolution process. 3D printed PVA samples were found to be dissolved a lot quicker in warm water. The PVA units were dissolved within 5 hours at 70° C, while it took 25 hours at room temperature. Dissolution period in hot water (70° C) is roughly four times faster than the ones in room temperature, and roughly 2 times faster than the ones in warm water (40° C). As for the samples in warm and hot water, the dissolving curves were very much overlapped in the first hour, and then the later experienced a much intensive dissolution in the following period before being fully dissolved.

As a result, PVA materials after extruding presented the resistance of pH during the dissolution process, and the dissolution period is highly sensitive with the temperature changes. For further PVA structure dissolving, a relatively high temperature is more ideal for speeding up the process.

5.2.3 PVA column unit early expansion

The water absorption of PVA, when immersed in water, leads to the volume expansion of the 3D-printed structures. This was found in the early stage of PVA dissolving test, where the weight of PVA structures peaked at around 1.2 g, nearly 20% of its initial weight. Figure 5.10 shows microscopic observations of PVA before and after dissolution, confirming the expansion as the outer layer of PVA formed a transitional zone of semi-liquid phase, which –OH uptook water molecules but not yet transformed into the liquid phase (Bonapasta et al., 2002). This is the main reason for volume expansion at the early stage of dissolution. According to the findings of the dissolution process, this early expansion tends to happen in the first 100 minutes for the column units. This indicated that the early expansion may interfere with the cement curing process when PVA structures were embedded into a relatively high water-cement ratio matrix.

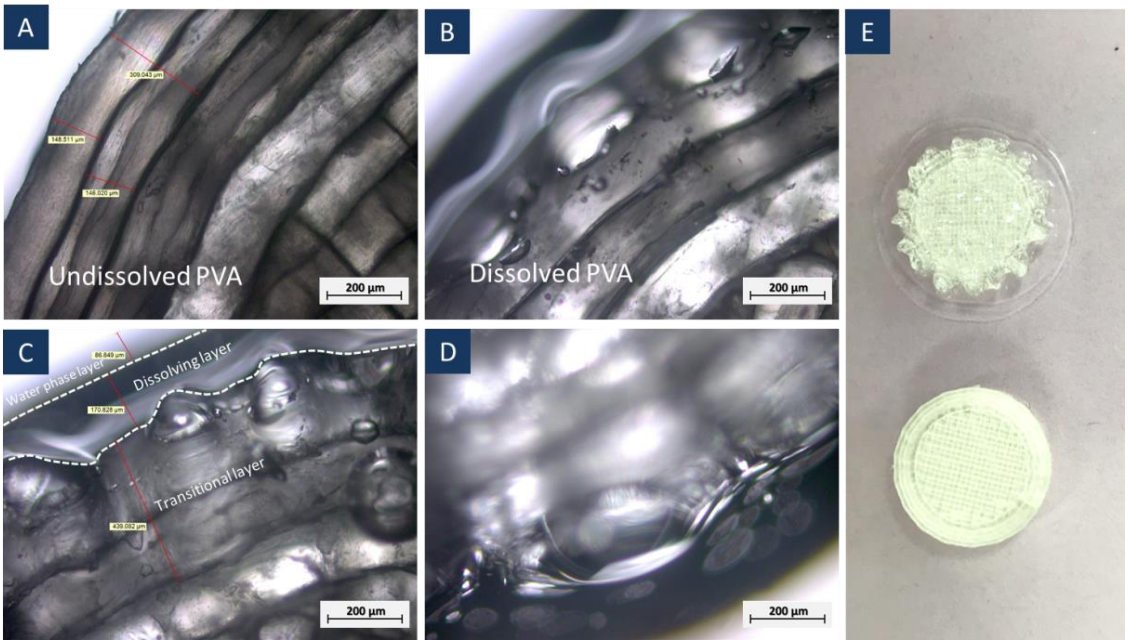

Figure 5.10 3D printed PVA cylinders dissolving behaviour under optical microscope. (A) undissolved PVA; (B) dissolved PVA when weight reached 20% of its original weight; (C) layer classification of PVA dissolving; (D) detailed image of dissolving layer; (E) general image of dissolved (top) and undissolved PVA cylinders.

5.3 PVA in cement matrix

5.3.1 PVA survival tests in cement matrix

PVA survival during cement curing became a large concern due to its water soluble ability. The amount of water in the cement mix would greatly affect the stableness and the shape of PVA prints. If the water-cement ratio increases, more PVA materials would tend to dissolve during the cement curing process, thereby de-shaping the original design. To examine the behaviour of PVA structures during curing, the 3D printed structures were embedded in cement paste with four different types of water/cement ratio, 0.25, 0.3, 0.4, and 0.5 in accordance with BS EN 196-1:2005. Designed a dual-channel model in section 5.1 was considered for the following cement survival tests. The prisms were cured in water for 28 days, with the aim of determining the successfulness of PVA survival in cement.

PVA expansion in cement prisms

Prisms containing dual-channel PVA prints with four different water-cement ratios were cured for 28 days and examined under a microscope. Micro surface cracks were found after samples being demoulded with a water/cement ratio of 0.3, 0.4 and 0.5. However,

no cracks were observed from 0.25 samples. Majority of initial surface crack widths were within 0.7 mm for samples with a water/cement ratio of 0.3 or 0.4. As for samples with a water/cement ratio of 0.5, widths of initial surface cracks were mostly between 1 to 2 mm (Figure 5.11). After 28 days of curing, with the specimens immersed in water, cracks expanded dramatically in the samples with water/cement ratios of 0.4 and 0.5. However, surface crack expansion in 0.3 water/cement ratio samples was controlled within 2 mm. This is because low water/cement ratio samples were dense and can somehow restrict the PVA expansion. Also, they had a large amount of unhydrated cement compared with that in high water/cement ratio samples, so that more water was used for the hydration process.

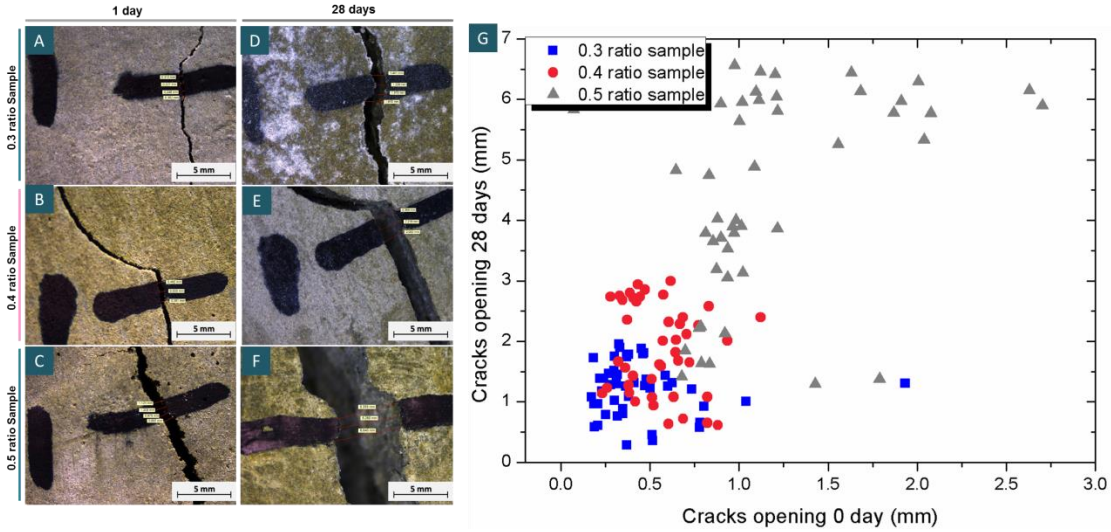

Figure 5.11 Surface crack widths of specimens with different water/cement ratios under microscope

These indicated that a high water/cement ratio would result in larger early-stage cracks due to the high amount of water in cement pastes provided for PVA expansion. However, early age cracks can be limited by applying low water/cement ratio, and can even be avoided when 0.25 w/c ratio is utilised. This is also correlated with the results in the previous section (section 5.2), where the PVA early expansion happened in the first 10% of its whole dissolving period and achieved a roughly 20 % of a weight increase at this stage. Higher water-cement ratio resulted in more free water remaining in the mix during the curing process, which led to more PVA materials starting its dissolving process, therefore a larger expansion appeared and more initial cracks in the cement matrix.

PVA survival in cement under CT

To investigate the effect of 3D printed PVA structures in cement, we used computed tomography (CT) for the four types of w/c ratio samples.

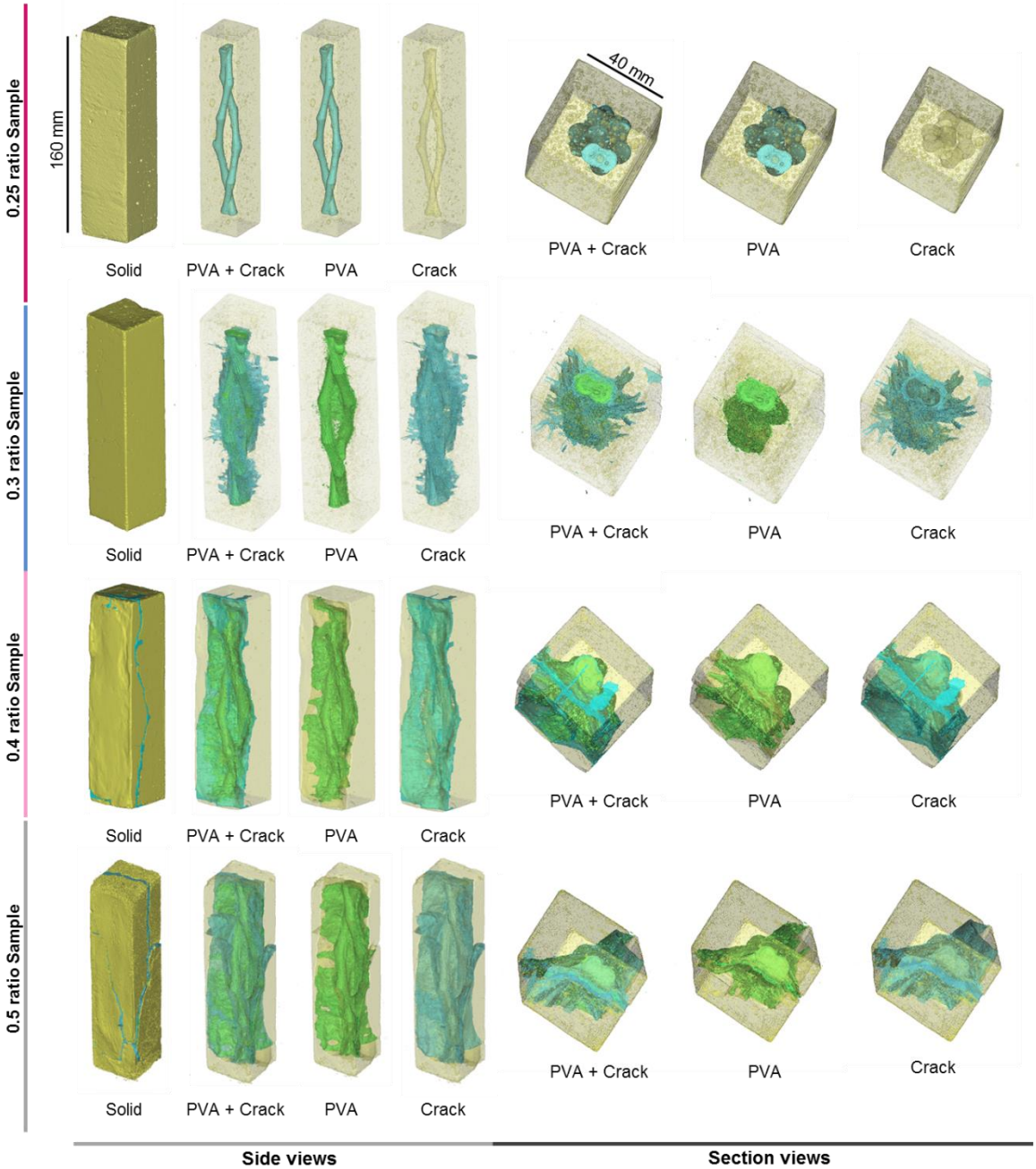

Figure 5.12 3D reconstructed images of reacted cement samples (turquoise represents PVA structure in 0.25 sample, yellow bulk shows cement prisms are shown in yellow bulk (all samples); the PVA structures in green (sample 0.3, 0.4 and 0.5); crack in light blue (sample 0.3, 0.4 and 0.5; 0.25 has no cracks))

From CT scanning reconstructed images (Figure 5.12), mainly three different materials could be identified in terms of density difference: yellow bulk represented cement paste; PVA related material were shown in green; light blue reflected cracks and dissolved

empty space in cement paste, with the bubbles removed from crack identification. In the 0.25 sample, the PVA structure was represented in turquoise, as there were no cracks appear within the cement paste.

Microcracks in samples with cement ratios of 0.3, 0.4 and 0.5 were formed and increased in length during the 28 days of the curing process, as observed before under with optical microscopy. Early PVA expansion resulted in free space. This was because PVA absorbed water from cement mixture and then expanded their volume for taking up more space. During this process, cement got harder and kept its shape, although the volume of PVA shrank due to dissolved part of PVA travelled out of pastes through cracks. However, the general shape of the PVA structure in 0.25 cement paste remained mainly unchanged compared with the one in 0.3, 0.4 and 0.5 cement pastes. And there were no significant cracks identified in the sample with a water/cement ratio of 0.25. This suggests that low water/cement ratio pastes could significantly minimise and even avoid early-stage cracking during the curing process and retain the original shape of the PVA structures.

To quantify the cement damage being made by early expansion, we defined a cement integrity ratio (I_c), describing initial crack volume in cement by comparing crack volume (v_{crack}, mm^3) with the cement volume (v_{cement}, mm^3) from CT reconstructed model as:

$$I_c = (1 - \frac{v_{crack}}{v_{cement}}) \times 100\% \quad (5.1)$$

From the CT reconstruction image, the integrity ratio of the specimen with a water-cement ratio of 0.5 was around 66%, which is followed by 69% in the specimen with a water-cement ratio of 0.4. As for the 0.3 water-cement ratio prism, its cement integrity ratio was roughly 82%. The lowest healing ratio was observed in the 0.25 water-cement ratio specimen, as high as 100%, since there were no identified microcracks in the CT reconstructed slices. Higher water-cement ratios linked with a lower cement integrity ratio and more cracks were generated during this process. This shared the same trend with microscope results from the surface, suggesting that higher water-cement ratio resulted in more early-stage cracks in the matrix, whereas a lower water-cement ratio like 0.25 is more ideal for the following tests.

As for the PVA de-shaping, we defined another indicator describing the level of PVA de-shaping. A de-shaping ratio (D_{PVA}) was introduced by comparing the original PVA

volume of PVA (v_{I-PVA}, mm^3) and the new volume added in the cracking volume (v_{C-PVA}, mm^3), as shown in the equation below:

$$D_{PVA} = \frac{v_{C-PVA}}{v_{I-PVA}} \times 100\% \quad (5.2)$$

Lower D_{PVA} represents a low level of PVA de-shaping, meaning the PVA structure survived well during the curing process, and vice versa.

The de-shaping ratio of the specimen with a water-cement ratio of 0.5 was around 31%, again shared the highest value. The specimen with a water-cement ratio of 0.4 had a de-shaping ratio of 27%. This is quite close to the former one, which indicated that the PVA would de-shape highly related with the crack shape and open mouths to the external environment. Since the prism with a water-cement ratio of 0.3 only has a 6% of de-shaping ratio, with significantly smaller crack mouths compared with the 0.4 and 0.5 samples. The lowest de-shaping ratio was observed again in the specimen with a water-cement ratio of 0.25, as small as 0. This shared a similar trend with the cement integrity ratio data, suggesting that PVA structures in a water-cement ratio of 0.25 samples had sufficiently survived with zero de-shaping ratios and 100% cement integrity.

As a result, specimens with a water-cement ratio of 0.4 and 0.5 exhibited no significant difference in terms of the de-shaping level or cement integrity level. In this case, those two types of samples were not quite suitable for directly developing PVA channels. Prisms with a water-cement ratio of 0.3 improved at both sides, and its relatively small crack mouth (0.7 mm) somehow restricted the amount water exchange through cracks and further protected the shape of PVA structure. As for the beams with a water-cement ratio of 0.25, these have the potential to be developed as vascular channels as they survived at the curing stage.

Coated PVA prints survival

Since the initial cracking in the cement matrix were mainly due to early PVA expansion while absorbing water, the idea of creating coating layers for PVA structures came naturally. As PVA structure survived in the cement with a water-cement ratio of 0.25, this type of mix was considered as a coating layer to PVA before the structures being formally embedded in the cement matrix. As shown in Figure 5.13, PVA was coated by 0.25 ratio

cement with different coating times from 1 to 3. While coating each time, the PVA was manually covered by cement with a roughly 1 mm layer. Then if the sample was needed to be coated twice, a second layer was added after 3 hours. And a third time continues as above.

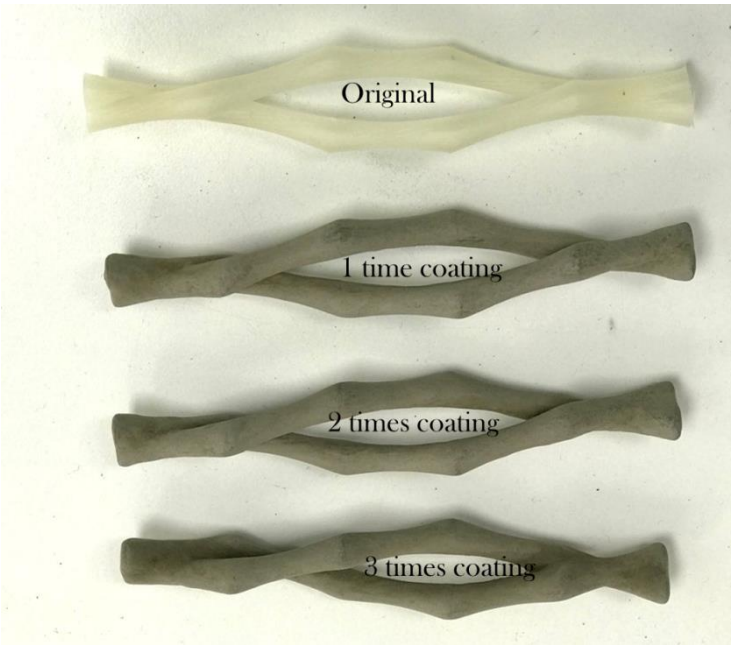

Figure 5.13 PVA were coated by cement with a water-cement ratio of 0.25, with different coating times from 0 to 3 (Top to bottom).

The coated PVA structures were embedded in the cement matrix with a water-cement ratio of 0.3, to see if there is any chance to avoid early-stage cracks. Cement with a water-cement ratio of 0.4 and 0.5 were not considered to get coated PVA embedded, since they are unlikely to succeed if the 0.3 ratio cement fails.

Early stage cracks were still detected in the cement matrix of three PVA coating types. There were no specific differences in cracks width among all three types from Figure 5.14. This is probably due to the complexity of the shape in PVA, and this would create an uneven curing surface, allowing cement slowly flow to the places that are lower and more stable for liquid cement mixture to stay before the cement being hardened. This unevenness would further create weak areas on the surface with thinner cement paste, where PVA could expand and generate unnoticeable cracks on the structures. Since the PVA structures were quite completed in shapes, tiny cracks may be hard to be focused under a microscope. When the coated PVA was embedded in the 0.3 cement pastes,

water could penetrate the tiny cracks on coated PVA surface and reach to the PVA, thereby resulting in further water absorption and initial cracks in 0.3 cement matrix.

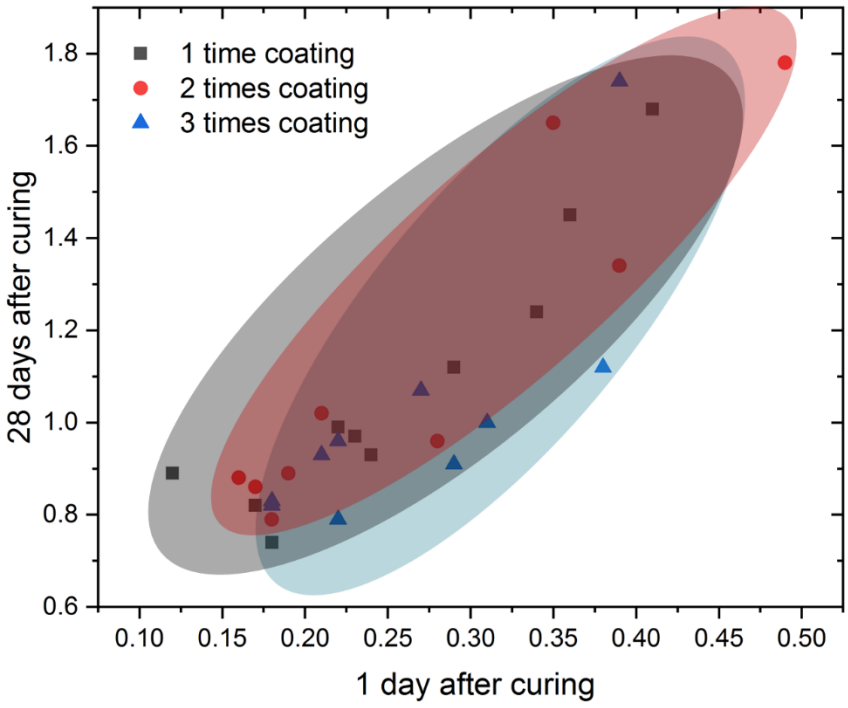

Figure 5.14 Crack widths difference of cement matrix with a water-cement ratio of 0.3 with different PVA cement coating times (from 1 to 3)

Applying more 0.25 cement coating layers for PVA could be a solution to avoid uneven distribution and reduce microcracks on PVA surface, but the times of coating cannot be added unlimitedly. Because as the matrix should still be dominated by its own water-cement ratio, and we cannot create a 0.25 (water-cement ratio) core to a 0.3 (water-cement ratio) matrix, which would present a hybrid mechanical behaviour. As shown in Figure 5.14, three layered 0.25 cement coating did not achieve a significant crack width or crack number decline, which means that it is less likely that we can create a thin layered 0.25 cement coating for PVA that could avoid initial cracking in cement matrix.

As a result, cement with a water-cement ratio of 0.25 is by far the only potential mix that was able to cooperate with PVA structures with no initial cracks appearing on the matrix.

5.3.2 PVA removal tests in cement matrix

In this section, we further conducted tests in PVA removing under different conditions. For this part, we only tested the specimens with water-cement ratio of 0.25 and 0.3, as the ones with higher water-cement ratio contain much wider cracks initially, which

brought difficulties in drilling extra holes (with the aim of removing the PVA). Details of the crack distribution and crack widths in different cement specimen were discussed in both expansion & CT sections. So for the prisms with a water-cement ratio of 0.25 and 0.3, holes with a diameter of 0.7 mm were drilled on the surface of the prisms, reaching the PVA structures, as shown in Figure 5.15.

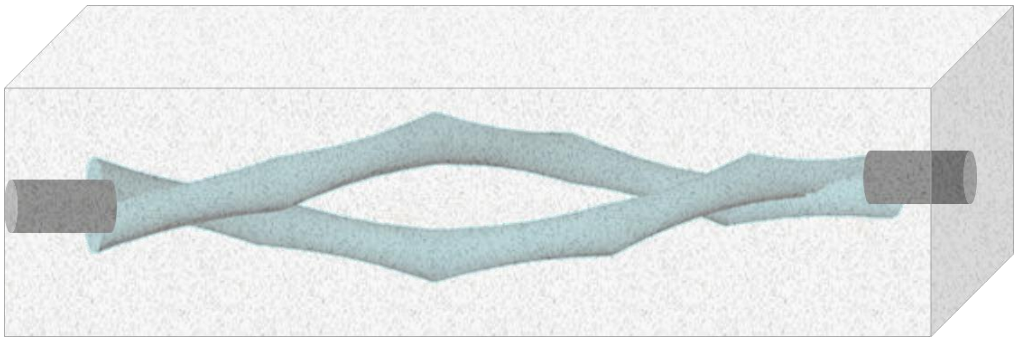

Figure 5.15 A schematic diagram of creating holes to reach PVA structures for further PVA removal tests

Holes from both sides of the prism were drilled to provide open areas that allowing water to reach to the PVA structure and eventually dissolve the entire structure. Three different water temperatures (25°C, 40°C and 70°C, same with the ones in the pure PVA dissolving tests in section 5.2) were investigated.

For the prisms with a water-cement ratio of 0.25, the removal tests here was to further investigate the feasibility of using PVA as a sacrificial material for creating interconnected hollow channels in cement. As this type of mix was the only suitable one in the PVA survival tests in cement. On the other hand, removal tests for the prisms with a water-cement ratio of 0.3 were to investigate if the initial cracks would accelerate the removal process.

During the PVA removal tests, all the prisms were immersed in water with different temperature, ranging from 25℃ to 70℃. After 24 hours, micro-cracks emerged in the prisms with a water-cement ratio of 0.25 under the condition of 40℃ and 70℃. The surface of the 25℃ sample remained unchanged (Figure 5.16). Micro-cracks appeared on the 0.25 mix surface after 40℃ and 70℃ water-bath could be related with the early expansion of the PVA structure. A more significant expansion might occur under a warmer water-bath environment. As for the prisms with a water-cement ratio of 0.3, PVA was dissolved and exchanged to the surface via the initial cracks. This further confirmed

that the initial cracks became extra water channels to dissolve PVA structures, thereby accelerating the removing process.

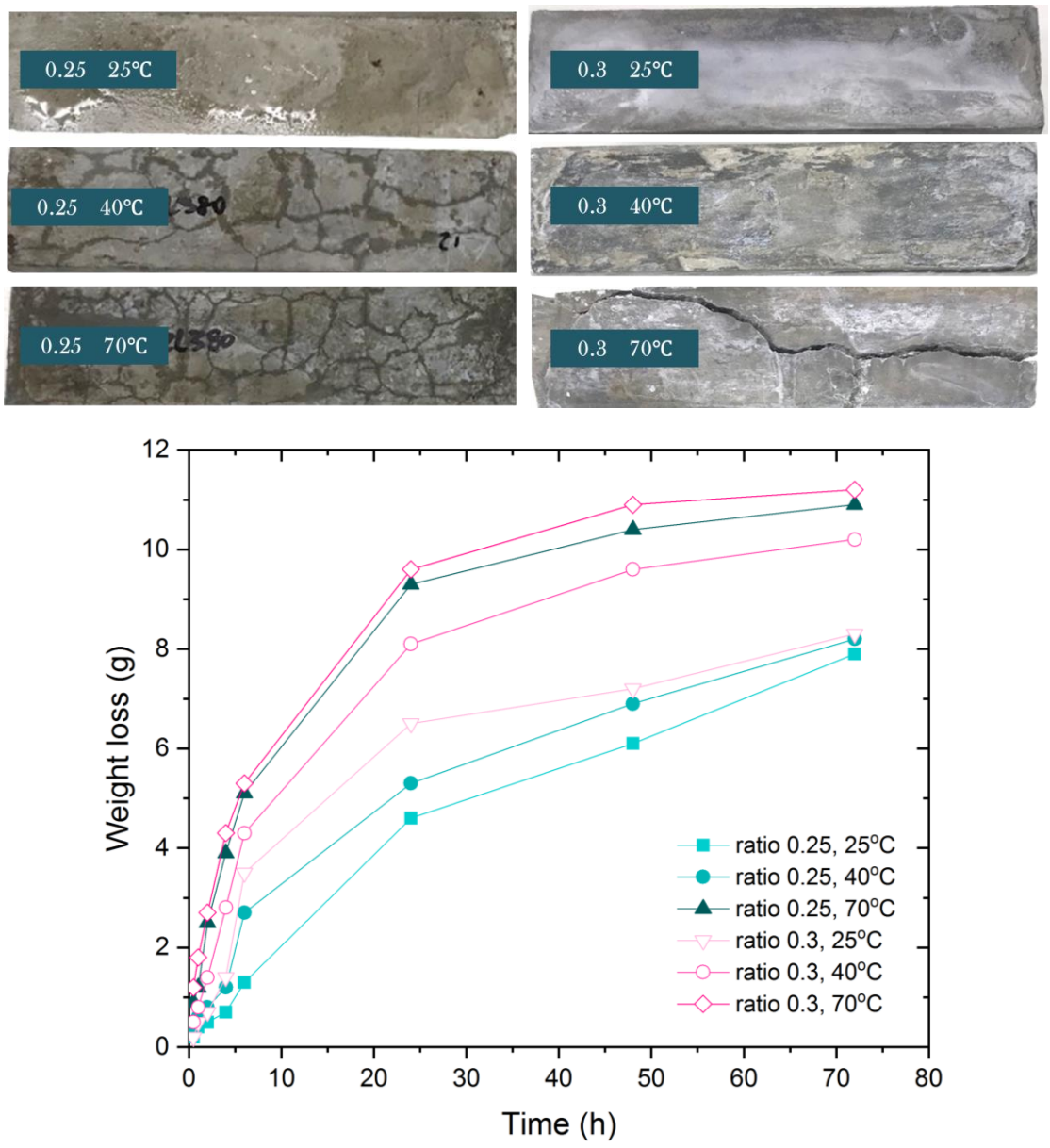

Figure 5.16 Photography of the surface of prisms being immersed in water-bath after 24 h, and the weight loss diagram over time

According to the weight loss diagram shown in Figure 5.16, it shared a similar trend with the pure PVA dissolving tests discussed in section 5.2, proposing that higher temperature was able to accelerate the dissolving process. At 70℃, both mix (0.3 and 0.25) were able to dissolve roughly 11 g of the PVA structure over the 72 h period, while in 25℃ or 40℃ water-bath, those mix with a water-cement ratio of 0.25 could hardly reach a weight loss of 8g within 72 h. Besides, prisms with a water-cement ratio of 0.3 had a more significant

weight loss than the ones hold a water-cement ratio of 0.25. This finding coincided with the photography pictures, as water also travelled through the initial cracks from 0.3 mixes, which allowing more contact surface with PVA structure, therefore accelerating its dissolution.

As a result, a higher water-bath temperature can surely accelerate the dissolution process, but it will create micro-cracks in cement since the expansion process endured more extensively in higher temperature. Thus, to successfully remove the PVA structures in cement, a room-temperature water-bath is more ideal to prevent cracking related with PVA expansion. For the mix with initial cracks, these cracks provided extra channels for water to contact with PVA and accelerate the dissolution process.

More interestingly, the PVA structure was printed and weighted as 12.5 g each. This means even for the PVA in beams (0.3 water-cement ratio) with initial cracks in 70℃ water-bath hadn't been fully dissolved over 72 h. So the picture of a broken prism after 72 h PVA removal is shown below (Figure 5.17 A).

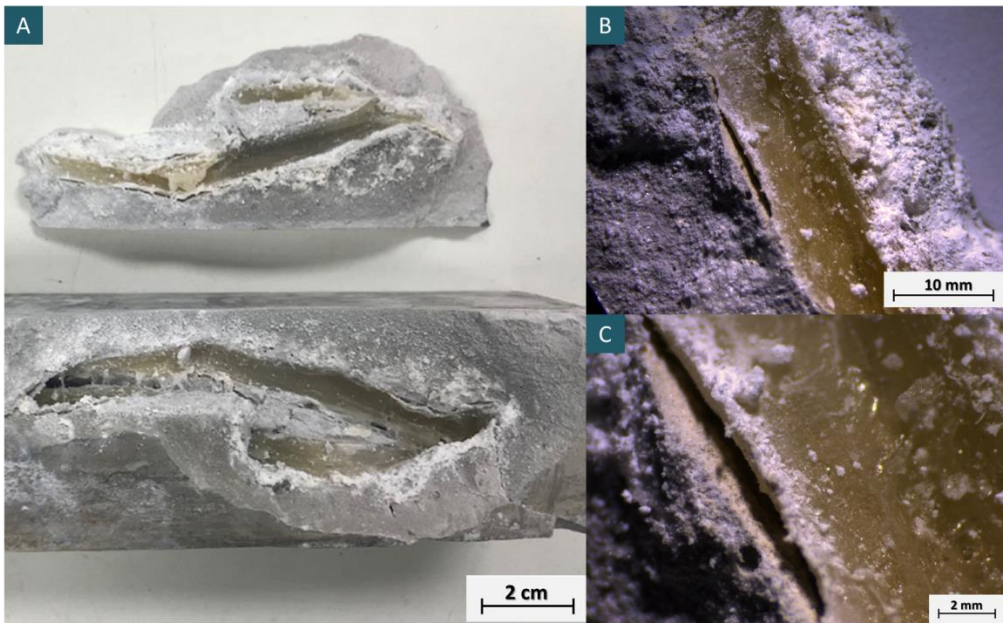

Figure 5.17 Photography of broken prism (A) and the microscope picture of the boundary layer (B & C).

According to this figure, a few PVA structure cannot be fully dissolved due to the complexity of the structure, especially at the corner and archer areas. This means that the slow dissolution process of PVA brought extra obstacle in terms of dissolving complex structures within cement bulk. Besides, a light coloured boundary was found by the edge

of PVA and cement under the microscope (Figure 5.17 B & C). The component of the layer will be discussed in detail in the next section (section 5.4).

This clear boundary shown between the PVA channel and cement material hinted that the PVA would potentially react with cement, and form a layer which would be different from either PVA or cement. If it is in that case, PVA would no longer be suitable for creating hollow channels for cement. This is because the potential new product would (i) vary the designed structure of the channel as it grows along and within the channel; (ii) might react with the epoxy based healing agent if polymer-based material involved; (iii) cracks could potentially go around through the layered boundary instead of directly penetrate to the channel, thereby reducing the sensitivity of diagnosing cracks.

Thus, further PVA-cement interaction was investigated and discussed in the following section.

5.4 PVA-cement interaction

In this section, experiments of testing interaction between PVA and cement were conducted, with the aim of further understanding the behaviour of PVA in cement and evaluating the feasibility of using PVA as a sacrificial material to create hollow channels in cement. After PVA-cement prism samples were cured for 28 days, products from PVA and cement under the microscope were analysed by SEM-EDX, FTIR and XRD. This was for further understanding the chemical components and 3D PVA -cement interaction mechanism.

EDX showed that calcite and Ca-polymer compounds were found in all specimens as illustrated in Figure 5.18.

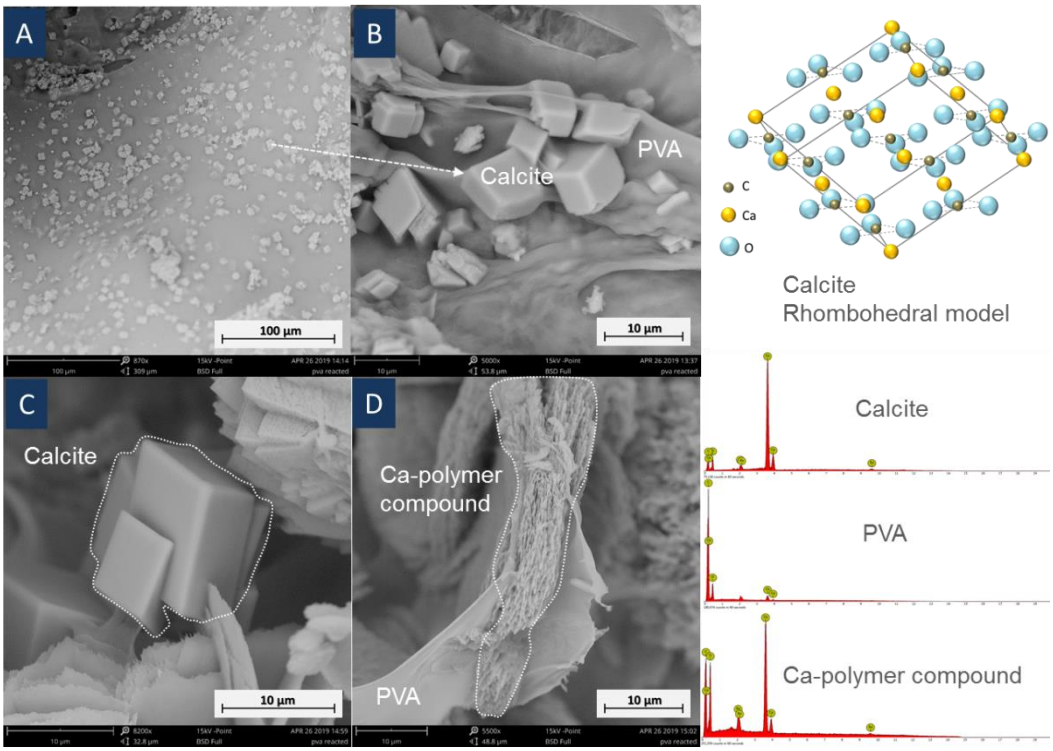

Figure 5.18 SEM images of cement samples reacted with 3D printed PVA structures showing (A,) boomed Calcite minerals with PVA background;(B) zoomed in image of PVA and Calcite; (C), Calcite crystals; (D) Ca-polymer compound generated on PVA. Also shown are Calcite crystal rhombohedral model and EDX spectra corresponding to calcite, PVA and Ca-polymer compound.

This evidence further proved that the layer between cement and PVA was a new product, a combination of calcite and a Ca-polymer, rather than PVA or cement.

The existence of Ca-polymer compound was also confirmed by FTIR (Figure 5.19). The peak at around 713 cm^{-1} corresponds to the Ca-O bond (Galván-Ruiz, 2009) and this can be found in reacted PVA sample. This strongly suggests that there are interactions between PVA and the Ca cations. Both the surface and the central cement parts reacted with PVA, as minor Ca-C bonds can be found in both FT-IR curves. The surface cement reacted with the surrounding water, which contained PVA polymers. Hydroxyl groups in reacted PVA were barely verified in FTIR compared with that from both standard PVA and 3D printed PVA samples. This is because –OH groups were replaced by Ca cations, forming Ca-polymer compound or lost and then formed water.

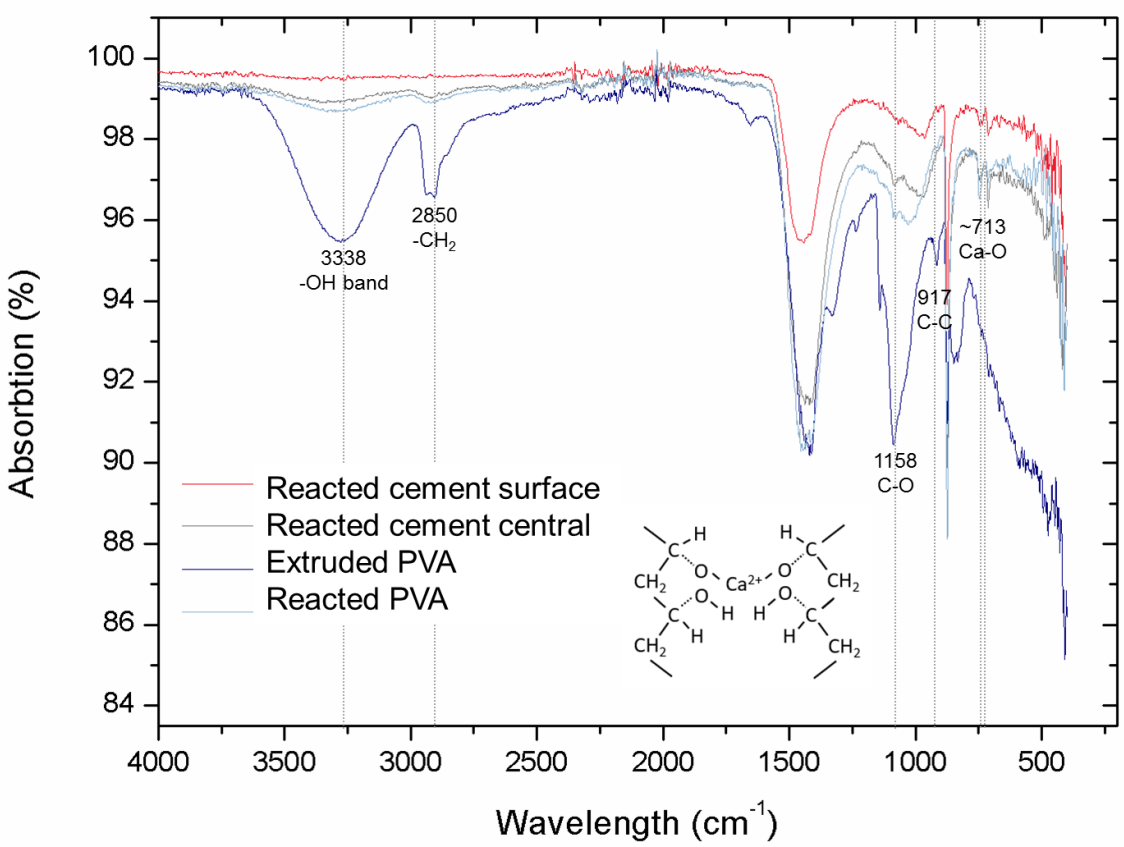

Figure 5.19 FT-IR image of cement samples reacted with 3D printed PVA structures

Bonapasta et al. (2002) found similar secondary products in PVA cement interaction. This reaction process can be explained by the following equation 5.3, where Ca^{2+} from calcium hydroxide replaced H^{+} from PVA polymer, the replaced H^{+} and remaining OH^{-} then resulted in water.

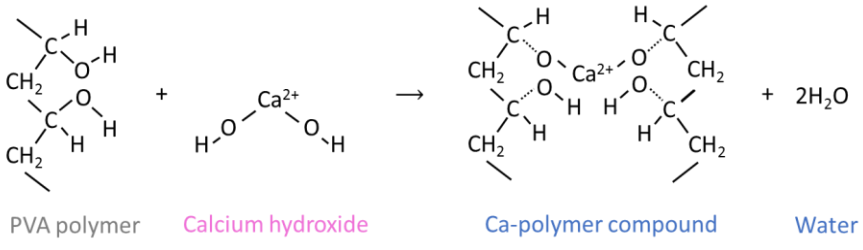

Equation 5.3

This was supported by XRD analysis (Figure 5.20). Peaks of Ca-compound were found in reacted cement sample, while these were not observed in the unreacted cement. Formation of this secondary material suggests that PVA lost H and hydroxyl groups in forming Ca-compound and water. This coincided with the FTIR data (Figure 5.19), which showed a drastic decline of -OH group intensity between unreacted and reacted PVA. A significant increase of calcite in PVA-cement reacted sample was found

compared to plain cement sample. Also, calcite peaks were found in PVA polymer after reaction with the cement, which was not present previously. This implies that the reaction between PVA polymer and $Ca(OH)_2$ somehow concentrated Ca cations near PVA polymer when CO_2 dissolved in water, it can easily be reacted with Ca cations near PVA polymers. Thus, we can see a clear white powdered layer being generated close to the edge of PVA from Figure 5.17 B & C.

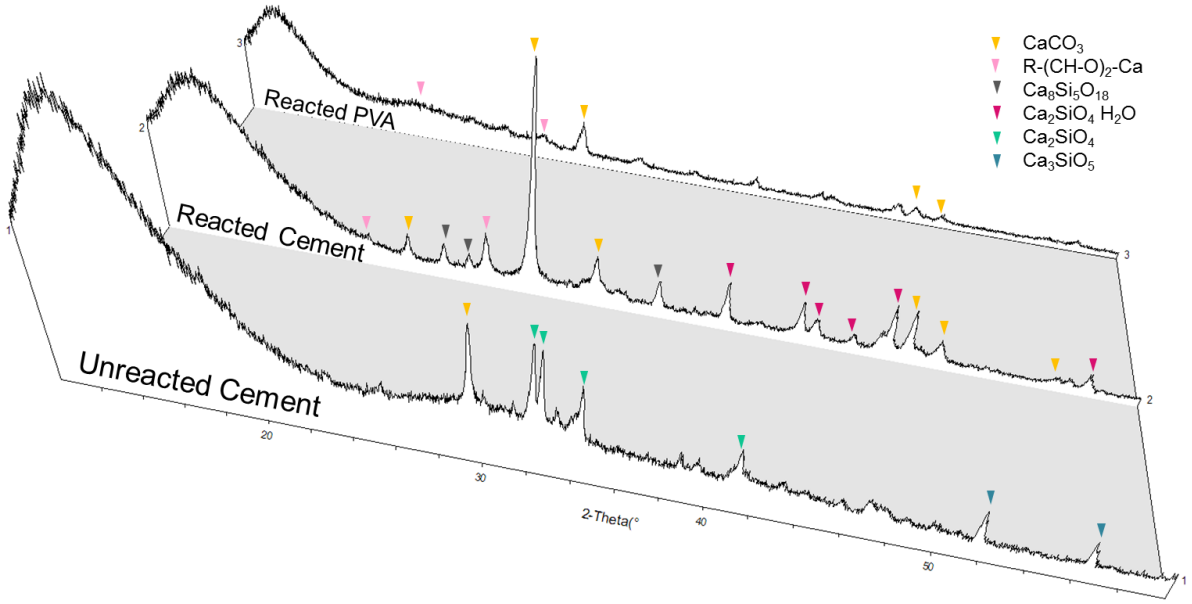

Figure 5.20 XRD diagrams of cement samples reacted with 3D printed PVA structures

As a result, the product generated from the reaction between cement and PVA was confirmed as a Ca-polymer material, which was not able to be dissolved by water in the previous PVA removal test. This indicates that PVA would not be a suitable material for creating hollow channels in cement, since the new polymer-based material would bring a few uncertainties in terms of varying the shape of channels and initiate complex reaction during the healing process.

5.5 Concluding remarks

Creating hollow channels for self-healing vascular system avoids long term tube monitoring and enables multi-scale healing over time. The present study has indicated our initial effort of using PVA as a complex tunnel creating material. PVA was selected as sacrificial material as it allows the 3D printing and the dissolution in water to create hollow tunnels. In this chapter, PVA water dissolution behaviour and printability were

firstly investigated (Figure 5.21). FTIR shows decreased in crystallinity of the PVA extruded in the 3D-printing when compared with un-extruded PVA, but the main functional groups remained unchanged. Then, a design with double twisted channel was selected due to its printability using PVA and able to provide a versatile way to deliver two-part healing agents.

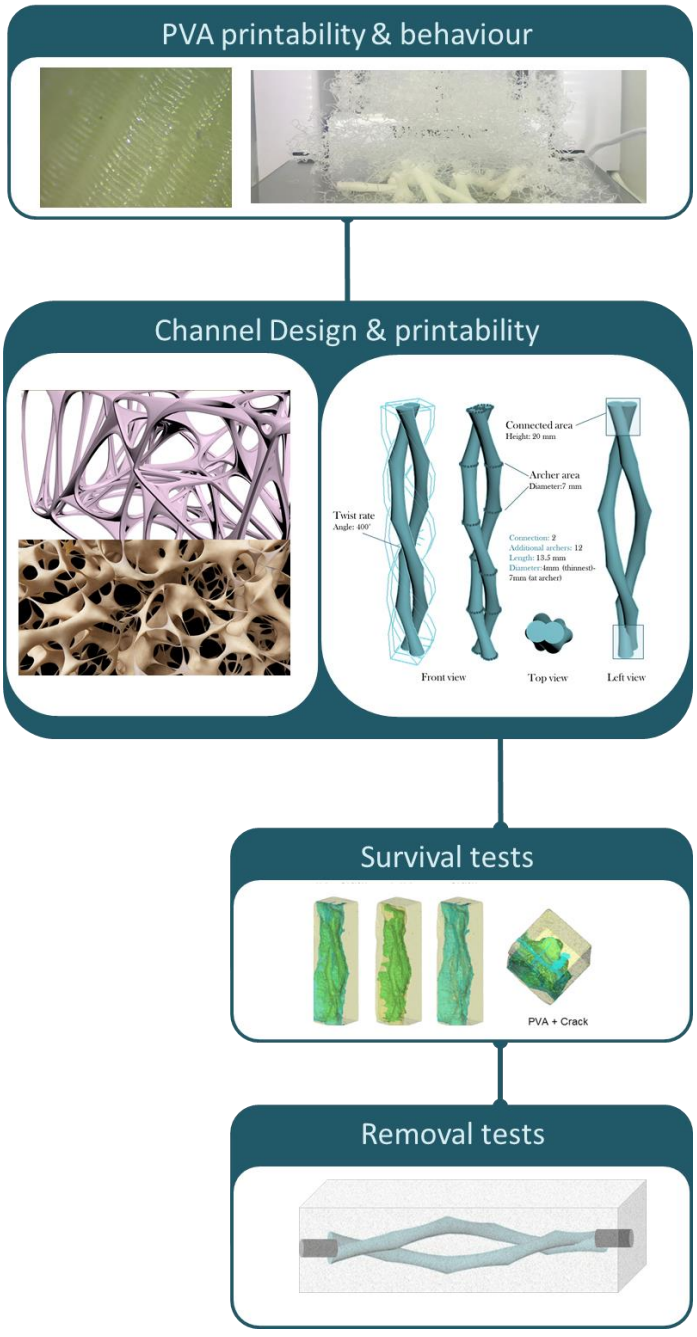

Figure 5.21 Schematic diagram of the channel exploration process using PVA as a sacrificial material

The resulting PVA structures completely dissolve in water; for example, 1g 3D printed PVA structure dissolves in water after 1300 minutes. Water uptake followed by dissolution can be used as a simple removal mechanism for these vascular networks. Additionally, the highly alkaline environment of the cement paste does not affect the dissolution of the PVA. We embed the PVA structures in cement paste to investigate the effect of structures' water uptake during curing. Through casting in different w/c ratios, we show the w/c ratio substantially contribute to increasing the water intake of PVA structure. Controlling the PVA expansion by decreasing the w/c ratio provides a promising approach to tailor dissolution kinetics during curing. Furthermore, CT-scan images show that low w/c ratio casting no dissolution of PVA is observed in the sample. On the other hand, for w/c ratio above 0.3, the water uptake of PVA results in the expansion and creates cracks in the whole structure. The PVA cement survival tests indicated that w/c ratio of 0.25 was the only possible mix that could potentially be used in creating hollow interconnected channels in cement.

However, this hypothesis was broken by the results of the PVA removal tests. Warm/hot water-bath were able to accelerate the PVA removal process than the ones in room-temperature water-bath. But the acceleration in the dissolving process also triggered significant early expansion in PVA, thereby generating cracks during the removal process. Only the ones were conducted under room-temperature hadn't observed cracks on the surface. Even for the samples being conducted under room temperature, it is less likely that that PVA removal could succeed. Since there were secondary products between the cement and PVA materials being produced and formed a layer of the boundary. This new material layer would bring more uncertainty in self-healing system, as the new product would (i) vary the designed structure of the channel as it grows along and within the channel; (ii) might react with the epoxy-based healing agent if polymer-based material involved; (iii) cracks could potentially go around through the layered boundary instead of directly penetrate to the channel, thereby reducing the sensitivity of diagnosing cracks.

In this case, interactions between PVA and cement, mainly $Ca(OH)_2$, were conducted, mostly formed a Ca-polymer compound layer in between the cement and PVA structure. This Ca-polymer material was observed not water-soluble in the experiments, which cannot be completely removed by water. In this case, there would always be a Ca-polymer layer appeared in the channel, rather than empty cement channels. Besides, calcite was

also found in reacted PVA polymers and reacted cement pastes due to air exposure to the water-bath.

The capability of PVA to be 3D-printed, dissolved in water and remain intact when cast at low w/c ratios should make it valuable as a potential sacrificial network for vascular based-self-healing. While its behaviour in cement removal process and secondary interaction between cement made it being screened out from the list.

Future studies regarding create hollow channels in cement for the self-healing system could focus on wax-liked materials. This is mainly because it is a proven casting process for generating metal and jewellery (Hunt, 1980). The fabricating process design and curve a wax-base structure, and then this structure would be embedded into the cementitious matrix. After that, the cement bulk was heated up to melt the wax and pour it out. Then this negative cement mould could fill in with melted metal. This approach was called "Lost-wax" process, which dated back to 1200 B.C. in ancient China (Peng, 2017).

The reasons for not using wax as a sacrificial material in this study was considering the capability of applying wax printing in our current 3D printer and the wax 3D printing price for out-reached services. Current wax 3D printers are mainly for jewellery design, which resulted in their limited size (normally less than 100 mm) for creating large structures for concrete. To order out-reaching wax printing service would normally cost at least 70 pounds for each model (twisted model, discussed in this study) from the Alibaba platform. In this case, we decided to use the current widely used PVA 3D printing material to print the designed model, due to its potential printability and water-soluble property.

This study proved that PVA is unlikely to be developed as a sacrificial material in cementitious materials; therefore it is pointless in further researching creating hollow channels using PVA and we should move the focus to other potential sacrificial materials that are available for 3D printing.

Chapter 6

A chemical sensitive coating for chemical triggered vascular system

The investigations reported in Chapter 4 involved the use of biomimetic 3D printed vascular systems in cementitious specimens to determine a suitable design for long-term self-healing cementitious materials via the physical trigger. Then, in order to avoid monitoring the plastic tubes, Chapter 5 describes an investigation of sacrificial vascular tunnels in the cementitious matrix using PVA. In this chapter, instead of physical triggering, the proposed vascular self-healing technology was further expanded to chemical triggering, using chloride ion triggers to release healing agents. This chapter is split into three main sub-sections. In the first section, a chloride sensitive material was synthesised and its chloride sensitivity was confirmed via characteristic methods such as UV spectra and TGA, which will be discussed in 6.1 and 6.2. Then, porous vascular systems were designed for coordinating chemical triggering materials, followed by a few tests in investigating the release behaviour of the designed models. Finally, proof-of-concept tests were conducted to investigate the efficiency of the proposed triggering mechanism in situ via rapid chloride penetration tests (RCPT).This part of work was affected mostly by COVID-19 due to lab closure and inaccessibility of out-reach tests earlier this year.

6.1 Synthesis of a chemically triggered material

A main concern for concrete is the decrease of alkalinity and depassivation of steel reinforcement caused by the ingress of chlorides especially the reinforced concrete structure in marine environments. And these normally results in cracking within the structure, causing further catastrophe. Specifically, steel is prone to corrosion induced

by chloride ions, which made this ions desirable triggers in a chloride-attack scenario. A chloride sensitive smart system has the potential to detect early corrosion cracks, and is able to react and release healing agents to further protect the structures.

Previous researches related to vascular self-healing systems were mainly focused on physical triggering. Using chemical triggering vascular to deliver agent would reduce the requirement of agents and improve self-diagnose sensitivity. However, few follow–up research report the chemical triggering mechanism and its feasibility in a time-controlled release.

6.1.1 Theory and the reaction

To design and synthesis a chemical sensitive material, the material should be able to detect and further bind certain ions, such as Cl^- ions, thereby leading to collapse of this chemical sensitive layer and release of the internal material.

Alginate is non-toxic, biodegradable, low in cost, and readily available, and has been found to be chemically modified to alter its properties (Paques et al., 2014). Specifically, sodium alginate can be cross-linked with many metal ions (such as Ca^{2+}) to form the hydrogel. To date, alginate has been used for encapsulating various cargos which have been employed in diverse applications including controlled drug delivery, bio-catalysis for chemicals production, stabilisation of ingredients, adsorption of pollutants, and energy storage (Leong et al., 2016). More recently, Xiong et al. (2015) introduced chloride ions triggered capsules to cement, via creating a silver-alginate shell.

So in this study, we chose a similar approach, using sodium alginate as original material. Ag^+ is chosen to be cross-linked with alginate skeleton to form silver alginate, which can provide characteristic “egg-box” structures to hold silver cations.

When chloride ions appear, metal cations within the “egg-box” are precipitated with chloride ions. And the ionically cross-linked silver alginate gels can be therefore dissolved by the release of the silver cations.

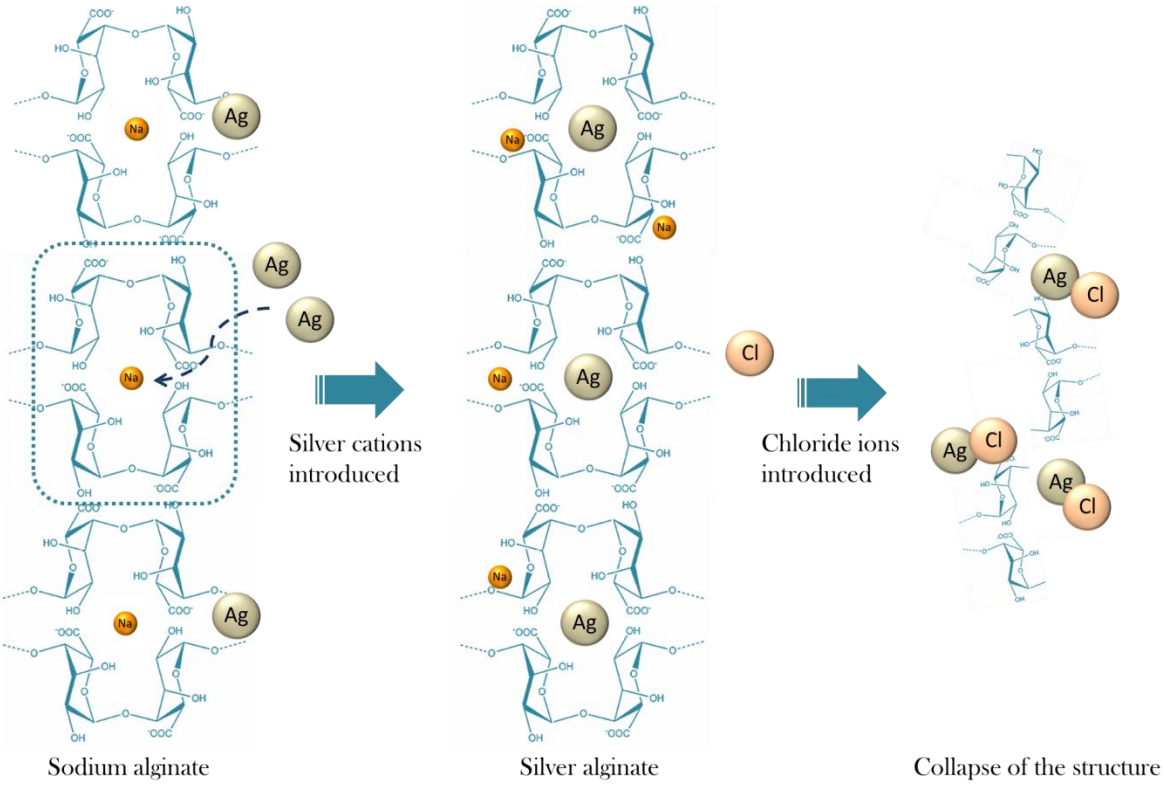

Figure 6.1 A schematic diagram of explaining silver alginate generation and this gel could be further dissolved by chloride ions appearance

Chloride ions provide a stable trigger for the synthesised silver alginate. This method can take place under gentle conditions (room temperature), making it ideal for the entrapment of sensitive materials.

6.1.2 Synthesis of silver alginate

The silver alginate synthesis was operated in a box covered by tinfoil since silver nitrate is sensitive to light and will start to hydrolyse when left exposed to light (Yadav et al., 2019) as shown in equation 6.1.

$$AgNO_3 \xrightarrow{light} Ag + NO_2 + O_2 \qquad (6.1)$$

Sodium alginate (Na-Alg) was first completely dissolved in deionised (DI) water. After stirring for 10 minutes, the sodium alginate mixture was placed on a shaking table with 200 rpm for 24 hours. Then silver nitrate was added to the dissolved sodium alginate solution under the cover of a tinfoil covered box. The mixture with silver nitrate and sodium alginate was again placed on the shaking table with 200 rpm for 3 hours. The

resulted silver alginate gel was separated by a separating funnel with 0.22 μm filter paper. This is followed by a few washing procedures using DI water.

If this process were exposed to light, rather than silver alginate, the resulted gel would become an alginate-nano silver particle (Alg-AgNPs) composite (Yang et al., 2015 and Zhang et al., 2016). This is because light could enhance the reduction of Ag, transforming Ag^{+} from "egg shell" of alginate to nano-scaled silver metal (Figure 6.2).

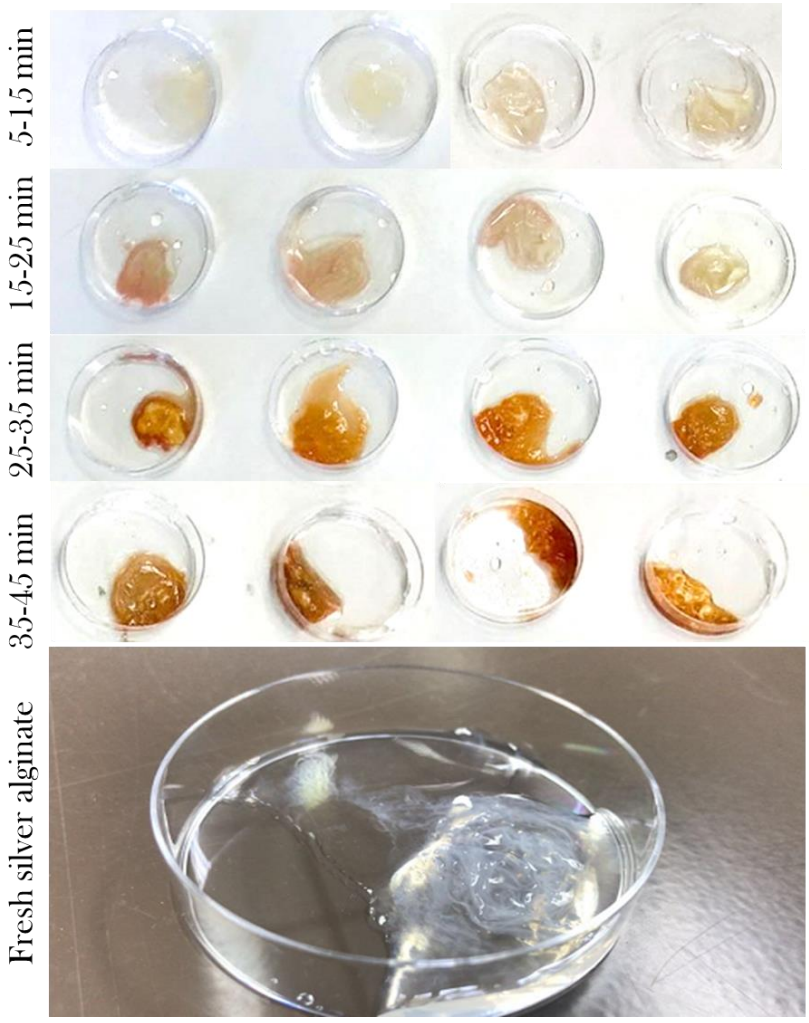

Figure 6.2 Silver alginate transformations under light over time and a comparison image of freshly made silver alginate

After roughly 0.3 h of reaction, the formation of silver nanoparticles (AgNPs) can be observed by colour change as they exhibit brown colour in aqueous solution. The colour of the reaction mixture changed from yellow to light brown to dark brown with increasing reaction time, indicating the formation of AgNPs (Sharma et al., 2012).

Alginate is able to change the heavy metal ion form in the bulk solution according to ion competition order (Becherán-Marón et al., 2004). Since the purchased sodium alginate (Na-Alg) from Sigma Aldrich® has not stated its cation exchange capacity (CEC), it is not possible to find a specific Na-Alg/$AgNO_3$ ratio of generating silver alginate. Thus, preliminary exploration on optimum Ag-Alg production ratio was conducted.

Different amounts (2 ml, 4 ml and 6ml) of 0.1M silver nitrate ($AgNO_3$) was added into 1, 2, 3, 4 and 5 wt% of 4 ml sodium alginate (Na-Alg) solution. The resulted gels were collected and weighted to explore its optimum combination of creating relatively large production. The diagram in Figure 6.3 showed the maximum production of silver alginate happened in a 4wt% sodium alginate mixture, with a Na-Alg/$AgNO_3$ volume ratio of 2:3.

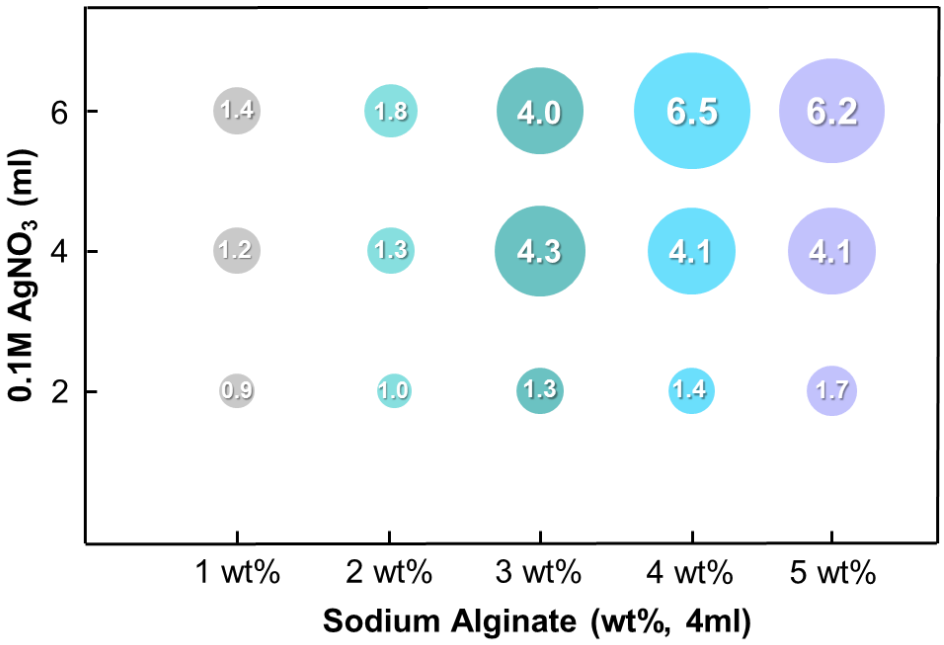

Figure 6.3 A bubble diagram revealed the optimum silver-alginate production ratio (Note the numbers in the bubble represent the weight of silver alginate produced) in gram

The amount of Ag-Alg increased when a more concentrated Na-Alg mixture was involved. As for the samples with the same Na-Alg concentration, an increased volume of silver nitrate often resulted in higher Ag-Alg production. However, this trend changes when the Na-Alg concentration increased to 3wt%, where the amount of Ag-Alg showed no significant difference between samples adding 4ml and 6ml silver nitrate. This is because the amount of Ag-Alg is restricted by the amount of alginate provided, adding more silver nitrate would not change its production. In the 4wt% Na-Alg samples, introducing more

silver nitrate can improve Ag-Alg production, since there was more alginate available for generating Ag-Alg. Interestingly, in the 5wt% Na-Alg samples, the amount of Ag-Alg were the same with the 4wt% samples. This means in both 4wt% and 5wt% Na-Alg samples, the amount of alginate provided was sufficient, and the silver alginate production was mainly restricted by silver nitrate. According to this diagram, we could then choose the optimum silver alginate producing recipe, which is the combination of 4wt% of Na-Alg and 6ml of $AgNO_3$. This combination was able to result in the largest amount of silver alginate with the minimum raw materials used.

6.1.3 Silver alginate characterisation

Synthesised silver alginate gels were characterised via UV spectroscopy, Thermogravimetric Analysis (TGA), and rheometer to confirm its components and behaviours.

UV spectroscopy characterisation for synthesised Ag-Alg

UV spectroscopy was employed to confirm the existence of silver alginate and differentiate it from sodium alginate.

In order to optimise the synthesis of silver alginate (Ag-Alg), the concentration of sodium alginate was varied (1.0, 1.5, 2.0, 2.5, 3.0, 3.5, 4.0 and 4.5 wt%) while keeping $AgNO_3$ concentration and reaction temperature constant at 0.1 M and 25 °C, respectively.

First, sodium alginate solutions with different concentrations (from 1 wt% to 4.5 wt%) were examined as shown in Figure 6.4 (Top). Figure 6.4 (top) depicts the UV spectra of sodium alginate with various concentrations, and it reveals the existence of an absorption band at approximately 265 nm (Shabbir et al., 2017).

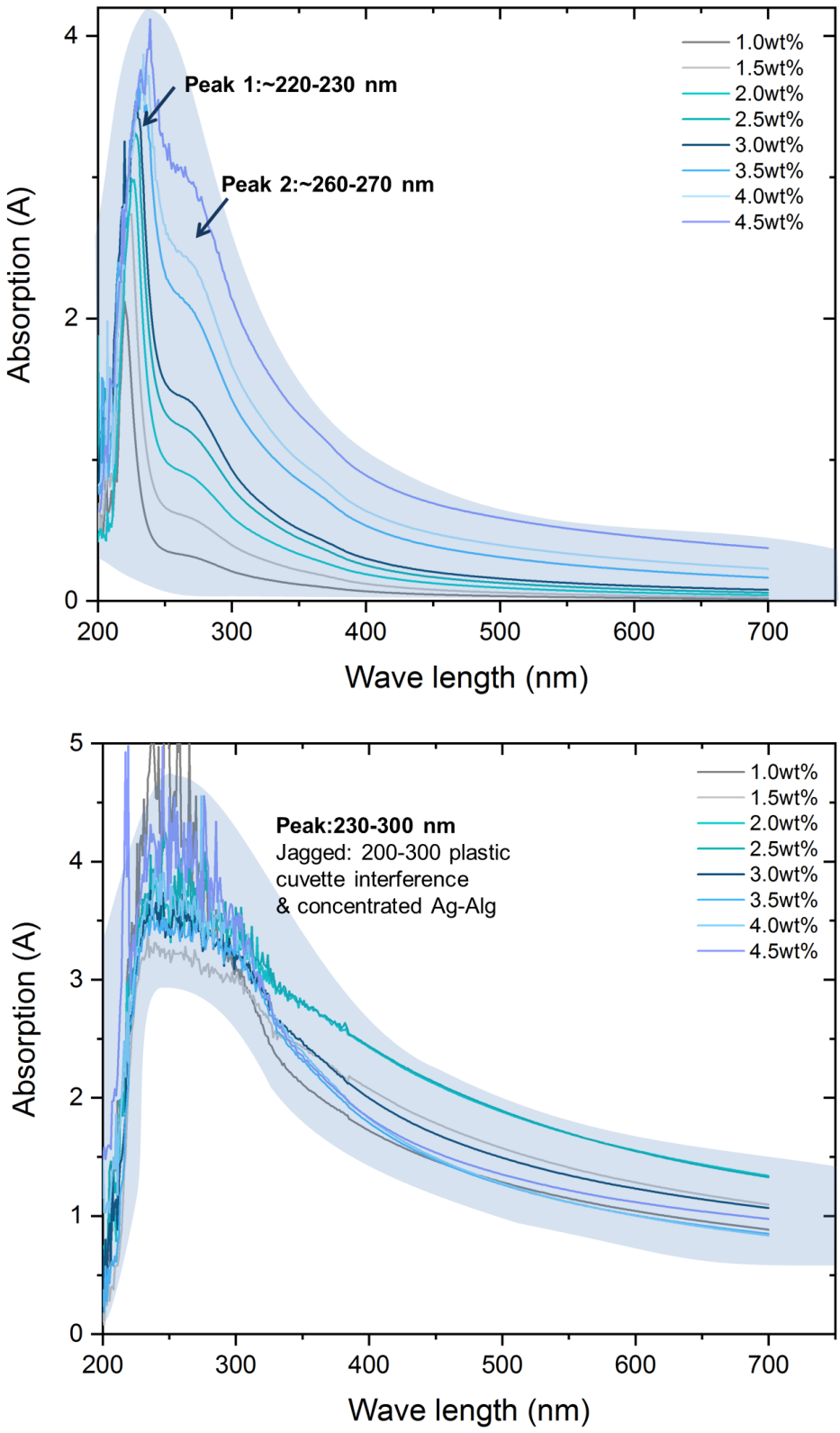

Figure 6.4 UV–Vis absorption spectrum of sodium alginate (Na-Alg, Top) and absorbance at 230-300 nm of silver alginate (Ag-Alg, Bottom)

The absorbance intensity maxima at around 220 nm was found in the UV spectra (Figure 6.4 Top) and coincided with the findings from Amara et al. (2016). Jagged curves appeared in the 4.5wt% sample due to the increased concentration of sodium alginate which was out of the measuring scope of the device (Inter-Chem-Net Instruction Manual, 2000).

The UV-Vis absorption spectroscopy of the synthesised silver alginate (Ag-Alg) samples revealed the appearance of a broad peak at around 230-300 nm (Figure 6.4 bottom). A broad peak indicates presence agglomeration of silver alginate which could be due to the absence of adequate stabilisation (Stevanovic et al., 2012). Besides, massive interference in the 200-300 nm range was found, which were produced by plastic cuvettes due to absorbance of ultraviolet light by plastics. In this case, plastic cuvettes could work perfectly in the range of 380-780 nm, whereas may provide interfered noise in the range of 200-300 nm in this study. The quality of the 200-300 nm (ultraviolet range) spectra could be improved by switching into a quartz cuvette, with the wavelength range of 190-2500 nm (Perkin Elmer Inc, 2006).

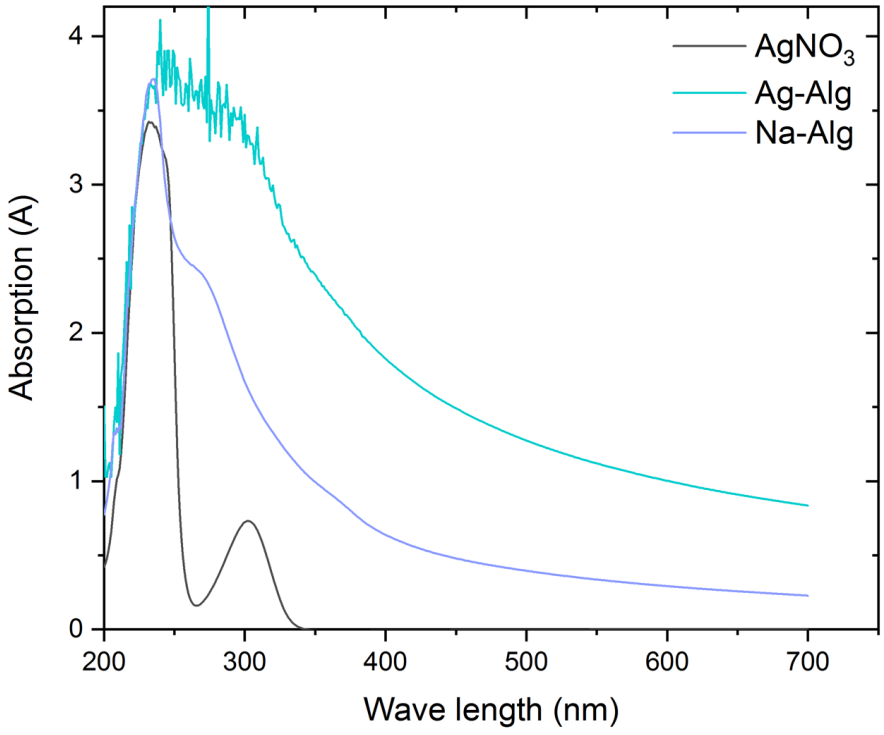

Figure 6.5 Comparison of UV–Vis absorption spectrum of sodium alginate (Na-Alg, 4wt%), silver alginate (Ag-Alg, 4wt%) and $AgNO_3$ (0.1M)

However, no peaks were found at the wavelength of 407 nm, a specific peak of surface plasmon resonance (SPR) of nanosilver particles (AgNPs), which indicating the resulted gel did not contain AgNPs.

As is evident from Figure 6.4 (Bottom), the intensity of the peak did not increase as the concentration of alginate increased and became constant, indicating the complete reaction of silver alginate.

A clear difference between Ag-Alg and Na-Alg were their band range and peak difference. The former has a relatively broader range, from roughly 250-320 nm. The later has one main peak and a side peak at 235 nm and 266 nm, respectively. As for silver nitrate solution, visible absorbance peak was found at around 302 nm which probably corresponds to interband transitions in silver (4d → 5s, p, Heinglein and Meisel, 1998).

The synthesis of silver alginate via sodium alginate and $AgNO_3$ solutions was confirmed by using UV–vis absorption spectra. UV spectra images show that a broad-ranged peak appeared when silver nitrate was formed, which mainly due to agglomeration of silver alginate. Jagged noise was interference produced by plastic cuvettes due to absorbance of ultraviolet light by plastics. To reduce this interference, quartz cuvettes would be more ideal for peaks in the 200-300 nm ultraviolet zone.

TGA characterisation for synthesised Ag-Alg

Thermogravimetric and DTG analyses were performed simultaneously on the sodium alginate and the resulted materials to further confirm silver alginate formation.
Hydrogels were air dried in room temperature and in dark condition, since light is able to enhance the reduction of Ag cations, transforming Ag+ from “egg shell” of alginate to AgNPs.

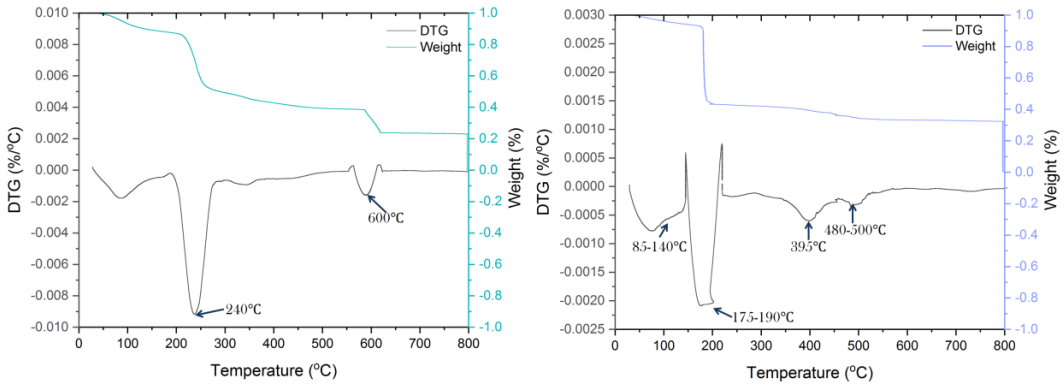

Figure 6.6 TGA curves of sodium alginate (Left) and silver alginate (Right)

The temperatures that sodium alginate decomposes are 240–600 and 600–800 ℃ as shown in Figure 6.6 (Left), where the weight losses are 42.7% and 32.2%, respectively. They correspond to two of DSC peaks at 240 and 600 ℃, respectively. The first peak indicates that energy is required to vaporise the adsorbed water molecules (Zhao et al., 2010). While the second peak represents rapid degradation in the final stage, due to the formation of sodium oxide at around 600 ℃. The thermal behaviour of sodium alginate sample is similar to the ones in Anuradha et al. (2016).

The thermal behaviour of resulted gel was completely different from sodium alginate, where the main decomposing process happened from 85-140 ℃, and then 175-200 ℃. Thermal degradation of Ag-Alg was previously reported by Yadav et al. (2019). The degradation around 200 ℃ might be due to the vaporisation of the adsorbed water molecules and polymer matrix Alg (Oun and Rhim, 2015). A further temperature increase to 800 ℃ showed third and fourth peaks at approximately 395 ℃ and 490 ℃, respectively, which were also reported by Yadav in 2019. However, the typical temperature peak of AgNPs, normally at around 240 ℃ (Rhim et al., 2014), was not found in Figure 6.6, which indicated the synthesised gel was silver alginate. As a result, thermal degradation diagrams further proved the successfulness of synthesised silver alginate, which coincided with the findings from UV spectra data.

Flow behaviour of Ag-Alg and Na-Alg

Shear stress/shear rate relation for both materials was measured to further differentiate their flow behaviour in various mixes. The range of the shear rate in our measurement and analysis was constantly chosen to be $10s^{-1}$ to $200s^{-1}$. We further expanded the concentration range of both alginate materials, from 0.5wt% to 10wt%, to thoroughly examine and differentiate their flow behaviours. This allowed the comparison of flow behaviours of the resulted silver alginate with sodium alginate, and identification of the optimum concentration suitable to be contained in the vascular design (this part will be discussed in the following section).

In a Newtonian fluid, the viscosity is a constant irrespective of the strain rate. In this case, the flow curve corresponding to a Newtonian fluid is expected to be a straight line passing through the origin in a linear scale plot, where the slope identifies the viscosity. However, in this study, a Herschel-Bulkley model was included in the processing program since sodium alginate is a typical material fit in this model (Soukoulis et al., 2016). In this case,

if the curve fit in well with the linear scale in this program, which implied the flow with any curve fell in the family of straight lines, we deduce that the measured sample is a non-Newtonian fluid following in Herschel-Bulkley model, where the effective viscosity (defined as the slope of the line connecting the origin and the corresponding point in the flow curve) is a function of the strain rate.

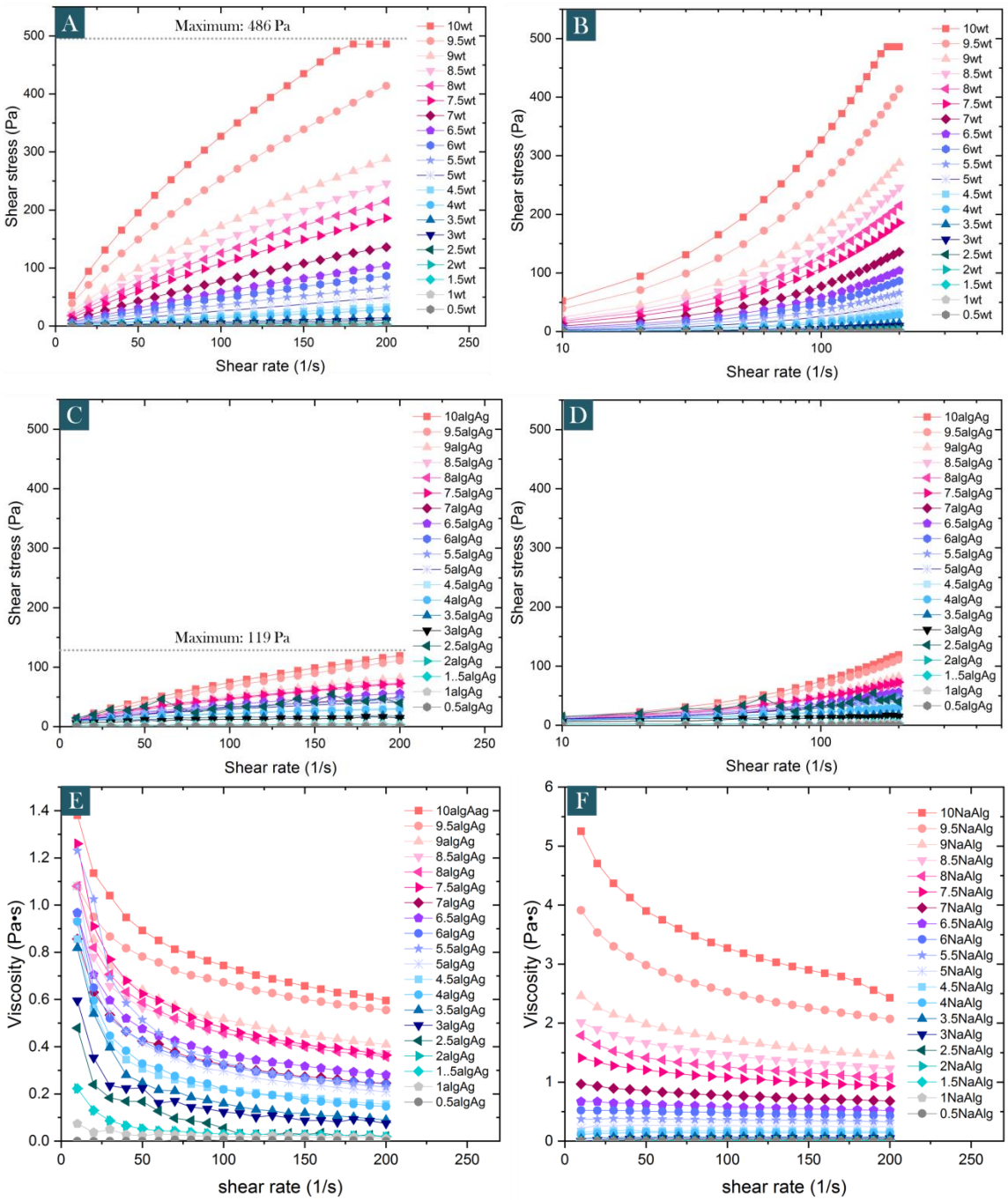

Figure 6.7 Flow curves of sodium alginate in a linear scale (A) and a logarithmic scale (B), and silver alginate in a linear scale (C) and a logarithmic scale (D); Viscosity-shear rate relation of silver alginate (E) and sodium alginate (F)

Figure 6.7 shows the results of sodium alginate (Na-Alg, A) and silver alginate (Ag-Alg, C) with various mixing ratios, it is seen that the relation between shear stress and shear rate are almost fit by a straight line in linear scaled diagrams which applied a Herschel-Bulkley model in the processing program, and also fit in well with its logarithmic scale, which implied the flow curve can be fitted to Herschel-Bulkley model (Nagasawa et al., 2019):

$$\tau = \tau_0 + K\gamma^n \quad (6.2)$$

where: τ_0 equals the yield stress (Pa), K is the consistency coefficient (mPa • s^n), and n is the rheological behaviour index (dimensionless).

The viscosimetric response of both sodium alginate and silver alginate fitting with Herschel-Bulkley model was significantly influenced by the structure conformational state of the biopolymer molecules present in the bulk aqueous phase (Soukoulis et al., 2016). Based on the flow behaviour data shown in the diagram (Figure 6.7 E and F), both Na-Alg and Ag-Alg materials exerted a shear thinning behaviour, where the viscosity of samples becomes lower at higher rates, and with pseudo plasticity being more pronounced in the case of ionic sheared gel structured systems.

Ag-Alg had a much lower viscosity and a much narrower shear stress range, compared with Na-Alg, implying the concentration of Ag-Alg would unlikely to be a significant factor in making great changes in its viscosity.

Silver alginate presented a much obvious shear thinning behaviour in low concentrated samples compared with that of sodium alginate (Figure 6.8), hinting a stronger pseudo plastic character of silver alginate.

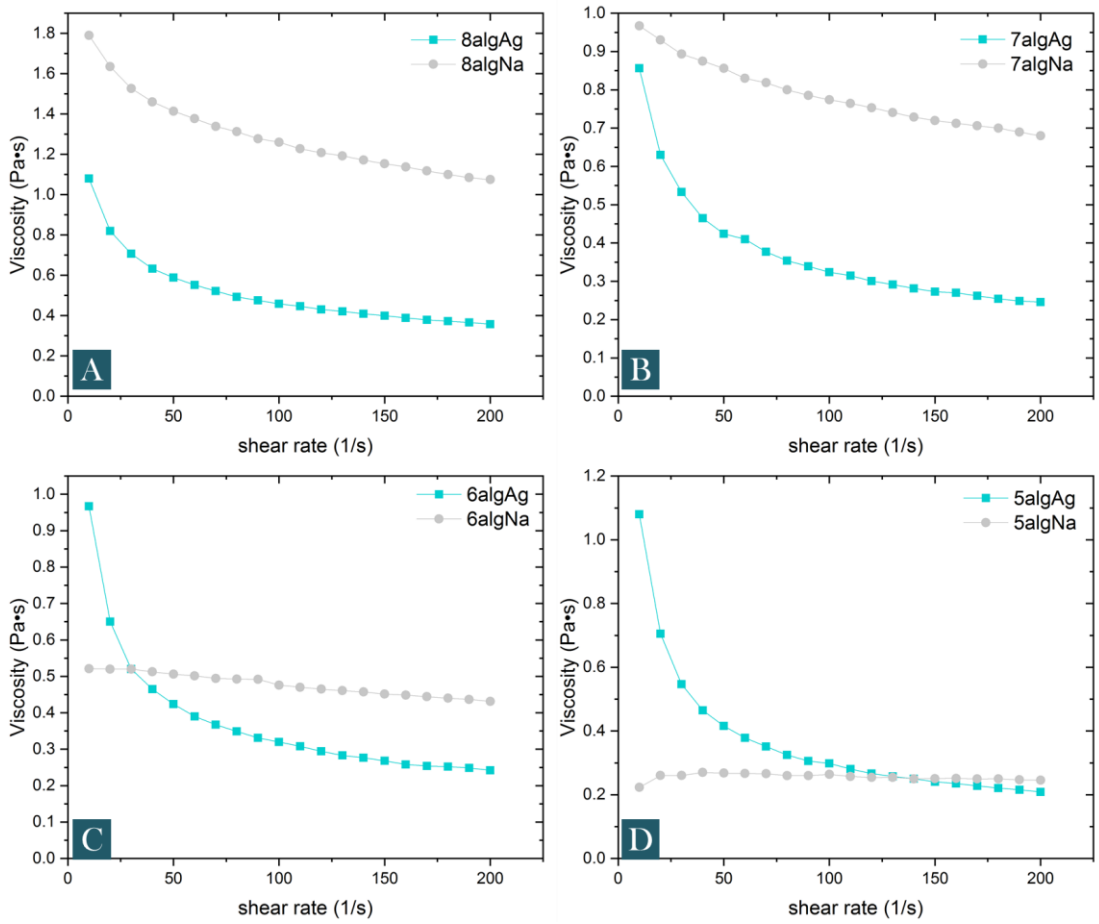

Figure 6.8 Viscosity shear thinning comparison of sodium alginate and silver alginate in 8wt%, 7wt%, 6wt% and 5wt% samples

In this case, it may be related with the intermolecular entanglement of the sodium alginate chains in the dissolved state is rather restricted leading to the formation of very weak structures in low concentration (Ma et al., 2014). On the other hand, silver alginate exerted a stronger pseudo plastic character compared to the sodium alginate indicating the presence of a biopolymer network due to the aggregation of Ag+ alginate "egg-box" structures via their intercluster bonding (Fernández Farrés & Norton, 2014).

In conclusion, both sodium alginate and silver alginate presented a non-Newtonian shear thinning behaviour, but the latter has a much stronger plastic character, specifically at low concentration, due to its aggregated ionic Ag+ alginate "egg-box" structure. This implied the concentration of Ag-Alg would unlikely be a significant factor in making great changes in its viscosity and viscosimetric response. Thus, it is unnecessary to increase the concentration of silver alginate to achieve high quality while producing silver alginate.

6.2 Chemical reaction between Ag-Alg and chloride ions

Silver alginate was successfully synthesised and characterised by UV, TGA and Rheometer in the former section. So in this section, its sensitivity, in terms of reacting with chloride ions was further examined, to establish its threshold value in interacting with Cl^-. Three different chloride source solutions were selected, which were NaCl, $MgCl_2$, and $CaCl_2$, with the aim of mimicking various Cl- sources in real environment.

The reaction between silver alginate and chloride ions is following the equation below:

$$Ag^+ + Cl^- \rightarrow AgCl \downarrow \quad (6.3)$$

Images of reaction between different chloride source were presented in Figure 6.9, where 0.1g, 0.2g and 0.3g 4wt% silver alginate was added to chloride solutions with various concentration: NaCl (0.1M, 0.01M, 0.001M), $MgCl_2$ (0.1M, 0.01M, 0.001M), and $CaCl_2$ (0.1M, 0.01M, 0.001M). As can be seen in the figure, precipitation was observed in the reacted $CaCl_2$ solution, where solid white silver chloride crystals gathered at the bottom of the test tubes, remaining clear solution above. Few unreacted gels was seen in the $CaCl_2$ samples with 0.001 M concentration, hinting that 0.001 M of $CaCl_2$ could unlikely fully dissolve silver alginate. Silver alginate in NaCl samples was mostly dissolved, rather than having precipitation gathered in the test tubes, and "cloudy" solution was also observed. When the reaction between NaCl and silver cations happened in a concentrated solution (above 1.7×10^{-4} M), the diameter of the particles was usually at around 4.16 nm (Greene and Frizzell, 1936). Similar "cloudy" phenomenon happened in $MgCl_2$ solutions, but with a few unreacted gels remaining in the 0.001M and 0.01M samples, which implied a higher threshold of $MgCl_2$ in reacting with silver alginate gels compared with NaCl and $CaCl_2$.This behaviour will be further examined via UV spectra in the following section.

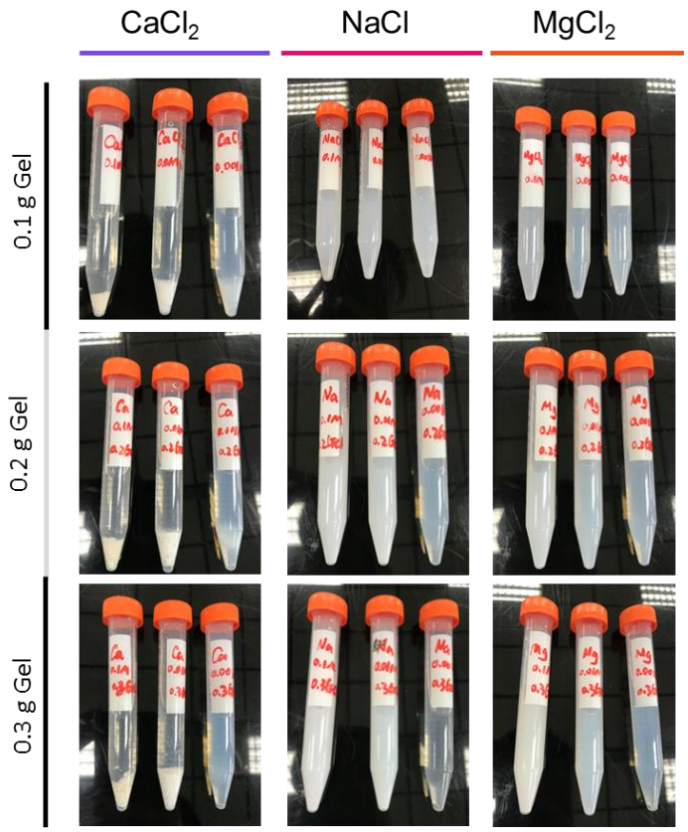

Figure 6.9 Photography of the silver alginate (0.1g, 0.2g, 0.3g) reaction with $CaCl_2$, $MgCl_2$ AND NaCl with various concentrations (0.1M, 0.01M, 0.001M) after 24 hours interaction

6.2.1 Aqueous behaviour under UV spectra

The effluent from the test tubes above was collected, filtered (0.22 μm) and tested via UV spectroscopy to provide useful molecules structure information to reveal the compositions. As shown in Figure 6.10 A, samples with excess $CaCl_2$ (all samples with 0.1M and 0.01M $CaCl_2$), presented a sharp clear peak at around 210-230 nm, representing discrete alginate phase (confirming previous results by Salgado et al., 2007), whereas no AgCl peak was found. This indicated that silver alginate was completely dissolved and all the Ag cations were precipitated at the bottom of the test tubes (see Figure 6.9). For the samples with 0.001M $CaCl_2$ and 0.1g Ag-Alg, UV irradiation showed intense peaks in the ultraviolet region (at around 240 nm and 265 nm) below 300 nm, which were the typical peaks from AgCl by chemical reduction of AgCl during the UV irradiation (Schürch et al., 2002). This might be related to the relatively low concentration of $CaCl_2$, which result in a few AgCl particles below 0.22 μm (filter) remaining in the tested solutions. As for the samples with more Ag-Alg and low $CaCl_2$, silver alginate was still remaining in the solution, which showed a similar UV spectra curve with original silver alginate curves in the previous section.

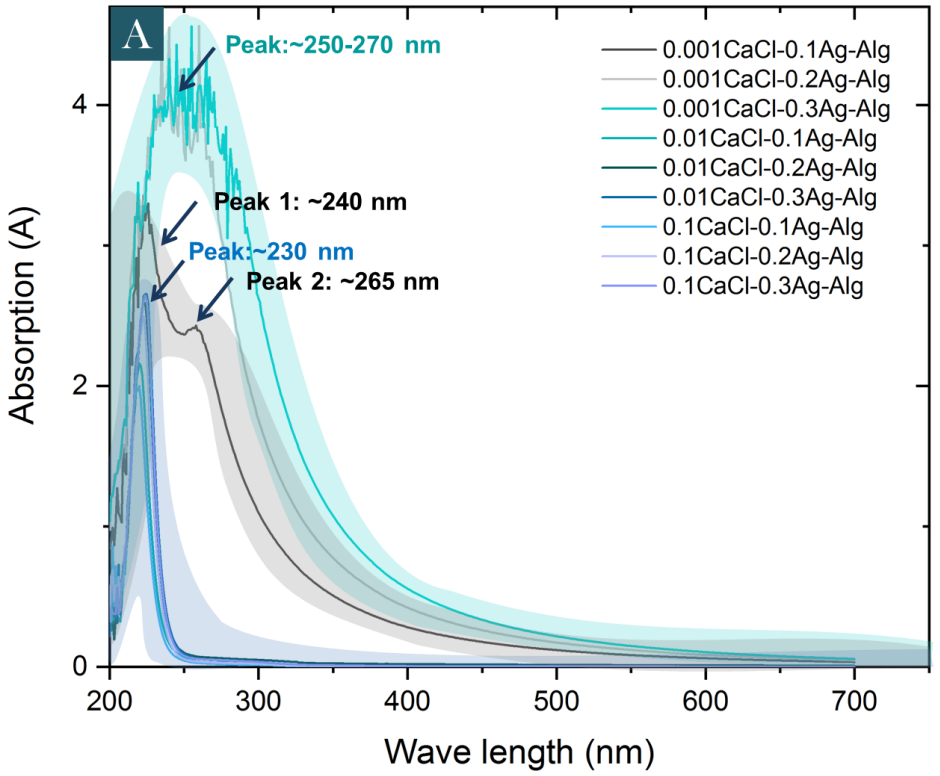
A
Peak:~250-270 nm
Peak 1: ~240 nm
Peak:~230 nm
Peak 2: ~265 nm
0.001CaCl-0.1Ag-Alg
0.001CaCl-0.2Ag-Alg
0.001CaCl-0.3Ag-Alg
0.01CaCl-0.1Ag-Alg
0.01CaCl-0.2Ag-Alg
0.01CaCl-0.3Ag-Alg
0.1CaCl-0.1Ag-Alg
0.1CaCl-0.2Ag-Alg
0.1CaCl-0.3Ag-Alg
Absorption (A)
Wave length (nm)
0
2
4
200
300
400
500
600
700

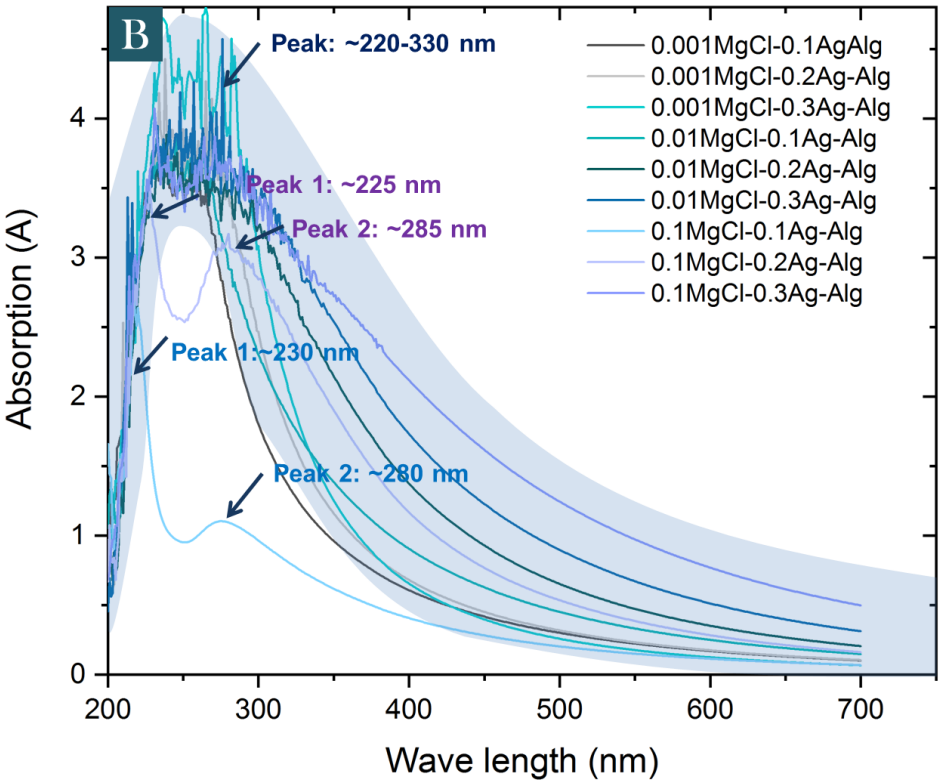
B
Peak: ~220-330 nm
Peak 1: ~225 nm
Peak 2: ~285 nm
Peak 1:~230 nm
Peak 2: ~280 nm
0.001MgCl-0.1AgAlg
0.001MgCl-0.2Ag-Alg
0.001MgCl-0.3Ag-Alg
0.01MgCl-0.1Ag-Alg
0.01MgCl-0.2Ag-Alg
0.01MgCl-0.3Ag-Alg
0.1MgCl-0.1Ag-Alg
0.1MgCl-0.2Ag-Alg
0.1MgCl-0.3Ag-Alg
Absorption (A)
Wave length (nm)
0
1
2
3
4
200
300
400
500
600
700

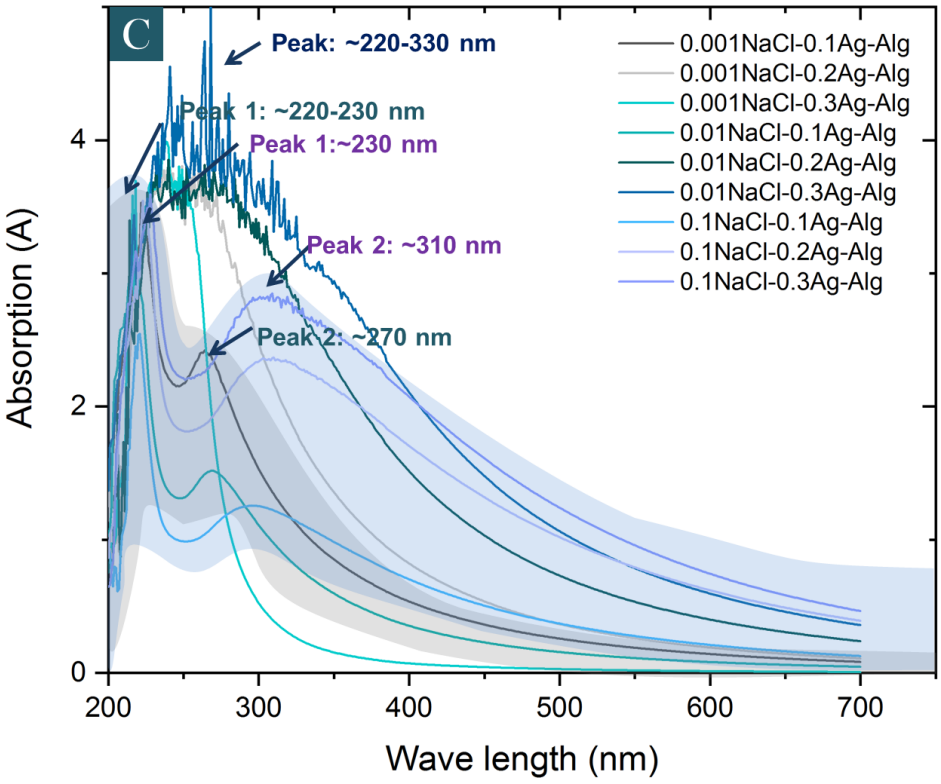

Figure 6.10 Absorption spectra of samples in $CaCl_2$ (A), $MgCl_2$ (B) and NaCl (C), with different concentration in aqueous solutions. The solution concentrations were adjusted using deionised water.

When the solution was changed to $MgCl_2$, the trend observed here is quite different compared with the ones shown in $CaCl_2$ samples. There were only two types of curves (Figure 6.10 B), (i)AgCl curves with main absorption peaks at around 225 nm and 280 nm, in the samples with 0.1 M $MgCl_2$ solution and below 0.2g Ag-Alg; and (ii) silver alginate curves in other samples. Interestingly, compared with the peaks in $CaCl_2$ samples, AgCl peaks in the $MgCl_2$ samples undergo a red shift (Bathochromic effect), meaning a change in absorbance to a longer wavelength, following the high concentration of chloride ions, which could cause significant red shift (Tong et al., 2020).

As for the samples with NaCl solution, the curve type can also be classified into three types (Figure 6.10 C): (i) silver alginate curves, (ii) AgCl curves (in the grey shade), and (iii) red-shifted (in the blue shade) AgCl curves. Similar to $MgCl_2$ samples, "cloudy" AgCl particles remained in solution, so that their typical absorption peaks were mostly detected via UV spectra. AgCl was found in all samples with high NaCl concentration (0.1M), and samples with low Ag-Alg gels (0.1g), indicating sufficient interaction. Remarkably, AgCl curves observed in 0.001 M and 0.01M NaCl solution also implies the threshold of NaCl is lower than $MgCl_2$, in which the later observed AgCl curves only in 0.1M solutions.

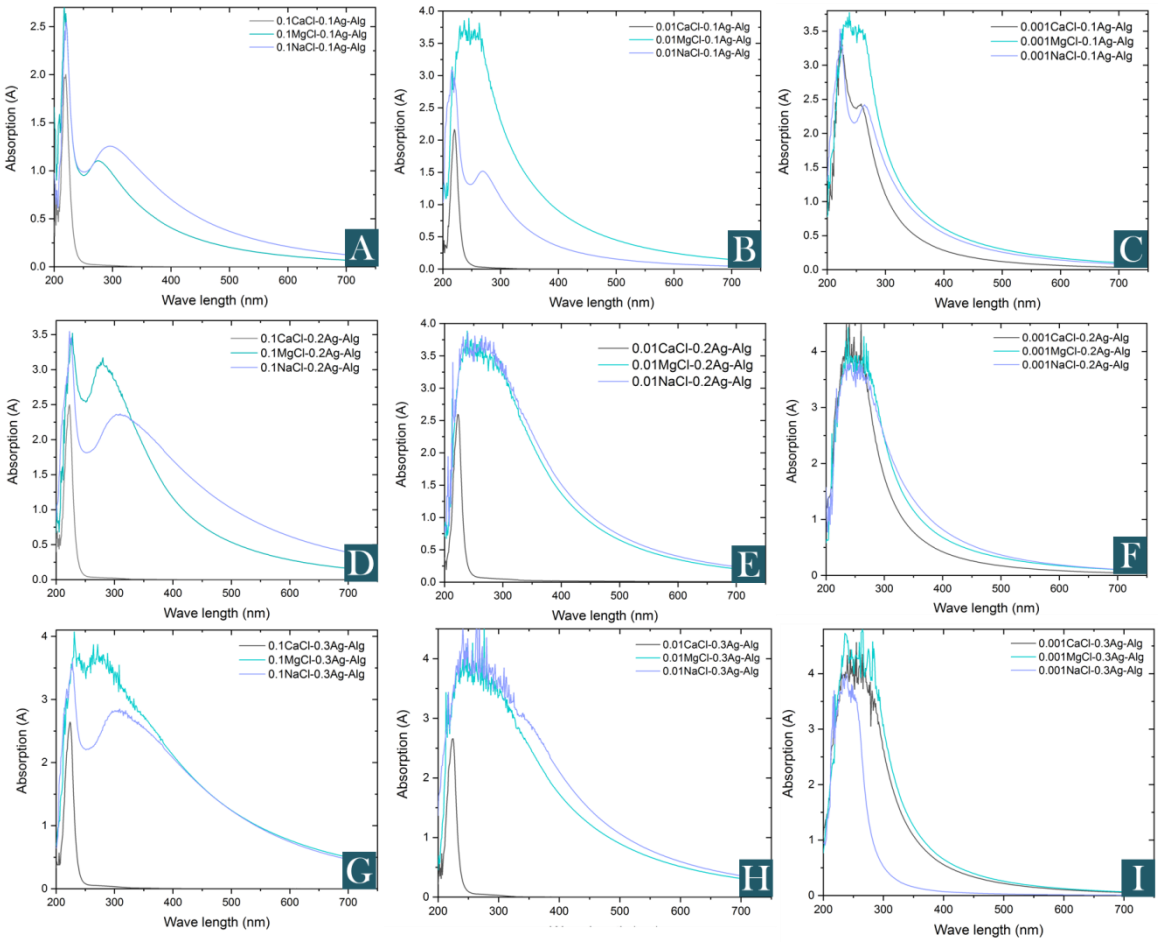

Figure 6.11 Absorption spectra comparison diagrams of samples in with different amount of Ag-Alg, 0.1g Ag-Alg (A, B, C), 0.2g Ag-Alg (D, E, F), 0.3g Ag-Alg (G, H, I) in various chloride source solution

If we compare the curves from different chloride source under the same condition (same solution concentration and amount of Ag-Alg gel, Figure 6.11), a clearer trend can be found as $MgCl_2$ samples (green curves) has the highest threshold in terms of reacting with Ag-Alg. Typical silver alginate curves were found in most of the $MgCl_2$ samples, AgCl curves were found only in 0.1M samples. This also coincided with the result of photography images in Figure 6.9. On the other hand, $CaCl_2$ was quite successful in terms of chloride sensitivity and reaction, whereas this process will result in macro-scaled AgCl crystals, thereby bringing potential risks in blocking the vessel system for self-healing. In this case, the NaCl solution is by far the most optimum candidates in providing chloride ions for the following chemical triggering tests.

6.2.2 Chloride ion concentration

Quantitative determination of Cl^- ion concentration in the solutions after Ag-Alg reaction were required for monitoring the progress of chloride removal and to determine when

the treatment is considered to be finished. All tests were carried out on 100 ml solutions containing variable Cl^- ion concentrations after Ag-Alg reaction. The 0.01 M chloride solutions were selected with the aim of matching the test range of EDT ISE-1261 device. Then 1g Ag-Alg gel was added, and the samples were tested at 0, 0.5, 1, 2, 4, 6, 24, 48 and 72h, as shown in Figure 6.12. Original concentrations of $CaCl_2$, NaCl and $MgCl_2$ before adding Ag-Alg were 241 ppm, 273 ppm and 219 ppm, respectively. All the data collected from EDT device were atomically tested three times and then provided an average number.

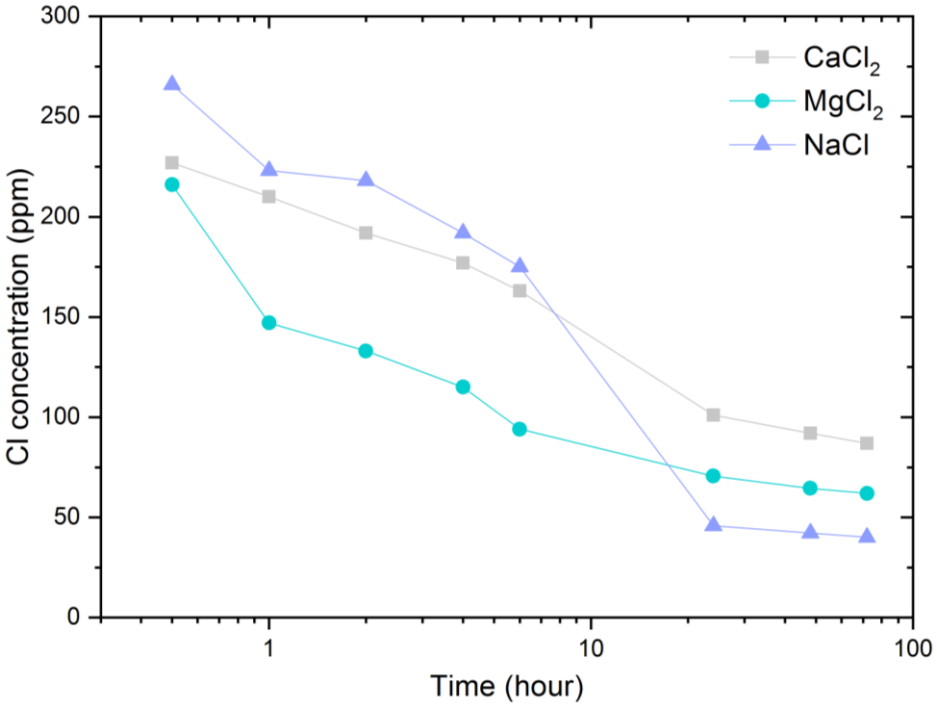

Figure 6.12 Chloride ion concentrations from different sources of Cl (0.01M, 100ml $CaCl_2$/$MgCl_2$/NaCl solution and 1g Ag-Alg) after 72 hours reaction via Chloride half-cell ISE-1261, provided by EDT directION®

The amount of Cl- ions remained in solutions after reacting with silver cations were detected. A significant decrease in Cl concentration appeared in $MgCl_2$ solution, dropping from 219 ppm to 147 ppm in the first hour, roughly 32% of decrease. A similar trend happened in NaCl solution, declining from 273 ppm to 223 ppm. $CaCl_2$ sample experienced a relatively moderate chloride ion decrease process. After 72 h of reaction, NaCl remained the least chloride ions in the solution, with only 40.1 ppm, roughly 14% of chloride ions remaining. Chloride concentrations after 72 hours in $MgCl_2$ and $CaCl_2$ were relatively higher, at 62 ppm and 87 ppm, which were approximately 28.3% and 36% remaining. The results indicated that for between NaCl and $MgCl_2$, the question is not if

they are able to dissolve silver alginate, but how efficient they can be. Obviously from both UV spectra and EDT chloride concentration tests, silver alginate gel was more sensitive to NaCl solution compared with $MgCl_2$. However, $CaCl_2$ could result in macro-scaled AgCl materials, which might potentially block the designed vascular system thereby hampering healing/inhibitor release.

6.2.3 TGA of silver chloride precipitation

TGA was also employed to further confirm the composition of the predicated material, as shown in Figure 6.13. Since the Ag-related materials were heat and light sensitive, the precipitation was filtered, washed (DI water) and air dried in a dark environment.

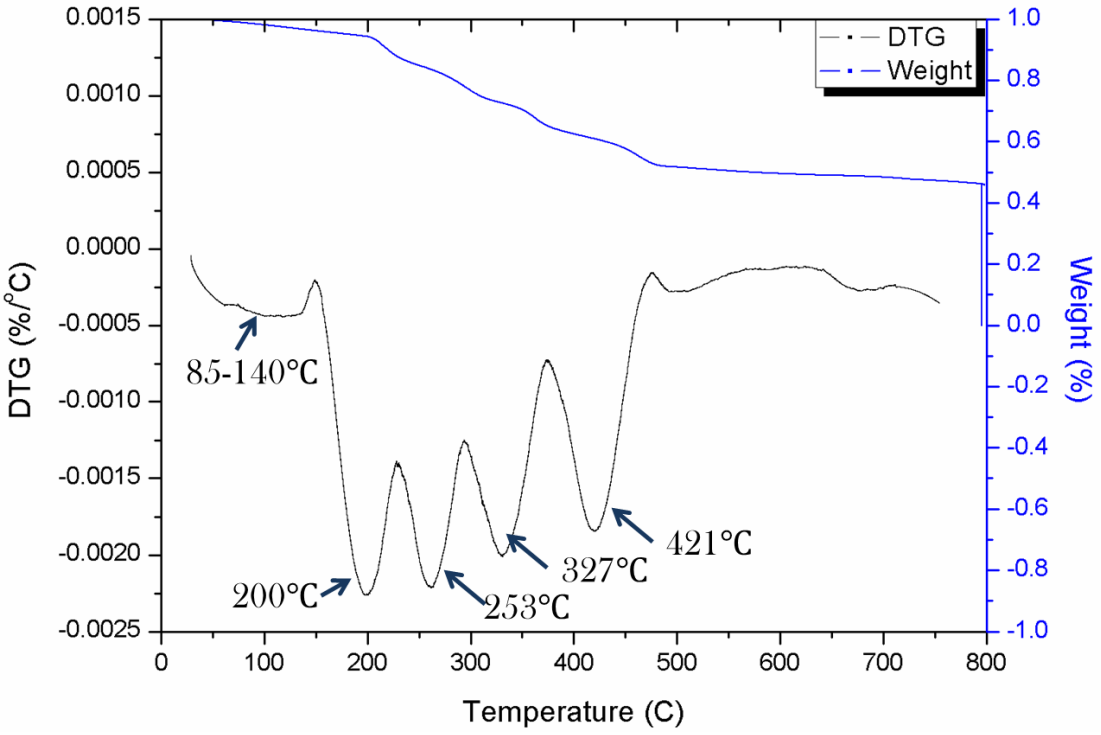

Figure 6.13 Weight loss and DTG curves of silver chloride precipitation

Weight loss before 200 ℃ was related with unreacted silver alginate. As stated in the previous section, the thermal behaviour of resulted gel happened from 85-140 ℃, and then 175-200 ℃. Thermal degradation of Ag-Alg was previously reported by Yadav et al. (2019). The degradation around 200°C might be due to the vaporisation of water and polymer matrix Alg (Oun and Rhim, 2015). For the peaks from 250-400 ℃, it was found that thermal decomposition of silver chloride particles started at around 250-300°C (Persin et al., 2014), whereas the peak at 421 ℃ was overlapped with silver alginate decomposing peaks.

6.3 Vascular design exploration for chemical triggering material

6.3.1 Double-layered lattice design

The idea of designing a chemical triggering vascular system is to provide a desirable structure that can host both the main healing agents and chemical triggered material (Ag-Alg). Ideally, the design for chemical triggering vascular system should achieve (i) be able to release the healing agents through the wall; (ii) contain host place for housing chemical sensitive materials; (iii) enable sufficient path flow for healing agents. In this chemical triggering system, the agents can be both inhibitors to prevent further corrosion and the healing agents when the crack happens. For the early stage, vascular networks containing inhibitors as agents could be able to react with the chloride ions and protect the cementitious structure. When the chloride ions already triggered cracks in the cementitious materials, healing agents in the vascular network can be responsible for healing the damage. Since the vascular system is a cyclic system, agents can be easily replaced by changing agent reservoir. At an early stage, inhibitors can be pumped into the network to react and prevent the corrosion; .then if the damage has already occurred, inhibitors can replace the healing agent.

Column shaped double-layer lattice design

A column shaped vessel was designed as shown in Figure 6.14. The whole structure was designed according to the size of the targeted beam (40 mm ×40 mm ×160 mm), with a length of 100 mm, an inner diameter of 7 mm and an outer diameter of 10 mm.

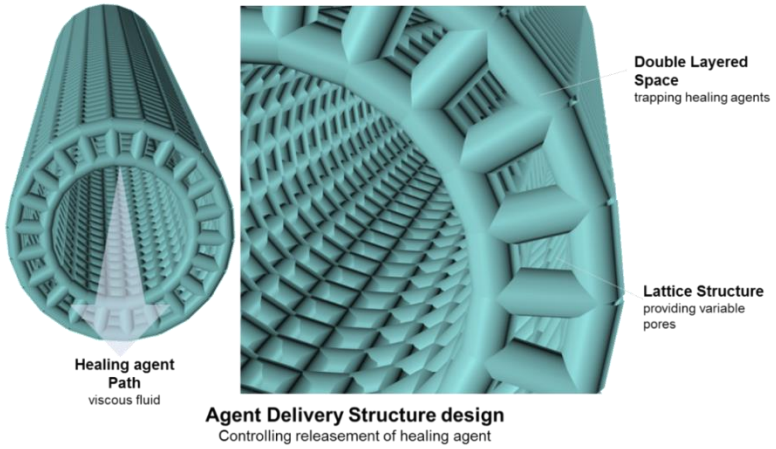

Figure 6.14 A schematic diagram of the column shaped double-layer lattice design, where the inner path allows healing agents traveling, and the double layered space provided a place to host chemical triggered materials, such as silver alginate in this case.

Lattice structure can provide sufficient channels for healing agent release. A double layered space was added to the lattice structure, ensuring the design to be able to host chemical sensitive materials. Moreover, the inner wall has smaller pore size compared with that of the outer wall, which made it easier for the double layered structure to be able to separate the healing agent traveling in the tunnel with the chemical sensitive materials from the outer layer.

With the aim of comparing and evaluating the agent release behaviour in different pore sizes, three different pores size models were designed, whilst keeping other parameters same. The polys in the design were firstly segmented into 400 parts (L sized model: 16 parts for each layer, 1.36 mm outer pore size, 0.77 mm inner pore size), 630 parts (M sized model: 18 parts for each layer, 1.14 mm outer pore size, 0.62 mm inner pore size) and 800 parts (S sized model: 20 parts for each layer, 0.97 mm outer pore size, 0.50 mm inner pore size), respectively. Then shell thickness was set to 0.6 mm for each model.

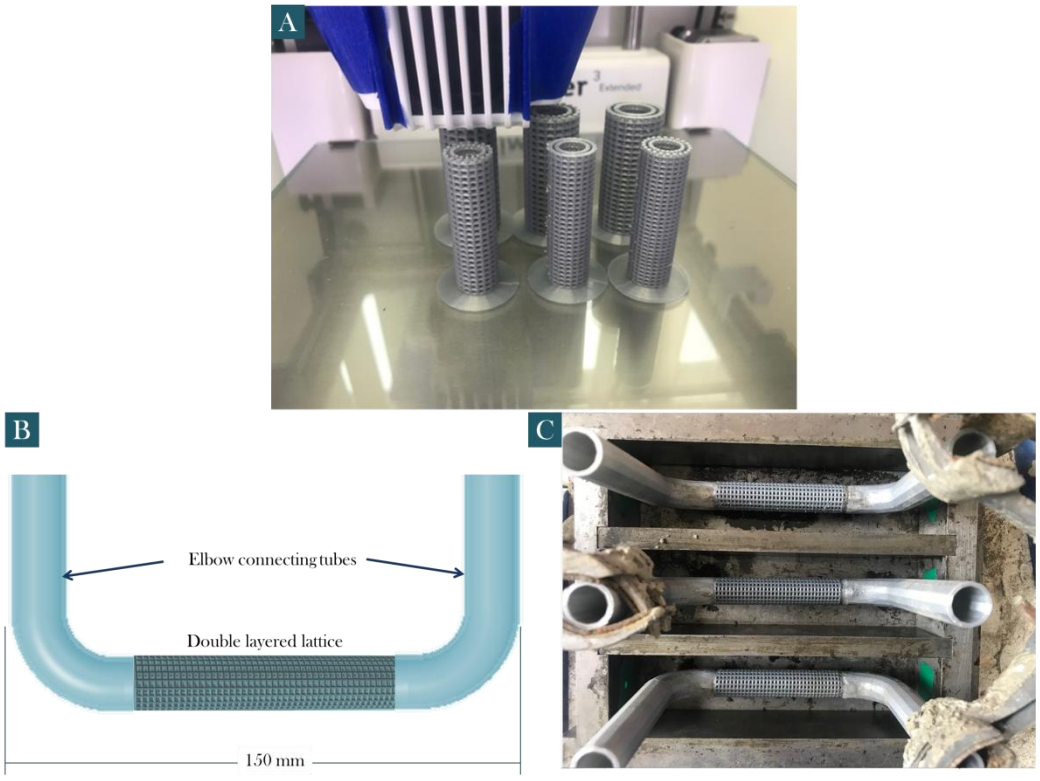

Figure 6.15 Photography of column lattice designs with different pore size (L, left; M, middle, S, right) being printed over time (A), connecting tubes added to the design (B), and fitting in cement mould (C)

The models were designed in AutoCAD® and then printed using a Ultimaker® 3 Extended 3D printer (Fused deposition modelling system, FDM) and Cura® software

using Polylactic acid (PLA, by Ultimaker®) filaments. Figure 6.15 A shows the three different pores sized (L, M, S sized) lattice model being built up over time. Multiple columns could be printed to improve printing productivity, since this design normally took 48 hours to be printed.

To adapt this column double layered lattice model to the cement matrix, connecting elbow tubes were added by soldering (Figure 6.15 B). The total length of column lattice tubes including elbow connecting tubes was 150 mm, which perfectly fit in the stainless-steel moulds (40 mm × 40 mm × 160 mm) for casting cementitious matrix (Figure 6.15 C).

Plate shaped double-layer lattice design

Similarly, a plate-shaped double layered design (Figure 6.16) might be beneficial to the surface area, since surface or areas that are close to the surface would have a higher chance in contacting with high chloride environment, such as sea water, saline water. A plate shape would provide relatively larger contact surface compared with column shape, bringing more chance in reacting with chloride ions, thereby triggering chemical sensitive layer to be dissolved and releasing healing agents/inhibitors from vessels.

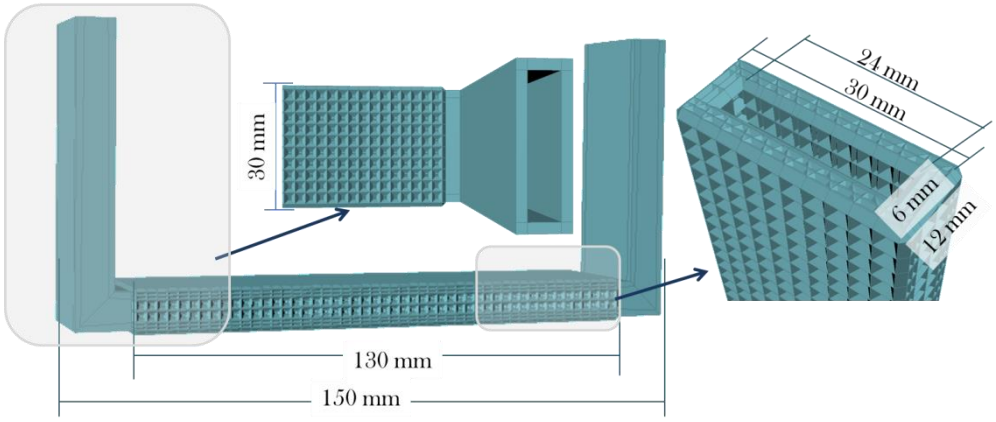

Figure 6.16 A schematic design of plate shaped double layer network

The polys in the design were firstly segmented into 2000 parts, excluding the edge area (3 mm in thickness), which resulted in the external pore size to 1.5 mm and the inner pore size to 0.6 mm. Similar with the idea in the column lattice design, a double layered space was designed for hosting chemical sensitive material (such as silver alginate in this case), with an inner tunnel (24 mm width × 6 mm height) allowing healing agents/inhibiter to pass through. Elbow connecting tubes were also attached to the main design in a

rectangular shape. Similar to the column shaped design printing process, the plate-shaped model can be also printed under the same printing condition using PLA as printing material.

Upgraded column double-layer lattice design

For specific healing agents, such as two-part epoxy, single channelled designs were not suitable to differentiate two part of the liquid. Thus, an upgraded version adding up from the column shaped double layered design was shown in Figure 6.17.

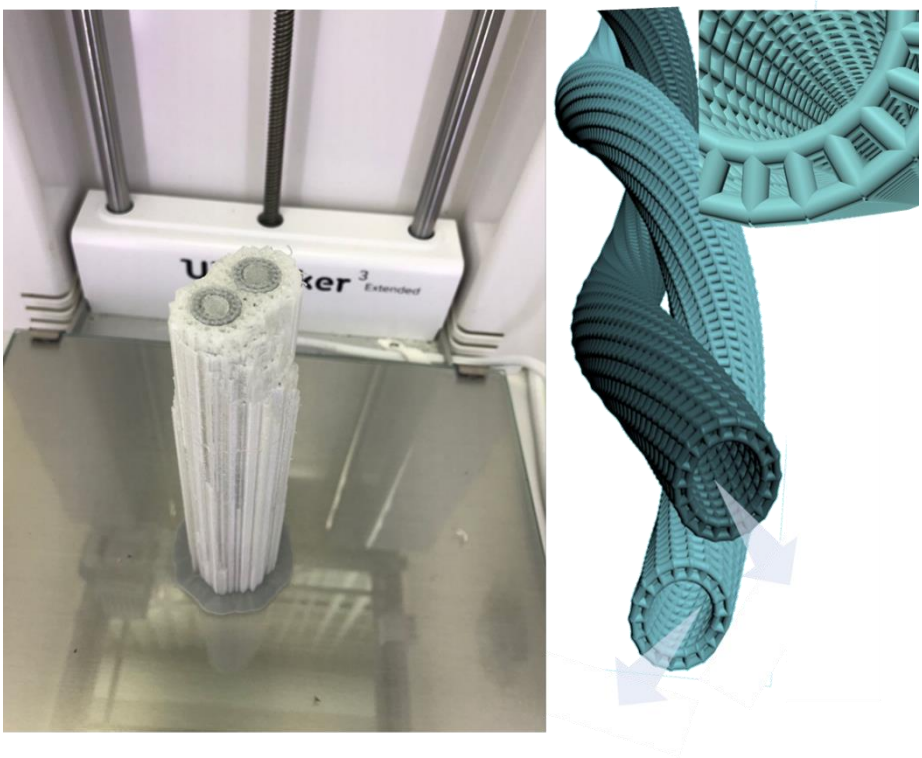

Figure 6.17 A schematic design of an upgraded column shaped double layer network (right), and a photography of the model being printed in an Ultimaker® 3D printed via two materials (PLA, silver; PVA, white)

Separate channels for both hardener and epoxy were designed with the double layered space, similar with the column shaped double layered design. An angle of 400 of twisting rate was added to ensure the channels were symmetrically distributed in cement matrix within the 30 mm width of the model size. For this upgraded design, a conceptual model was only printed at this stage, since the original column shaped double layered design need to be proved first. Evaluation of the column-shaped and plated shaped designs will be discussed in the following section.

This upgrade model was printed via two different materials, PLA and PVA. This is because this model contained two separate tubing structures, which need to be connected during printing process, otherwise would result in printing failure. The former, PLA was the material for generating the main model structure, whereas PVA (which was also mentioned in Chapter 5) was a supporting material that filled up with the empty space to provide a more stable condition for printing process. The silver-coloured part in Figure 6.17 was PLA material, and the white part was PVA, a supportive material. The PVA can be either broke out manually or removed within 1 hour when the structure was dipped into water.

In the following sections, only the first two designs, namely the column shaped and plate shaped, were evaluated. The upgrade spiral design is considered a derivative of the column model (basically the same design), with only an additional tube added, and this could be validated by the results from the column shaped model.

6.4 Behaviour of lattice models in cement

Survival of both column shaped and plate shaped models during cement curing became a large concern due to its lattice structures. Since those porous structures could potentially allow cement to occupy the double-layered space, thereby forming a solid cement layer, making the vascular could neither be able to release the healing agents to heal the cracks, nor release inhibitors to reduce chloride ions concentration for avoiding further damage.

In this study, an extreme testing situation was considered, assuming the double layered space was empty, and to understand that to what extent could cement occupy this space in various models. Thus, both column-shaped and plate-shaped models were tested in cement matrix, to evaluate their feasibility in cement without adding any chemical sensitive materials.

6.4.1 Column shaped model in cement

Prismatic specimens were prepared for testing the viability and performance of the 3D printed porous Polylactic acid (PLA) vasculature within a cement matrix, with the aim of evaluating if PLA porous structure can survive in cement paste and determining ideal pore size range for preventing cement travelling into the inner tube.

The cement paste mix was prepared with Ordinary Portland Cement (PC) (CEM-I, 52.5 by Hanson) and water (detailed information can be found in Chapter 3).Following the mixing, models were first stabilised by a few iron support stands in the mould, and then loaded cement paste into the moulds with PLA structures settled (Figure 6.18).

Figure 6.18 General set-up for cement casting (Left), and a cured beam after 7 days (Right)

Double layered space occupation under CT

To understand the resistance of lattice structure in reacting to the cement during the curing process and the distribution of cement/secondary minerals in the double layered structure, CT-scan was employed to obtain a three-dimensional map of the various sized column models in cement as shown in Figure 6.19.

The grey level images of prisms incorporating L/M/S sized column shaped double-layered models were obtained from CT scanning software. The light grey parts represented the cement matrix, as cement had a relatively high density and elements atomic number, compared with the dark grey parts indicate PLA tubes. Bubbles within cement were represented by black, indicating empty space. Cement, PLA structures and empty space were recognised, picked and separated by using Mimic software and were marked by various colours. Specifically, the fluorescent green colour in Figure 6.19 represented the cement intruded into the double layered space. Violet marked the S sized column shaped model with 1.36 mm outer pore size and 0.77 mm inner pore size. Similarly, pink and cyan marked M sized model and L sized model, respectively. It revealed that in all sized models, cement was able to penetrate the porous structure and reach the double-layered zone. Specifically, more cement was seen in the double-layered space from L sized model, and we could even observe the cement in the inner tunnel. There was also low-density mineral appeared in L sized inner tunnel, which was shown

in Figure 6.19 in relatively dark grey. In the M sized model, low-density mineral was also found in the inner tunnel, but with a much fewer amount. As for the S sized model, no low-density mineral was found, and the cement only occupied few areas of its double-layered space.

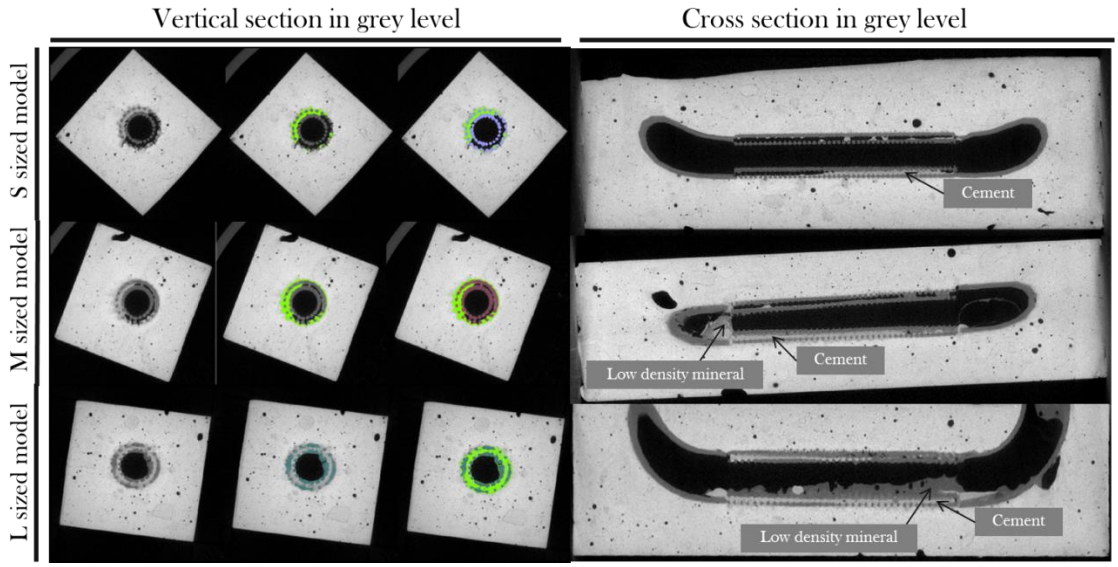

Figure 6.19, CT gray level images of cement matrix incorporating with L/M/S model, where the fluorescent green coloured part represents cement in the model; violet coloured part represents PLA structure of S sized model; pink coloured part represents PLA structure of M sized model; cyan coloured part represents PLA structure of L sized model

With the aim of further understanding cement occupation in double-layered space quantitatively, bulk cement, PLA structures, cementitious mineral in PLA structures and empty space were then separated by using Mimic software and reconstructed in a three dimensional images showed in Figure 6.20.

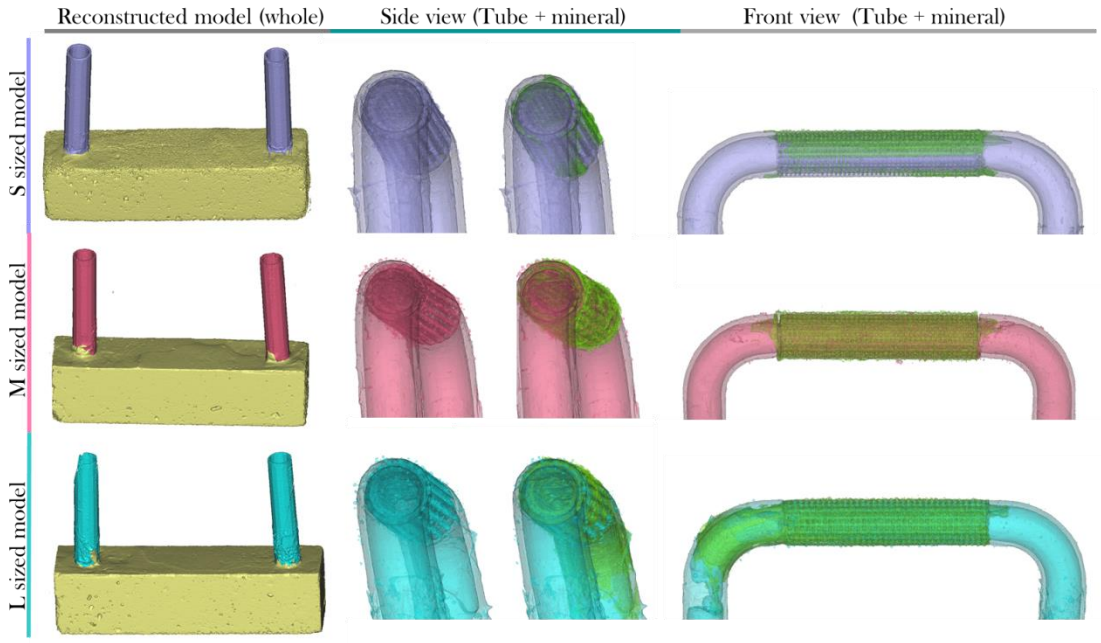

Figure 6.20 3D reconstructed images of column double layered lattice samples (violet represents PLA structure in S sized model, pink represents PLA structure in M sized model, cyan represents PLA structure in L sized model, yellow bulk shows cement prisms are shown in yellow bulk (all samples); the penetrated materials were marked in green

To quantify the cement/cementitious mineral occupation in PLA double-layered structure, we defined a double layer space integrity ratio (I_{dy}), by comparing cement volume within double layered space (v_{c-dy}, mm^3) with the empty space volume remaining in (v_e, mm^3) from CT reconstructed model as:

$$I_{dy} = (1 - \frac{v_{c-dy}}{v_e + v_{c-dy}}) \times 100\% \quad (6.4)$$

As we can observe from the CT reconstruction image, the integrity ratio I_{dy} of the double layered space in L sized model was around 73%, which is followed by 51% in the specimen cooperated with M sized model. As for the prism with S sized model in violet, its cement integrity ratio was roughly 36%. The lowest healing ratio was observed in the S sized model sample, this figure was roughly half to the one with L sized model, since small pores below 1 mm in diameter could significantly block cement from penetrating to the double-layered space with full pore open. More interestingly, a 0.5 mm inner pore size in the S sized model managed to avoid cement or any other secondary mineral penetrate to its inner tunnel, which brought great potential in introducing S sized model for further research. However, for both M sized and L sized model, relatively higher the integrity ratio I_{dy} of the double layered space were observed in this study. This implied

models with pore size larger than 1 mm were unlikely to be able to prevent cement from entering.

Low density mineral in inner tunnel

Crystallised materials near the joint of PLA tubes and inside PLA tunnels were found in both L sized and M sized model from photography in Figure 6.18 (right) and Figure 6.19 from CT scanned images. Crystallised mineral expanded to the inner tunnel zone of the model, in a darker grey level compared with cement, as described in the previous section.

To figure out the component of this mineral, the mineral was collected from the PLA inner tunnel using measuring spoon, and then detected via a SEM-EDX device. Fine filamentary crystal was found both under Leica microscopy and SEM device as shown in Figure 6.21.

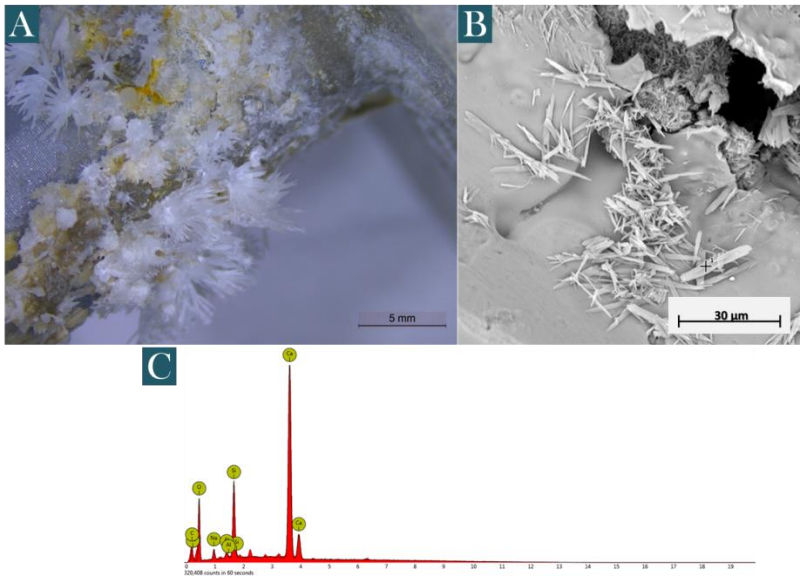

Figure 6.21. Microscopic image of crystalised material near the joint of PLA tube (A), SEM image of crystalised mineral(B), and its EDX pattern (C)

Porous structure in the lattice models provided an ideal zone for cement paste and air (CO_2) interaction, and generated are as calcium monocarbonaluminate hydrate, which was confirmed by SEM-EDX (Figure 6.21 C). This can be explained by the equation below (Berman et al., 1961 and Kakali et al., 2000):

$$3CaO \cdot SiO_2 + 3CO_2 + nH_2O \rightarrow SiO_2 \cdot nH_2O + 3CaCO_3 \quad (6.5)$$

$$3CaO \cdot Al_2O_3 + CaCO_3 + 11H_2O \rightarrow 3CaO \cdot Al_2O_3 \cdot CaCO_3 \cdot 11H_2O \quad (6.6)$$

As a result, porous structure provided an ideal zone for cement paste and air (CO_2) interaction, and generated areatus calcium monocarbonaluminate hydrate, which was confirmed by SEM-EDX. Areatus minerals were found in the beam embedded with L sized model and M sized model, with an outer pore size larger than 1mm, whereas, this mineral was not found in the inner tunnel of the S sized model. This indicates that pore size smaller than 1 mm could significantly reduce cement penetration to the double-layered space, and a size pore of 0.5 mm could almost prevent cement penetration. S sized model by far is more ideal for controlling unexpected mineral generation within tubes. On the other hand, this could also help with stabilise chemical sensitive materials within the double-layered space from contacting with cement at early stage.

6.4.2 Plate shaped model in cement

Similar to column shaped models, plate shaped model were also prepared with Ordinary Portland Cement (PC) (CEM-I, 52.5 by Hanson) and water at water/cement (w/c) ratio of 0.4. Stainless-steel moulds (40 mm × 40 mm × 160 mm). Plated shaped models were also stabilised by a few iron support stands in the mould, and then loaded cement paste into the moulds with PLA structures settled. After 7 days of curing, specimen with plate shaped model was also examined under CT scan, to further its performance in cement matrix with full pores open.

Double layered space occupation under CT

CT-scan was applied to obtain a three dimensional images of the plate shaped model in cement as shown in Figure 6.22. Grey level images of the specimen embedded by plate shaped double-layered models were obtained from CT scanning software. Similarly to the CT scan images from the column sized models, the light grey parts represented the cement matrix due to high density and elements atomic number; dark grey reflected the PLA structures, and the bubbles within cement were represented by black, indicating empty space. Different materials were recognised, picked and separated via Mimic software and were marked by various colours. The fluorescent pink colour in Figure 6.22 represented the cement intruded into the double layered space, and cyan marked the plate shaped model. Bulk cement, PLA structures, cementitious mineral in PLA structures and empty space were also separated via Mimic software and reconstructed in a three dimensional images showed in the bottom

of Figure 6.22, to further study its cement occupation in double-layered space quantitively.

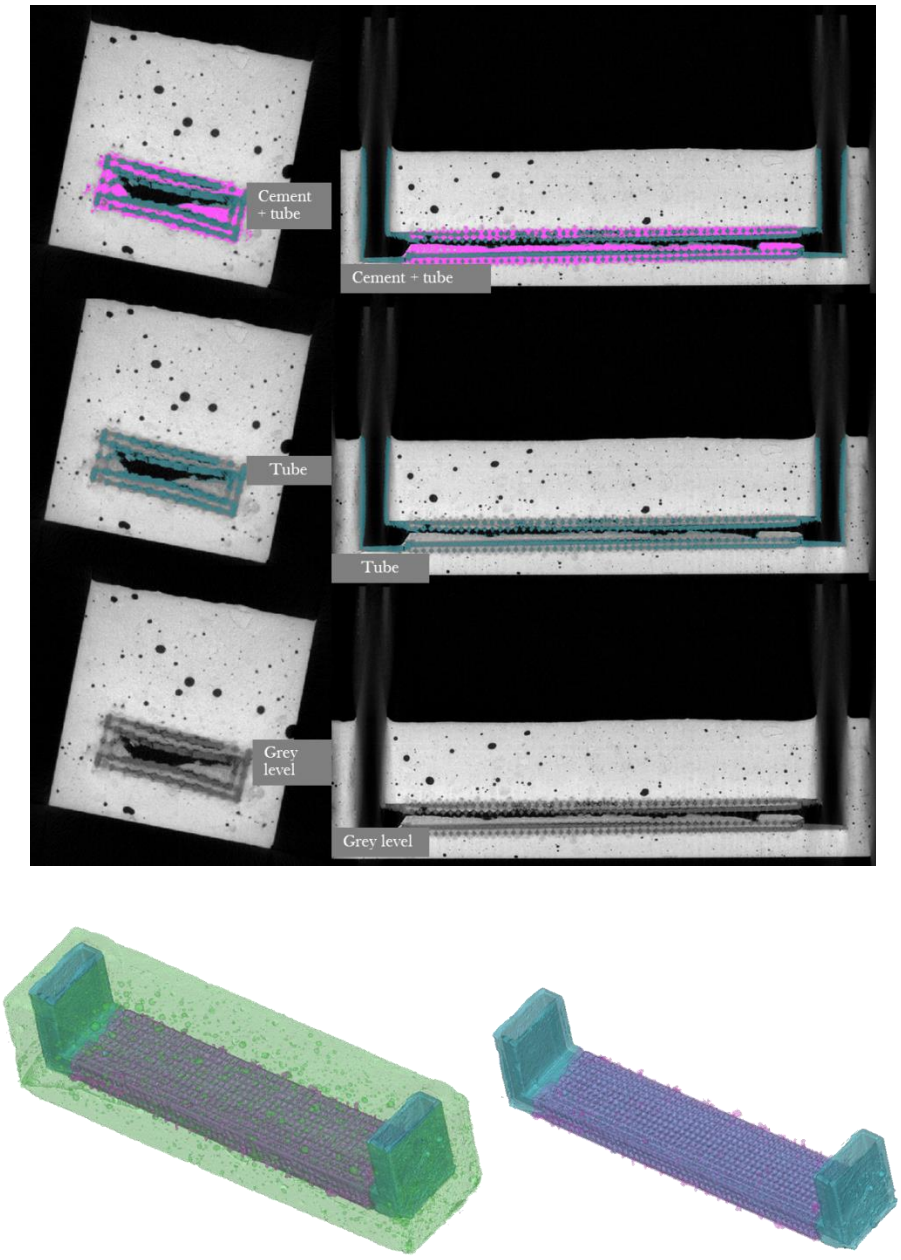

Figure 6.22, CT gray level images of cement matrix incorporating with plate shaped model, where the fluorescent pink coloured part represents cement penetrate to the model; cyan coloured part represents PLA structure; reconstructed images were presented at the bottom, same colour code was applied to the reconstructed image, with green colour added representing cement bulk

Using the double layer space integrity ratio (I_{dy}) defined in the previous section, cement penetration to the double-layered space in plate shaped model can be also evaluated quantitatively. According to the calculated data from the Mimic software, the integrity ratio I_{dy} of the double layered space in plate shaped model was around 82%, which is

much higher than the column shaped material with the similar pore size (L sized column model). As for its inner tunnel, the cement coverage went up to 53%, meaning most of the inner channel was blocked by cement. This thin layered inner channel brought higher chances of being blocked, hinting it is unlikely to be a suitable design for chemical triggered system when all the pores were open.

In conclusion, column shaped lattice design was relatively more suitable for the chemical triggering system than plate shaped model, as cement could penetrate to the inner tunnels. Specifically, a pore size smaller than 1 mm in the column could significantly reduce cement penetration to the double-layered space, and a size pore of 0.5 mm could almost prevent cement penetration. S sized model is by far the most ideal model for controlling unexpected mineral generation within tubes. Moreover, this could also help with stabilising chemical sensitive materials within the double-layered space from contacting with cement at the early stage. On the other hand, the thin inner channel design of plate shaped model brought higher chances of blocking the tunnel, hampering healing agent/inhibitor travelling. Thus, the plate shaped model was screened out from the list.

6.5 Chemical triggering test in Ag-Alg-column lattice design

In this section, agent release and Ag-Alg dissolution were studied by combining column shaped lattice model to investigate the potential of this chemical triggering system. Firstly, the effect of different pore size was examined by immersing the column shaped models in a DI water. Then, Ag-Alg was added to the most optimum S sized model and immersed in the visualise cell in a 0.001 M Cl in NaCl solution environment to further confirm if Ag-Alg was able to be triggered by low chloride ion concentrated solution.

6.5.1 Agent release in water

Before adding Ag-Alg (silver alginate) to the column shaped lattice model, all different pore sized models were tested in a visualised device mentioned in Chapter 3, also as shown in Figure 6.23, to determine if the S sized model (selected in cement survival test) could also perform well in the agent release process. The aim of this test is to better understand the agent release behaviour in various models. Viscous sodium silicate (60 cps) was selected as the agent passing through the inner tunnel of the lattice model (dyed in blue for the size M & L model aiming to enhance its visibility). In the device, DI water

was filled in the cell to provide an environment that would allow us to observe the agent release from the lattice structure when all the pores were exposed.

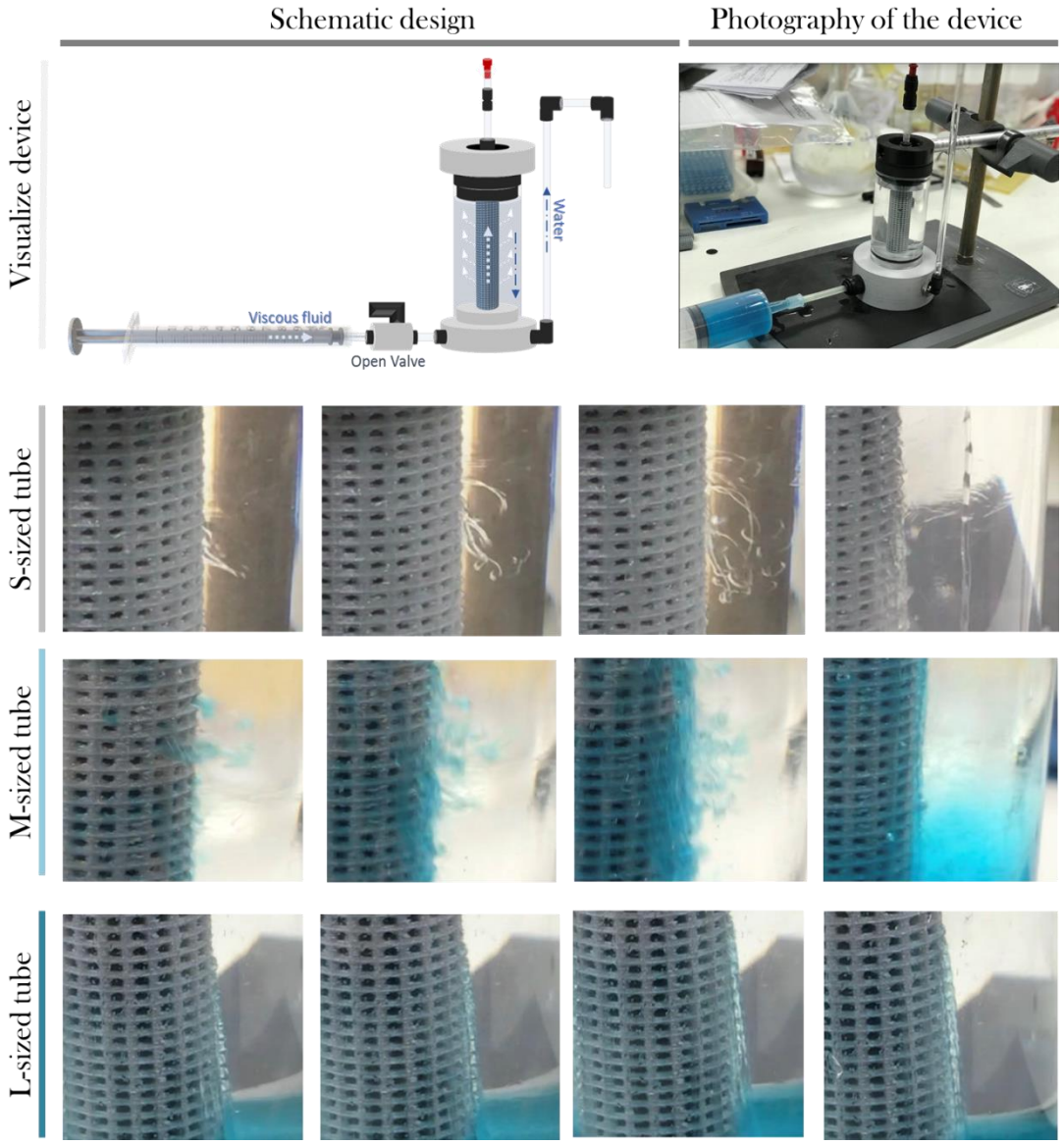

Figure 6.23, Schematic design and photography of the visual device (Top), and the agent releasing process over time (1s, 2s, 3s and final state, from left to right) of column shaped lattice model (Bottom)

As shown in Figure 6.23, agent travel distance of varied in three pore-sized lattice models. In S sized model, average travel distance was around 8.27 mm, which was followed by that of the M sized model, at 5.95 mm. L sized model, on the contrary, could barely observe horizontal travel path of the agents, but formed free stream flowing down along the tube surface. This may be attributed to the lower pressure difference across the perforations when the pore sizes expanded (Gautam et al., 2017). In this case, S sized

model had a relatively higher pressure while releasing agents in the water environment, which means it might also bring advantages in spreading agents in the cement matrix.

6.5.2 Ag-Alg dissolution in visual cell

Ag-Alg was manually filled into the double layered structure, and then the Ag-Alg-lattice model was put into visual device right after Ag-Alg was added, as Ag-Alg is a light sensitive material. To better capture the dissolution process in the visual cell, no light protection tinfoil was added to cover the process. As shown in Figure 6.24, silver alginate instantly reacted with chloride ions, since a few "foggy" liked AgCl appeared on the surface of the lattice structure. After 20s, we could observe the Ag-Alg layer started to collapse, and the solution started to change into a pinkish colour due to Ag cation light effect. Then at 30s, a few pores were exposed since a few silver alginate dissolved at this stage. 10 seconds later, more pores started to appear with few Ag-Alg remaining in the lattice structure.

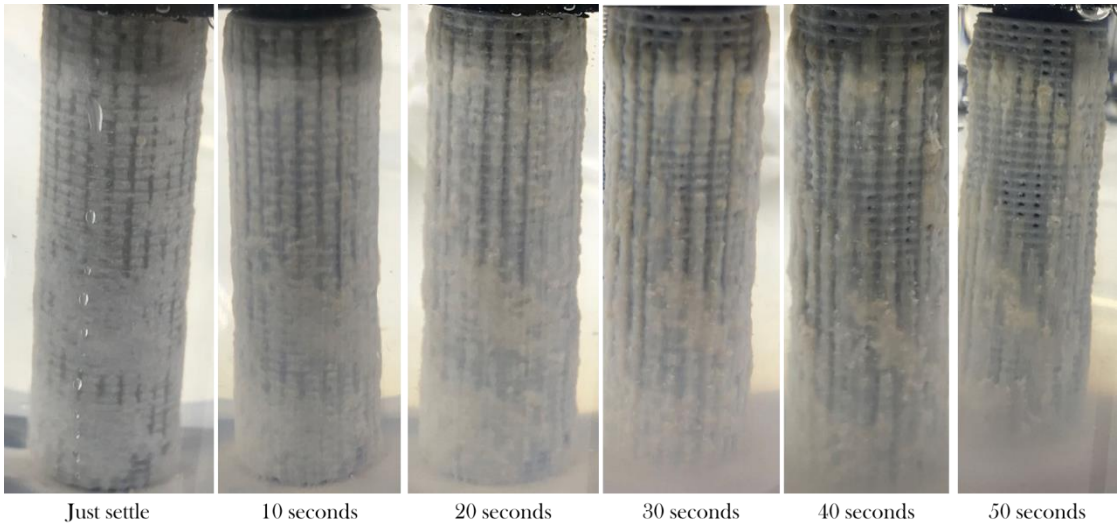

Figure 6.24, Photography of Ag-Alg-lattice system in a 0.001M NaCl solution over time

This indicates that low concentrated chloride solution successfully triggered the Ag-Alg layer while being embedded in the double-layered space of the lattice structure.

6.6 Preliminary investigations in situ

Rapid Chloride Permeability Test Equipment (RCPT) was used to evaluate the resistance of a concrete sample to the penetration of chloride ions. The test is performed by placing a 50 mm diameter concrete cylinder into the sample cells that contain a 10 % NaCl solution and a 0.3 N sodium hydroxide solution. Specifically, in this study, a PLA printed

lattice disc (containing Ag-Alg, 80 mm in diameter and 5 mm in height, shown in Figure 6.25) were embedded in the ordinary test cylinder to mimic the column lattice structure surface, in order to investigate its chloride resistance changes. Concrete cylinders were casted following the standard, which was mentioned in Chapter 3, together with a comparison pure concrete cylinder tested.

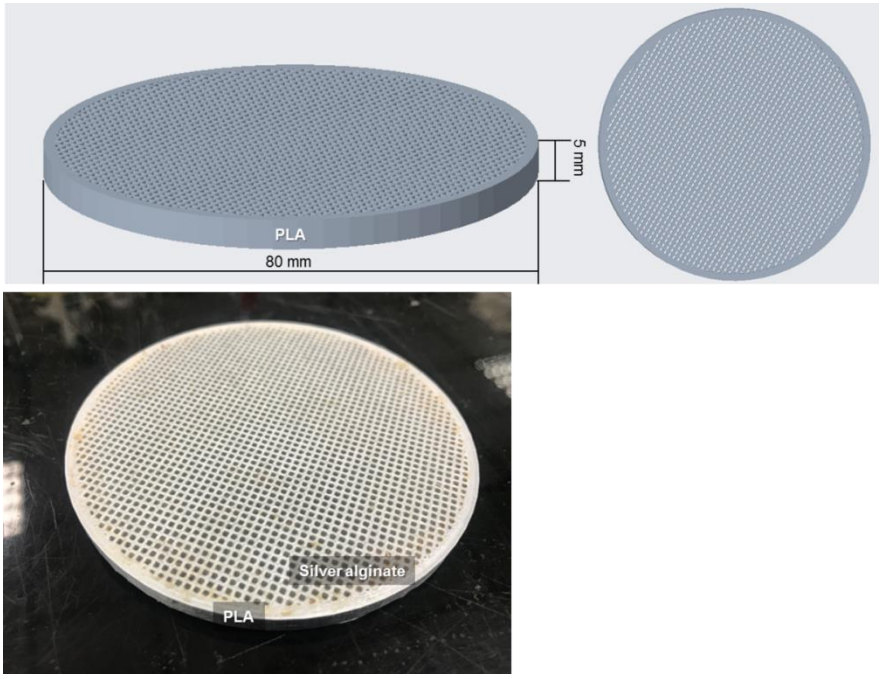

Figure 6.25, Schematic design of a lattice disc mimicking column lattice structure surface for rapid chloride penetration test cylinder; and a photo of printed lattice disc incorporating with Ag-Alg gel in the pores

Chloride migration coefficient was calculated using the equation below, according to the standard sheet (NT BUILD 492, Nordtest method):

$$D_{nssm} = \frac{0.0239(273+T)L}{(U-2)t} \cdot \left(x_d - 0.0238\sqrt{\frac{(273+T)Lx_d}{U-2}} \right) \qquad (6.7)$$

Where, non-steady-state migration coefficient ($\times 10^{-12} m^2/s$); U represented an absolute value of the applied voltage (V), T represented an average value of the initial and final temperatures in the anolyte solution (°C). L is the thickness of the specimen (mm), x_d is the average value of the penetration depths (mm), and t represented test duration (hour). Rapid chloride penetration tests were conducted in a 24 h period, and samples were collected and split into two parts, then was sprayed silver nitrate solution to measure chloride penetration depth according to the standard. The purple part after spraying

silver nitrate shown in the concrete was the area with chloride ions. The penetration depth can be measured from the centre to both edges at intervals of 10 mm (with an accuracy of 0.1 mm).

As shown in Figure 6.26, concrete with lattice disc increased the capacity for chloride resistance compared with the control group. The lattice disc sample presented a much lower non-steady-state migration coefficient after 24 hours of testing, at around 14 ($\times 10^{-12}$ m^2/s). However, the non-steady-state migration coefficient in the controlled group was 20.9 ($\times 10^{-12}$ m^2/s).

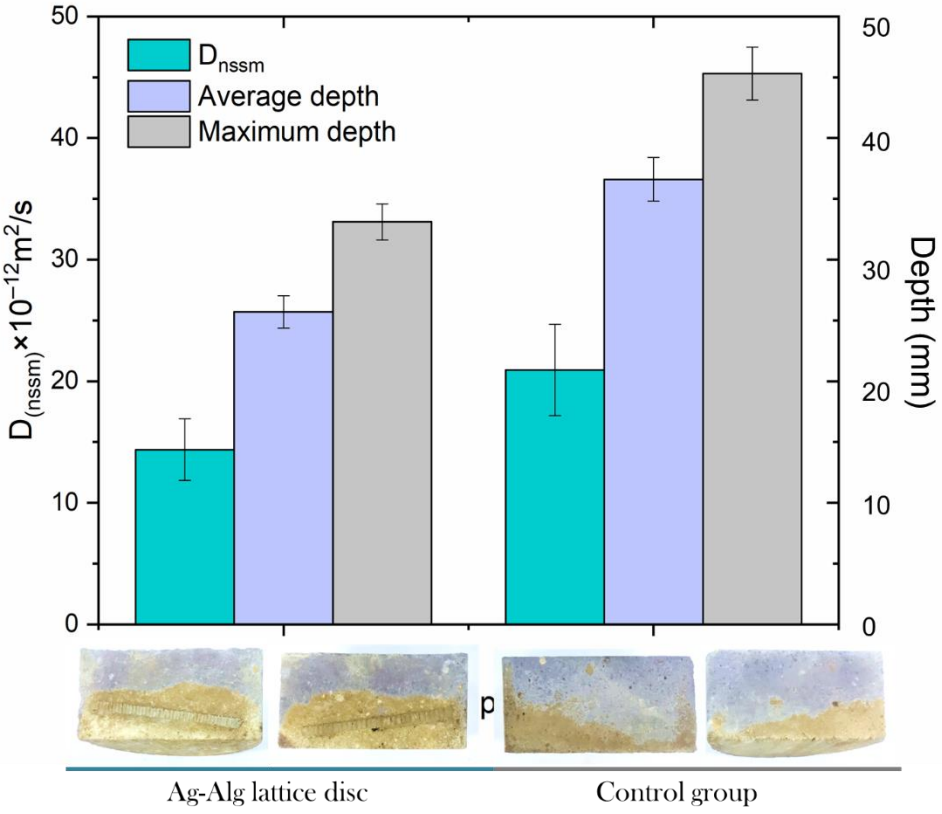

Figure 6.26, non-steady-state migration coefficient of both lattice disc cylinder and controlled cylinder, and photography of split concrete cylinder after RCPT, where the purple-coloured area shows the part containing chloride ions

The existence of the PLA structure might act as a physical barrier from chloride ion in this experiment. As shown in the controlled group, chloride penetration depth in the pure concrete cylinder could reach 36 mm. PLA lattice disc was placed at around 27 mm-43 mm. If lattice disc had no influence on chloride penetration, chloride could easily reach the lattice disc and potentially react with Ag-Alg gel. In this case, chloride failed to

reach the lattice structure. This indicated that applying plastic barriers in cementitious material could potentially be assistant in protecting concrete from being attacked by chloride ions. However, the chemical trigger in this test was not achieved since chloride ions did not reach to trigger the chemical reaction with silver alginate. Further research could focus on chloride ion interaction with Ag-Alg lattice system in cement.

6.7 Concluding remarks

Chapter 6 has investigated a potential chemical triggered vascular system based on silver alginate material (Figure 6.27).

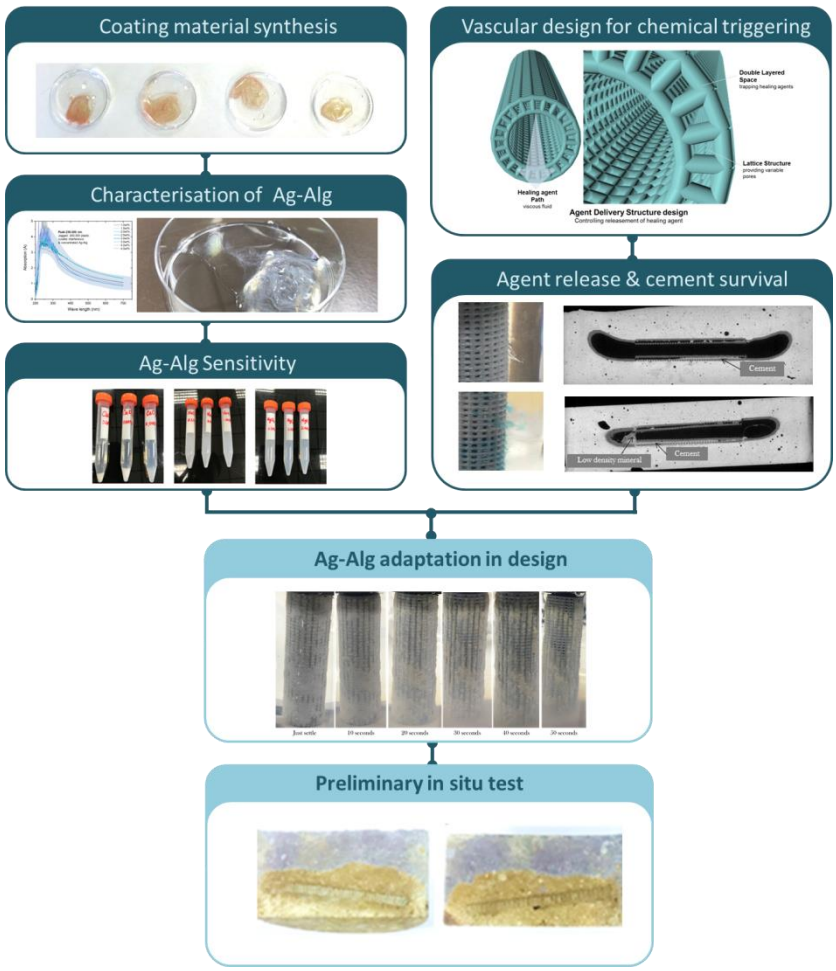

Figure 6.27, A schematic process on chemical triggered vascular system investigation process

Research in this chapter can be grouped mainly into three parts. Coating materials synthesis and vascular design were two parallel sectors.

The synthesis process of a chloride triggered material—Silver alginate via sodium alginate and $AgNO_3$ solutions. Ag^+ is chosen to be crosslinked with alginate skeleton to form silver alginate, which can provide characteristic "egg-box" structures to hold silver cations. When chloride ions appear, metal cations within the "egg-box" are precipitated with chloride ions. And the ionically crosslinked silver alginate gels can be therefore dissolved by the release of the silver cations. Silver alginate was successfully synthesised and proven by UV, TGA and Rheometer in this chapter. Besides, its sensitivity, in terms of reacting with chloride ions was further examined, with the aim of knowing its threshold value in interacting with Cl-. The results generally suggest that silver alginate gel was more sensitive to NaCl solution compared with $MgCl_2$. However, $CaCl_2$ could result in macro-scaled AgCl materials, which might potentially block the designed vascular system and thereby hampering healing/inhibitor release.

Then, a few vascular networks with the double-layered design was developed for time-controlled agents delivery. Cement survival results revealed that porous structure provided an ideal zone for cement paste and air (CO_2) interaction, and generated areatus calcium monocarbonaluminate hydrate, which was confirmed by SEM-EDX. Most areatus minerals were found in the beam with large PLA pore size (L sized sample), whereas, few were found in the M sized sample. This indicates that small PLA pore size is more ideal for controlling unexpected mineral generation within tubes, and further coatings will be needed for preventing this procedure and react with target ions/cations for chemical triggering. On the other hand, the thin inner channel design of the plate-shaped model brought higher chances of blocking the tunnel, hampering healing agent/inhibitor travelling. Thus, the plate-shaped model was not suitable for delivering agents in a chemical triggered system.

The third part of the research is to combine the chemical sensitive materials together with selected vascular structure. Agent release and Ag-Alg dissolution were studied by combining the column-shaped lattice model to investigate the potential of this chemical triggering system. The results showed that S sized model had a relatively higher pressure while releasing agents in the water environment, which means it might also bring advantages in spreading agents in the cement matrix. Moreover, a low concentrated chloride solution successfully triggered the Ag-Alg layer while being embedded in the double-layered space of the lattice structure.

Finally, rapid chloride tests were conducted to investigate the resistance of a concrete sample to the penetration of chloride ions. Although chemical trigger in this test wasn't achieved as the chloride ions did not reach to trigger the chemical reaction with silver alginate. The preliminary study revealed an exciting result that applying plastic barriers in cementitious material could potentially be assistant in protecting concrete from being attacked by chloride ions. For the future studies, the Ag-Alg coated vascular networks could be adapted into the cementitious materials and test its general behaviour during chloride attacks. Traceable materials can be also added in healing agents to examine how the agents migrate from the porous vascular surface.

Chapter 7

Conclusions and recommendations for the future work

Biomimicry is the idea of transferring biological principles to technology, which is generally the most powerful sources of innovation that is going to help us go beyond conventional approaches to sustainable design to achieve resilient infrastructure. Applying vascular self-healing systems in cementitious material could increase infrastructure sustainability and boost biosphere stability, which perfectly fit the requirements of future cementitious materials. In this study, a self-healing technique based on vascular design has been investigated to create fast diagnosed, advanced, and durable systems. This final chapter brings together all the conclusions that could be drawn in this work, which is followed by recommendations for the future research.

7.1 Conclusions

7.1.1 Overview

In chapter 1, general background and the key motivation associated with infrastructure were presented. The motivation of this work was to borrow solutions from nature to solve the durability challenge encountered in cementitious structures. This is followed by an overview of the thesis and the aim and objectives.

7.1.2 Literature review

In Chapter 2, a critical state-of-the-art review of literature relevant to this field was given. Literature review began by highlighting the sustainability and durability concerns and challenges outlining the global problems associated with the cement and concrete

industries in section 2.1. In the developed world, construction maintenance costs in existing cement-based structures account for approximately 50% of the total expenditure of the construction industry. On the other hand, there is still a huge demand for expanding their infrastructure among developing countries in line with economic growth and urbanisation. In both developed and developing countries, the value lies in improving the quality of construction and the quality of materials used, in contributing to a more durable infrastructure, increasing its sustainability and reducing its cost.

In reacting with the challenges of cost-effective, durability and sustainability encountered in the construction industry, a quest for the design of resilient infrastructure responding to both mechanical and environmental needs, has led to the development of biomimetic materials. Self-X materials for the construction industry were summarised in section 2.2. Applying the concepts of self-healing in cementitious material could increase infrastructure sustainability and boost biosphere stability, which perfectly fit the requirements of future cementitious materials.

In the past few decades, a large number of papers and scholars have emerged in the self-healing field, which is developing vigorously. A data-driven literature scientometric analysis on self-healing research development is presented in section 2.3, which is followed by a deep-dive review on detailed self-healing approaches. For cementitious materials, the mechanisms for achieving self-healing can be classified broadly into two main categories: Autogenous healing and Autonomic healing. Cementitious materials have autogenic abilities to heal their cracks and naturally occur in cementitious materials due to the presence of unhydrated cement particles. Without further modification or improvement, the efficiency of autogenous healing activities is relatively low. Hence their ability is limited for crack widths up to 50-150μm (Li and Yang, 2007).

Therefore, autonomic self-healing strategy has been developed in recent years to improve healing performance. Autonomic healing process uses engineered addition of materials or components for filling gaps that cannot be found in cementitious materials, and this type of healing is widely divided into intrinsic healing, capsule-based healing and vascular-based healing (Souza, 2017).

Capsule based self-healing systems have become increasingly popular over the past decade and were discussed in section 2.4. These type of systems allow the easy addition of during the mixing of concrete followed by controlled release of the healing agent upon

damage (Souza, 2017). Compared with autogenous healing, the capsule-based system mainly targets on cracks that are larger than 200 μm. However, discrete distribution of capsules and limited of healing agent carried limit the crack healing, remaining discrete crack sections in the matrix. Intending to overcome the limits above, cylindrical capsules were emerged (Thao, 2011, Van Tittelboom et al. 2016), since (i) they have a relatively larger internal area of influence for the same volume of healing agent compared with spherical capsules, (ii) the advantage of being able to store a larger amount of repairing agent, and (iii) have a stronger bond between capsules and cement matrix (Maes et al., 2014). However, neither spherical capsules nor cylindrical-shaped capsules can provide unlimited healing agents for long term repairing damage in the cementitious matrix. Damage scenarios require larger volumes of healing agents and the capability of dealing with repeated damage, therefore larger reservoirs are needed.

Vascular systems were mainly discussed in section 2.5. They house the healing agents in hollow channels that allows a healing agent to be distributed from a reservoir throughout a structure so that damage can be completely infiltrated with the healing agent was identified as an advance for liquid-based healing approaches (Trask et al. 2007a, Williams et al., 2008). Dry (1992) was the first one who demonstrated a vascular self-healing system in 1992, which was for repairing cracks in concrete and restoring its mechanical properties. Early pilot studies were mainly one-dimensional vessels embedded in the composites directly. However, discrete 1D structures are limited by the difficulty in replacing fluid to depleted channels. The need for each channel to fill specific damage volumes for complete healing process places constraints on how sparsely the channels can be distributed, which affects the healing efficiency. Creating interconnected networks reduces that constraint while opening up alternative applications for the network that takes advantage of fluid flow. Later studies followed up and developed two-dimensional (2D) and three-dimensional (3D) structures, since those interconnected networks may act as useful intermediates between discrete channels and increased degree of interconnectivity (Blaiszik et al., 2010).

Various forms of vascular networks have been recently applied in concrete and gained increasing popularity in the last 2 years. Physical cracking of cementitious matrix causes the brittle vascular branches to rupture, and then the healing agent is released into crack faces for repairing. Vascular self-healing in cementitious materials was demonstrated mostly in laboratory-scale tests. It was proved an ideal solution to the most difficult

challenges of overcoming water ingress and cracking prevalent in long-term period (De Belie et al., 2018; Gardener et al., 2018).

The design of vascular networks plays a significant role in efficiently diagnosing damages in the environment and ensuring the healing agents delivery and reaches the damaged zones. It is also critical to understand how the flow may change around these branched networks and how the vascular system can be designed to reduce the global resistance to flow, thereby adopting this mechanism into vascular manufacture process (Qamar et al., 2020). Learning from nature, mammal vascular inspired structure has been widely adopted into numerical and engineered designs containing microvascular networks, especially in self-healing materials (Bejan, 2000; Wang et al., 2006, 2007). Studies revealed that optimal solution for microvascular network designs highly depended on parameters, required functions and potential constraints. It is theoretically possible to design a vascular system that could efficiently deliver healing agents to crack zones with low energy cost and minimised impact on structural integrity.

In practical, challenges faced in vascular design were most rooted from insufficient support from manufacturing technique, the finical cost in prototype development, and the uncertainty of the currently available materials (Qamar et al., 2020). For simple structures, directly applying tubes and creating hollow channels within cementitious matrix were achievable. However, it is hard to establish complicated and consist of interconnected structures, which are capable of transporting healing agent to the damaged areas across the specimen's volume. To create connective networks in the matrix, obtaining natural vascular shapes via soft lithography and electrostatic discharge could be another option. However, the flexibility of these techniques is limited in terms of coverage area and branching diameters in real applications due to the limited number of real vasculature samples and uncontrollability of electrostatic discharge. These problems could be solved by using sacrificial materials combing additive manufacturing as coverage area and branching diameters are depending on designing models, which can be fully controlled by developers. One of the biggest problems is scaling up since current additive manufacturing devices are limited by its enclosed printing workplace. Alternatively, manufacture outreach is an ideal option for massive production considering the time required for fabrication, and less size restriction in commercial scaled machines.

In section 2.6, chemical triggered system was explained since chemical ions attack and acid attack have been the most reasons for inducing corrosion in concrete structures.

Intending to deal with the damage resulted by corrosion, various studies have investigated the use of self-healing materials based on encapsulation technique (Pelletier et al., 2011, Hilloulin et al., 2015), which were mechanically triggered by the cracks when damage appears. The healing agent, such as sodium silicate, is released when the capsule was triggered by physical cracks, and deposits on the metal reinforcement bars, forming a passive film on the surface of the metal to protect it from further corrosion (Pelletier et al., 2011). However, it is unlikely that this mechanical triggered system is able to respond to early corrosion when Cl concentration increases or the pH in the cementitious matrix goes down (Liang et al., 2018). Recent investigations on the chemical triggering system have been focused on investigating of pH-sensitive and ion sensitive coating materials and these have been detailed discussed in this section.

Finally, methods and tests to describe the self-healing process and behaviour were summarised in section 2.7. Three categories of characterise methods including visualisation and determination, mechanical properties recovery, and durability regaining were explained. These methodologies make it possible to provide a unified framework in conducting comparative studies among various research groups and also pave the way towards consistent incorporation of self-healing concepts to provide a feasible and reliable evaluation in analysing the life cycle of self-healing systems.

7.1.3 Materials and experimental procedures

The materials and experimental procedures used in the subsequent research work were given in Chapter 3. Various designs of vascular networks, including different printing materials, were applied in this study. Then a detailed description of the experimental procedures is followed to evaluate the mechanical, durability and microstructure of the vascular self-healing systems.

7.1.4 3D self-healing vascular model design & performance in cementitious materials

In Chapter 4, a biomimetic vascular network was designed following Murray's Law. Murray's law was obeyed during the design of the 3D-vascular network, aiming at minimising turbulent flow at junctions while also broadening the distribution of healing agents. The biomimetic three-dimensional design was then 3D-printed using polylactic acid (PLA) for the production of the vascular network. PLA structures presented brittle

fractural response and suitable interfacial bond for mechanically triggered use in self-healing.

In the first scenario, biomimetic vasculatures were compared with non-biomimetic systems (including one dimensional vascular and two dimensional vascular networks) in cement paste based samples. Comparison between the vascular systems (1D/2D/3D) with their mechanical properties and healing performance was used to shed light on their relative suitability for self-healing in cementitious systems. Initial cracks (between 700 to 800 μm) from all systems were observed to be healed over 28 days. A recovery in mechanical properties of ~20% for 1D and 2D-structures and 34% for 3D vascular network specimens were attributed to self-healing. Additionally, sorptivity tests were performed to evaluate the recovery in water tightness. The inclusion of 1D, 2D and 3D vascular network led to around 25, 69 and 77% reduction of the sorptivity index values in comparison with the values of the cracked control specimens. The crack mouth opening was non-uniformly closed in the 1D vascular-cement system, resulting in healed and unhealed cracks. Alternatively, an increased number of healed cracks were observed in the 2D vascular-cement system and virtually all the crack mouth opening was reduced in the 3D vascular-cement system. The crack closure efficiency was 52, 69 and 81% for the 1D, 2D and 3D vascular networks specimens, respectively. The circular pumping of sodium silicate for 28 days provided excessive sodium silicate in the three networks. Through SEM-EDX, Na_2HCO_3 and silica mixed gel were proposed as healing products as the sodium silicate was exposed to air and reacted with CO_2 and water vapour. The volume of healed crack was investigated using CT-scan and calculated as 36%, 49% and 72% for the 1D, 2D and 3D vascular networks specimens, respectively. In this case, partial healing could be drastically reduced by applying a 3D vascular structure, which contains more connected daughter tubes and enables large tube coverage. The systematic improvement in the healing performance of the 3D vascular networks specimens was attributed to the design obeying Murray's law and therefore broadening the coverage of healing agent distribution while reducing the energy required for pumping. Details of the vascular designs were provided in section 4.2.

For the second scenario, the 3D (biomimetic vascular system) was used in subsequent mortar investigations following in-depth characterisation. Pumping (closed) system and non-pumping (open) systems were applied to investigate the healing efficiency of the amount of agent provided over time. A thorough investigation into the effect of healing

agent providing methods on the mechanical properties, healing performance as well as their mechanisms during healing process is presented. In the closed system, continuous circulation of the healing agent was achieved through pumping. While in the open system, a fixed amount of healing agent was enclosed while the system remained open to the environment. These achieved healing through different healing mechanisms. The latter was found to react with calcium hydroxide leaching from the matrix to generate C-S-H and hydration products to fill in cracks. However, the former reacted with open air to form silica-based gels in the cracking area. This approach, of pumping a large volume of sodium silicate was identified as the ideal choice to improve the self-healing of a cementitious matrix as it was able to not only react with the calcium hydroxide in the cementitious matrix but the gelled excess healing agent acted like glue, allowing better loading recovery and water sorptivity ability than encapsulating limited amount of sodium silicate. These results confirm not only the great potential of the vascular network but also of a mineral-based healing agent to deliver consistent healing offering a pragmatic solution to the demands for prolonged and long term damage management.

7.1.5 Feasibility of creating PVA (Poly-vinyl alcohol) channels

Chapter 5 mainly discusses the feasibility of using PVA (Poly-vinyl alcohol) as a sacrificial material to create hollow channels within cementitious materials. This is because a hollow vascular channel for self-healing system could avoid long term tube monitoring and enables multi-scale healing over time. Complex channel structures could be design and printed using PVA, which will be dissolved to create hollow channels within the cement matrix.

To validate its workability, the printability of PVA was firstly being investigated. Then, a few interconnected vascular channel models were designed coordinating with PVA printing behaviour. A double twisted channel design was selected due to its stableness during the 3D printing process and its potential to be used to deliver two-part healing agents. Then, the crystallinity and functional groups of PVA before and after extrusion were investigated using FTIR to confirm the extruded PVA has similar properties with the standard PVA materials.

The following section discussed the dissolution behaviour and duration of 3D printed PVA structures in water. The survival behaviour of the 3D-printed structures during the curing of cement paste at different water content was investigated using optical

microscopy and computed-tomography (Micro-CT). Then, PVA removal tests were conducted under different water-bath temperatures by immersing the cured PVA-cement samples under the water. PVA reacted with cement paste during the 28 days of curing and the reaction products were analysed using SEM-EDX, FTIR and XRD. The research focuses on the potential of PVA to be used as a sacrificial material to create hollow tunnels in the cementitious material to promote self-healing. FTIR shows decreased in crystallinity of the PVA extruded in the 3D-printing when compared with un-extruded PVA, but the main functional groups remained unchanged. We design and 3D-print a PVA double twisted channel as it provides a versatile way to deliver two-part healing agents.

We embed the PVA structures in cement paste to investigate the effect of structures' water uptake during curing. Through casting in different w/c ratios, we show the w/c ratio substantially contribute to increasing the water intake of PVA structure. Controlling the PVA expansion by decreasing the w/c ratio provides a promising approach to tailor dissolution kinetics during curing. Furthermore, CT-scan images show that low w/c ratio casting no dissolution of PVA is observed in the sample. On the other hand, for w/c ratio above 0.3, the water uptake of PVA results in the expansion and creates cracks in the whole structure. The PVA cement survival tests indicated that w/c ratio of 0.25 was the only possible mix that could potentially be used in creating hollow interconnected channels in cement.

However, this hypothesis was broken by the results of the PVA removal tests. Warm/hot water-bath were able to accelerate the PVA removal process than the ones in room-temperature water-bath. But the acceleration in the dissolving process also triggered significant early expansion in PVA, thereby generating cracks during the removal process. Only the ones were conducted under room-temperature hadn't observed cracks on the surface. Even for the samples being conducted under room temperature, it is less likely that that PVA removal could succeed. Since there were secondary products between the cement and PVA materials being produced and formed a layer of the boundary. The capability of PVA to be 3D-printed, dissolved in water and remains intact when cast at low w/c ratios should make it valuable as a potential sacrificial network for vascular based-self-healing. While its behaviour in cement removal process and secondary interaction between cement made it being screened out from the list.

7.1.6 A potential chemical sensitive material for vascular system

The investigations reported in Chapter 6 involved the use of chemical sensitive material to trigger agent release rather than traditional physical triggering release. This chapter is split into three main sub-sections. In the first section, a chloride sensitive material was synthesised and its chloride sensitivity was confirmed via characteristic methods. Synthesis process of a chloride triggered material—Silver alginate via sodium alginate and $AgNO_3$ solutions was presented in section 6.1. Ag^+ is chosen to be crosslinked with alginate skeleton to form silver alginate, which can provide characteristic "egg-box" structures to hold silver cations. When chloride ions appear, metal cations within the "egg-box" are precipitated with chloride ions. And the ionically crosslinked silver alginate gels can be therefore dissolved by the release of the silver cations. Silver alginate was successfully synthesised and proven by UV, TGA and Rheometer in this chapter.

Besides, its sensitivity, in terms of reacting with chloride ions was further examined, with the aim of knowing its threshold value in interacting with Cl-. The results generally suggest that silver alginate gel was more sensitive to NaCl solution compared with $MgCl_2$. However, $CaCl_2$ could result in macro-scaled AgCl materials, which might potentially block the designed vascular system and thereby hampering healing/inhibitor release.

Then, a porous vascular system was designed for coordinating chemical triggering materials, followed by a few tests in investigating the release behaviour of the designed models. Agent release and Ag-Alg dissolution were studied by combining the column-shaped lattice model to investigate the potential of this chemical triggering system. The results showed that S sized model had a relatively higher pressure while releasing agents in the water environment, which means it might also bring advantages in spreading agents in the cement matrix. Moreover, a low concentrated chloride solution successfully triggered the Ag-Alg layer while being embedded in the double-layered space of the lattice structure.

Cement survival results revealed that porous structure provided an ideal zone for cement paste and air (CO_2) interaction, and generated areatus calcium monocarbonaluminate hydrate, which was confirmed by SEM-EDS. Most areatus minerals were found in the beam with large PLA pore size (L sized sample), whereas, few were found in the M sized sample. This indicates that small PLA pore size is more ideal for controlling unexpected mineral generation within tubes, and further coatings will be needed for preventing this

procedure and react with target ions/cations for chemical triggering. On the other hand, the thin inner channel design of the plate-shaped model brought higher chances of blocking the tunnel, hampering healing agent/inhibitor travelling. Thus, the plate-shaped model was not suitable for delivering agents in a chemical triggered system.

Finally, tests were conducted to investigate the resistance of a concrete sample to the penetration of chloride ions via rapid chloride penetration tests (RCPT). The preliminary study showed that applying plastic barriers in cementitious material could potentially assistant in protecting concrete from being attacked by chloride ions. However, the chemical trigger in this test wasn't achieved since chloride ions did not reach to trigger the chemical reaction with silver alginate. Further research could focus on chloride ion interaction with Ag-Alg lattice system in cement.

7.2 Future outlook

7.2.1 Interruption from COVID-19

Like many working in research, we are facing huge disruption to our research projects as the COVID-19 outbreak unfolds across the world since the beginning of this unusual year. Labs and offices were shut down; Laboratory tests were paused or adjusted; out-reach tests are unlikely to happen anytime soon.

Luckily for me, I have had most of my tests conducted and data collected before lab being shut. But then, there are still a few out-reach tests, such as contact-angle, ICP, and CT scanning tests for chapter 6 that have been influenced by this issue. These tests could have provided more evidence from different aspects to support the findings discussed in the content.

7.2.2 Future works from this study

As mentioned in the previous section, chemical triggering vascular system works in this research has the most potential and also need the most investigation. In this work, the preliminary study successfully synthesised alginate-based chemical sensitive material and confirmed this material was able to be triggered in the Cl ion solution when adapted to vascular structure. However, the chemical trigger in the cementitious environment hasn't studied much due to the time limit and pandemic interruption. Further research could focus on chloride ion interaction with Ag-Alg vascular system in the cement matrix. Also,

the chemical triggered should ideally provide the designer/operator with direct feedback on the state of the structure's performance before, during and after self-healing. This may require other techniques such as sensing to be able to equip the vascular systems with remote monitoring function.

Besides, in Chapter 5, the use of PVA material as a sacrificial material to create hollow channels would bring more uncertainty, such as early age cracking and interaction with cement in self-healing system. In this case, PVA is unlikely to be developed as a sacrificial material in cementitious materials. Future studies regarding create hollow channels in cement for the self-healing system could focus on wax-liked materials. This is mainly because it is a proven casting process for generating metal and jewellery (Hunt, 1980). The fabricating process design and curve a wax-base structure, and then this structure would be embedded into the cementitious matrix. After that, the cement bulk was heated up to melt the wax and pour it out. Then this negative cement mould could fill in with melted metal. This approach was called "Lost-wax" process, which dated back to 1200 B.C. in ancient China (Peng, 2017). The reasons for not using wax as a sacrificial material in this study was considering the capability of applying wax printing in our current 3D printer and the wax 3D printing price for out-reached services. Current wax 3D printers are mainly for jewellery design, which resulted in their limited size (normally less than 100 mm) for creating large structures for concrete. To order out-reaching wax printing service would normally cost at least 70 pounds for each model (twisted model, discussed in this study). In this case, we decided to use the current widely used PVA 3D printing material to print the designed model, due to its potential printability and water-soluble property.

For future studies, specifically, research and tests about vascular self-healing systems could focus on:

- Shape designing and manufacturing breakthroughs for the reduction in diameter and wall thickness of vascular networks.
- Sustainability challenge in maintaining the functional interconnected channels.
- Suitable sacrificial materials that are ready for creating hollow channels in cementitious materials.
- Chemical triggered coating materials, mechanism and suitable vascular designs.

More generically, the main challenges of vascular self-healing technology in the construction industry remain: (i) the difficulties in scaling up, (ii) the additional costs involved and (iii) the validation of long-term durability performances on site. This highlighted the needs in developing designs of the self-healing system, manufacturing techniques and long term monitoring for large scale trials.

References

Abergel, T., Dean, B., Dulac, J., Hamilton, I., Wheeler, T., 2018. Global Status Report - Towards a zero-emission, efficient and resilient buildings and construction sector. ISBN 978-92-807-3729-5

Adam, J. A., 2011. Blood Vessel Branching: Beyond the Standard Calculus Problem. Mathematics Magzine. Vol. 84, No. 3. 196-207.

Ahn, T. H., Kim, H., Ryou, J. S. 2016. New Surface-Treatment Technique of Concrete Structures Using Crack Repair Stick with Healing Ingredients. Materials (Basel) 9:654.

Ahn, T. H., Kishi, T. 2010. Crack Self-healing Behavior of Cementitious Composites Incorporating Various Mineral Admixtures. Journal of Advanced Concrete Technology, 8:171–186.

Akai, N., 2016. Estimating Future Renewal Costs for Road Infrastructure and Financial Burden in Japanese Prefectures, Policy Research Institute, Ministry of Finance, Japan, Public Policy Review, Vol.12, No.1

Akers, A., Gassman, M., and Smith, R., Hydraulic Power System Analysis (CRC, Florida, 2006).

Al-Ansari, M., Abu-Taqa, A. G., Hassan, M. M., Senouci, A., & Milla, J., 2017. Performance of modified self-healing concrete with calcium nitrate microencapsulation. Construction and Building Materials, 149, 525-534.

Aldea, C. M., Song, W. J., Popovics, J. S. Shah, S. P. 2000. Extent of healing of cracked normal strength concrete. Journal of Materials in Civil Engineering,12, 92–96.

Alghamri, R. J. and Al-Tabbaa, A. 2016. "Self-Healing Performance of Magnesia-Based Pellets in Concrete." In 2nd International Conference on Concrete Sustainability (ICCS16). Madrid, Spain.

Alghamri, R., Kanellopoulos, A., Al-Tabbaa, A. Impregnation and encapsulation of lightweight aggregates for self-healing concrete. Construction Building Materials, 2016, 124, 910–921.

Alghamri, R.J., and Al-Tabbaa, A., 2016. Self-Healing Performance of Magnesia-Based Pellets in Concrete. In 2nd International Conference on Concrete Sustainability (ICCS16) Madrid , Spain), International Centre for Numerical Methods in Engineering (CIMNE): Barcelona, SpainMadrid , Spain, 2016.

Allahverdi, A., and Škvára, F., 2000. Acidic corrosion of hydrated cement based materials. Ceram. Silik. 44, 152–160.

Al-Omari, M. M., Rashid, I. S., Qinna, N. A., Jaber, A. M., Badwan, A. A., 2016. Calcium carbonate, Profiles of Drug Substances, Excipients and Related Methodology, 41, 31-132.

Al-Tabbaa, A., Lark, B., Paine, K., Jefferson, T., Embley, T., 2018. Smart Biomimetic Construction Materials for Next Generation Infrastructure. International Symposia for Next Generation Infrastructure.

Amara, C. B., Eghbal, N., Oulahal, N., Degraeve, P., Gharsallaoui, A., 2016. Properties of lysozyme/sodium alginate complexes for the development of antimicrobial films. Food Research International, 89, 272–280.

Angst, U. M., 2018. Challenges and opportunities in corrosion of steel in concrete. Materials and Structures, 51:4

Anuradha, K., Bangal, P., Madhavendra, S. S., 2016. Structural characterisation and water turbidity removing efficacy of Portulaca mucilage–alginate (PMA) beads, Desalination and Water Treatment, 57:10, 4386-4397.

Araujo, M., Gurdebeke, S., Chatrabhuti, S., Alderete, N., Van Tittelboom, K., Raquez, J. M., Van Vlierberghe, S., Cnudde, V., De Belie, N., 2018. Poly(methyl methacrylate) capsules as an alternative to the ''proof-of-concept'' glass capsules used in self-healing concrete Gruyaert, Cement and Concrete Composites, 89, 260.

Asakura, Y. and Kashiwadani M., Road network reliability caused by daily fluctuation of traffic flow, Proceedings of the 19th PTRC Summer Annual Meeting, Brighton, UK, 1991.

ASTM C1585, 2013. Standard Test Method for Measurement of Rate of Absorption of Water by Hydraulic Cement Concretes. ASTM International, pp.1-6

ASTM D6272-02, 2008. Standard Test Method for Flexural Properties of Unreinforced and Reinforced Plastics and Electrical Insulating Materials by Four-Point Bending. ASTM International, pp.1-9

Baker, M.I., Walsh, S.P., Schwartz, Z., Boyan, B.D. 2012. A review of polyvinyl alcohol and its uses in cartilage and orthopedic applications. Journal of Biomedical Materials Research Part B: Applied Biomaterials, 100B, 1451–1457.

Balbas, E. M., 2010. Optical Techniques for the study of living tissue. Doctoral Thesis Delft: Technische Universtiteit Delft.

Bazaldúa-Medellín, M.E., Fuentes, A.F., Gorokhovsky, A., Escalante-García, J.I., 2015. Early and late hydration of supersulphated cements of blast furnace slag with fluorgypsum. Materiales de Construcción 65, e043.

Bejan, A., 1996. Street network theory of organisation in nature. Journal of Advanced Transportation, 30, 85-107.

Bejan, A., 2000. Shape and Structure, from Engineering to Nature (Cambridge: Cambridge University Press)

Bentz, D.P., 2008. A Review of Early-Age Properties of Cement-Based Materials. Cement and Concrete Research, 38, 196–204.

Berman, H., and Newman, E., 1961. Heat of formation of calcium aluminate monocarbonate at 25 C, Journal of research of the National Bureau of Standards Aa. Physics and Chemistry, 65 (3)

Bettermann, P. 1975. The transformation of amorphous silica to crystalline silica under hydrothermal conditions. Contributions to Mineralogy and Petrology. Volume 53, Issue 1, pp 25–36.

Biernacki, J. J., Bullard, J. W., Sant, G., Banthia, N., Brown, K., Glasser, F. P., Jones, S., Ley, T., Livingston, R., Nicoleau, L., Olek, J., Sanchez, F., Shahsavari, R., Stutzman, P. E., Sobolev, K., Prater, T., 2017. Cements in the 21st Century: Challenges, Perspectives, and Opportunities. Journal of the American Ceramic Society,100(7): 2746–2773.

Blaiszik, B. J., Kramer, S. L. B., Olugebefola, S. C., Moore, J. S., Sottos, N. R., White, S. R., 2010. Self-Healing Polymers and Composites. Annual Review of Materials Research, 2010, 40, 179.

Bleay S. M., Loader C. B., Hawyes V. J., Humberstone L., Curtis P.T., 2001. A smart repair system for polymer matrix composites. Composites A 32:1767-1776.

Bonapasta, A.A., Buda, F., Colombet, P., Guerrini, G., 2002. Cross-linking of poly (vinyl alcohol) chains by Ca ions in macro-defect-free cements. Chemistry of Materials, 14, 1016–1022.

British Standards Institution, BS EN 00196-1-2005. Methods of Testing Cement; BSI: London, UK, 2005.

Brown, E. N., White, S. R., Sottos, N. R. 2004. Microcapsule induced toughening in a self-healing polymer composite. Journal of Materials Science, 39, 1703–1710.

Buenger, D., Topuz, F., Groll, J., 2012. Hydrogels in sensing applications. Progress in Polymer Science, 37, 1678–1719.

Burchell, R. W., Crosby, M. S., Russo, M., 2010. Infrastrcuture need in the United States, 2010-2030: What is the level of need? How will it be paid for?, The urban lawyer, Vol.42/43, No.4/1, pp.41-66

Cailleux, E. and Pollet, V. 2009. Investigations on the development of self-healing properties in protective coatings for concrete and repair mortars. Proceedings of the 2nd International Conference on Self-healing materials, page 120.

Campbell, I., Bourell, D., Gibson, I., 2012. Additive manufacturing: rapid prototyping comes of age. Rapid Prototyping Journal, 18 255–8

Cetkin, E., Lorente, S., Bejan, A., 2011. Hybrid grid and tree structures for cooling and mechanical strength. Journal of Applied Physics, 110, 064910

Charron, K., 2015, WinSun China builds world's first 3D printed villa and tallest 3D printed apartment building

Chen, C.M., 2006. CiteSpace II: Detecting and visualizing emerging trends and transient patterns in scientific literature. Journal of the American Society for Information Science and Technology, 57, 359–377

Chen, C.M., 2017. Science Mapping: A Systematic Review of the Literature. Journal of Information Science, 2, 1–40.

Choi, S., Lee, M. G., & Park, J. K. 2010. Microfluidic parallel circuit for measurement of hydraulic resistance. Biomicrofluidics, 4(3), 034110.

Clear, C. A., 1985. The Effects of Autogenous Healing upon the Leakage of Water through Cracks in Concrete, Cement and Concrete Association: Slough, UK, 1985; p. 28.

Concrete Society. Non-Structural Cracks in Concrete: A Concrete Society Report; Concrete Society: London, UK, 2010.

Conner, B. P., Manogharan, G.P., Martof, A.N., Rodomsky, L.M., Rodomsky, C.M., Jordan, D.C., Limperos, J.W., 2014. Additive Manufacturing, 1–4, 64–76

Damtoft, J. S., Lukasik, J., Herfort, D., Sorrentino, D., Gartner, E. M. 2008. Sustainable development and climate change initiatives. Cement and Concrete Research, Vol.38, Issue 2, 115-127.

Danner, R.P.; High, M.S. Handbook of Polymer Solution Thermodynamics; American Institute of Chemical Engineers: New York, NY, USA, 1993.

Davies, R., Teall, O., Pilegis, M., Kanellopoulos, A., Sharma, T., Jefferson, A., Gardner, D., Al-Tabbaa, A., Paine, K. and Lark, R., 2018. Large scale application of self-healing concrete: Design, construction, and testing. Frontiers in Materials, 5, p.51.

Davies, R., Jefferson, A., Lark, R., Gardner, D., 2015. A novel 2D vascular network in cementitious materials. In Proceedings of the Concrete—Innovation and Design, Fib Symposium, Copenhagen, Denmark, 18–20 May 2015.

De Belie, N., Gruyaert, E., Al-Tabbaa, A., Antonaci, P., Baera, C., Bajare, D., Darquennes, A., Davies, r., Ferrara, L., Jefferson, T., Litina, C., Miljevic, B., Otlewska, Ranogajec, A. J., Roig-Flores, M., Paine, K., Lukowski, P., Serna, P., Tulliani, J., Vucetic, S., Wang,

J., Jonkers, H.M., 2018. A Review of Self-Healing Concrete for Damage Management of Structures, Volume 5, Issue17, Special Issue: Self - Healing Materials.

De Muynck, W., De Belie, N., Verstraete, W., 2010. Microbial carbonate precipitation in construction materials: A review. Ecological Engineering, Vol.36, Issue,2. 118-136.

De Rooij, M., Van Tittelboom, K., De Belie, N., Schlangen, E., 2013. State-of-the-Art Report of RILEM Technical Committee 221-SHC: Self-Healing Phenomena in Cement-Based Materials, page 8-12.

De Rooij, M., Van Tittelboom, K., De Belie, N., Schlangen, E., 2013. Self-Healing Phenomena in Cement-Based Materials, Springer, Dordrecht, The Netherlands

De Rooij, M., Van Tittelboom, K., De Belie, N., Schlangen, E., 2013. State-of-the-Art Report of RILEM Technical Committee 221-SHC: Self-Healing Phenomena in Cement-Based Materials; P ublisher: Springer: New York citycity, United Statescountry, pp. 8–12.

Dermanaki-Farahani, R., Lebel, L.L., Therriault, D. Manufacturing of Three-dimensionally Microstructured Nanocomposites through Microfluidic Infiltration. Journal of Visualized Experiments, (85), e51512.

Detrembleur, C., Debuigne, A., Hurtgen, M., Jérôme, C., Pinaud, J., Fèvre, M., Coupillaud, P., Vignolle, J., Taton, D., 2011. Synthesis of 1-vinyl-3-ethylimidazolium-based ionic liquid (co) polymers by cobalt-mediated radical polymerisation. Macromolecules, 44(16), pp.6397-6404.

Dizona, J.R.C., Espera Jr, A.H., Chen, Q. and Advincula, R.C., 2018. Mechanical characterisation of 3D-printed polymers. Additive Manufacturing, 20, pp.44-67.

Dong, B., Ding, W., Qin, S., Han, N., Fang, G., Liu, Y., Xing, F., Hong, S., 2018. Chemical self-healing system with novel microcapsules for corrosion inhibition of rebar in concrete. Cement and Concrete. Composite, 85, 83-91.

Dong, H., Esser-Kahn, A. P., Thakre, P. R., Patrick, J. F., Sottos, N.R., White, S. R., Moore, J. S., 2012. Chemical treatment of poly (lactic acid) fibers to enhance the rate of thermal depolymerisation . ACS Applied Materials & Interfaces, 4, 503–9.

Dry, C. 1992. Passive tuneable fibres and matrices. International Journal of Modern Physics B, 6:2763–71.

Dry, C. and Corsaw M. A time-release technique for corrosion prevention. Cement and Concrete Research, Vol. 28, No. 8, pp. 1133–1140, 1998.

Dry, C. Passive tuneable fibres and matrices. International Journal of Modern Physics B, 1992, 6, 2763–2771.

Dry, C., 2001. In-Service Repair of Highway Bridges and Pavements by Internal Time-Release Repair Chemicals, NCHRP-IDEA Program Project, Final Report 2001.

Dry, C.M. 1999. Repair and prevention of damage due to transverse shrinkage cracks in bridge decks. Smart Materials and Structures, 3671, 253–256.

Dry, C.M. 2000. Three designs for the internal release of sealants, adhesives, and waterproofing chemicals into concrete to reduce permeability. Cement and Concrete Research, 2000, 30, 1969–1977.

Dry, C.M., 1994. Matrix cracking repair and filling using active and passive modes for smart timed release of chemicals from fibers into cement matrices. Smart Materials and Structures, 3, 118–123.

Dry, C.M., 2000. Three designs for the internal release of sealants, adhesives, and waterproofing chemicals into concrete to reduce permeability. Cement and Concrete Research, 30:1969–1977.

Dry, C.M., 2015. Paradigm for design of biomimetic adaptive structures. Proc. SPIE 9429, Bioinspiration, Biomimetics, and Bioreplication 2015, 942907

Dry, C.M., Corsaw, M.J.T., 1998. A Time-release technique for corrosion prevention. Cement and Concrete Research, Vol. 28, No. 8, pp. 1133–1140

Dry, C.M., McMillan, W., 1996. Crack and damage assessment in concrete and polymer matrices using liquids released internally from hollow optical fibers. Proc. SPIE 2718, Smart Structures and Materials 1996: Smart Sensing, Processing, and Instrumentation

DTI, 2006. Construction statistics annual report. London.

Du, H., Liu, M., Yang, X., Zhai, G., 2015. The design of ph-sensitive chitosan-based formulations for gastrointestinal delivery. Drug Discovery Today, 20, 1004–1011.

Edvardsen, C., 1999. Water permeability and autogenous healing of cracks in concrete. ACI materials journal, Vol.96, Issue 4, page 448-454

Erbektas, A.R., Isgor, O.B., Weiss, W.J., 2020. Comparison of Chemical and Biogenic Acid Attack on Concrete. ACI Mater. J. 117, 255–264.

European Commission, 2019. Overview of transport infrastructure expenditures and cost.

Fang, G., Liu, Y., Qin, S., Ding, W., Zhang, J., Hong, S., Xing, F., Dong, B. 2018. Visualised tracing of crack self-healing features in cement/microcapsule system with X-ray microcomputed tomography. Construction and Building Materials, 179, 336–347.

Feng, X., Zhuo, N., Ningxu, H., Biqin, D., Xuexiao, D., Zhan, H., Ming, Z., 2008. Self-healing mechanism of a novel cementitious composite using microcapsules. In Proceedings of International Conference on Durability of Concrete Structures, Hangzhou, China, 2008.

Fernández Farrés, I., & Norton, I. T., 2014. Formation kinetics and rheology of alginate fluid gels produced by in-situ calcium release. Food Hydrocolloids, 40, 76–84.

Ferrara, L., Van Mullem, T., Alonso, M. C., 2018. Experimental characterisation of the self-healing capacity of cement based materials and its effects on the material performance: A state of the art report by COST action SARCOS WG2. Construction and Building Materials, 167:115–142.

Flatt, R. J., Roussel, N., Cheesemen, C. R. 2012. Concrete: An eco material that needs to be improved. Journal of the European ceramic society, vol. 32., 2787-2798.

Flyvbjerg, B., Bruzelius, N. and Rothengatter, W., 2003. Megaprojects and Risk: An Anatomy of Ambition. Cambridge: Cambridge University Press.

Formia, A., Irico, S., Bertola, F., Canonico, F., Antonaci, P., Pugno, N. M., Tulliani, J-M., 2016. Experimental analysis of self-healing cement-based materials incorporating extruded cementitious hollow tubes Journal of Intelligent Material Systems and Structures, 27 2633–52.

Formia, A., Terranova, S., Antonaci, P., Pugno, N., & Tulliani, J. 2015. Setup of Extruded Cementitious Hollow Tubes as Containing/Releasing Devices in Self-Healing Systems. Materials, 8 (4): 1897–1923.

Frangopol, D. M., Liu, M., 2007. Maintenance and management of civil infrastructure based on condition, safety, optimisation, and life-cycle cost. Structure and Infrastructure Engineering. 3:1, 29-41

Freeman, B. L., Jefferson, T., 2020. The simulation of transport processes in cementitious materials with embedded healing systems, International Journal for Numerical and Analytical Methods in Geomechanics, vol. 44, no. 2, pp. 293–326

Galván-Ruiz, M., Hernández, J., Baños, L., Noriega-Montes, J., Rodríguez-García, M.E., 2009. Characterisation of calcium carbonate, calcium oxide, and calcium hydroxide as starting point to the improvement of lime for their use in construction. Journal of Materials in Civil Engineering, 21, 694–698.

Ganesh, V. A., Raut, H. K., Nair, A. S., 2011, A review on self-cleaning coatings, Journal of Materials Chemistry, vol.21: 16304–16322.

Garba, M. D., 2012. Sodium silicate cement squeeze in massive salt formations: chemistry and chemical evolutions. Elixir Applied Chemsitry, 51, 10923-10931.

Gardner, D., Jefferson, A., Hoffman, A., Lark, R., 2014. Simulation of the capillary flow of an autonomic healing agent in discrete cracks in cementitious materials. Cement and Concrete Research, 58:35–44.

Gautam, A. K., Panigrahi, P. K., Kumar, S., 2017. Hydrodynamics around a shroud tube assembly of a fast breeder reactor. Nuclear Engineering and Design, 324, 297–314.

Giannaros, P., Kanellopoulos, A., Al-Tabbaa, A., 2016. Sealing of cracks in cement using microencapsulated sodium silicate. Smart Materials and Structures, 25, 84005.

Gibson, I., Rosen, D., Stucker, B., 2015. Development of Additive Manufacturing Technology (New York, NY: Springer New York)

Gilford, J., Hassan, M. M., Rupnow, T., Barbato, M., Okeil, A., 2014. Dicyclopentadiene and Sodium Silicate Microencapsulation for Self-Healing of Concrete. Journal of Materials in Civil Engineering, Vol. 26, Issue 526, 886.

Greenberg, S.A. & Sinclair, D. 1955, The Polymerisation of Silicic Acid, The Journal of physical chemistry, vol. 59, no. 5, pp. 435-440.

Greene, C. H., Frizzell, L. D., 1936. Studies of the precipitation of silver chloride. II. From silver nitrate and hydrochloric acid. Journal of the American Chemical Society, 58, 516-522.

Grosse, C.U., Ohtsu, M., 2008. Acoustic emission testing. Basics for research – applications in civil engineering Springer, pp. 396

Gu, G., Su, I., Sharma, S., Voros, J., 3D-printing of bio-inspired composites. Journal of Biomechanical Engineering, 138(2)

Guo, N., Leu, M.C., 2013. Additive manufacturing: technology, applications and research needs. Frontiers in Mechanical Engineering, 8, 215–43

Hager, M. D., Greil, Peter., Leyens, C., van der Zwaag, S., Schubert, U. S., 2010. Self-Healing Materials, Advanced materials, Vol.22, Issue 47, 5424-5430

Hall, C. and Tse, T. K. M., 1986. Water movement in porous building materials-VII. The sorptivity of mortars. Building and Environment, 21(2), 113-118.

Hamilton, A., Sottos N., White, A., 2010. Self-Healing of Internal Damage in Synthetic Vascular Materials, Advanced Materials, vol. 22, no. 45, pp. 5159-5163

Han, B., Wang, Y., Dong, S., 2015, Smart concretes and structures: A review, Journal of Intelligent Material Systems and Structures, Vol.26 (11): 1303–1345.

Hansen, C. J., Wu, W., Toohey, K. S., Sottos, N. R., White, S. R., Lewis, J. A., 2009. Self-healing materials with interpenetrating microvascular networks. Advanced Materials, 21(41):4143–47

Hassan, M.M., Mill, J., Rupnow, T., Al-Ansari, M., Daly, W.H., 2016. Microencapsulation of Calcium Nitrate for Concrete Applications. Transportation Research Record. 2577(1):8-16.

Heinglein, A., Meisel, D. 1998. Spectrophotometric Observations of the Adsorption of Organosulfur Compounds on Colloidal Silver Nanoparticles. The Journal of Physical Chemistry B, 102, 8364–8366.

Heywood, D. 2015. Biomimetic Vascular Networks for Self-Healing Concrete. CUED.

Hilloulin, B., Van Tittelboom, K., Gruyaert, E., De Belie, N., Loukili, A., 2015. Design of polymeric capsules for self-healing concrete. Cement and Concrete Composite, 55 (2015), pp. 298-307.

Hoff, G.C., 1991. Durability of offshore and marine concrete structures; 2nd international conference, pp.33-64.

Homma, D. Mihashi, H. Nishiwaki, T. 2009. Self-healing capability of fibre reinforced cementitious composites. Journal of Advanced Concrete Technology, 7, 217–228.

Hong, S., Qin, S., Dong, B., Xing, F., 2019. Corrosion Features of the Reinforcing Bar in Concrete with Intelligent OH- Regulation of Microcapsules. Materials, 2019, 12, 3966

Huang, H., Ye, G. 2011. Application of sodium silicate solution as self-healing agent in cementitious materials. In Proceedings of International Conference on Advances in Construction Materials through Science and Engineering, Hong Kong, China, 2011.30, 1969–1977.

Huang, H., Ye, G., Shui, Z., 2014b. Feasibility of self-healing in cementitious materials - By using capsules or a vascular system? Construction and Building Materials 63, 108–118.

Huang, J., Kim, J., Agrawal, N., Sudarsan, A.P., Maxim, J.E., Jayaraman, A. and Ugaz, V.M. (2009). Rapid Fabrication of Bio-inspired 3D Microfluidic Vascular Networks, Advanced Materials, 21(35): 35673571.

Hunt, L. B., The long history of lost wax casting, 1980. Gold Bulletin, 13, 63-79.

Hwang, J., Jeong, Y., Park, J. M., Lee, K. H., Hong, J. W., Choi, J., 2015. Biomimetics: forecasting the future of science, engineering, and medicine. International Journal of Nanomedicine, 10: 5701–5713.

Intergovernmental Panel on Climate Change (IPCC), 2004. Sources of CO_2. In IPCC, Special Report on Carbon Dioxide Capture and Storage. IPCC, 77–103.

Intergovernmental Panel on Climate Change (IPCC), 2018. Summary for Policymakers. Global warming of 1.5°C. An IPCC Special Report on the impacts of global warming of 1.5°C above pre-industrial levels and related global greenhouse gas emission pathways, in the context of strengthening the global response to the threat of climate change, sustainable development, and efforts to eradicate poverty. ISBN978-92-9169-151-7.

Irico, S., Bovio, A.G., Paul, G., Boccaleri, E., Gastaldi, D., Marchese, L., Buzzi, L., &Canonico, F. 2017. A Solid-State NMR and X-Ray Powder Diffraction Investigation of the Binding Mechanism for Self-Healing Cementitious Materials Design: The Assessment of the Reactivity of Sodium Silicate Based Systems. Cement and Concrete Composites 76. 57–63.

Isaacs, B. Lark, R. Jefferson, T. Davies, R. Dunn, S. 2013. Crack healing of cementitious materials using shrinkable polymer tendons. Structural Concrete, 14(2013), No.2, 138-147.

Jamróza, W., Kurek, M., Łyszczarz, E., Szafraniec, J., Knapik-Kowalczuk, J., Syrekb, K., Paluch, M., Jachowicz, R., 2017 3D printed orodispersible films with Aripiprazole. International Journal of Pharmaceutics, 533, 413–420.

Jefferson, A., Joseph, C., Lark, R.J., Isaacs, B., Dunn, Weager, S. B. 2010. A new system for crack closure of cementitious materials using shrinkable polymers. Cement and Concrete Research, 40, 795–801.

Jensen, O. M. and Hansen, P. F. 2001. Water-entrained cement based materials: I. Principles and theoretical background. Cement and Concrete Research, 31(4), 647–654.

Jensen, O. M. and Hansen, P. F. 2002. Water-entrained cement based materials: II. Experimental observations. Cement and Concrete Research, 32(6), 973–978.

Jiang, Z., Li, W., Yuan, Z. 2015. Influence of mineral additives and environmental conditions on the self-healing capabilities of cementitious materials. Cement and Concrete Composites, 57:116–127.

Jonkers, H.M., 2007. Self healing concrete: A biological approach. In Self Healing Materials: An Alternative Approach to 20 Centuries of Materials Science; van der Zwaag, S., Ed.; Springer: Dordrecht, The Netherlands, pp. 195–204.

Joseph, C., Jefferson, A.D., Isaacs, B., Lark, R., Gardner, D., 2010. Experimental investigation of adhesive-based self-healing of cementitious materials. Magazine of Concrete Research, 62, No. 11, November, p.831–843.

Joseph, C., 2008. Experimental and numerical study of the fracture and self-healing of cementitious materials. PhD thesis, Cardiff University.

Joseph, C., Jefferson, A. Isaacs, B., Lark, R., Gardner, D., 2010. Magazine of Concrete Research, 62, 831.

Joseph, C., Jefferson, A.D., Isaacs, B., Lark, R., Gardner, D., 2010. Experimental investigation of adhesive-based self-healing of cementitious materials. Magazine of Concrete Research, 62, 831–843.

Kacmarcik, J., Spahic, D., Varda, K., Porca, E. and Zaimovic-Uzunovic, N., 2018, August. An investigation of geometrical accuracy of desktop 3D printers using CMM. In IOP Conference Series: Materials Science and Engineering (Vol. 393, p. 012085).

Kakali, G., Tsivilis, S., Aggeli, E., Bati, M., 2000. Hydration products of C3A, C3S and Portland cement in the presence of $CaCO_3$, Cement and Concrete Research, 30 (7)

Kanellopoulos, A., Qureshi, T.S., Al-Tabbaa, A. 2015. Glass encapsulated minerals for self-healing in cement based composites. Construction and Building Materials, Vol. 98, 780-791.

Ke, J., McNeil, M., Price, L., Khanna, N. Z., Zhou, N., 2013. Estimation of CO_2 emissions from China's cement production: methodologies and uncertainties. Energy Policy. 57:172–81.

Kim, B. and Han, Y., 2017. Flexural performance of transparent plastic bar Reinforced concrete. Applied Sciences. 2018, 8, 325.

Koch, K., Bhushan, B., Barthlott, W., 2008, Diversity of structure, morphology and wetting of plant surfaces, Soft Matter, vol.4: 1943–1963.

Kolbasov, A., Sinha-Ray, S., Joijode, A., Hassan, M. A., Brown, D., Maze, B., Pourdeyhimi, B., Yarin, A. L., 2016. Industrial-scale solution blowing of soy protein nanofibers. Industrial & Engineering Chemistry Research, 55:323–33.

Lee, M.W., An, S., Jo, H.S., Yoon, S. S., Yarin, A.L., 2015b. Self-healing nanofiber-reinforced polymer composites: 2. Delamination /debonding, and adhesive and cohesive properties. ACS Applied Materials & Interfaces, 7:19555–61.

Lee, M.W., An, S., Jo, H.S., Yoon, S.S., Yarin, A.L., 2015a. Self-healing nanofiber-reinforced polymer composites: 1.Tensile testing and recovery of mechanical properties. ACS Applied Materials & Interfaces, 7:19546–54.

Leong, J., Lam,W., Ho, K., Voo, W., Lee, M. F., Lim, H., Lim, S., Tey, B., Poncelet, D., Chan, E. 2016. Advances in fabricating spherical alginate hydrogels with controlled particle designs by ionotropic gelation as encapsulation systems, Particuology, Vol. 24, p44-60

Lewins, J. D., 1994. Introducing the Lagrange multiplier to engineering mathematics. International Journal of Mechanical Engineering Education, 22, 191–207.

Li, V. C., Lim, Y. M., Chan, Y. M., 1998. Feasibility study of a passive smart self-healing cementitious composite. Composites Part B, 29 (B) (1998), pp. 819-827

Li, V., Yang, E., 2007. Self-healing in concrete materials, selfheal. mater. An Altern. Approach to 20 centuries. Materials Science. 100:161

Li, W., Jiang, Z., & Yang, Z., 2017. Acoustic characterisation of damage and healing of microencapsulation-based self-healing cement matrices. Cement and Concrete Composites, 84, 48-61.

Li, W., Zhu, X., Zhao, N., & Jiang, Z., 2016. Preparation and properties of melamine urea-formaldehyde microcapsules for self-healing of cementitious materials. Materials, 9(3), 152.

Li, Z., Souza, L. R., Litina, C., Markaki, A. E., Al-Tabbaa, A. 2020. A novel biomimetic design of a 3D vascular structure for self-healing in cementitious materials using Murray's law. Materials & Design, 190, 108572.

Liang, Z., Wang, Q., Dong, B., Jiang, B., Xing, F., 2018. Ion-triggered calcium hydroxide microcapsules for enhanced corrosion resistance of steel bars. RSC Adances, 8, 39536–39544

Lim, D., Kamotani, Y., Cho, B., Mazumder, J., Takayama, S. 2003. Lab on a Chip - Miniaturisation for Chemistry and Biology 3, 318–323.

Lim, L.S., Ahmad, I., Lazim, M.A.S.M., 2015. pH sensitive hydrogel based on poly (acrylic acid) and cellulose nanocrystals. Sains Malays, 44, 779–785.

Litina, C., Kanellopoulos, A., Al-Tabbaa, A., 2014 Alternative repair system for concrete using microencapsulated healing agents. Concrete Solutions, 97–103.

Liu, S. and Zuo, M., 2010. Influence of slag and fly ash on the self-healing ability of concrete. Advanced Materials Research, 306–307, 1020–1023.

Lopez-tendero, M. J. Diaz, P. Lloris, J. M. Gamon, C. 2011. Optimised hydrogel for application as repairing agents in cement based products. In Proceedings of 3rd International Conference on Self Healing Materials, Bath, UK, 27–29 June 2011.

Lv, S., Zhu, X., Qian, H., Qin, J., Jin, Q., Wang, X., 2016. Impact of ionic liquid properties on selective enrichment of glycerides in direct lipase-catalysed esterification. RSC Advances, Issue 10

Ma, C., Qin, Z., Zhuang, Y., Chen, L., Chen, B., 2015. Influence of sodium silicate and promoters on unconfined compressive strength of Portland cement-stablised clay. Soils and Foundations, Vol. 55, Issue 5, 1222-1232.

Ma, J., Lin, Y., Chen, X., Zhao, B., & Zhang, J., 2014. Flow behavior, thixotropy and dynamical viscoelasticity of sodium alginate aqueous solutions. Food Hydrocolloids, 38, 119–128.

Maes, M., Tittelboom, K. V., Belie, N. D., 2014.The efficiency of self-healing cementitious materials by means of encapsulated polyurethane in chloride containing environments. Construction and Building Materials, 71:528–537.

Mansur, H.S., Ore'fice, R.L., Mansur, A.A.P., 2004. Characterisation of poly (vinyl alcohol)/poly (ethylene glycol) hydrogels and PVA-derived hybrids by small-angle X-ray scattering and FTIR spectroscopy. Polymer, 45, 7193–7202.

Mansur, H.S., Sadahira, C.M., Souza, A.N., Mansur, A.A.P., 2008. FTIR spectroscopy characterisation of poly (vinyl alcohol) hydrogel with different hydrolysis degree and chemically crosslinked with glutaraldehyde. Materials Science and Engineering: C, 28, 539–548.

Marcilla, R., Alberto Blazquez, J., Rodriguez, J., Pomposo, J.A. and Mecerreyes, D., 2004. Tuning the solubility of polymerised ionic liquids by simple anion - exchange reactions. Journal of Polymer Science Part A: Polymer Chemistry, 42(1), pp.208-212.

MarketsandMarkets, Concrete Repair Mortars Market AD4535. Available online: https://www.marketsandmarkets.com/Market-Reports/concrete-repair-mortar-market-160103226.html (accessed on 5th August 2018).

Melchels, F.P., Feijen, J., Grijpma, D.W., 2010. A review on stereolithography and its applications in biomedical engineering. Biomaterials. 31(24):6121e30.

Meyer, W., Engelhardt, S., Novosel, E., Elling, B., Wegener, M. Krüger, H., 2012. Soft Polymers for Building up Small and Smallest Blood Supplying Systems by Stereolithography. Journal of Functional Biomaterials, 3 257–68

Mignon, A., Snoeck, D., Dubruel, P., Van Vlierberghe, S., De Belie, N. 2017. Crack Mitigation in Concrete: Superabsorbent Polymers as Key to Success? Materials (Basel), 10(3): 237.

Miguel, A. F., 2016. Toward an optimal design principle in symmetric and asymmetric tree flow networks. Journal of Theoretical Biology, 389, 101-109.

Mihashi, H., Kaneko, Y., Nishiwaki, T., Otsuka, K. 2000. Fundamental study on development of intelligent concrete characterised by self-healing capability for strength. Concrete Research and Technology 11(2):21-28.

Minnebo, P., Thierens, G.; de Valck, G., van Tittelboom, K., de Belie, N., van Hemelrijck, D., Tsangouri, E., 2017. A novel design of autonomously healed concrete: Towards a vascular healing network. Materials, 10, 49.

Mookhoek, S.D., Fischer, H.R., & Zwaag, S. Van Der. 2009. A Numerical Study into the Effects of Elongated Capsules on the Healing Efficiency of Liquid-Based Systems. Computational Materials Science, 47 (2), 506–11.

Morita T., Ambe D., Miki S., Kaeriyama H., Shigenobu Y., 2020. Impacts of the Fukushima Nuclear Accident on Fishery Products and Fishing Industry. In: Fukumoto M. (eds) Low-Dose Radiation Effects on Animals and Ecosystems. Springer, Singapore.

Murray, C. D. 1926a. The physiological principle of minimum work applied to the angle branching of arteries, Proceedings of the National Academy of Sciences of the United States of America, xii, 207, 835-841.

Murray, C. D. 1926b. The physiological principle of minimum work—I: The vascular system and the cost of blood volume. Proceedings of the National Academy of Sciences of the United States of America, 12, 207–214.Sangadji, S. 2017. Can self-healing mechanism helps concrete structures sustainable? Procedia Engineering 171, 238-249.

Nagasawa, K., Suzuki, T., Seto, R., Okada, M., Yue, Y., 2019. Mixing sauces: a viscosity blending model for shear thinning fluids. ACM Transactions on Graphics, Vol.38, No.4, article 95.

Nanthagopalan, P., & Santhanam, M. 2009. A New Empirical Test Method for the Optimisation of Viscosity Modifying Agent Dosage in Self-Compacting Concrete. Materials and Structures 43: 203–12.

Neville, A. 2002. Autogenous healing—A concrete miracle? International Journal of Concrete, 24, 76–82.

Ni, F., Wang, C., Zhao, H., 2017. Fabrication of water-soluble poly (vinyl alcohol)-based composites with improved thermal behavior for potential three-dimensional printing application. Journal of Applied Polymer Science, 134. doi:10.1002/app.44966.

Nishiwaki, T., Kwon, S., Homma, D. Yamada, M. Mihashi, H. 2014. Self-Healing Capability of Fiber-Reinforced Cementitious Composites for Recovery of Watertightness and Mechanical Properties. Materials, 7(3), 2141-2154.

Norris, C.J., Meadway, G.J., O'Sullivan, M.J., Bond, I.P., Trask, R.S., 2011a. Self-healing fibre reinforced composites via a bioinspired vasculature. Advanced Functional Materials, 21, 3624–33.

Norris, C.J., Bond, I.P., Trask, R.S., 2011b. The role of embedded bioinspired vasculature on damage formation in self-healing carbon fibre reinforced composites. Composites A. 42, 639–48.

Norris, C.J., Bond, I.P., Trask, R.S., 2011c. Interactions between propagating cracks and bioinspired self-healing vascular embeddeding glassfibre reinforced composites. Composites Science and Technology, 2011;71:847–53.

Nurudeen, S. and Abdulkarim, S. A., 2014, Characterisation of sodium silicate prepared from Kankara kaolin. Nigerian Journal of Scientific Research, 13(1).

OECD, 2020. Infrastructure maintenance (indicator). doi: 10.1787/c73dc965-en (Accessed on 2 August 2020)

Oeffner, J., and G. V. Lauder. 2012. The Hydrodynamic Function of Shark Skin and Two Biomimetic Applications. Journal of Experimental Biology, 215.5, 785-95.

Oun, A.A., Rhim, J.W., 2015. Preparation and characterisation of sodium carboxymethyl cellulose/cotton linter cellulose nanofibril composite films. Carbohydrate Polymers, 101, 101–109.

Pang, J. W. C., & Bond, I. P., 2005. A hollow fibre reinforced polymer composite encompassing self-healing and enhanced damage visibility. Composites Science and Technology, 65, 1791–1799.

Pang, J.W.C., Bond, I.P., 2005. 'Bleeding composites': damage detection and self-repair using a biomimetic approach. Composites A, 36(2):183–88

Pang, S.D., Tran Diep, P.T., Quek, S.T., 2009. On implementation of self-healing function in concrete—Proof of concept and practical issues. In Proceedings of 2nd International Conference on Self Healing Materials, Chicago, IL, USA, 28 June–1 July 2009.

Paques, J. P., van der Linden, E., van Rijn, C. J. M. & Sagis, L. M. C., 2014. Preparation methods of alginate nanoparticles. Advances in Colloid and Interface Science, 209, 163–171.

Park, S.J., Lee, J.E., Park, J.H., Lee, N.K., Lyu, M., Park, K., Koo, M.S., Cho, S.H., Son, Y., Park, S., 2018. Enhanced Solubility of the Support in an FDM-Based 3D Printed Structure Using Hydrogen Peroxide under Ultrasonication. Advances in Materials Science and Engineering, 2018, 3018761.

Patrick, J. F., Hart, K. R., Krull, B. P., Diesendruck, C. E., Moore, J. S., White, S. R., 2014. Continuous self-healing life cycle in vascularise dstructural composites. Advanced Materials, 26: 4302–8.

Patrick, J. F., Krull, B. P., Grag, M., Mangun, C. L., Moore, J. S., Sottos, N. R., White, S. R., 2017. Robust sacrificial polymer templates for 3D interconnected microvasculature in fiber-reinforced composites, Composites: Part A, 100, 361-370.

Pelletier, M.M., Brown, R., Shukla, A., Bose, A., 2011. Self-Healing Concrete with a Microencapsulated Healing Agent, Technical Report, Kingston. University of Rhode Island

Peng, P., 2017. A study on the origin of Chinese Lost-wax Casting from the perspectives of Art, Technology and social agency. Sino-platonic papers, No. 265.

Perkin Elmer Inc. 2006. An Introduction to Fluorescence Spectroscopy. Spectroscopy – via Retrieved 15 August 2013.

Persin, Z., Maver, U., Pivec, T., Maver, T., Vesel, A., Mozetic, A., Stana-Kleinschek, K., 2014. Novel cellulose based materials for safe and efficient wound treatment. Carbohydrate Polymers, 100, 55–64.

Polder, R. B., Peelen, W. H. A., Courage, W. M. G., 2012. Nontraditional assessment and maintenance methods for aging concrete structures—technical and non-technical issues. Materials and Corrosion, 63(12):1147–1153

Qamar, I.P., Sottos, N.R. and Trask, R.S., 2020. Grand challenges in the design and manufacture of vascular self-healing. Multifunctional Materials, 3(1), p.013001.

Qureshi, T. S., 2016. The role of expansive minerals in the autogenous and autonomic self-healing of cement based materials. PhD Thesis.

Qureshi, T. S., and Al-Tabbaa, A. 2016. Self-healing of drying shrinkage cracks in cement-based materials incorporating reactive MgO. Smart Materials and Structures, 25, 84004.

Qureshi, T., Al-Tabbaa, A., 2015. Influence of Expansive minerals on the Self-healing of Cement Paste and Mortar Systems, in: Fifth International Conference of Self-Healing Materials.

Qureshi, T., Al-Tabbaa, A., 2016. Self-healing of drying shrinkage cracks in cement-based materials incorporating reactive MgO. Smart Materials and Structure, 25, 1–16.

Rao, R., 2014. Biomimicry in Architecture, International Journal of Advanced Research in Civil, Structural, Environmental and Infrastructure Engineering and Developing, volume: 1 Issue: 3.

Razavi, M. S., Shirani, E., Salimpour, M. R. 2014. Development of a general method for obtaining the geometry of microfluidic networks, AIP Advances 4, 017109.

Reinhardt, H. W., Jooss, M., 2003. Permeability ans self-healing of cracked concrete as a function of temperature and crack width. Cement and Concrete Research, Vol. 33, Issue 7, page 981-985.

Rhim, J.W., Wang, L.F., Lee, Y., Hong, S.I., 2014. Preparation and characterisation of bio-nanocomposite films of agar and silver nanoparticles: Laser ablation method. Carbohydrate Polymers, 103, 456–465.

Risbud, M. V., Hardikar, A. A., Bhat, S. V., Bhonde, R. R., 2000. pH-sensitive freeze-dried chitosan–polyvinyl pyrrolidone hydrogels as controlled release system for antibiotic delivery. Journal of Controlled Release, 68 (2000) 23–30

Rodbard, S., 1975. Vascularcaliber.Cardiology. 60, 4–49.

Rodríguez-Mosqueda, R. and Pfeiffer, Heriberto. 2013. High CO_2 Capture in Sodium Metasilicate (Na_2SiO_3) at Low Temperatures (30–60°C) through the CO_2–H_2O Chemisorption Process. The Journal of Physical Chemistry C, 117 (26), 13452-13461.

Sachs, E. M., Haggerty, J. S., Cima, M. J. et al. US Patent 5,387,380, 1995.

Safiuddin, M., Kaish, A. B. M., Woon, C., Raman, S. N., 2018. Early-Age Cracking in Concrete: Causes, Consequences, Remedial Measures, and Recommendations. Applied Sciences, Vol. 8, Issue 10, 1730

Sahmaran, M., Yildirim, G., Ozbay, E., Ahmed, K., Lachemi, M., 2014. Self-healing ability of cementitious composites: effect of addition of pre-soaked expanded perlite. Magazine of Concrete Research, Volume 66 Issue 8.

Salentijn, G.I., Oomen, P.E., Grajewski, M., Verpoorte, E., 2017. Fused deposition modeling 3D printing for (bio) analytical device fabrication: Procedures, materials, and applications. Anal. Chem. 89, 7053–7061.

Salgado, L. T., Carvalho, R. T., Cinelli, L. P., Farina, M., 2007. The influence of brown algae alginates on phenolic compounds capability of UV absorption in vitro. Brazilian Journal of Oceanography, 55(2).

Sangadji, S. 2017. Can self-healing mechanism helps concrete structures sustainable? Procedia Engineering 171, 238-249.

Schlangen E., Joseph, C., 2009. Self-Healing Processes in Concrete, in Self- Healing Materials, Wiley-VCH Verlag GmbH & Co. KGaA, pp. 141–182.

Schmaljohann, D., 2006. Thermo- and pH-responsive polymers in drug delivery. Advanced Drug Delivery Reviews, 58, 1655–1670.

Schneider, M., Romer, M., Tschudin, M., Bolio, H., 2011. Sustainable cement production—present and future. Cement and Concrete Research, 41(7):642–50.

Schürch, D., Currao, A., Sarkar, S., Hodes, G., Calzaferri, G., 2002. The Journal of Physical Chemistry B, 106 12764.

Selvarajoo, T., Davies, R. E., Gardner, D. R., Freeman, B. L., Jefferson, A. D., 2020b. Characterisation of a vascular self-healing cementitious material system : Flow and curing properties, Construction and Building Material, vol. 245, p. 118332

Selvarajoo, T., Davies, R.E., Freeman, B.L., Jefferson, A.D., 2020a. Mechanical response of a vascular self-healing cementitious material system under varying loading conditions. Construction and Building Materials, 254 (2020), 119245

Sersale, R., Frigione, G., Bonavita, L., 1998. Acid depositions and concrete attack: Main influences. Cement and Concrete Research, 28, 19–24.

Shabbir, A., A Khan, M. M., Haroon, Y. S., Jaleel, H., 2017. Regulation of functional activities and essential oil production in Vetiveria zizanioides L. Nash after γ-irradiated sodium alginate elicitation. Turkish Journal of Biology, 41, 661-672.

Sharma, S., Sanpui, P., Chattopadhyay, A., Ghosh, S., 2012. Fabrication of antibacterial silver nanoparticle—sodium alginate–chitosan composite films. RSC Advances, 2012, 2, 5837-5843.

Shim, Y., Hong, G., Choi, S. 2018. Autogenous healing of early-age cementitious materials incorporating superabsorbent polymers exposed to wet/dry cycles. Materials, 11, 2476.

Sinha-Ray, S., Pelot, D. D., Zhou, Z. P., Rahman, A., Wu, X-F, Yarin, A. L., 2012. Encapsulation of self-healing materials by coelectrospinning, emulsion electrospinning, solution blowing and intercalation. Journal of Materials Chemistry, 22, 9138–46.

Sisomphon, K., Copuroglu, O., Fraaij, A., 2011. Application of Encapsulated Lightweight Aggregate Impregnated with Sodium Monofluorophosphate as a Self-Healing Agent in Blast Furnace Slag Mortar. Heron 2011, 56, 17–36.

Snoeck, D., Dewanckele, J., Cnudde, V. De Belie, N. 2016. X-ray computed microtomography to study autogenous healing of cementitious materials promoted by superabsorbent polymers. Cement and Concrete Composites, 65, 83-93.

Snoeck, D., Van Tittelboom, K., Steuperaert, S., Dubruel, P., De Belie, N. 2012. Self-healing cementitious materials by the combination of microfibres and superabsorbent polymers. Journal of Intelligent Material Systems and Structures, Vol 25(1) 13–24.

Sood, A.K., Ohdar, R., Mahapatra, S., 2010. Parametric appraisal of mechanical property of fused deposition modelling processed parts. Materials & Design, 31(1): 287e95.

Soukoulis, C., Fisk, I. D., Bohn, T., Hoffmann, L., 2016. Study of intragastric structuring ability of sodium alginate based o/w emulsions under in vitro physiological pre-absorptive digestion conditions. Carbohydrate Polymers, Vol. 140, 26-34.

Souza, L. Design and Synthesis of Microcapsules Using Microfluidics for Autonomic Self-Healing in Cementitious Materials. Ph.D. Thesis, University of Cambridge, Cambridge, UK , 2017.

Souza, L., 2017. Design and synthesis of microcapsules using microfluidics for autonomic self-healing in cementitious materials. PhD Thesis.

Söylev, T. A., Richardson, MG., 2008. Corrosion inhibitors for steel in concrete: state-of the-art report. Construction and Building Materials, 22(4):609–22.

Statista, 2019. Infrastrcuture needs-regional forecast 2017-2035

Stevanovic, M., Savanovic, I., Uskokovic, V., Skapin, D. S., Bracko, I., Jovanovic, U., Uskokovic, D. P., 2012. A new, simple, green, and one-pot four-component synthesis of bare and poly(α,γ,L-glutamic acid)-capped silver nanoparticles, Colloid PolymSci, vol.290, pp.221–231.

Sun, L., Yu, W., Ge, Q. 2011. Experimental research on the self-healing performance of micro-cracks in concrete bridge. Advanced Materials Research, 250–253:28–32

Taheri, S., Delgado, G.P., Agbaje, O. B. A., Giri, P., Clark, S.M., 2020. Corrosion Inhibitory effects of Mullite in Concrete Exposed to Sulfuric Acid Attack. Corrosion and Materials Degradation, 283-294

Teall, O., Davies. R., Pilegis, M., Kanellopoulos, A., Sharma, T., Paine, K., Jefferson, A., Lark, R., Gardner, D., Al-Tabbaa, A., 2016. Self-healing concrete full-scale site trials. 11th FIB Int. PhD Symp. Civil Eng, Tokyo.

Thao, T.D.P. 2011. Quasi-Brittle Self-Healing Materials: Numerical Modelling and Applications in Civil Engineering. PhD Thesis, National University of Singapore.

The Boston Consulting Group., 2014. Overview of 2014 WEF and BCG report: Strategic infrastructure.

The Boston Consulting Group., 2015. The Lean Advantage for Large Construction Projects: Industrializing Project Execution to Create Value. Boston: Boston Consulting Group.

Therriault, D., Shepherd, R. F., White, S. R., Lewis, J. A., 2005. Fugitive inks for direct write assembly of three-dimensional microvascular networks. Advanced material, Vol. 17, No 4

Tilly, G. and Jacobs, J. 2007. Concrete repairs: Performance in service and current practice, ; Taylor and Francis, BRE Press.

Tognonvi, M.T., Rossignol, S., Bonnet, J. 2011. Physical-chemistry of sodium silicate gelation in an alkaline medium. Journal of Sol-Gel Science and Technology, 58, 625–635.

Tong, A., Tang, X., Zhang, F., Wang, B., 2020. Study on the shift of ultraviolet spectra in aqueous solution with variations of the solution concentration, Spectrochimica Acta Part A: Molecular and Biomolecular Spectroscopy 234, 118259.

Toohey, K. S., Hansen, C. J., Lewis, J. A., White, S. R., Sottos, N. R., 2009. Delivery of two-part self-healing chemistry via microvascular networks. Advanced functional materials, 19, 1399-1405.

Trask, R. S., Williams, H. R. & Bond, I. P. 2007a Self-healing polymer composites: mimicking nature to enhance performance. Bioinspiration & Biomimetics, 2, 1–9.

Tsangouri, E., Lelon, J., Minnebo, P., Asaue, H., Shiotani, T., Van Tittelboom, K., De Belie, N., Aggelis, D.G. and Van Hemelrijck, D., 2019. Feasibility study on real-scale, self-healing concrete slab by developing a smart capsules network and assessed by a plethora of advanced monitoring techniques. Construction and Building Materials, 228, p.116780.

UK Treasury, 2016. National Infrastructure Delivery Plan 2016-2021. HM Treasury, London, UK.

United Nations, Department of Economic and Social Affairs, Population Division, 2018. World Urbanisation Prospects: The 2018 Revision, Online Edition. (Accessed on 2 August 2020)

Van Belleghem, B., Montoya, R., Dewanckele, J., Van den Steen, N., De Graeve, I., Deconinck, J., Cnudde, V., Van Tittelboom, K. and De Belie, N., 2016. Capillary water absorption in cracked and uncracked mortar–A comparison between experimental study and finite element analysis. Construction and Building Materials, 110, pp.154-162.

Van Tittelboom, K. and De Belie, N. 2013. Self-Healing in Cementitious Materials—A Review. Materials, 6, 2182-2217.

Van Tittelboom, K., De Belie, N., Van Loo, D., Jacobs, P. 2011a. Self-healing efficiency of cementitious materials containing tubular capsules filled with healing agent. Cement and Concrete Composites, 33, 497–505.

Van Tittelboom, K., Adesanya, K., Dubruel, P., Van Puyvelde, P. De Belie, N. 2011b. Methyl methacrylate as a healing agent for self-healing cementitious materials. Smart Materials and Structures, 20.

Van Tittelboom, K., De Belie, N., Lehmann, F. and Grosse, C.U., 2012. Acoustic emission analysis for the quantification of autonomous crack healing in concrete. Construction and Building Materials, 28(1), pp.333-341.

Van Tittelboom, K., Gruyaert, E., Rahier, H., De Belie, N., 2012. Influence of mix composition on the extent of autogenous crack healing by continued hydration or calcium carbonate formation. Construction and Building Materials, 37, 349–359.

Van Tittelboom, K., Tsangouri, E., Van Hemelrijck, D. and De Belie, N., 2015. The efficiency of self-healing concrete using alternative manufacturing procedures and more realistic crack patterns. Cement and Concrete Composites, 57, pp.142-152.

Van Tittelboom, K., Wang, J., Araújo, M., Snoeck, D., Gruyaert, E., Debbaut, B., Derluyn, H., Cnudde, V., Tsangouri, E., Van Hemelrijck, D. and De Belie, N., 2016. Comparison of different approaches for self-healing concrete in a large-scale lab test. Construction and Building Materials, 107, pp.125-137.

Vibhooti, P., Rajan, G., Seema, B., 2013. Eudragit and Chitosan – The Two Most Promising Polymers for Colon Drug Dilevery. International Journal of Pharmaceutical & Biological Archives, 4(3): 399 – 410

Wang, J. Y., Soens, H. Verstraete, W., De Belie, N. 2014. Self-healing concrete by use of microencapsulated bacterial spores. Cement and Concrete Research, 56:139–152.

Wang, J., De Belie, N., Verstraete, W. 2012a. Diatomaceous earth as a protective vehicle for bacteria applied for self-healing concrete. Journal of Industrial Microbiology & Biotechnology, 39, 567–577.

Wang, J., Van Tittelboom, K., De Belie, N. 2012b. Verstraete, W. Use of silica gel or polyurethane immobilised bacteria for self-healing concrete. Construction and Building Materials, 26, 532–540.

Wang, K.M., Lorente, S. Bejan, A. 2006. Vascularised networks with two optimised channel sizes Journal of Physics D: Applied Physics, 39, 3086–96

Wang, K.M., Lorente, S. Bejan, A. 2007. Vascularisation with grids of channels: multiple scales, loops and body shapes. Journal of Physics D: Applied Physics, 40, 4740–9

Wang, X., Jiang, M., Zhou, Z., Gou, J., Hiu, D., 2017. 3D printing of polymer matrix composites: A review and prospective. Composites Part B, 110, 442-458

Wang, X., Sun, P., Han, N., Xing, F.,2017. Experimental Study on Mechanical Properties and Porosity of Organic Microcapsules Based Self-Healing Cementitious Composite Materials, 10, 20.

Wang, X., Xing, F., Zhang, M., Han, N., & Qian, Z., 2013. Experimental study on cementitious composites embedded with organic microcapsules. Materials, 6(9), 4064-4081.

Wang, Y. S., Ding, W. J., Fang, G. H., Liu, Y. Q., Xing, F., Dong, B. Q., 2016. Feasibility study on corrosion protection of steel bar in a self-immunity system based on increasing OH^- content. Construction and Building Materials, 125, 742–748

Wang, Y., Pham, D. T., Ji, C., 2015. Self-healing composites: A review. Self-healing composites: A review, Cogent Engineering, 2:1.

White, S. R., Sottos, N. R., Geubelle, P. H. Moore, J. S., Kessler, M. R., Sriram, S. R., Brown, E. N., Viswanathan, S., 2001 Autonomic healing of polymer composites. Nature. 409, 794–797.

Wiener, M.S., Salas, B.V., 2005. Corrosion of the marine infrastructure in polluted seaports, Corrosion Engineering. SciTechnol, 40, 137–142.

Williams, H. R., Trask, R. S., Knights, A. C., Williams, E. R. Bond, I. P. 2008. Biomimetic reliability strategies for self-healing vascular networks in engineering materials. Journal of the Royal Society Interface, 5, 735–747.

Williams, H.R., Trask, R.S. and Bond, I.P., 2007. Self-healing Composite Sandwich Structures, Smart Materials and Structures, 16(4): 11981207.

Williams, H.R., Trask, R.S. and Bond, I.P., 2008b. Self-healing Sandwich Panels: Restoration of Compressive Strength After Impact, Composites Science and Technology, 68(1516): 31713177.

World Bank, 2014. Putting a price on carbon with a tax.

World Economic Forum., 2015. Strategic Infrastructure: Mitigation of Political & Regulatory Risk in Infrastructure Projects. Geneva: World Economic Forum.

World Economic Forum., 2016. Shaping the Future of Construction A Breakthrough in Mindset and Technology. Geneva: World Economic Forum.

Xiong, W., Tang, J., Zhu G., Han N., Schlangen E., Dong, B., Wang, X., Xing F., 2015. A novel capsule-based self-recovery system with a chloride ion trigger. Scientific Reports, 5:10866.

Xue, C., Li, W., Li, J., Tam, V.W.Y., Ye, G., 2018. A review study on encapsulation-based self-healing for cementitious materials. Structural Concrete, 20:198–212.

Yadav, M., Liu, Y., Chiu F., 2019. Fabrication of Cellulose Nanocrystal/Silver/Alginate Bionanocomposite Films with Enhanced Mechanical and Barrier Properties for Food Packaging Application. Nanomaterials, 9, 1523.

Yang, J., Zheng, H., Han, S., Jiang, Z., Chen, X. 2015. The synthesis of nano-sliver/sodium alginate composites and their antibacterial properties. RSC Advances, 5, 2378-2382.

Yuhazri, M. Y., Hafiz, K.M., Myia, Y. Z. A., Jia, C. P., Sihombing, H., Sapuan, S. M., Badarulzaman, N. A., 2017. The Effect of Different Shape and Perforated rHDPE in Concrete Structures on Flexural Strength. IOP Conf. Series: Journal of Physics: Conf. Series 914 (2017) 012023.

Zeng, L. W., Song, R. X., 2013. Controlling chloride ions diffusion in concrete. Scientific Reports, 3, 3359.

Zhang, X., Han, Q., Sheng, G., 2016. Light-induced reduction of silver ions to silver nanoparticles in aquatic environments by microbial extracellular polymeric substances (EPS). Water research, 106 (2016) 242-248.

Zhang, Z., Hu, J., Ma, H., 2019. Feasibility study of ECC with self-healing capacity applied on the long-span steel bridge deck overlay. International Journal of Pavement Engineering, Vol. 20, Issue 8, 884-893

Zhao, Y.L., Huang, Z., Zhang, J., Wu, W., Wang, M. and Fan, L., 2010. Thermal degradation of sodium alginate-incorporated soy protein isolate/glycerol composite membranes. In Proceedings of the 17th Iapri World Conference on Packaging (pp. 402-405).

Zheng, G.Q., Li, X.D.; Wang, X.M., Ma, J.F., Gu, Z.W., 2008. Structural characteristics of poly (vinyl alcohol)–calcium carbonate composites prepared by sequential method. Advances in Applied Ceramics,107, 46–51.

Zhou, H., Zhu, H., Yang, X., Zhang, Y., Zhang, X., Cui, K., Shao, L., Yao, J., 2014. Temperature/pH sensitive cellulose-based hydrogel: Synthesis, characterisation, loading, and release of model drugs for potential oral drug delivery. BioResources 10, 760–771.